A model to study the consequences of human actions in the Guadalquivir River Estuary

PHD PROGRAMME ON DYNAMICS OF BIOGEOCHEMICAL FLUXES AND ITS APPLICATIONS

UNIVERSIDAD DE GRANADA

Dinámica Ambiental
UNIVERSIDAD DE GRANADA

cei·mar
campus de excelencia internacional del mar

IISTA

Manuel Cobos Budia

GRANADA 2020

Directores:
Asunción Baquerizo Azofra
Miguel Ángel Losada Rodríguez

Tutor:
Manuel Díez Minguito

Editor: Universidad de Granada. Tesis Doctorales
Autor: Manuel Cobos Budia
ISBN: 978-84-1306-581-6
URI: http://hdl.handle.net/10481/65374

Agradecimientos


```
print('Gracias Mundo')
```

Así comenzó el primer script en Python que escribí allá por septiembre de 2013. Lo hice con el objetivo de cambiar de lenguaje de programación a la par que aprender a vectorizar y paralelizar procesos de cálculo para mejorar el rendimiento del programa de evolución de la costa que desarrollé durante el máster de Hidráulica Ambiental de la Universidad de Granada. Medio año más tarde, el Campus de Excelencia Internacional del Mar (CeiMar) concedía cinco contratos que financiaban la tesis doctoral durante un límite de tres años. Casi dos años después del término de este plazo, me encuentro cumpliendo el requisito ISCED 8 y trabajando en diversos proyectos de investigación en el Grupo de Dinámica de Flujos Ambientales. Por todo esto, gracias grupo.

El requisito se cumple, fundamentalmente, por la formación recibida, el inestimable apoyo y la dedicación de los profesores Miguel Ángel Losada, Asunción Baquerizo y Manuel Díez. A Miguel, por creer en mí, darme la oportunidad y enseñarme el oficio de "pelotari científico", el cual todavía no controlo. A Asunción Baquerizo, por insistir en el rigor, la disciplina y la perseverancia. A Manuel Díez, por esas charlas de física y por su humanidad tan precisas en determinados momentos de mi vida. Los tres habéis guiado y arrojado luz en mi camino. Gracias, profesores.

Como en todo camino, vivo, real e intenso aparecen personas cuyas trayectorias coincidieron en mayor o menor medida con la mía. Parte de estas personas se encuentran o encontraban en el seno del Grupo de Dinámica de Flujos Ambientales de la Universidad de Granada y los recuerdos de conversaciones, risas, aclaraciones, discusiones y gestos, me producen nostalgia hoy. No voy a dar una lista interminable de ellas, simplemente, si algún día leen estas palabras sabrán que me refiero a ellas. A todas estas personas, gracias.

Las personas y los recuerdos no sólo han aparecido en el ámbito académico: una charla tranquila con los amigos explicando el "exchange flow" en Sanlúcar de Barrameda con los pies en el Guadalquivir, o una noticia que te envía tu hermano al que le suena algo que hablaste sobre el puerto de Sevilla. Tengo la suerte, a mi parecer, de que todas estas personas han contribuido positiva y significativamente en mi vida, y por ende, en esta tesis. A todas ellas, gracias.

Hay una cita que me gusta mucho que dice: *Sé paciente, las cosas siempre son difíciles antes de pasar a ser fáciles*. Y es que si hay algo que ha permitido que finalmente se escriba esta tesis, es eso mismo, la paciencia, y su aliado, el tiempo. Paciencia no sólo por mi parte, que tengo mucha, sino por mi familia, que me ha visto trabajando duro hasta altas horas, me ha visto avanzar, retroceder, maldecir y hasta conjurar en diversas lenguas, y aún así, me siguen apoyando cada día. Familia, gracias, esta tesis también es vuestra.

Se termina un trayecto de mi camino y comienza otro. Toca recibirlo como se merece, con fuerza y más positivo que nunca; con los brazos bien abiertos. Así que sólo me queda añadir:

```
print('Hola Mundo')
```

Acknowledgements of figures

- Image of TOC, List of Figures and List of Tables: "Flamencos en Doñana al atardecer" - Diego López/WWF España
- Image of Chapter 2: "A oceanographic buoy at the museum of the port of Seville", own image.
- Image of Chapter 5: "Fort Denison Tide Gauge" by Peter L. Johnson in Wikipedia.
- Image of Chapter 6: "Sea and clouds at the sunset" by Maysam Yabandeh in Pixnio.
- Image of Chapter 7: "The Guadalquivir River Estuary from the harbor lock of the port of Seville" by David Ramírez Lopera.
- Image of Chapter 8: "Freshwater in a fountain" by Josep Monter in Pixabay.
- Image of Bibliography: "Trinity College library, University of Dublin, Ireland" by David Lliff in Wikipedia.

Abstract

Estuaries are places located in the transition region between rivers and seas. Their waters may be used for navigation and fishing and their lands for farming activities. They are among the most productive, complex and vulnerable ecosystems on Earth. Despite their fragility, they have been suffering the effects of many human interventions, such as the occupation of plains, modification of channels, meander cuts and deepening works and control of the flowing water. This situation has been a constant source of conflict of interests and competencies between users and the administration due to the adoption of uncoordinated and inefficient management decisions. The Guadalquivir River Estuary (hereinafter GRE), located in the southwest of Spain, is a hot spot that is not alien to this situation. The Chapter 1 presents a historical overview of the management activities of the estuary promoted mainly by politicians, port managers, environmentalists and farmers and the human induced changes associated to them. The future of the GRE in the shadow of climate change adds more uncertainty to the current critical situation. In this context, the main objective of this thesis is to analyze and characterize the dynamics of the GRE by developing a model for the analysis of the temporal and spatial variation of the longitudinal anomaly of the potential energy. The model can be used with management purposed to improve the water quality of the estuary. Six specific goals were proposed and addressed in Chapters 2 to 7 in order to meet this overall objective.

A brief review of the fundamentals of hydrodynamic estuarine processes and of the main observational datasets at GRE are presented in Chapter 2.In relation to the first ones, the state of-art in estuarine dynamics in water column mixing and stratification processes associated to the potential energy and its transport are presented. On the other hand, the main observational and modeled datasets are explored. Luckily, a real-time monitoring network along the GRE was deployed within a project leaded by the University of Granada and the Institute of Marine Sciences of Andalusia (ICMAN, Spanish acronym) (CSIC) with the same name as the present thesis. This information allowed gaining knowledge about the spatial/temporal variability of water levels, salinity, temperature, turbidity, water currents and wind fields, solar radiation and fresh-water discharges. The review ends with some important conclusions regarding the need to modify the dynamic equation of potential energy anomaly to include from weakly stratified to well-mixed conditions and the characteristics of the GRE that allow the application of the model.

On the basis of those conclusions, Chapter 3 presents the formulation of a subtidal-scale dynamic equation of energy that evaluates the Longitudinal Anomaly of Potential Energy (LAPE). The LAPE integrates salinity, temperature, suspended solid concentration and flow velocity throughout the estuary in different fluvial regimes (i.e. low-river flow, $Q_d \leq 40$ m^3/s; high-river flow, $Q_d > 400$ m^3/s; and post-riverflood recovery) and tidal regimes (neap and spring tides) and the transport processes that control them. Results show the informative capacity of the LAPE analysis. Among other information extracted from the analysis, it is found that the LAPE transports are modulated by neap and spring tides during low-river flows; the tidal pumping term is dominant upstream; an area is found where transport convergence and divergence occur and where the estuarine turbidity maxima are found; during high-river flows, longitudinal profiles of LAPE are inverted due to both the longitudinal dispersion and differential advection, terms that bring energy to the estuary; during the post-river flood recovery period all transport processes are intensified except the Stokes-induced transport, and the longitudinal gradient of LAPE transport is amplified, which favors the reappearance of the convergence and divergence zone.

The LAPE balance equation together with the mass balance is applied to the GRE in Chapter 4.The water density and the semidiurnal water mass exchanges are determined as a linear system of equations in five-interconnected stretches of the estuary. The model does not only include the

effects of freshwater discharges, Stokes transport, solar radiation and tidal and wind mixing, but also the tidal pumping term. The results provide valuable information that might serve as a tool for the design of new effective management strategies for water discharges at the upstream dam (Alcalá del Río). The results highlight that at the mid-estuary, during neap-spring transitions, a negative (upstream directed) water mass exchange causes the blockage of the estuary. The water mass exchange is directly related to the residence and flushing times. The residence times of every box are equal during neap tides. Conversely, it takes almost 80% of the time for the water to travel along the middle part of the estuary (35.3 to 57.6 km) during spring tides. The model reveals that the flushing time of the GRE in normal conditions ranges from 40 to 90 days and increases before blockage conditions.

Chapter 5 addresses the forecasting of climatic and tidal conditions at GRE. Field observations are used to validate the statistical analysis, and theoretical and empirical models are used to forecast the freshwater discharges, the velocity field, the tidal elevations and currents, the radiation fluxes and the mean sea-level in a mid- to long-term basis. The simulated time series are compared to the original dataset by using iso-probability percentiles, Q-Q plots, correlation and cross-correlation functions, bivariate relationship between variables, peaks or extreme values. The spatial and temporal variability are adequately represented, so it provides the inputs to define and test the performance of several management scenarios and strategies.

In Chapter 6, a special emphasis is given to the study of the changes of tidal constituents in the GRE due to the key role that tides play in the estuarine hydrodynamics. The study is based on the short-time harmonic analysis to extract M_2, S_2, N_2, K_1, O_1, and M_4 from hourly sea-level records longer than 17 years. The generalized linear squared fit method is used to estimate the rate of change of the tidal amplitudes and phases. The analysis is extended to the tidal gauges along the Spanish coast. The results show that both semidiurnal and diurnal tidal amplitudes decrease with time. Overall, their values are lower than relative sea level rates analyzed in one and two orders of magnitude, respectively. The largest negative trends of M_2 are found at the mouth of some major estuaries, such as Ria de Vigo ($-1.28 \pm 0.07\,\mathrm{mm/yr}$) and the Guadalquivir River Estuary ($-2.88 \pm 0.12\,\mathrm{mm/yr}$). The seasonal variability of the M_2 is, in average terms, an order of magnitude greater than the mean sea-level rise. Therefore, it is recommended that the temporal variability of the M_2 is included in the hydrodynamic and flooding models since its concomitance with storm events could lead to extreme flooding events.

Finally, in Chapter 7, the model is set up to reproduce six scenarios: (i) current conditions; (ii) including climate change-induced sea-level and tidal current changes; (iii) freshwater decrease; (iv) with a channel deepening; (v) considering a strong regulation of Q_d; and (vi) maintaining a given density in a specific stretch. The results validate the new hydrodynamic model for accounting exchange flows, mixing densities and flushing times, and at the same time, enabling some strategies for an effective control of water quality as the maintaining of a minimum water discharge (Q_d between 80 and 120 m^3/s) to promote natural circulation, reducing the flushing time which equivalently increase the water quality. The estuary of the Guadalquivir River has now a model that allows evaluating water quality in terms of its dynamics using flushing times.

Resumen

Los estuarios se encuentran en la transición de ríos y mares. Sus aguas se utilizan para navegar o pescar y sus tierras para cultivar. Los estuarios no son solo uno de los ecosistemas más productivos de la Tierra, sino también uno de los más complejos y vulnerables. A pesar de su fragilidad, se invaden sus llanuras, se modifican sus canales, se realizan cortas y se profundizan sus fondos, habitualmente, con el objetivo de controlar el agua que fluye o de reducir la distancia que existe hasta el puerto. Estas actuaciones suelen ser el origen de diversos conflictos de intereses y competencias entre los usuarios y los gestores de sus aguas que lleva a la adopción de medidas de gestión descoordinadas e ineficientes, visibles en la mayoría de los estuarios del planeta. En este sentido, el estuario del río Guadalquivir (GRE, en lo sucesivo), que se encuentra en el suroeste de España, es un enclave que no es ajeno a esta situación. Así, el Capítulo 1 presenta una visión histórica general de los cambios en el GRE. Estos cambios han sido propiciados por los principales agentes interesados (políticos, gestores de puertos, agricultores y defensores del medioambiente) que definieron las pautas de funcionamiento del estuario. A ellos hay que añadir la incertidumbre del futuro del estuario en un escenario de cambio climático. En este contexto se define como objetivo principal de esta tesis el análisis y la caracterización de la dinámica del GRE para desarrollar un modelo que integre las variables principales que definen el sistema, que los administradores de estuarios puedan usar para mejorar la calidad del agua del estuario. Para cumplir con este objetivo general, se proponen seis objetivos específicos que se abordan en los Capítulos 2 hasta 7.

En el Capítulo 2 se presenta una breve revisión de los fundamentos hidrodinámicos de los procesos estuarinos, así como de los principales conjuntos de datos observados en el GRE. Por un lado, se presenta el estado del arte sobre los procesos de estratificación y mezcla en estuarios que se relacionan con la energía potencial y su transporte. Por otro lado, se exploran los principales conjuntos de datos observacionales y obtenidos a partir de ellos. Afortunadamente, durante un proyecto liderado por la Universidad de Granada y el ICMAN (CSIC) con el mismo nombre que esta tesis, se implementó una red de monitorización en tiempo real a lo largo del GRE. El análisis de los datos registrados durante un año ha aportado información relevante sobre la variabilidad espacial y temporal de los niveles del mar, salinidad, temperatura, turbidez, corrientes y campo de vientos, radiación solar y descargas de agua dulce. La revisión termina con algunas conclusiones sobre la necesidad de modificar la ecuación de balance de la anomalía de energía potencial para incluir condiciones de estratificación débil o mezcla completa y las características del GRE que permiten la aplicación de un modelo para estudiar la calidad de sus aguas.

En el Capítulo 3 se desarrolla una ecuación dinámica de la energía a escala submareal para evaluar la Anomalía Longitudinal de Energía Potencial (LAPE). La LAPE integra la salinidad, la temperatura, la concentración de sólidos en suspensión y la velocidad del flujo en todo el estuario y para diferentes regímenes fluviales (es decir, régimen de aguas bajas, $Q_d \leq 40$ m^3/s; régimen de descargas, $Q_d > 400$ m^3/s; y recuperación posterior a la descarga) y regímenes de mareas (mareas vivas y muertas), además de los transportes que los controlan. Los resultados muestran la capacidad informativa del análisis de la anomalía longitudinal de la energía potencial (LAPE). Se observa cómo el transporte de LAPE está modulado por las mareas vivas y muertas durante el régimen de aguas bajas o cómo la convergencia y divergencia del transporte señalan la ubicación de los máximos de turbidez del estuario. Además, durante el régimen de descargas, los perfiles longitudinales de LAPE se invierten, siendo la dispersión longitudinal y la advección diferencial, los términos que transportan energía al estuario. Durante los periodos de recuperación, todos los procesos de transporte se intensifican excepto el transporte inducido por Stokes. En estas condiciones, el gradiente longitudinal del transporte de LAPE se amplifica, lo que provoca la reaparición de las zonas de convergencia y divergencia. Finalmente, el término de bombeo mareal aparece como el término dominante aguas arriba.

El balance de LAPE junto con el balance de masa se aplica al GRE en el Capítulo 4. Con dichas ecuaciones se determinan los intercambios de masa de agua y la densidad de mezcla a escala semidiurna de cinco tramos interconectados del estuario, obteniéndose un sistema lineal de ecuaciones. El modelo no solo incluye los efectos de la descarga fluvial, el transporte de Stokes, la radiación solar y la mezcla por la corriente de marea o el viento, sino también el término de bombeo mareal. Los resultados resaltan que, en la mitad del estuario, en las transiciones entre mareas muertas y vivas se produce un intercambio negativo (dirigido aguas arriba) de las masas de agua produciendo lo que se ha denominado como bloqueo del estuario. El intercambio de masa de agua se relaciona con los tiempos de residencia y de renovación. Se ha encontrado que los tiempos de renovación de cada tramo son similares en condiciones de mareas muertas. Por el contrario, durante mareas vivas el agua tarda casi el 80% del tiempo en viajar a lo largo de la parte media del estuario (del kilómetro 35.3 hasta el 57.6). El modelo revela que el tiempo de residencia del GRE en condiciones normales varía de 50 a 90 días y que aumenta antes de producirse el bloqueo. Los resultados que se obtienen en este capítulo proporcionan información muy valiosa que puede servir de guía para el diseño de estrategias de gestión de las descargas de agua desde la presa de cabecera (Alcalá del Río).

El capítulo 5 aborda la simulación de las condiciones climáticas y de marea en el GRE. Las observaciones de campo se utilizan para validar el análisis estadístico y los modelos teóricos y empíricos para pronosticar las descargas de agua dulce, el campo de velocidades, las elevaciones y corrientes de marea, los flujos de radiación y el nivel medio del mar a medio y largo plazo. Las series temporales obtenidas se comparan con el conjunto de observaciones mediante curvas de iso-probabilidad, gráficos Q-Q, funciones de auto-correlación y correlación cruzada, relación bivariada entre variables o el análisis de picos sobre un umbral y valores extremos. La variabilidad espacial y temporal se representa de manera adecuada, lo que proporciona la base para la definición y comprobación de varios escenarios y estrategias de gestión.

En el Capítulo 6, se centra en el estudio de los cambios de las constituyentes mareales debido al papel clave que desempeñan éstas en la hidrodinámica del GRE. El estudio se basa en el análisis armónico a corto plazo para extraer M_2, S_2, N_2, K_1, O_1 y M_4 de un registro horario de nivel del mar superior a 17 años. Además, se utiliza el método de mínimos cuadrados generalizados para estimar la tasa de cambio de las amplitudes y fases de las constituyentes. El análisis se extiende a los mareógrafos de toda la costa española. Los resultados muestran una tendencia decreciente de las amplitudes de las mareas semidiurnas y diurnas. En general, los valores son más bajos que las tasas relativas de descenso de nivel medio del mar analizados, en uno y dos órdenes de magnitud, respectivamente. Las tendencias negativas más importantes de la M_2 se encuentran en la desembocadura de algunos estuarios importantes, como la Ría de Vigo (-1.28 ± 0.07 mm/año) y el estuario del río Guadalquivir (-2.88 ± 0.12 mm/año). La variabilidad estacional de la M_2 es, en términos medios, un orden de magnitud mayor que el aumento del nivel medio del mar, por lo que se deduce que es recomendable incluir la variabilidad temporal de la M_2 en los modelos hidrodinámicos y de inundaciones ya que su concomitancia con tormentas podría dar lugar a eventos de inundación extremos.

Finalmente, en el Capítulo 7 se configura el modelo para permitir seis escenarios: (i) en las condiciones actuales, (ii) incluyendo el ascenso del nivel medio del mar y la reducción de las constituyentes mareales como resultado del cambio climático global, (iii) con una reducción del caudal de descarga, (iv) incluyendo una profundización del canal principal, (v) con una regulación fuerte de Q_d, y (vi) manteniendo una densidad dada en un tramo concreto. Los resultados validan el nuevo modelo hidrodinámico para cuantificar los flujos de intercambio, la densidad de mezcla y los tiempos de residencia, y al mismo tiempo, permitir algunas estrategias de control efectivo de la calidad del agua como, por ejemplo, el mantenimiento de una descarga mínima de agua (Q_d

entre 80 y 120 m^3/s) para promover la circulación natural, reduciendo el tiempo de descarga que aumenta de manera equivalente la calidad del agua. El estuario del Río Guadalquivir cuenta desde este momento con un modelo que permite evaluar el estado de la calidad de sus aguas en términos de su dinámica y aprovechando el concepto de tiempo de residencia.

Contents

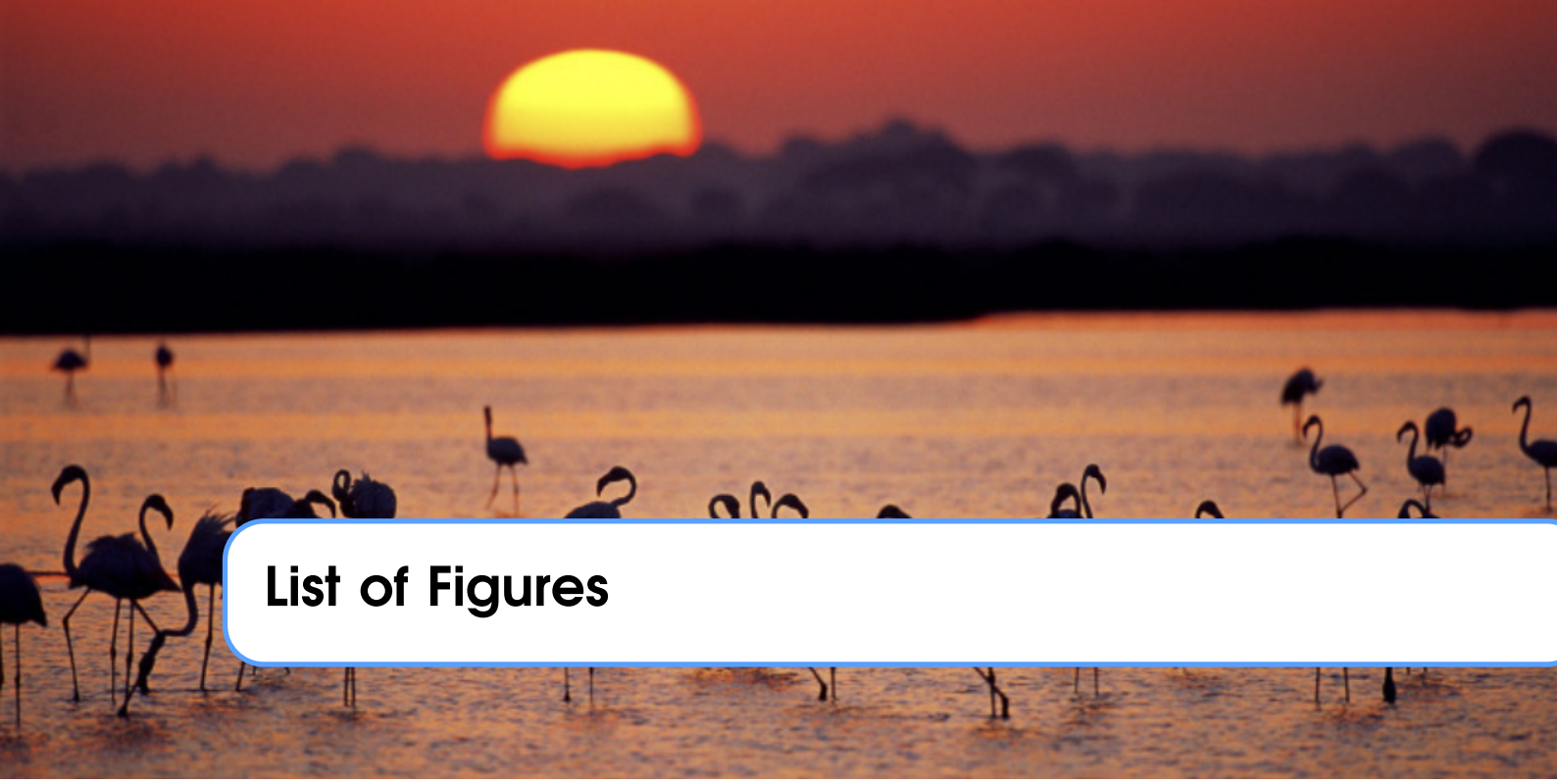

List of Figures

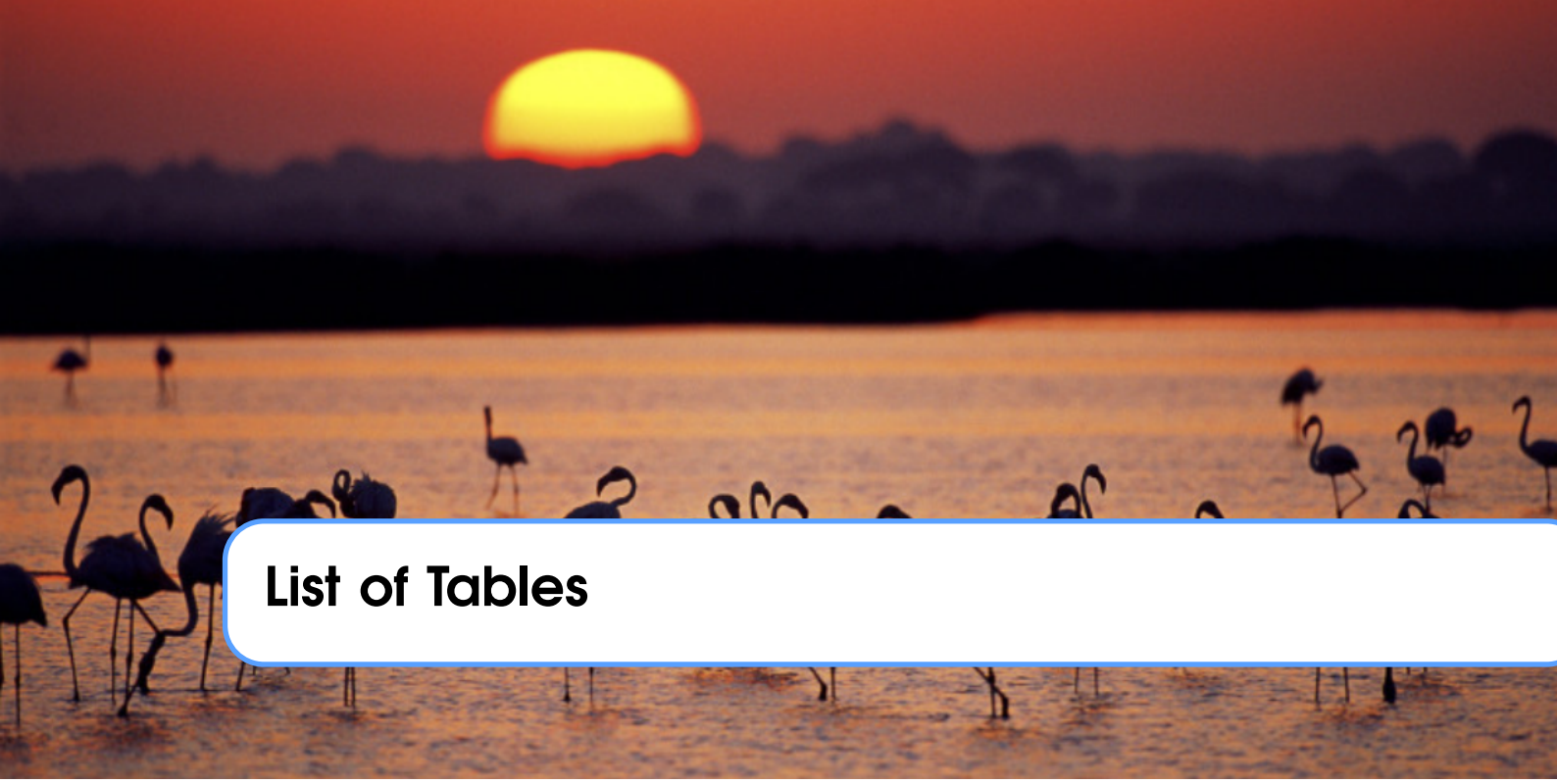

List of Tables

1. MOTIVATION & RESEARCH OBJECTIVES

> The more facts one has, the better the judgment one can make, but one must never forget the corollary that the more facts one has, the easier it is to put them together wrong.
>
> *Sir G. Heyworth*
> *The use of statistics in business, 1950*

In this chapter a brief introduction to estuarine systems is presented. It addresses not only their social, economic and environmental interest but also their dynamics, the effects that human activities have on them and the derived conflicts that are common to most worldwide estuaries. These systems are practically impermeable floodplains of mud and sand drained by various channels with a dense network of creeks in which transport of salt and other substances takes place at different spatiotemporal scales. They carry freshwater river discharges, incoming seawater leaded by tides or waves from the continental shelf, and organic and inorganic substances. Some of these substances are nutrients that are used by marine organism for their metabolism. Some other are pollutants that results harmful to the great variety of the marine biota and to the population that use these natural resources. The Guadalquivir river estuary (southwest of Spain) is a representative example of a system where a knowledge-based analysis may help decision makers to implement strategies that take into account the interests of different stake-holders (politicians, port managers, environmentalists and farmers). It usually shows reduced water quality levels and its current status is highly determined by the cumulative effects of human activities during the last two centuries, such as dredging, channeling and flood protection works, land reclamations, freshwater regulation and river damming. The complexity of its dynamics and the shadow of climate change are additional threats that managers also need to account for.

In Section 1.1 a general definition and classification of estuaries is provided beside the main processes that take place therein. Section 1.2 presents the study area, the Guadalquivir River

Estuary, a perfect example of a hot spot where human action is notorious and controversial. A brief spatial and temporal track of its main changes is also outlined. Section 1.3 describes the major advances in previous studies that constitute the framework of this thesis. The main and specific objectives of the research are described in section 1.4. Section 1.5 highlights the relevance of the investigation and, in section 1.6, it is described the feasibility of the research. Finally, the studies and activities derived from the research close the first chapter.

1.1 Estuaries for human life

River mouths are perfect transitional ecosystem between the continent and the ocean. In unspoiled conditions they are biologically more productive than rivers and the adjacent ocean due to their high concentration of nutrients which stimulate primary production (Miranda et al., 2017). The river mouth is the seaward end of an estuary, which encompasses a larger area from the mouth landward. There are many definitions of estuaries. In Dionne (1963) words: “It is an inlet of the sea, reaching into a river valley as far as the upper limit of tidal elevation, usually being divisible into three sectors: (i) a marine or lower estuary, in free connection with the open sea; (ii) a middle estuary, subject to strong salt and freshwater mixing, and (iii) an upper of fluvial estuary, characterized by fresh water but subject to daily tidal action". This definition already highlights some of the elements that might coexist and trigger spatial and temporal variabilities of most estuarine properties that drive estuarine processes. Among them, one of the more important is the exchange flow, also referred estuarine circulation in the literature. The exchange flow is the tidally averaged or subtidal along-channel velocity at an estuarine cross section (Geyer and MacCready, 2014). The period used for average is usually a representative period of the principal lunar semi-diurnal tidal constituent. At the mouth of an estuary, dense shelf-water flows into the estuary at the deeper region while freshwater outflows in surface. The exchange flow is, therefore, bidirectional. It is typically an order of magnitude weaker than the tidal flow and, often, many times greater than the river flow (Geyer and MacCready, 2014). The importance of the exchange flow lies on its contribution to the longitudinal dispersion. Without a significant buoyancy input, the exchange flow may favor rapid dispersion of dissolved contaminants (Smith, 1976), high biological productivity (Malone et al., 1988), and also frequent hypoxia and acidification of the deepest water (Feely et al., 2010).

These processes vary longitudinally and vertically within the estuary, a fact that reveals the necessity to characterize estuaries by means of unified principles with the aid of key parameters that lead to their classification. Some common characterizations are based on their morphology, tidal action or river discharge. Many global and interesting properties can be extracted from the morphological characterization.

Figure 1.1 depicts the classification attending to the morphology (Dyer, 1973; Fairbridge, 1980). **Fjords** have a small width-depth ratio, steep sides and an almost rectangular cross-section. The river discharge is usually small compared with its volume. They have also restricted the tidal range. A lot of examples of fjords can be found in Norway. **Bar-built estuaries** have a characteristic bar across their mouth. These estuaries are common in areas with active sediments transport. This bar is normally the breaking region for nearshore waves, limits tidal influence and makes available lots of sediments. Punta-Umbría or Tinto-Odiel at southwest of Spain are examples of this type of estuaries (Reyes-Merlo et al., 2017). The dominance of tides is very representative of **coastal-plain estuaries** which present a convergent longitudinal morphology upward. The sedimentation process is not as important as in the previous type. Their width-depth ratio is usually large. Extensive mudflats are often present and the main channel is usually sinuous. River flow is generally small compared with the volume of tidal prism. In all types of estuaries, the morphology is dynamic (Dalrymple, 1992). However, it can be assumed non significant at a time scale short enough for

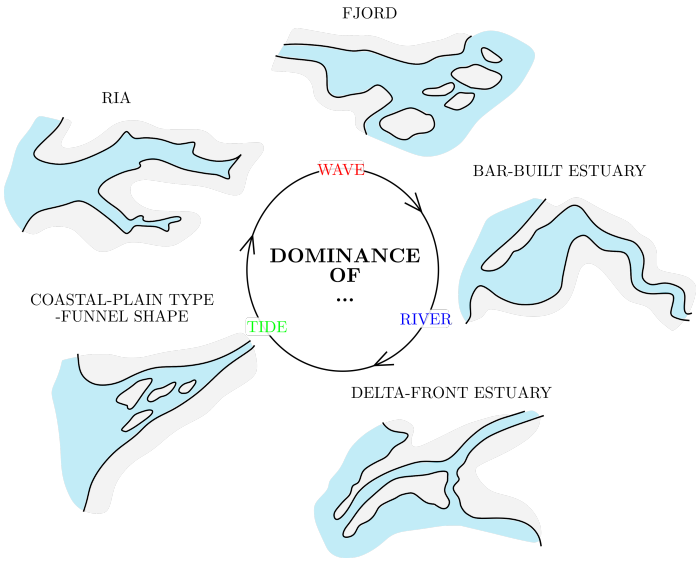

Figure 1.1: Estuarine physiographic types according to major forcing. Adapted from Dyer (1973).

managing. In chapter 2 other classifications that will be needed in the methodological foundations will be discussed.

The natural processes that take place in estuaries are due to marine, fluvial and atmospheric agents. The former is mainly associated to the propagation of the tidal wave landward and seaward, flooding and ebbing the estuary. The tidal currents influx salt into the estuary. These currents are able to generate turbulence which might mobilize the bottom sediment (Díez-Minguito et al., 2014). The suspension of the sediment limits the penetration of light in the water column. The marine dynamic also acts through the waves by modifying the orientation of the beaches and causing erosion or accretion of the mouth river banks. The fluvial dynamics is the main source of freshwater. The freshwater alters the buoyancy of the salty water mass which also drag the bed sediments and transports nutrients and oxygen. The latter agent radiates heat and light energy, modifying the buoyancy of water at the surface. Wind field also acts stressing the water surface layer. All these processes trigger spatial and temporal changes on the amount of salt (Reyes-Merlo et al., 2013), nutrients, oxygen, light and sediment within the estuary. Under certain conditions, several undesired events that radically affect the global productivity of the estuary can be observed, such as the salinization or eutrophication of some regions, and episodes of hypoxia or erosion of beaches. Natural processes can be altered by human activities such as river engineering works (like channeling or deepening of the cross section), tidal flat occupation, riverbank protections or beach regenerations. These activities may also trigger a shift from low-turbid conditions with weak tidal amplification to high-turbid conditions with strong tidal amplification (Winterwerp and Wang, 2013).

This thesis moves in this framework, where the recognition of the effect of a single process is full of uncertainty. For the sustainable management of these systems, the identification of the thresholds under/over which unwanted episodes occur, the uncertainty associated to their frequency and intensity, as well as insights into the mechanisms behind them is a real need. In this context, taking into account that the cumulative impact of human activities may lead to irreversible stages it is important to have models capable to simulate these processes accounting for the uncertainty.

1.2 The Guadalquivir River Estuary

The high productivity of the Guadalquivir river estuary is a source of conflicts because several activities coexist in it, such as salt extraction, agricultural activities -mainly of rice with a high demand of fresh water-, fishing of species such as shrimp and sea bass and navigation of various ships sizes. The beauty of the beaches surrounding the area and its extensive protected wetlands also attracts a lot of tourists. The progressive use of estuary resources has jointly affected the system. It is therefore important to revise the historical human interventions on the estuary and their effects on the fundamental processes (Cronin, 1967). This analysis is aimed at contemplating future beneficial and harmful influences on this fascinating, complex and important environment. Some hints about the natural and human induced changes on its geomorphology, which influences the hydrodynamic and also some legislative decisions that had a huge impact on the estuary are remarked next.

1.2.1 Geological and historical context

The current configuration of the Guadalquivir estuary is due to the stabilization of the mean sea level during the Holocene, specifically during the Flandrian transgression, approximately 6500 years ago (Zazo et al., 1994). A huge bay reached the city of Seville (figure 1.3). The erosion of the surrounding mountains and cliffs and the fluvial contributions provided fine sediments, especially sand and mud, and the southwestern swell developed the coastal drift that transported the sediment from the west of the province and that gave rise to a rate of sediment accumulation and advance of the coast, on average, up to 6 mm/year (Morales and Borrego, 2008). At the same time, a littoral sandbar grew up until closing the gulf, transforming it into a lagoon. The sediment river supply contributed to its final clogging. Then, river sediment, highly influenced by tides, settled down on the marshes. The first settlements in the valley date from VIII century B.C., where early civilizations already began to build small dikes to cross the riverine areas. Although Seville was a small island at that time, it was a commercial enclave since the Guadalquivir was navigable to that location (Álvarez, 2011).

The “al-wadi al-Kabi” (big basin) allowed the entrance of ships from Sanlúcar de Barrameda and connected the maritime transport to farm production during the Muslims period (VIII century AD). The first law that controlled the use of rivers dates from this period (Girard, 2006). The continuous sedimentation of the navigational channel caused the decay of the Indian trade along the Guadalquivir during the XVII century (Athané, 2012). The increase of the ship size and the progressively more difficult navigation favored the relocation of the port of Indias from Seville to Cádiz in 1717.

1.2.2 The occupation of tidal marshes

During the XX century, the politic pressure to dry the marshes increased. They argued that marshes were non-hygienic and unhealthy for the population and promoted the agricultural, salt extraction and urban activities to economically advantageous shallow areas. Wetlands, the more valuable from an ecologic point of view and more productive, were severely threatened. Sponsored by the Cambó’s law (July 24th of 1918), Guadalquivir Marsh and Guadalquivir Island companies dried part of the mashes, built up dikes and drainage channels. The state legislation (Ley de Obras de Puesta en Riego urgente O.P.E.R.) that enter into force in 1932 gave a decisive impulse to the interventions in the estuary, creating a well-defined grid of drainage channels of rice fields in the marshes, that sharply modified the landscape. The marsh was dried, the soils desalinated and the intensive agriculture became extensive. These works were the basis for the beginning of the

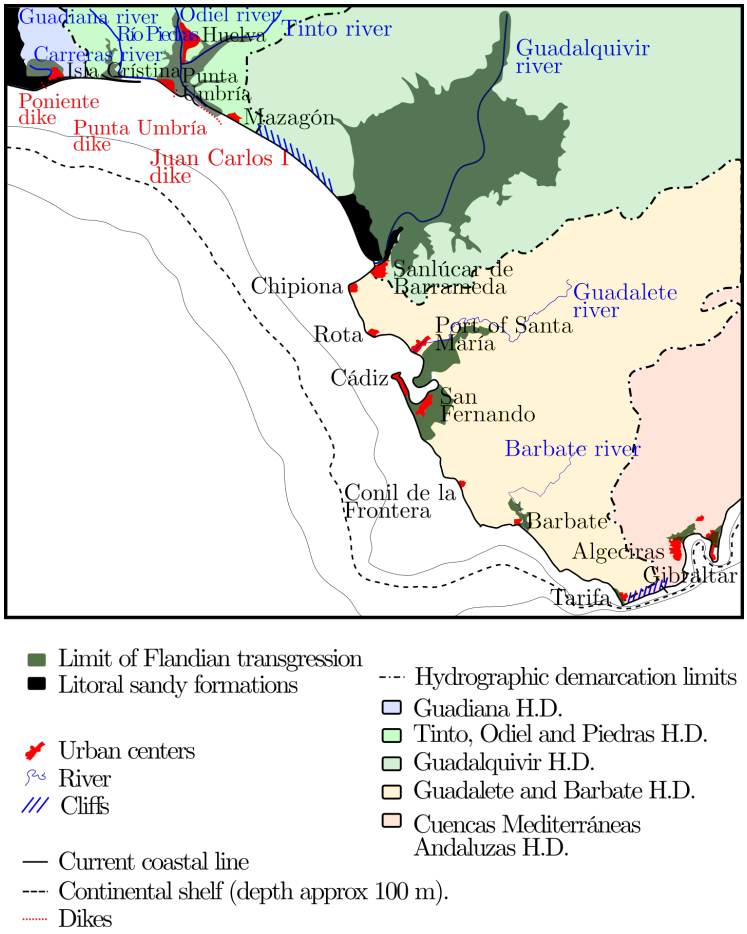

Figure 1.2: Sketch of main geological and geographic features and administrative divisions next to the lower stretch (last 80 km) of the Guadalquivir river.

agrarian transformation with the first rice fields from the Guadalquivir Island Society in 1929.

The implementation of those laws and the construction of a floodgate to inhibit the tide made the area at the right riverbank of the Guadalquivir the largest extension of rice crops in Spain. Currently the amount of rice production rises up 0.3 MTm of rice every year, the 92% of total Andalusian crops. This rice field demands high amounts of water because about a third part is lost due to evapotranspiration. The high-water supply requirements of rice fields collided with the limited availability of water in the Guadalquivir. There is a clear relation between freshwater discharge and the mean salinity which limits the potential rice production. The low water discharges kept the salinity values near the threshold for rice growth of 1.5 gr/l. Indeed, the water requirements of the field rice are 300 Hm^3 for own supply and 170 Hm^3 to reduce the salinity intrusion. The sustainability of the system required that certain European policies like the Community Agricultural Politics (PAC) limited the rice production.

Otherwise, the sturgeon and caviar were overexploited until their extinction at the GRE in the sixties. Marine aquaculture, or the cultivation of fish, mollusks, crustaceans and aquatic plants, started in Andalucía in the first decades of XX century as an alternative and/or complement of the fishing and shellfish. The hand fishing of elvers and shrimps as well as aquiculture were conceived as promising industries. Aquiculture activities started in 20s and 30s of the last century (Regional Council of Fishing and Agriculture, 2009). The cultivation of these species requires a highly controlled range of salinity, temperature, pH and dissolved oxygen. The temperature range enable a

wide range of species as prawns, bass, shrimps or goldfish. During the 80s of the last century, the improvement of fishing methods favored the development of the activity that got to reach 5 million of fry captures in Cádiz bay, and near of 7500 Tm in 2008. The aquaculture required the usage of some areas that were previously abandoned.

The tidal marshes were also occupied by the intense urbanization occurred during 1956-2007, which increased the inhabitants about 86 % in the estuary and 350 % upstream of it. This situation also affected the increase of the surface dedicated to anthropogenic activities (communications, industries, etc.). These significant changes had an impact on the ecological state of the water masses due to the water supplies to meet the demand of the domestic and industrial sectors that reduced the freshwater flow, and especially, because they create the need to store water in the basin for agricultural purposes. The surface occupied by reservoirs and channels increased during this period. The current area of marshes is approximately 27,000 Ha, the middle of the Doñana National Park surface and just a 20 % of the area at the beginning of the XX century.

1.2.3 The dredging actions for keeping the port activities

The difficulties to navigate along the river up to Seville, lead to the modification of its course with cuts that affect the natural dynamics of meanders. The first meander was cut in 1794. Before the beginning of XX century, three cuts modified the main channel (Merlina, 1794; Fernandina, 1816; and de los Jerónimos, 1888). Since then, numerous human interventions were done to facilitate the navigability in the main channel. One of them was the known as Plan Molini in the first quarter of the last century, which ended with some works as the Alfonso XIII channel and the Tablada cut (figure 1.3). In addition, the construction of Alcalá del río dam in 1930, with a water capacity of 20.6 Hm^3 used for irrigation and hydroelectric supply, had severe consequences on the estuarine system associated not only to the regulation of the river discharges but also to the limitation of the propagation of the tide upstream. Later, a new floodgate was built in 1951 downstream the dike aimed at reducing the tidal influence and the flooding of the city of Seville due to the sea level increase. In 1950, in addition to what was mentioned above, it was created the cap of Chapina, the cut of the Vega de Triana and the floodgate of the Punta del Verde. Port interests were behind these changes (Moral, 2018). These works partially avoid the flooding of the center of Seville that kept exposed under extreme circumstances. Four more river cuts were done during the last part of the XX century (Punta del Verde, 1965; Olivillos, 1971; Isleta, 1972; and, Cartuja, 1982). Currently, the distance from the mouth to Sevilla port is less than a third of the original river length. Figure 1.3 depicts the main human interventions at the Guadalquivir estuary.

The rapid transformation of the GRE during the last century gave rise to new legislative figures with the purpouse of identify economic benefits and impact on nature and regulate the location of new activities in the estuary. The law of Ports that came into force in 1992 (BOE-A-1992-26146) created a management model. Among its duties were the management of the economic heritage and resources of the port and the promotion of industrial and commercial activities related to maritime or ship traffic. On the other hand, the Guadalquivir Hydrological Planning of 2013 (BOE-A-2013-5319) stablished the general objectives to get a good state and the adequate protection of water masses of the watershed, the satisfaction of the demands and the equilibrium of the regional and sectorial development. In the text, it is said that these objectives have to be reached by (i) increasing the availability of sources; (ii) protecting the quality; (iii) including the cost of their uses, and (iv) rationalizing the uses in harmony with the environment and other natural sources.

However, the port authority of Seville established as a main objective the increase of the port activities, in particular, deepening the main channel and allowing the access of larger ships to the port of Seville. The Guadalquivir Hydrological Planning of 2013 (BOE-A-2013-5319) included

Figure 1.3: Sketch of the human interaction with the Guadalquivir estuary. The figure in the subset depicts the location of the estuary. Guadalquivir river estuary extends up 105 km from the mouth at Chipiona and Sanlúcar de Barrameda to the Alcalá del río dam (Seville). Spatial domain of the estuary includes an area of 2000 km^2 distributed in Huelva, Cádiz and Sevilla provinces.

this work as “complementary”, a label that avoid the requirement of presenting an environmental impact analysis.

1.2.4 Drowning the estuary

Due to the aforementioned activities, the basin of the Guadalquivir river is a highly modified watershed. The human activity has colonized and compartmentalized the estuary throughout the history to host, among other, intensive greenhouse agriculture and rice cultivation, commercial, fishing and recreational navigation, fisheries and aquaculture, salt extraction, urban developments and their infrastructures, and an extensive network of roads, irrigation channels and drainage on both sides of the main channel of the estuary. As it is shown in figure 1.4, natural and human-induced processes interact with the environment in several spatial and temporal scales. Thus, while the stratification of the water column may significantly last about a tidal cycle (other longer periods

can also be observed), changes in depth due to, for example, a dredging work may have effects over large areas that remain permanent in time.

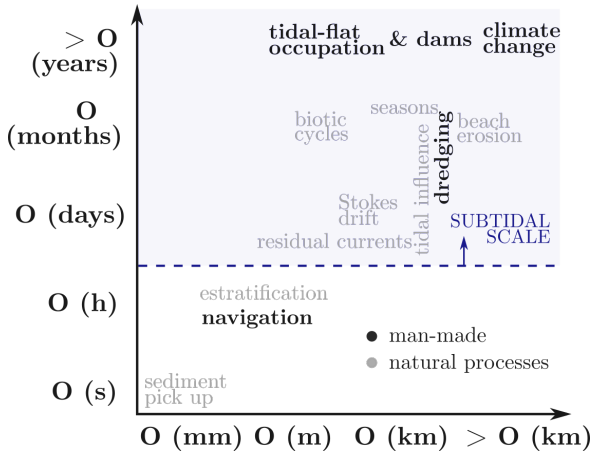

Figure 1.4: Spatial-temporal scales of natural and human-induced processes in estuaries. Residual or subtidal scale includes the major contributions in which human can interact to prevent or enhance the estuarine dynamics.

In addition, the GRE is suffering a period of hydric stress motivated by the increasing demand of water, the two-century effects of human actions and climate change. This pressure goes also ahead at the politic framework where management decisions may sometimes simply transfer gains and position from any region to the adjacent one without any added value (Moral, 2018). Another axis could be added to the previous figure, representing the economic benefits or losses that suppose any alteration of the current state. The analysis (out of the scope of this thesis) could help to manage environmental conservation and economic development. Table 1.1 shows some of the possible benefits and impacts of three common works in estuaries undertaken by harbor authorities.

	Dredging		Navigation		Port ampliation
-	Degradation of habitats	-	Introduction of exotic species	?	Speculative activities
-	Margin erosion	-	Margin erosion	+	Expansion of the logistic platforms
-	Sediment issues	-	Water contamination	+	New employment
-	Fishing issues	+	Increasing in trade	+	European economic founds
-	Increasing velocities	+	More tourism		
-	Change in sandbar dynamic				
?	More mixing				
-	Coastal regression				

Table 1.1: Impacts (-) and benefits (+) of some activities or interventions related to the port. The symbol ? stand for the cases where it is not clear a benefit or impact on the surrounding media.

1.2.5 Legislative and scientific efforts

From 1962, certain steps for the protection of the Guadalquivir estuary were taken as in recorded in table 1.2. However, these labels and their legislative framework, did not prevent that early in the morning of April 25th of 1998, Aznalcollar pond broke. The toxic muds contained in the pond traveled downstream the Guadiamar river, a tributary next to Guadalquivir mouth and affected more than 4000 hectares.

In 2000, the European Water Framework Directive (Kallis and Butler, 2001, WFD hereinafter) introduced a profound change in water quality programs. The WFD seeks the improvement and

maintenance of good ecological and chemical status of the water masses, incorporating a new integrated and ecosystemic approach. In regards to transitional waters and therefore to estuaries, it establishes the standards values of physicochemical quality indicators, providing a new framework to protect them.

At the beginning of 2005, the Spanish Ministry of Environment funded the second biggest project of the World until date focusing on the recovering of wetlands, called Doñana 2005. In that project, it was suggested that the bed deepening enhances the inflow of salt water, affecting to the fauna and the flora. This was a point of no-return, as it was understood the limited capacity of the estuary to recover from impacts. It was also recognized that the search of social and economic benefits at the expenses of the depletion of its resources does not justify the environmental damages. The project ended with the proposal of eleven measures, some of them not yet completely implemented, that focused on the recovery of the connection of the main arms of the Guadalquivir (Eastern, Jerónimos, and de la Torre branches).

YEAR	LEGISLATION		HUMAN ACTIONS	EVENTS
	To Act	To Preserve		
1717				Port of Indias to Cádiz
1795			Merlina RC	River shortened
1816			Fernandina RC	River shortened
1888			Jerónimos RC	River shortened
1903	Moliní Plan			Alfonso XIII channel
1918	Cambo's law			Marshland drying
1926			Tablada RC	River shortened
1929	Delgado Brackenbury Plan			Chapina earth dam
1930				First rice field
1931			New dam	Alcalá del río
1948			Vega de Triana RC	River shortened
1951			New floodgate	
1963				A huge flooding
1965			Punta del verde RC	River shortened
1971			Olivillos RC	Ybarra closes
1972			Isleta RC	
1980		Biosphere Reserve		
1982			Cartuja RC	River shortened
1986			Chapina earth dam removed	
1988		ZEPA and LIC		
1990		World Heritage		
1992	Law 27/1992		Expo 92	Law of ports
1998		Red Nature		Aznalcollar pond broke
2005			Doñana Project	
2007			GRE Project	
2009	RD 255/2013			Guadalquivir HP (1st cycle)
2010			New harbor lock	
2011	RD 2/2011			New law of ports
2013			WWF complaint	New project funded by the Seville Port
2015	Judgment of SC			Dredging cancellation
2016	RD 1/2016			Guadalquivir HP (2nd cycle)
2019	Judgment of SC			Dredging cancellation
2021	-			Guadalquivir HP (3rd cycle)

Table 1.2: Summary or major human-induced actions in the Guadalquivir river estuary. HP: Hydrological Planning; RC: River Court; ZEPA and LIC: Area of special protection for birds and Place of community importance; SC: Supreme Court; and RD: Royal ordinance.

Later, in 2007, the Port Authority of Seville signed a contract with the Superior Conceal of Scientific Research and the Environmental Fluid Dynamics Group to lead the study named 'Methodological proposal to diagnose and forecast the consequences of human actions in the

Guadalquivir Estuary' (Losada and Ruiz, 2010). This study analyzed the status of the estuary and the adjacent marine area, especially after the human actions carried out in the last two centuries. The work also focused on the prognosis of what the estuary would come about in the future if current and planned activities human were implemented. This research concluded that it was not recommended to carry on the dredging works to deepen the estuary until the conditions of the estuary improve.

Meanwhile, although the water masses are considered modified or highly modified, the new hydrological planning continues with it dredging proposal. In fact, the works of the new harbor lock ended in 2010. The new lock enables 10 m depth ships. Later, in June of 2013, the UNESCO, through the World Patrimonial Committee, did not allow the deepening of the low Guadalquivir while the scientific recommendations were not ensured. Next, World Wildlife Fund (WWF) wrote a manifest against the Hydrological planning of the Guadalquivir in which they show that among the activities carried out in the Guadalquivir estuary, harbor activities, and in particular, the dredging works had the most severe impacts. The long-term management strategy of the port just still pursued the economic benefit, proposing the enlargement of the harbor, passing through the deepening of main channel to ensure the navigation of larger ships (with bigger draughts). Furthermore, the actions carried out by the managers ignored everything but their sectorial goal (Agua, 2014). Harbor managers justified their position by carrying the banner of the socio-economic benefit to the vast area of influence of their activities. In response, WWF proposed 10 challenges to recover the Guadalquivir estuary in accordance to Doñana project and GRE-research. Some of these challenges were: (i) to delimit the Maritime and Terrestrial Public Domain in the Low Guadalquivir. This intervention should also include the several arms of the river and streams taking into account the mean sea level increase due to the global climate change $\sim$0.5 - 1 m; (ii) to recover the tidal flats in order to mitigate the effects of climate change; (iii) to increase the discharge volume of fresh water, that currently have to range between 150 and 300 m^3/s.

In February 26th of 2015, the final decision of the Spanish Supreme Court was to forbid the deepening dredging works included in the first cycle of the Hydrological Planning of the Guadalquivir (read the news). It seems that the Port Authority finally abandoned the idea of the deepening dredging work (personal communication of the Head of Business Development).

The current stage of the last scientific project at GRE highlights the poverty of the benthic communities of the bed and finds the explanation in the strong hydrodynamics of the main channel, the high turbidity, the irregular flow of freshwater due to inefficient water regulation, the loss or shortage of tidal plains that contribute heterogeneity to the environment, among other aspects. Beside those problems, the sedimentation rate shows an average value of six millimeters per year and exceeding at sometimes one centimeter per year. This high sedimentation induces saturation processes that lead to greater sedimentation (read the news).

1.3 A Summary of hydrodynamic processes in the GRE

Although chapter 2 will thoroughly review the hydrodynamic foundations that give rise to the so-called estuarine processes, in this section some of their key aspects are addressed. More precisely those related with sea water elevations, currents, temperature, salinity and turbidity along the estuary and under different hydraulic regimes. It is important to point out that this distinction in low and high river flow conditions is made along the manuscript. As stressed in the WFD for transitional waters, the analysis of water quality requires a profound knowledge of estuarine hydrodynamics and in particular about exchanged volumes and residence times of water masses.

The Guadalquivir watershed is located in a region governed by the Mediterranean climate where

precipitation shows a marked interannual variability. Moreover, in general, the periods of higher water demand (mainly associated to agricultural use and drinking water supply) and availability do not coincide. The storage of large volumes of water are, therefore a need to guarantee the supply in a short- and long-term basis. At the Alcalá del Rio dam, the last regulation point of the basin, managers have to adapt the water discharge, Q_d, to meet the demand. This fact can be observed in figure 1.5 where the time variation of the seasonal distribution of the yearly mean values of Q_d are shown together with (1) the ratio of summer and winter values, that show a great reduction in dry-years and (2) the 16 years moving average values that reveal a clear descending trend.

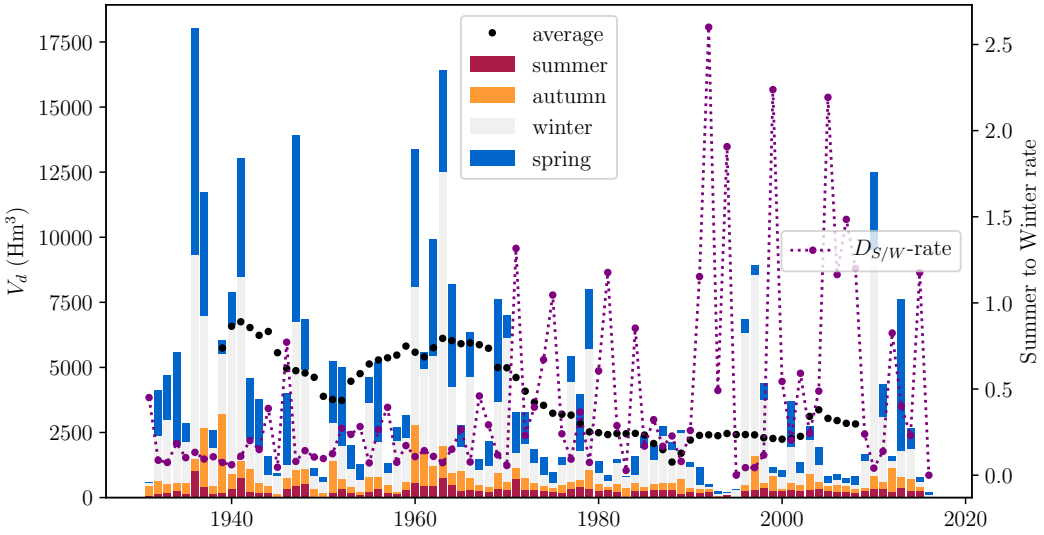

Figure 1.5: Time series of water volume discharge (V_d) at the Alcalá del río dam. Black dots represent a 16-year moving average. Purple dots stand for the ratio of summer to winter volume discharges. Blue, gray, orange and red filled boxes indicate the spring, winter, autumn and summer water volumen.

The time series of the river flow at the Alcalá del Río dam shows an average value of 63 m^3s^{-1} with a most frequent value of 30 m^3s^{-1}. In the research study of Díez-Minguito et al. (2012), three river discharge regimes were identified. The estuarine processes change in magnitude as well as in variability in those regimes. The thresholds of those hydraulic regimes are: (i) $Q_d \leq 40$ m^3s^{-1} which defines the low river-flow regime where tidal dominance is observed (and estuarine processes are associated to tide propagation), (ii) $Q_d \geq 400$ m^3s^{-1}, where fluvial processes dominate, and an intermediate transition region in between. The processes also change along the estuary.

Figure 1.6 shows the cumulative distribution functions for river discharges in summer and winter during the periods 1931-1951 and 1996-2016. As can be seen in the figure 1.6, there is a significant reduction in discharges between the first 20 years after the construction of the dam, and the most recent ones. The reduction in winter has been widespread. The probability of non-exceedance for any value always reports a lower discharge rate at present than it was in 1931. The difference in flows is more pronounced with low non-exceedance probability values. In summer, flows above 40 m^3/s are reduced from the first to the second period, however, the lower flows increase. This result shows the efforts by the administration and the managers of the estuary and the dam, to maintain the ecological flows of the estuary. Although, they are still far from the 150 m^3/s that WWF pointed out. It is worthy noted that currently near the forty percent of water discharged in winter is done

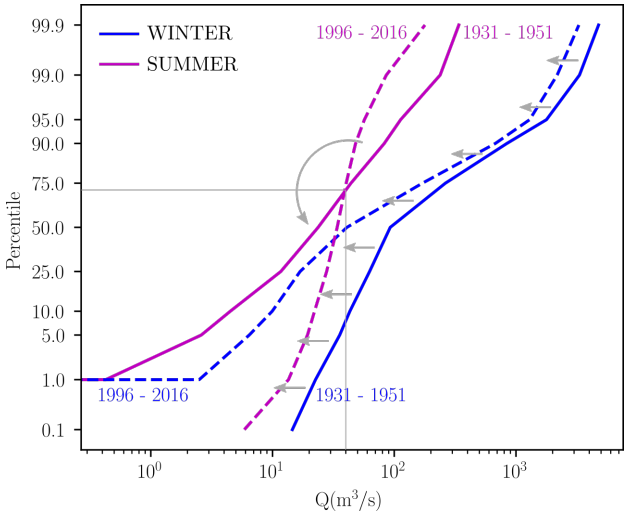

Figure 1.6: Cumulative distributions of water discharge during summer and winter of two 20-years period comprising 1931 - 1951, and 1996 - 2016. The arrows depict the regions where freshwater flow decreases or increases.

with a lower flow than summer.

1.3.1 Low river-flow regime (Q_d < 40 m^3/s)

The GRE is tidally-dominated or in low river-flow regime for most of the year (Díez-Minguito et al., 2012). Due the non-linear interactions during the tidal propagation, flood currents are greater than ebb currents (Díez-Minguito et al., 2012). The temporal and spatial distribution of the residual current plays a relevant role in the rate of water renewal in the estuary and in the spatial distribution of sediments, especially, the maximum turbidity and its persistence (Contreras and Polo, 2012). Under such circumstances, three stretches can be distinguished attending to the relative importance of the processes involved (Díez-Minguito et al., 2012). There is a first stretch that extends from the mouth to x = 25 km where the dominant processes are related to tidal propagation. In the following 35 km, channel convergence and friction are in balance. The last (third) zone of approximately 50 km length is dominated by tidal reflection on the Alcalá del Río dam. This region coincides with over-tides node located approximately at km 60. The modules of the reflection coefficients are approximately 0.4, 0.22, 0.65 for semidiurnal (M_2), diurnal (O_1) and quartic-diurnal (M_4) components, respectively (Díez-Minguito et al., 2012). At that point are observed residual currents of the order of 1-5 cm/s, of the same order as the Stokes currents, Ekman wave and river circulation.

The water temperature is primarily controlled by shortwave radiation, latent heat transfer through the free surface and tidal advection, whereas it depends less on freshwater discharge and longitudinal dispersion (Padilla et al., 2016). At the estuary mouth, the linear superposition of tidal and fluvial contributions offers a fairly well description of η (Díez-Minguito et al., 2012; Losada et al., 2017). This behavior persists at the mouth for high river-flow regime. Where the estuary widens, the river discharge varies more gradually, and its effect on water levels is less significant.

The baroclinic circulation shows an effective vertical turbulent viscosity one order of magnitude larger at the mouth O(10^{-3}) than at the head O(10^{-4}) m^2/s (Reyes-Merlo et al., 2013). For low river-flow regime, the saline intrusion depends more on the mean-tidal fluctuations, and to a lesser extent on the river flow. Tidal-pumping, lateral stirring, and baroclinic circulation seems to be the main mechanisms that control the transport of salt.

Regimen	Q_d (m^3/s)	a	b
Low river-flow	< 20	0	57.0 ± 2.1
Intermediate river-flow	20 < Qd < 1000	0.428 ± 0.016	5.37 ± 0.06
High river-flow	> 1000	1.0 ± 0.5	10 ± 4

Table 1.3: Length of the saline intrusion X_2 (in km) compared to freshwater discharge Q_d ($X_2 = bQ_d^{-a}$) (from Díez-Minguito et al., 2013). The value that defines the low river-flow regime change slightly for salinity.

Regarding its saline structure, the decrease in the freshwater discharge in the estuary has triggered the gradual salinization of its waters. The salt intrusion reaches the middle and upper part of the estuary in normal conditions, highly motivated by the dominance of flood currents. During the low river flow regime, the main salt transport mechanisms are: (i) the non-oscillatory salt fluxes, (ii) the Stokes transport, and (iii) the tidal pumping associated with the correlation between tidal variations of salinity and current (Díez-Minguito et al., 2013). The tidal pumping term, associated to the correlation of tidal deviations of current and salinity, is negative until km 23 approximately, after which it becomes positive. The transport changes of sign may be due to local topographic features which may have considerable influence on the lateral mixing driven by secondary flows and hence on the salt transport (Díez-Minguito et al., 2013). The saline intrusion does not change significantly in this regime (Table 1).

The net suspended solid concentration (SSC) transport is generally directed upstream because of the dominance of flood currents. During low river-flow conditions, numerous episodes of permanent turbidity occur which reduces the water renovation. This situation triggers the clogging of the estuary and the reduction of low water renewal rate. Under certain circumstances, it is observed high SSC (larger than 1000-20000 mg L^{-1}) in the low estuary during spring tides (Bramato et al., 2010). The transport is largely controlled by the mean advection, the tidal pumping associated with the covariance between suspended particle matter (SPM) concentration and current, and the tidal Stokes transport. The convergence of the transport associated to these terms explains the presence of a primary (x = 35 km and SSC $\sim 0.86 \pm 0.08$ kg/m^3 at z = -4 m) and a secondary (x = 58 km and SSC $\sim 0.99 \pm 0.09$ kg/m^3 at z = -4 m) estuarine turbidity maxima (ETM) (Díez-Minguito et al., 2014). The ETM at 35 km has been also detected using the DEIMOS-1 satellite imagery (Caballero et al., 2014). The second ETM may well correspond to the classic turbidity optimum due to the salt intrusion null-point.

Elevated levels of suspended solids might endanger the already fragile balance of an ecosystem punished by the pressure of human activities. They also difficult the supply water with a quality enough to irrigation and operational works related to aquaculture. These conditions are aggravated when they coincide with increases in water salinity. In fact, the control of the salt intrusion and its displacement towards the mouth is one of the objectives pursued during the irrigation campaign. These episodes of turbidity and high salinity in the estuary waters, have revealed the need to identify the processes that causes their persistence (Contreras and Polo, 2012).

The net specific growth rate of chlorophyll-a (Chla) containing biomass is inhibited by turbidity throughout the year (Díez-Minguito and Swart, 2020). The stretches closest to the mouth exhibited larger Chla concentration during the summer period characterized by winds favorable to upwelling and improved light conditions. Upstream, the stretches show the opposite behavior; larger Chla concentration during the wet season. Local maxima of averaged Chla levels were observed between the two ETM.

1.3.2 High river-flow regime (Q_d > 400 m^3/s)

When the freshwater discharges are greater than 400 m^3/s, the estuary is fluvially-dominated and the water level cannot be calculated as the linear superposition of tide and river contributions (Losada et al., 2017). Large discharges cause the blockage of the tidal wave. Field data shows a 60-day post-discharge amplification of tidal current and elevation amplitudes in the upper layers. The decrease of amplitudes predominates near the bed (Losada et al., 2017). Furthermore, extreme discharge events that last more than 2 weeks with peaks above 2000 m^3/s dampen tidal harmonics of the diurnal period and shorter periods and reduce the tidal wave propagation velocity (Losada et al., 2017). These discharge events disrupt the low-frequency seasonal variability of Chla and SSC, and they may even induce shifts in both SSC and Chla concentrations (Díez-Minguito and Swart, 2020). During these conditions, the longitudinal temperature gradient decreases, except near the mouth; hence, the semidiurnal amplitude of temperature decreases in the middle and upper parts of the estuary but increases at the mouth (Padilla et al., 2016). Freshwater discharges between $\sim$ 500 m^3/s and $\sim$ 1000 m^3/s may induce a regime shift due to high SSC. High sediment concentrations that reach several orders of magnitude higher than those under normal conditions and that last over two months increase the stratification of the water column. This stratification process restricts frictional influence to the bottom layer and partially decouples the overlying flow from the bottom (Losada et al., 2017).

During extreme conditions, the saline intrusion is displaced towards the mouth. It is found that the dependence of the salt intrusion on the river flow increases with the flow, and the gravitational circulation is greatly enhanced during the fluvially-dominated regime. The influence of tides increases after high discharges due to the reduction of the boundary shear stresses associated to the mud entrainment. Easterly winds favor the baroclinic circulation, increasing the injection of saltier water, which replaces the superficial, low-salinity water flushed out of the estuary (Reyes-Merlo et al., 2013). The recovery of the salinity to normal conditions requires almost 60 days (Díez-Minguito et al., 2013). The fact that the saline intrusion moves towards the mouth during high river-flows may explain the increase in the differential advection, which is generally related to the regime of strain-induced periodic stratification. The nature of saline intrusion at a subtidal scale is adequately reproduced through the tidal velocity amplitude, river discharge and wind conditions (Reyes-Merlo et al., 2013). The dependence of the salt intrusion on the river flow and the gravitational circulation greatly increases. The role of tides also increases after peak discharges due to the mud entrainment induced by turbulence.

The temperatures recover their averaged values prior to the discharge within 2 weeks (Padilla et al., 2016). It is worthy to note that under these conditions, where a sudden and strong decrease of salinity occurs, just euryhaline species (that tolerate and adapt to rapid variations in salinity) can be found. This environmental condition limits the habitat of, i.e., salmonids, that migrate at some period of their life cycle between fresh and salty water.

However, water discharges $>$ 90 m^3/s also produce high SSC in the mid-low section when they coincide with spring tides. In this case, the SSC reaches the middle and lower section of the estuary far superior to those of the discharge, indicating resuspension processes and movement of the maximum zone turbidity (ETM) during spring tides. On the other hand, winds from the southeast affect wave propagation and prevents the outflow of sediments to the sea, a situation that may favor that turbidity events last several months. However, water discharges larger than 1500 m^{3}s^{-1} have sufficient capacity to export sediments to the sea, whatever the tidal and climatic conditions.

1.3.3 The effect of climate change

The interventions of the last century, such as the deepening of the navigation channel in the middle section from 4 to 6 meters, have hydraulic effects. For example, the increase of the amplitude of the tide upstream of the estuary (Álvarez et al., 2001) under high flow conditions promotes the flood of the low land areas, already reduced in more than an 85% of its area for agricultural purposes from the beginning of XX century.

During the XXI century, the mean sea level will rise (Pachauri et al., 2014), the freshwater discharges in the Guadalquivir river estuary will decrease at a probably mean rhythm of 15% in the next 15 years (Reyes-Merlo et al., 2013), an tidal amplitudes will increase at Seville tidal gauge and decrease at Bonanza station (SENSES), it is, therefore, expected an increase of the mean saline intrusion length which will probably affect the natural habitats and human activities.

1.4 Main and specific objectives of the thesis

The aim of this thesis research is to understand estuarine hydrodynamic processes at subtidal and larger time scales that affect water quality in the Guadalquivir river estuary and to develop a physical model capable to (1) quantify the exchange of water masses along the estuary and with the adjacent sea and the residence times, taking into account the stochastic character of climate agents and to (2) assess the consequences of human activities on the estuary in terms of water quality.

The following specific objectives were defined to accomplish the main objective:

1. To analyse recorded dataset in order to gain knowledge of the estuarine processes that governs the dynamics of the Guadalquivir river estuary (chapter 2).
2. The development of a box model that adequately represents the spatial-temporal energy balances within the estuary (chapter 3).
3. The validation of the model recognizing episodes of low water quality during the past (chapter 4).
4. The development of a tool to simulate multivariate time series that describe the natural forcing agents of the estuary (chapter 5).
5. The analysis of tides (amplitudes and phases of major harmonics) and their future trend in a climate change scenario (chapter 6).
6. The proposal of management strategies to increase the ecological status of the estuarine waters and the assessment of their effectiveness.(chapter 7).

1.5 Relevance of the investigation

The interest of the work presented in this thesis is:

1. To gain insight into the estuarine processes driven by natural agents and the impact that human activities have on this hot-spot estuary and other estuaries with similar problems.
2. The development of a knowledge-based tool to predict the consequences of human activities on estuarine processes related to water quality, taking into account the stochastic character of climate agents. This tool will help managers in the decision-making process about management strategies, in particular, in a climate change scenario. The valuable information obtained may establishes the main criteria for developing regional politics (hydrographical reservoirs), filling the usual gap between science and operational management.

1.6 Feasibility of the research

It was possible to undertake this research because the following circumstances took place:

Availability of local datasets

A previous project, carried out by the Superior Conceal of Scientific Research and the Environmental Fluid Dynamics Group diagnosed the current status of the Guadalquivir estuary and the adjacent marine area, and forecasted the consequences of future human action and climatic variability in the GRE (Losada and Ruiz, 2010). A full dataset during the three-year period (2008 - 2010) of salinity, temperature, turbidity, surface radiation fluxes, currents, sea levels, wind field, among others (Navarro et al., 2019) were available. All these datasets were used to analyze the variables and longitudinal variability of processes and to calibrate the models. These datasets are now available in Zenodo repository (Navarro et al., 2019). In addition, data about freshwater discharge at the dam located at the head of the estuary (provided by Junta de Andalucía) and sea levels (data provided by Puertos del Estado), temperature and salinity at the continental shelf (downloaded from the Copernicus Marine and Environment Monitoring Service, CMEMS) was also retrieved.

A ample knowledge of local estuarine processes

The research carried out in the framework of the above-mentioned project gave insight into estuarine processes in the Guadalquivir river estuary which at that moment was poorly studied from a hydrodynamic perspective. Among other results: more than 15 models were developed (distributed turbidity analysis, tidal wave propagation, spatial and temporal distribution of salinity and temperature,...) ; more than 75 papers in peer-review journals and 8 chapters of books were published, more than 100 national and international contributions to conferences were presented and 8 doctoral thesis and more than 15 final master thesis, final degree and final degree projects were developed (see link to web page, https://gdfa.ugr.es/guadalquivir/). This previous work has been the foundation of the research work done in this thesis.

Economic resources

This research has been done with the following funds that allowed a full-time dedication:

- Predoctoral contract of Campus of international excellence of the sea (CEIMAR). Training of research staff (2014) which finally granted this research study from April 2015 to April 2018.
- Contracts with the Environmental Fluid Dynamics Group, which finally allow to the finishing of PhD thesis. From May 2018 to March 2020.
- A Mobility Scholarship for Graduate Students related to the predoctoral contract of Campus of international excellence of the sea (CEIMAR). Resolution of April, 2016. This scholarship has allowed the realization of a research stay in the Department of Geography (San Diego State University, California, USA) from September to December 2017 under the tutelage of the Professor George Christakos.
- A Mobility Grant of the Environmental Fluid Dynamics Group in 2016. This scholarship has allowed the realization of a research stay in the Department of Civil Engineering at the University of Parma in September 2016 under the tutelage of the Professor Sandro Giovanni Longo.

1.7 Publications and activities derived from the research period

The following publications derived from the research work done in this thesis:

Journal papers

- **Cobos, M.**, Baquerizo, A. Díez-Minguito, M., and Losada, M.A. (2020). A Subtidal Longitudinal Anomaly Potential Energy model to assess the water mass exchanges and mixing density along an estuary. Application to the Guadalquivir River Estuary. Journal of Geophysical Research: Oceans, 125 ,https://doi.org/10.1029/2019JC015242.
- Lira-Loarca, A., **Cobos, M.**, Losada, M.A., and Baquerizo, A. (2020). Storm characterization and simulation to use in damage evolution models for maritime structures. Coastal Engineering, 156, p. 103620.
- **Cobos**, M., Chiapponi, L., Longo, S., Baquerizo, A., and Losada, M.A. Ripple and sandbar dynamics under mid-reflecting conditions with a porous vertical breakwater, Coastal Engineering, 125, 95-118 (2017).
- Chiapponi, L., **Cobos**, M., Losada, M.A., Longo, S. Cross-shore variability and vorticity dynamics during wave breaking on a fixed bar, Coastal Engineering, 127, 119-133 (2017).
- Serrano, M.A., **Cobos**, M., Magaña, P.J., Díez-Minguito, M. Sensitivity of Iberian estuaries to changes in sea water temperature, salinity, river-flow, mean sea level, and tidal amplitudes. Estuarine, Coastal and Shelf Science, 236, 106624.

Chapters of books

- **Cobos M.**, Lira-Loarca, A., Christakos, G., and Baquerizo, A. (2018). Storm Characterization Using a BME Approach. In: Valenzuela O., Rojas F., Pomares H., Rojas I. (eds) Theory and Applications of Time Series Analysis (pp. 271-284). Springer, Cham.

International conferences

- **Cobos, M.**, Díez-Minguito, M., Ortega-Sánchez, M., Losada, M. A., and Baquerizo, A. Recent perspectives on the hydrodynamics and transport processes in the Guadalquivir estuary under anthropogenic stresses, Journal of Coastal Research. Accepted at the International Coastal Symposium, Seville (Spain), 20th-23th April 2020.
- **Cobos, M.**, Lira-Loarca, A., Millares, A., Losada, M. A., and Baquerizo, A. Extreme flood events at the river mouth of a Mediterranean basin, accepted at the International Conference on Coastal Engineering, 10th International Conference on Fluvial Hydraulics, Delft, Netherlands, from 7 to 10 July 2020.
- Lira-Loarca, A., **Cobos, M.**, Besio, G., Díez-Minguito, M., Ortega-Sánchez, M., Losada, M. A., and Baquerizo, A.. Local impact due to extreme events in the Mediterranean Coast of Spain, accepted at the International Coastal Symposium, Seville (Spain), 20th-23th April 2020.
- Lira-Loarca, A., **Cobos, M.**, Baquerizo, A., and Losada, M. A. A multivariate statistical model to simulate storm evolution, International Conference on Coastal Engineering, Baltimore, Maryland, USA (2018).
- Díez-Minguito, M., Serrano, M. A., and **Cobos, M.**. Multidecadal trend analysis of tidal constituents in the Spanish estuaries, EGU General Assembly, en Viena, Austria (2018).
- **Cobos, M.**, Clavero, M., Baquerizo, A., Longo, S., and Losada M.A. Laboratory experiments about bed patterns in the shoaling region under regular waves and reflecting conditions, International Conference on Coastal Engineering, Turkey, Coastal Engineering Proceedings (2016).

National conferences

- **Cobos, M.**, Baquerizo, A. Díez-Minguito, M., and Losada, M.A. Análisis de los cambios de densidad en el estuario del río Guadalquivir mediante la Anomalía Longitudinal de la Energía Potencial. XV Jornadas Españolas de Ingeniería de Costas y Puertos. Málaga, 8 y 9 de mayo de 2019.
- **Cobos, M.**, Serrano, M.A., Marcos, M., Pérez-Gómez, B., Díez-Minguito, M. Tendencias climáticas de las amplitudes y fases mareales de las observaciones de los mareógrafos en la costa española. XV Jornadas Españolas de Ingeniería de Costas y Puertos. Málaga, 8 y 9 de mayo de 2019.
- **Cobos, M.**, Siles-Ajamil, R., Serrano, M.A., and Díez-Minguito, M. Estimación de los Efectos del Cambio Climático de la Amplitud y Fase Mareal en las Elevaciones y Salinidad del estuario del Río Guadalquivir (póster). XV Jornadas Españolas de Ingeniería de Costas y Puertos. Málaga, 8 y 9 de mayo de 2019.
- **Cobos, M.**, Lira-Loarca, A., Christakos, G., and Baquerizo, A. Storm characterization using a BME approach, 5th International Conference on Time Series and Forecasting, Granada, Spain, 19th - 21th of September 2018.
- Lira-Loarca, A., **Cobos**, M., An Integrated Statistical modeling framework of Maritime Data in a Climate Change Context: Application to M.Sc. Teaching. X International Conference on Education and New Learning Technologies, Palma, Mallorca, Spain, 2nd - 4th of July 2018.
- Serrano, M.A., **Cobos, M.**, Pérez-Gomez, B., Tel, E., and Díez-Minguito, M. Climatic trends of tidal constants. Impacts on estuarine vulnerability indices, VI International Symposium on Marine Sciences, Vigo, Spain, 20th - 22th of June 2018.
- **Cobos, M.**, Clavero, M., Longo, S., Baquerizo, A., and Losada, M. A. Interacción entre la reflexión y la generación de formas de lecho, XIV Jornadas Españolas de Ingeniería de Costas y Puertos, Alicante, España (2017).
- **Cobos, M.**, Lira-Loarca, A., Magaña, P., and Baquerizo, A. Caracterización espacial del viento en el entorno portuario basada en técnicas estadísticas a partir de registros SIMAR, JIFFI, University of Granada, Spain (2016).
- **Cobos, M.**, Clavero, M., Bujedo, I., Baquerizo, A., and Losada, M. A. Formación de barras en playas reflejantes, XIII Jornadas Españolas de Ingeniería de Costas y Puertos, Avilés, Spain (2015).
- Martín-Flores, C., **Cobos, M.**, Losada, M. A., and Moyano, J. Oscilaciones en el puerto de Málaga, origen, comportamiento e hidrodinámica, XIII Jornadas Españolas de Ingeniería de Costas y Puertos, Avilés, Spain (2015).

Projects

A precompetitive project for young researchers belonging to the Plan Propio of the University of Granada has also been leaded during the research period (February 2018 to 2019). The project is entitled "Climate change in the Mediterranean waves (CCOM)". The main objective of the project was to define a methodology to determine the wave field in the Mediterranean Sea for the period 2018 - 2100 considering the effects of climate change.

Patents

- Corpora. Herramienta para el cálculo de operatividad portuaria, GR-199-16, Junta de Andalucía.
- Flume. Formación y evolución de formas de lecho España. 26/07/2017. Instituto interuniversitario de investigación del sistema tierra en Andalucía.

Datasets

- Navarro, G., Ruiz, J., **Cobos, M.**, Baquerizo, A., Díez-Minguito, M., Ortega-Sánchez, M., & Losada, M. . (2019, September). Atmospheric, hydrodynamic and water quality observations from environmental-quality stations, water level sensors, acoustic Doppler velocimeters, and meteorological stations located at the Guadalquivir river estuary (2008 - 2010). Retrieved from https://doi.org/10.5281/zenodo.3459610 doi: 10.5281/zenodo.3459610

Research stays

A short stay has been made at the University of Parma (Dipartimento di Ingegneria Civile, Ambiente, Territorio e Architettura. Idraulica e Costruzioni Idraulich, Parco Area delle Scienze, 181/A) in September 2016 under the tutoring of Professor Sandro Giovanni Longo. The main objective to deepen the knowledge of the wave-ground interaction in conditions of partial reflection.

The second research stay was in the department of Geography at the San Diego State University (California, USA) from September to December 2017 under the tutelage of Professor George Christakos tutelage. The purpose of the research stay was to learn the theory of uncertainty assessment of physical variables (fields random) that evolve in space and time in order to incorporate multicriteria techniques and risk assessment both spatially and temporally into the analysis.

Participation in competition

The participation in the '3MThesis' competition in order to disseminate to the general public the main findings observed in the improvement of the current situation of the Guadalquivir river estuary that was agreed with the application of the model. I went to the final that was held on March 9, 2017 in Granada.

Radio

As a result of the competition, the main findings of the research were disseminated in a radio program of Canal Sur radio, titled "the Radioscope".

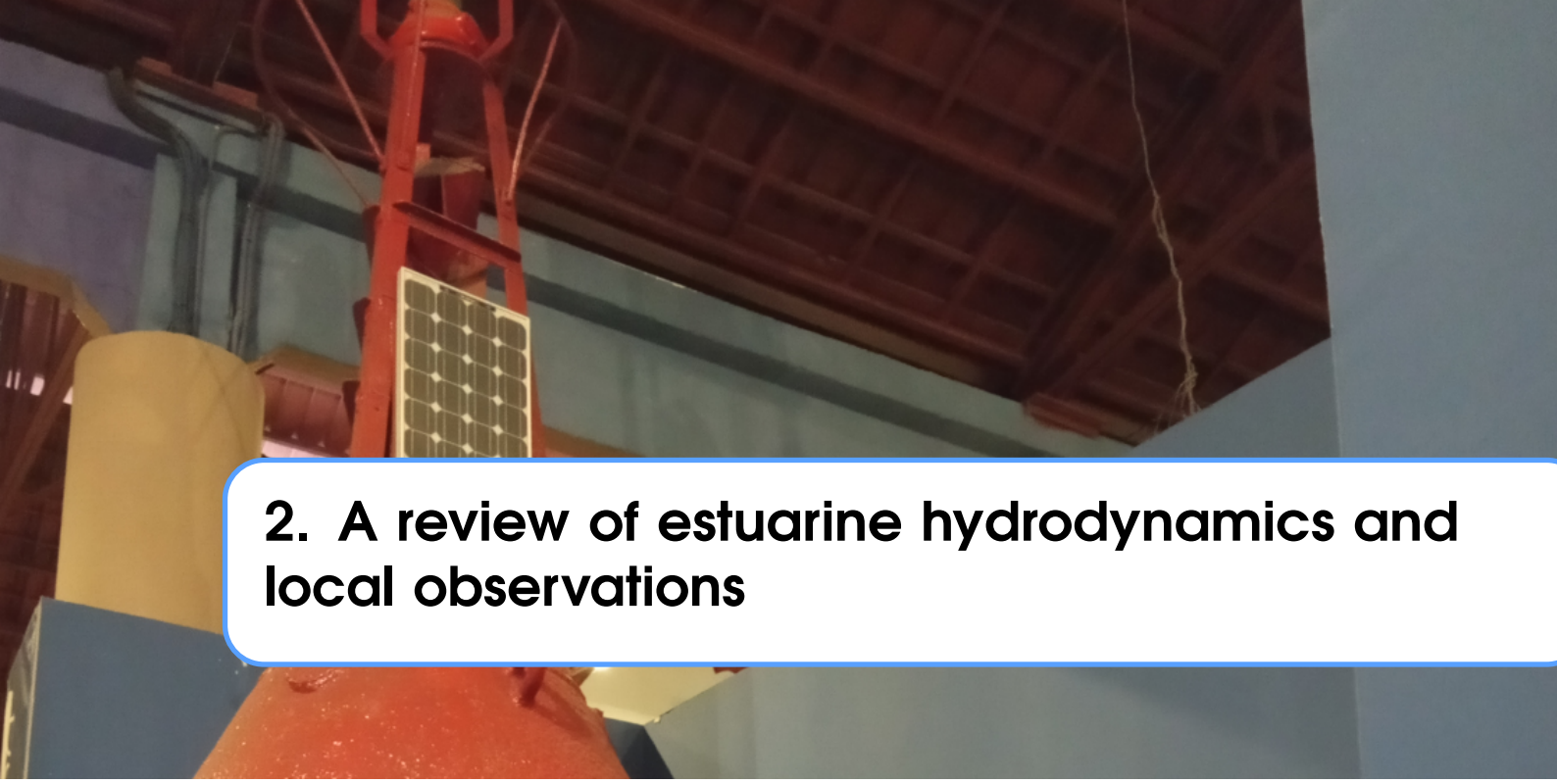

2. A review of estuarine hydrodynamics and local observations

"Nature dislikes gradients."

Miguel Ángel Losada

The aim of this chapter is twofold: (i) to briefly review the fundamentals of hydrodynamics and transport mechanisms in estuaries; and (ii) to gain knowledge about processes from the datasets of the Guadalquivir River estuary.

With these purposes, section 2.1 provides a description of estuaries based on tidal range, vertical density profile, lateral and longitudinal circulation. These classifications provide clues about main estuarine processes related to stratification and potential energy anomaly (PEA) (§ 2.2). Other causes of stratification or mixing are found in solar radiation, tidal and wind stresses, gravitational circulation or tidal straining (§ 2.2.1). An issue appeared when the potential energy anomaly concept is applied to weakly stratified or well-mixed estuaries. The solution is presented in section 2.2.2 with the definition and description of the longitudinal anomaly of potential energy. It will be in the next chapter where a general formulation of the Longitudinal Anomaly of Potential Energy be developed.

Secondly, the main datasets of water levels, salinity, temperature, turbidity, water currents and wind fields, solar radiation and fresh-water discharges are explored (§ 2.3). The objective is to gain knowledge of spatial/temporal variability of those quantities within the estuary. In addition to those datasets, it was also used salinity and temperature reanalysis datasets and observational data from tidal gauge stations in order to infer some general patterns in density, mixing and their relation with other important variables.

2.1 Classification of estuaries

In chapter 1, a morphological classification of estuaries was presented and some information about the underlying forces that depict the estuarine morphology was retrieved. Now, it is the moment to

characterize an estuary in-depth.

Figure 2.1 shows a sketch to identify different parts of an estuary and the main agents and processes on them. At the mouth, waves propagate towards shallow water where wave steepness is not stable, causing their break that moves sediments and mixes waters. Tides propagates along the estuary as oscillations of well-defined frequencies that ebb and flood it during decreasing and increasing sea-level periods, respectively. Tidal propagation pumps salt, sediments and nutrients, and mixes waters.

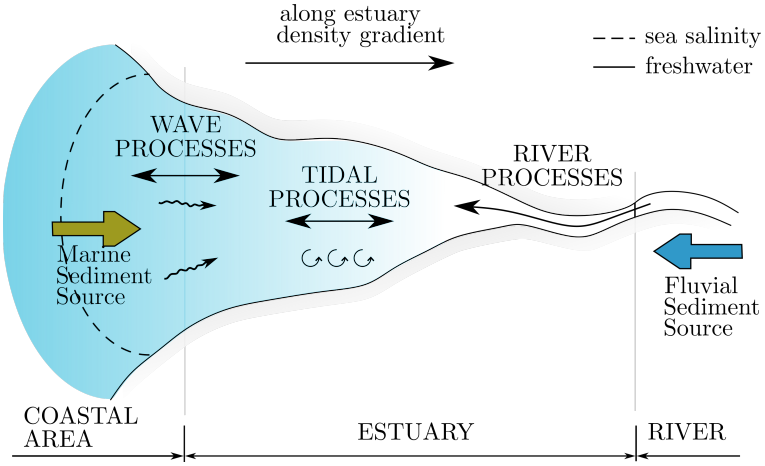

Figure 2.1: Classic estuarine zonation depicted from the head region, where fluvial processes dominate, to the mid- and mouth regions where tidal and wave processes are the dominant controlling physical forces, respectively. Differences in the intensity and sources of physical forcing throughout the estuary also result in the formation of distinct sediment facies. Modified from Dalrymple (1992).

Further details about tides and the mechanisms that modify tidal propagation nearshore are found in chapter 6. The intensity of tides is described by the tidal range H which measures the difference between high and low water level during a tidal period, usually 12.42 hours. According to the tidal range estuaries are classified into: **micro-** ($H < 2$ m), **meso-** ($2 < H < 4$ m), **macro-** ($4 < H < 6$ m) and **hyper-tidal** ($H > 6$ m) (Dronkers, 1964).

This range determines the **tidal prism** which is defined as the amount of water that flows into and out of an estuary or bay with the flood and ebb of the tide, excluding any contribution from freshwater inflows (Hume, 2005). The tidal prism is widely used to assess tidal contribution or water exchange in estuaries, and it is very useful for estimating residence times and concentrations of dissolved and suspended particle matter in well-mixed estuaries (Luketina, 1998).

The morphology leads to important spatial variations in the tidal range and the strength of the tidal currents (Dyer, 1973), affecting also mixing processes during ebb and flood phases. Convergence and friction are the major processes. The landward convergence of river banks increases tidal elevations while friction reduces them. When convergence exceeds friction, the estuary is said to be **hyper-synchronous**; when friction exceeds the effect of convergence, it is called **hypo-synchronous**, and finally, on **synchronous** estuaries both processes are in balance. Along an estuary may be found several typologies.

Estuaries are also classified as positive or inverse depending on the prevailing terms in the water balance. A **positive estuary** is found when the freshwater inputs from river discharge and precipitation exceeds the output due to evaporation. Under such circumstances, the vertical density profile is curved seaside (Valle-Levinson, 2010). The longitudinal density gradient is the origin

of an estuarine circulation or, the also called, residual or gravitational (Geyer and MacCready, 2014). In **inverse or positive estuaries** the longitudinal density gradient has the opposite sign than positive estuaries, i.e., water density increases landward. In regards to the vertical structure of salinity buoyancy forces from river discharge and mixing from tidal forcing are in competition (Pritchard, 1955). Figure 2.2 depicts the typical 2DV variation of density together with arrows that qualitatively indicate the magnitude and direction of river discharge, tidal mixing and the residual circulation.

Salt wedge estuaries depict a sharp interface below which salty water flows landward while large fresh water flows above seaside (figure 2.2.a). River flow is dominant over tidal flow in **strongly stratified** estuaries (Dyer, 1973). The stratification remains strong and the isohaline layer is quite deep. The mean flow exhibits the classical estuarine circulation, being weak landward (figure 2.2.b). When the effect of tides is in balance or slightly larger than river freshwater buoyancy, mixing from tides modify the vertical density profile and **partially mixed** or **weakly stratified** estuaries are found (figure 2.2.c). Finally, **well-mixed** estuaries are found when tides homogenize the vertical density profile due to the turbulence induced by friction. While the vertical variation of density shows a sharp change in salt wedge estuaries (see figure 2.2.a), it progressively becomes more regular (see figure 2.2.b and c), and even vertical, in well-mixed estuaries (see figure 2.2.d). In well-mixed and salt-wedge estuaries, the depth-averaged flow will be similar in magnitude to the surface outflow.

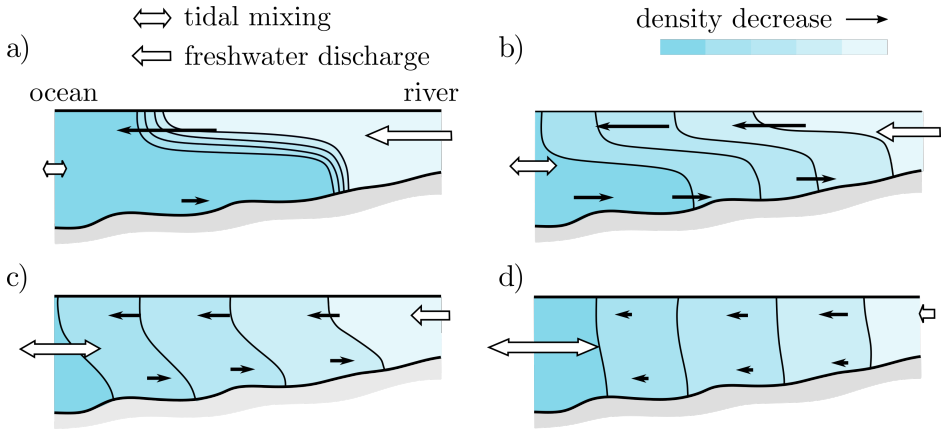

Figure 2.2: Classification of estuaries according to the vertical structure of salinity or density. From Valle-Levinson (2010). *a)* Salt-wedge; *b)* strongly stratified; *c)* weakly stratified; and *d)* well-mixed estuaries.

It is worth to mention that the along-estuary density gradient also modifies the water column properties, which are critical in determining the amount of available light and nutrients for phytoplankton in shallow coastal regions (Miranda et al., 2017; Valle-Levinson, 2010). Both factors are decisive and have a fundamental role in the knowledge of the behavior of the ecosystems that live therein.

2.1.1 Stratification-circulation diagram

A widely accepted classification of estuaries was proposed by Hansen and Rattray (1966). This classification is anchored in two hydrodynamic non-dimensional parameters: (a) the circulation parameter and (b) the stratification parameter.

The circulation parameter represents the ratio of near-surface flow (U_s), which is usually related

to the river discharge, and the depth-averaged flow (U_f). The stratification parameter stands for the ratio of the vertical salinity difference (ΔS) to the mean salinity over the section (S_0).

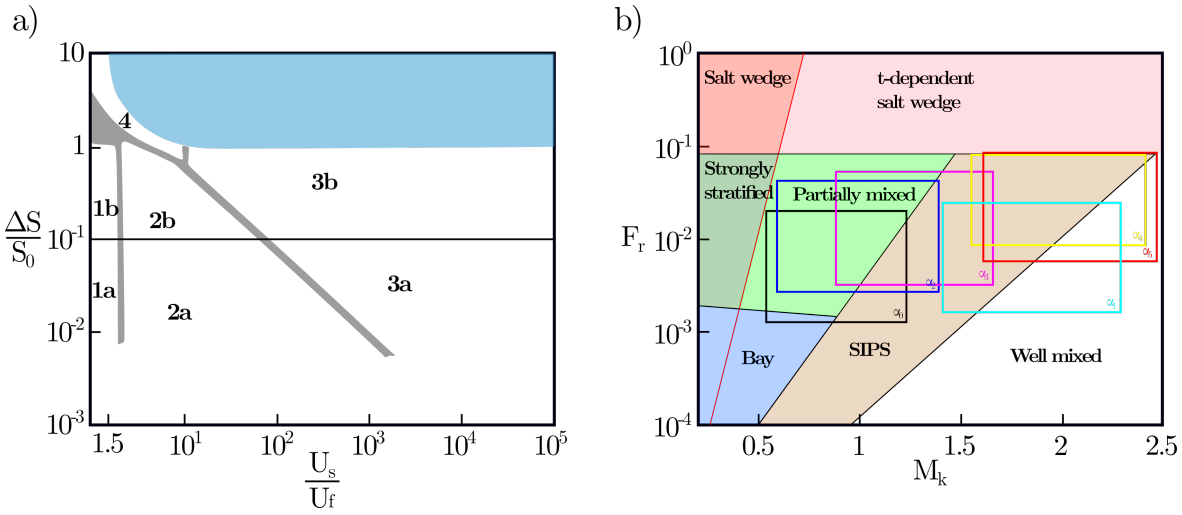

Figure 2.3: Classification of estuaries according to the stratification-circulation diagrams. *a)* Hansen and Rattray (1966); and *b)* Geyer and MacCready (2014). In panel *b)*, it is drawn the approximate influence of spring-neap variations and river flow (Díez-Minguito and Swart, 2018). The location of devices is plotted in figure 2.10.

The lower-left corner of the parameter space (fig. 2.3.a) describes well-mixed estuaries with unidirectional net outflows, i.e., seaward flows with no vertical structure or type 1 estuaries. Type 1a corresponds to strong tidal forcing and weak river discharge (or large tidal prisms relative to freshwater volumes).

Type 2 estuaries are those where flow reverses at the bottom, and include most temperate estuaries (fig. 2.3.a). These systems show a well-developed gravitational circulation and contribute to the upstream salt transport by advective and diffusive processes. Type 2a estuaries are well-mixed or weakly stratified and type 2b estuaries are strongly stratified. Note that strongly stratified and weakly stratified estuaries may exhibit similar features in terms of the relative contribution from diffusive processes to the upstream salt transport.

Geyer and MacCready (2014) proposed a new approach to classify estuaries based on tidal velocity and freshwater flow. This stratification-circulation diagram is based on the freshwater Froude number ($F_{r,f} = U_R/\sqrt{-bd}$) and a mixing parameter ($M^2 = C_d U_T^2/wNd^2$), being $N = \sqrt{-b/d}$, the buoyancy frequency, $b = -g(\rho - \rho_0)/\rho_0$), U_R and U_T are representative velocities of river discharge and tide, respectively. This approach is reasonably effective at separating different estuarine regimes. These parameters are computed locally at different stretches along the Guadalquivir River estuary (frames in figure 2.3.b).

Figure 2.3.b points out the limitations of classifying estuaries as a whole solely based on stratification-circulation diagrams (Díez-Minguito and Swart, 2018). Even spatially close stretches may transit between different regions of the G&M14 diagram (Geyer and MacCready, 2014). At the mouth, the estuary is mainly partially-mixed. Remarkably, it is revealing that conditions in the inner stretches fall most of the time in the Strain-Induced Periodic Stratification (SIPS) regime mapped in the G&M14 diagram (Simpson et al., 1990), that refers periodic variations in the stratification induced by the vertical shear of the tidal flow acting over an horizontal salinity gradient. This phenomenon drives a tidal straining circulation with a magnitude that may significantly exceed the gravitational circulation.

Freshwater discharges may shift the state of the lower stretches toward a salt-wedge structure whose location depends strongly on the fresh water volume discharged. This buoyancy forces are related to the turbulent production of kinetic energy through the flux Richardson number as:

$$R_f = \frac{k_z}{N_z} \frac{\frac{g}{\rho}\frac{\partial \overline{\rho}}{\partial z}}{\left(\frac{\partial U}{\partial z}\right)^2} = \frac{k_z}{N_z} Ri_x = \frac{k_z}{N_z} \frac{N^2}{S_v^2}, \tag{2.1}$$

where N is the buoyancy frequency. In eq. 2.1, the first term of the last part is the Prandtl number which is in general proximate to the unity. The second term is the horizontal Richardson number or Simpson number (Si, Monismith et al. (1996), Stacey et al. (2001), and Stacey and Ralston (2005)). Based on the analysis of Burchard and Hetland (2010), the ratio of potential energy changes due to straining to the rate of production of turbulent kinetic energy can be expressed as:

$$Ri_x = \frac{(\partial b/\partial x)d^2}{C_d U^2}. \tag{2.2}$$

Ri_x, or equivalently Si, is used to determine turbulence, therefore $Ri_x < 0.25 \approx 0.2$ is often a criterion for the maintenance of turbulence (Miles, 1961) or equivalently to assumed that the water column is well-mixed even during ebb tide; it develops SIPS for $Ri_x \approx 0.2$; and, it develops partial or permanent stratification for values greater than 0.2.

2.1.2 Lateral circulation

Analogous to the classification of estuaries in terms of the two non-dimensional parameters discussed above, estuarine systems can also be classified in terms of the lateral structure of their net exchange flows (Valle-Levinson, 2008; Valle-Levinson, 2010). The lateral structure may be strongly influenced by bathymetric variations and may exhibit vertically sheared net exchange flows, i.e., net outflows at the surface and near-bottom inflows, or laterally sheared exchange flows with outflows over shallow parts of a cross-section and inflows in the main channel (e.g., Wong (1994)). The lateral structure of exchange flows may ultimately depend on the competition between Earth's rotation (Coriolis) and frictional effects, characterized by the vertical Ekman number (E_k), or the lateral structure of exchange flows, that depend on the Kelvin number (K_e). The Ekman number is a non-dimensional dynamical depth of the system. Low values of E_k imply that frictional effects are restricted to a thin bottom boundary layer (weak frictional, nearly geostrophic conditions), while high values of E_k indicate that friction affects the entire water column.

For the rest of the thesis, it is hypothesized that the transversal processes are negligible. This hypothesis is quantified in the Kelvin (K_e) and Ekman (E_k) numbers parameter space (Valle-Levinson, 2008). The channel width is related to the internal Rossby radius of deformation through the Kelvin number whereas the Ekman number establishes the relation between the viscosity and Coriolis forces. For the mean value of the vertical eddy viscosity coefficient, typical of the GRE $\sim 3.3 \cdot 10^{-4}\,\mathrm{m^2 s^{-1}}$ (Reyes-Merlo et al., 2013), values, $K_e \sim -2$ and $E_k \sim -2.5$, clearly points out a vertically-sheared exchange. Near the estuary mouth, where channel widths are greater and where the values of the vertical eddy viscosity coefficient are $\sim 1.2 \cdot 10^{-3}\,\mathrm{m^2 s^{-1}}$ ($K_e \sim -2$ and $E_k \sim -1.25$), a certain degree of lateral variability is expected. It will consider that the GRE is a narrow (channeled) estuary.

2.1.3 Outline of GRE classification

The GRE is a positive estuary, narrow, flood-dominated and mesotidal estuary (~4 m tidal range at the mouth), where the mainly supported tidal constituents are the semi-diurnal M_2, S_2 and N_2.

The estuary number is lower than 0.05; the densiometric Froude number is smaller than 0.014; and the estuarine Richardson number is usually lower than 0.3. This indicates that the GRE is tidally dominated and poorly stratified (type 2.a) when freshwater discharges are smaller than 40 m^3/s (Díez-Minguito et al., 2013).

Eventually, processes and transport mechanisms are generally spatially zonate but it is also important in time. A coastal-plain estuary largely dominated by tides as the Guadalquivir estuary, might be dominated by river discharges during storm conditions, altering the estuary hydro-morphodynamics (Díez-Minguito et al., 2012; Díez-Minguito et al., 2013; Díez-Minguito et al., 2014; Losada et al., 2017).

While the stratification-circulation diagram showed both well-mixed (generally upstream) to partially-mixed conditions (near the mouth), the observations also evidenced the existence of SIPS, which may drive part of the residual circulation and compete with the density-driven flow. Estimates of the Simpson number during the same period confirm this picture. The SIPS regime implies that the covariance between eddy viscosity and vertical shear of the longitudinal current drives part of the subtidal circulation, even more efficiently than the classical gravitational circulation does (Burchard and Hetland, 2010). This may have a significant impact on the estuarine suspended matter distribution.

2.2 The Potential Energy Anomaly

The competition between buoyancy and mixing increases and decreases the density along the water column, allowing the evolution of two or more layers. Following the experiments of Thompson and Turner (1975) and Turner and Kraus (1967), it supposes a full tank of water with a constant salinity gradient that is positive in depth. This can also be done with heat as figure 2.4 shows. This will give a stable density profile; whose density also grows in depth. They put a mesh attached to an engine that made it turns and at the same time roses and fells, generating turbulence and mixing.

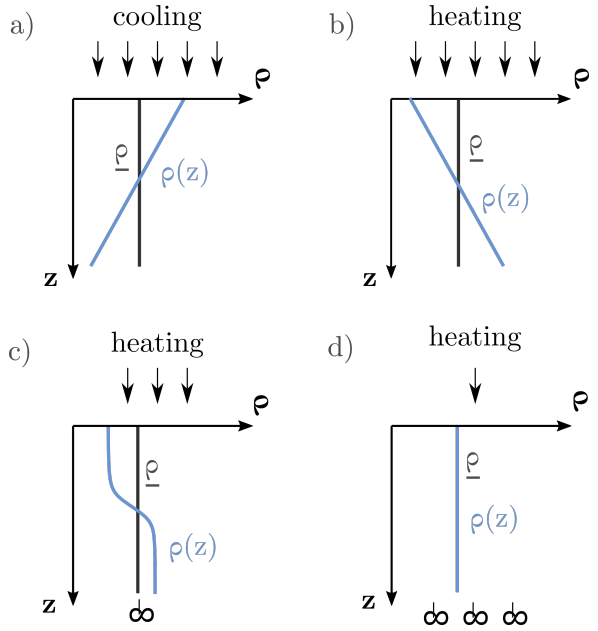

Figure 2.4: Vertical density profiles for different intensities of the sources of buoyancy and mixing. *(a)* Surface cooling without mixing; *(b)* surface heating without any mixing force; *(c)* stratified conditions; *(d)* well-mixed conditions.

In figure 2.4 is observed some vertical density profiles respecting the vertically-averaged density ($\underline{\rho}$). Instable vertical density profiles are found when the surface is cooling without mixing (fig. 2.4.a). The opposite is observed for heating (fig. 2.4.b). Panels *(c)* and *(d)* show vertical density profiles with an increasing mixing forces at the bottom. Where mixing is much larger than heating-induced buoyancy, well-mixing conditions are found (panel *d*).

The consistence of the transition between stratified and unstratified regimes, essentially with the intensity of tidal mixing, brought to consider the balances of energy fluxes as the main descriptors (Simpson and Hunter, 1974). The mechanical energy includes kinetic and potential energy in the balance. In estuaries, the kinetic energy density is $\rho_0 q^2/2$ where q is the flow speed. The available potential energy/unit volume is given as $\rho_0 N^2 h^2/2$ (Cushman-Roisin, 1994) where ρ_0 is a reference density, and h the vertical displacement of an isopycnal. For a buoyant coastal plume, h is approximately the plume depth. Hence, the ratio of kinetic to potential energy is $(q/Nh)^2 = F_r^2$, the internal Froude number squared, typically quite small compared to unity (see figure 2.3.b). Consequently, it is expected that the bulk of mechanical energy associated with buoyant river discharge is potential energy (Garvine and Whitney, 2006). It was not until 1974 when Simpson & Hunter proposed a potential energy anomaly equation to relate the potential energy before and after the mixing with the sources of buoyancy. They used it to describe the shape and position of the fronts in the Irish Sea (Simpson and Hunter, 1974). The potential energy anomaly ϕ_S describes the competition between stratification and destratification processes in shallow coastal seas. It is defined as the amount of mechanical energy per m^3 required for an instantaneous vertical homogenization of the water column. Stratification is usually due to surface heating (figure 2.4) or to the horizontal gradient induced by the freshwater flow and derived processes. Conversely, destratification (or mixing) processes are mainly due to tidal and wind stirring. Mathematically, it reads as:

$$\phi_S(\mathbf{x},t) = \frac{g}{d}\int_{-d}^{0}(\rho - \underline{\rho})z\,dz, \quad \text{where} \quad \underline{\rho}(\mathbf{x},t) = \frac{1}{d}\int_{-d}^{0}\rho\,dz, \tag{2.3}$$

Therefore, we can verify that the more stratified the water column is, the greater the potential energy anomaly. It was defined considering the change in surface density by heating and the mixture due to the shear generated by the tide at the bottom.

2.2.1 Description of estuarine dynamics in terms of potential energy anomaly

Thinking on an estuary or an area near the mouth of a river, the structure of the water column is the result of many processes that take place: freshwater flowing from the river, saline intrusion from the sea, warming surface water by solar radiation, surface mixing by the tangential effort of the wind, deep mixing by the tangential effort of the tide, etc. The great progress in estuarine dynamics the last decades has provided insights to identify and analyze the hydrodynamic processes in estuaries (Geyer and MacCready, 2014; Simpson and Sharples, 2012; Valle-Levinson, 2010, and references herein). In particular, strain-induced periodic stratification (Aken, 1986; Simpson et al., 1990); changes in stratification due to enhanced tidal currents (Jay, 1991); gravitational variability due to longitudinal salinity gradients (Monismith et al., 2002); wind-induced straining (Scully et al., 2005); or spring-neap variations in horizontal dispersion (Geyer et al., 2008), among others. More recent studies on estuarine dynamics focus on the full description of velocity field under several conditions using numerical models. So, contributions of several mechanisms to estuarine circulation (Burchard and Hetland, 2010); implications of river discharge and geometry on tides and net water transport in the estuary network (Alebregtse and Swart, 2016); transverse variations of tidal and subtidal flow (Ross et al., 2017); estuarine circulation due to local and remote wind

(Giddings and MacCready, 2017); or even tidal response to sea-level rise (Du et al., 2018), were figured out.

The following subsections show the formulation of the major estuarine processes in terms of the potential energy anomaly.

The solar radiation

In figure 2.5, it can be observed how solar radiation flux per unit area (ΔQ) entering into the water column by the surface modifies the vertical profile of temperature. This heat input will be absorbed close to the surface in a thin layer (h_l). The buoyancy of this layer is the change of density by gravity whose force is applied at the gravity center of the layer which is approximately the half of its thickness. The density change is written as:

$$\Delta\rho = \alpha\rho_0\Delta T = \frac{\alpha\Delta Q}{c_p h_l}, \tag{2.4}$$

where α is the water thermal expansion coefficient ($1.67 \cdot 10^{-4}$ ºC^{-1}) and c_p is the water heat capacity (4000 J kg^{-1} ºC^{-1}). In this way, the complete mixing of this layer is achieved with an

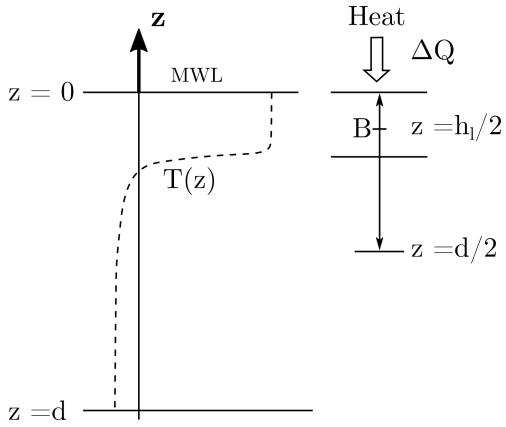

Figure 2.5: The buoyancy input due to surface heating (modified from Simpson and Sharples (2012)).

increase of the potential energy equals to the buoyancy force created by the density difference (eq. 2.4) in the motion of a half of the thickness. Therefore, supposing that the heat is supplied in a short time interval $\Delta t \to 0$ at a rate Q:

$$\left(\frac{\partial\phi_S}{\partial t}\right)_h = \frac{1}{h_l}\frac{\partial\Delta E_p}{\partial t} = \frac{gh_l\Delta\rho}{2h_l\Delta t} = \frac{\rho\alpha gQ}{2c_p}, \tag{2.5}$$

which units are Wm^{-3}.

The tidal and wind mixing

In this case, the mixture is produced by turbulence. Assuming that the gradient is uniform, and the shear in surface and velocity at the bottom are both null, the production of turbulent energy in the direction of tidal propagation for a steady vertically sheared flow can be written as:

$$P_T = -\int_{-h}^{0} \tau\frac{\partial u}{\partial z}\,dz = \tau_b\overline{u} = C_d\rho_0|\overline{u}|^3, \tag{2.6}$$

where $C_d = 2.5 \cdot 10^{-3}$ is the drag coefficient. We have rather little knowledge of these stresses and the way in which they vary with the properties of the mean flow (Burchard and Hofmeister, 2008). To get around this problem, it is commonly assumed that a stress component can be related to the velocity gradient. Therefore, τ_b is usually substituted by the quadratic drag law. Hence, the rate of change of potential energy anomaly due to tidal mixing reads as:

$$\left(\frac{\partial \phi_S}{\partial t}\right)_m = \frac{e_b P_T}{d} = \frac{e_b C_d \rho_0 |\overline{u}|^3}{d}, \tag{2.7}$$

where $e_b = 0.005$ is the mixing efficiency parameter. Analogously, the wind mixing is parameterized as:

$$\left(\frac{\partial \phi_S}{\partial t}\right)_m = \frac{e_w P_T}{d} = \frac{e_w C_w \rho_a |\overline{W}|^3}{d}, \tag{2.8}$$

with $e_w = 0.023$; $C_w = 2.5 \cdot 10^{-4}$. The mixing efficiency parameter e_b is larger than e_w because it is near of the pycnocline.

The gravitational circulation

The flow of freshwater from the river to the estuary establishes and maintains a horizontal salinity gradient and, therefore of density (figure 2.6), that produces circulation. Taking derivatives to

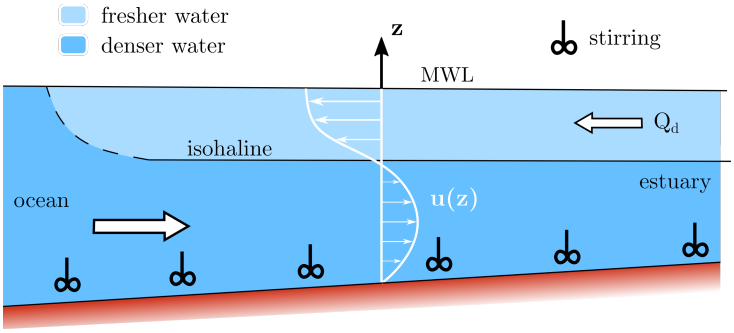

Figure 2.6: Sketch of the estuarine circulation (modified from Simpson et al. (1991)).

equation 3.1 gives:

$$\frac{\partial \phi_S}{\partial t} = \frac{g}{d} \int_{-d}^{0} \left(\frac{\partial \overline{\rho}}{\partial t} - \frac{\partial \rho}{\partial t}\right) z dz. \tag{2.9}$$

Assuming that density changes due to advection are dominant (it is neglected the periodic change in ϕ_S due to the tidal variation in d), $\partial \rho / \partial x$ is independent of z, and the flow is only in the x direction, then, the advection-diffusion equation (Simpson et al., 1990) reads:

$$\frac{\partial \rho}{\partial t} = -u \frac{\partial \rho}{\partial x}, \qquad \text{and,} \quad \frac{\partial \overline{\rho}}{\partial t} = -\overline{u} \frac{\partial \rho}{\partial x}. \tag{2.10}$$

Then, substituting equation 2.10 into equation 2.9, yields:

$$\frac{\partial \phi_S}{\partial t} = \frac{g}{d} \frac{\partial \rho}{\partial x} \int_{-d}^{0} (u - \underline{u}) z dz, \tag{2.11}$$

where the velocity profile (figure 2.6) is obtained from the momentum equation (Hansen and Rattray, 1966; Officer, 1976) with the following premises: it is neglected Coriolis; it is assumed

stationary flow and hydrostatic pressures; and, the shear stress through eddy viscosity and boundary conditions on surface (null shear) and bottom (null velocity). Then, the estuarine circulation is obtained (eq. 2.12):

$$u(z) = u_s(1 - 9z^2 - 8z^3), \qquad \text{with} \quad u_s = \frac{g\varsigma d^3}{48N_z}, \tag{2.12}$$

where $\varsigma = \frac{1}{\rho_0}\frac{\partial \rho}{\partial x}$ and N_z is the eddy viscosity.

Finally, substituting eq. 2.12 into eq. 2.11, yields:

$$\left(\frac{\partial \phi_S}{\partial t}\right)_g = \frac{1}{320}\frac{g^2 d^4}{N_z \rho_0}\left(\frac{\partial \rho}{\partial x}\right)^2. \tag{2.13}$$

The gravitational circulation is also responsible for stratifying the density profile. The horizontal density gradient is really a part of the 'solution' rather than the external forcing. Nevertheless, if the density gradient is available, the use of equation 2.13 enables the separation of the gravitational contribution to others, i.e., the tidal straining.

The tidal straining

The tidal straining is the result of the interaction between the tidal current (usually the semidiurnal component) and the horizontal density gradient. It can be described as the covariance between the eddy viscosity and the vertical shear of the along-channel component of the velocity. It is also often referred to as Strain-Induced Periodic Stratification (SIPS). This process, unlike the previous one, is a mixing process.

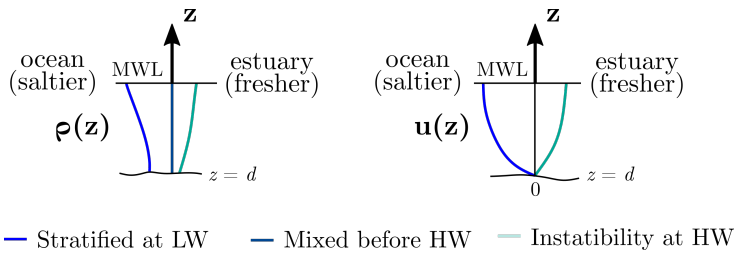

Figure 2.7: Density and current profiles at certain timestamps during the ebb/flood cycle.

At the beginning of the ebb, it may assume that the water column is fully mixed and the salinity isohalines are vertical. As the ebb current about develops, the bottom friction causes that currents decrease towards the bed resulting in the fresher water going seaward faster than the denser water of the bottom (figure 2.7). This fact produces stable stratification that continues until the end of the ebb. During flood, the shear stress is opposite and the denser water is advected to landward faster than the water near the bed. The stratification is gradually vanished, and in the absence of mixing, the system will return to the complete mixing. This process is symmetrical unless there is a significant mixture by the tidal flow during the ebb. As this happens, the complete vertical mixing is achieved before the end of the flood, when the isohalines will be vertical.

Following the same procedure as the gravitational circulation (eq. 2.11) and assuming that the tidal current is now defined by:

$$u(z) = \overline{u}(a - bz^2) \tag{2.14}$$

where a and b are parameters fitted to vertical profile of water currents, the tidal straining is written in term of potential energy anomaly as:

$$\left(\frac{\partial \phi_S}{\partial t}\right)_{st} = gh\bar{u}\frac{\partial \rho}{\partial x}\left(\frac{b}{4} - \frac{a-1}{2}\right) \tag{2.15}$$

This equation of the density gradient contribution to SIPS is of the same form as that for the contribution of estuarine stratification but with the important difference that the numerical constant is an order of magnitude lower. SIPS, therefore, occurs more readily than enduring estuarine stratification (Simpson and Sharples, 2012). Tidal straining can also occur in well-mixed estuaries (Burchard and Schuttelaars, 2012).

Examples of PEA from different sources

After the definition and description of the key estuarine processes, it is important to assess their variability. Figure 2.8 shows how the previous terms vary with their dependent variables. The variables given in eqs. 2.5, 2.7, 2.8, 2.13, and 2.15 are assessed taking into account the reference values for the GRE. Therefore, the following values of the parameters were used: d = 7 m, α = 1.67·10^{-4}, c_p = 4000 J kg^{-1} ºC^{-1}, g = 9.81 m s^{-2}, u_{M_2} = 0.4 m s^{-1}, ρ_0 = 1000 kg m^{-3}, $N_z = 0.003 * u_{M_2} * d$ (Bowden et al., 1959), ρ_a = 1.26 kg m^{-3}, a = 1, and b = 1/8.

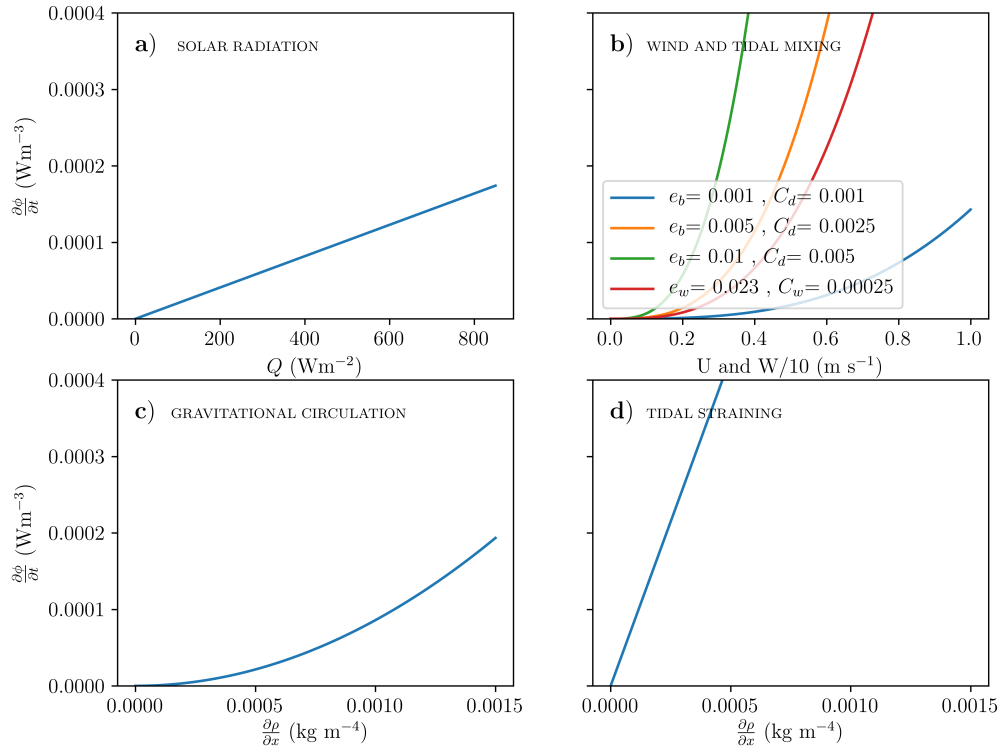

Figure 2.8: Terms of potential energy anomaly at the GRE. Several combinations of parameters were used for wind and tidal mixing (panel *b*)).

As it can be observed in Figure 2.8, tidal straining and tidal mixing prevail in the GRE during

normal conditions, while the contribution of solar radiation and gravitational terms is relatively modest and becomes larger for high radiation flux and longitudinal density gradients, respectively.

2.2.2 The longitudinal anomaly of potential energy

A basic review of the estuarine fundamentals was given in previous sections (Dean and Dalrymple, 1991; Dronkers, 1964; Dyer, 1973; Ippen, 1966; Officer, 1976, further information). The usefulness of the balances in term of the potential energy were also shown. The PEA balances provide lot of information about how the estuary behaves and the stratification-mixing competition is accounted and assessed. However, in the case of the GRE, a narrow, shallow and well-mixed estuary, the vertical density profiles are relatively vertical (figure 2.9.a) which means that equation 3.1 is generally zero (figure 2.9.b). It is a quite common vertical profile under low river-flow conditions at the GRE. If equation 3.1 is applied, it is obtained a potential energy anomaly almost null since $\rho(z)$ is almost equal to $\underline{\rho}$ for every t and z.

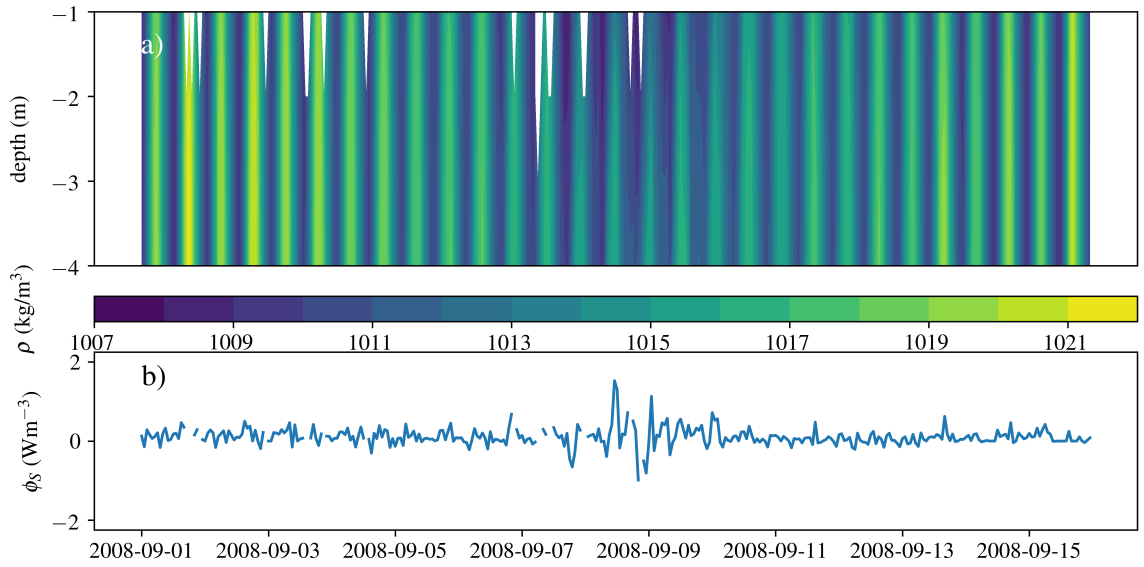

Figure 2.9: Time series of vertical density near the mouth of the GRE *a)*, and potential energy anomaly *b)*. As it can be observed, it exists large density differences between spring (maximum tide next to September, 2nd) and neap (minimum tide next to September, 9th) tides. However, the vertical density profiles remained almost constant which means $\phi_S = 0$. Some gaps are observed in the figure.

Here, it is followed the approach of Garvine and Whitney (2006) (GW06). They decided to change the reference density, which was established as the depth-averaged density at the measuring point (Simpson and Hunter, 1974), to a depth-averaged density in another position located downstream x_0. Hence, the **longitudinal anomaly of potential energy** reads as:

$$\phi(\mathbf{x},t) = \frac{g}{d}\int_{-d}^{0}(\rho - \underline{\rho_0})z\,dz, \quad \text{where} \quad \underline{\rho_0}(x_0,t) = \frac{1}{d}\int_{-d}^{0}\rho(x_0)\,dz, \tag{2.16}$$

In GW06 work, the water exchange was assessed between the estuary and continental shelf. They located the reference density ρ_0 at the continental shelf and proposed an energy balance that

considers some of the most important transport mechanisms. In chapter 3, a complete energy balance considering the major estuarine processes will be given following the theoretical analysis of Burchard and Hofmeister (2008).

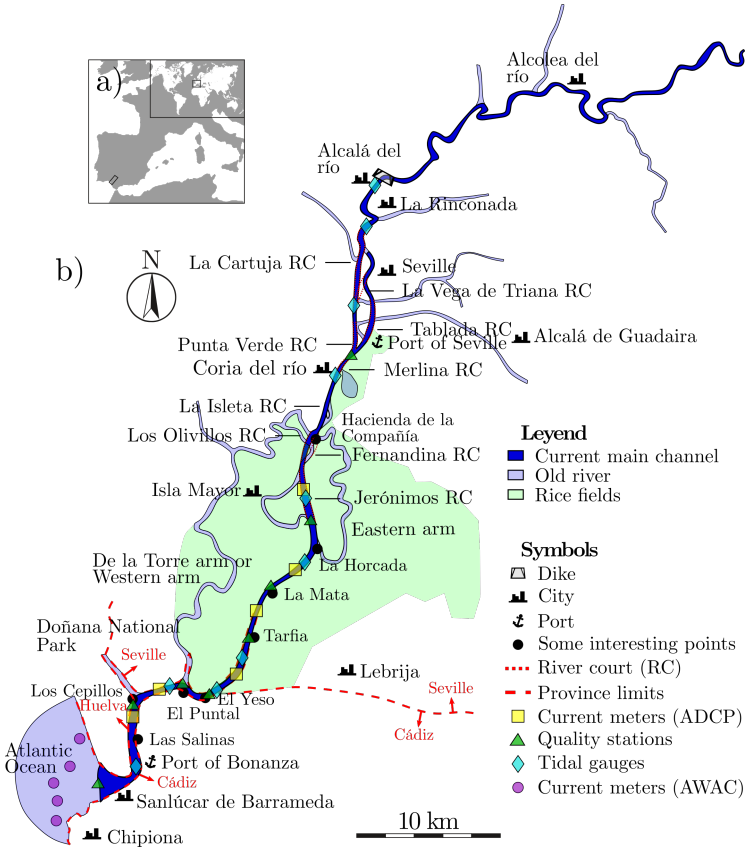

Figure 2.10: Map of study area with the location of the monitoring network stations. The monitoring network is composed of current profilers (ADCPs), tidal gauges, meteorological station (M.S.) and environmental quality probes or CTDs (see Navarro et al. (2012), for more details). The sensors were located near the main estuary channel. In this thesis, the origin of the along-channel coordinate (triangle next to Sanlúcar de Barrameda) was established at the mouth and follows the thalweg upstream.

2.3 Observations at the study area

The GRE is located in the south-west of Spain (36°43'N - 37°32'N, 5°56'W - 6°30'W) and is a transition area between the river basin of the same name and the Gulf of Cádiz (figure 2.10). It comprises the final 110 km of the river, where the last stretch of 85 km, is navigable as far as Seville. The Alcalá del Río dam is located at the upper-stream edge. The width of the main channel exponentially increases seawards while the depth gently increases linearly and is maintained uniform and equal to approximately 7 meters for navigation purposes. A broad description can be found in chapter 1.2.

The data was recorded with a remote real-time monitoring network installed by the Institute for Marine Sciences of Andalusia (ICMAN-CSIC) from 2008 to 2010 (see Navarro et al. (2011) and Ruiz et al. (2015), for further details). The estuary instrumentation used in the present thesis comprised eight environmental quality stations, two tidal gauges, six Acoustic Doppler Current

Profilers (ADCP), and a meteorological station located at Chipiona (see figure 2.10).

In the following subsections, an exploratory data analysis of datasets included in Navarro et al. (2019) is done (further details can be found in Bramato et al. (2010), Navarro et al. (2011), and Navarro et al. (2012)). The dataset was recently upload as part of the research study that established the foundations of this thesis (Cobos et al., 2020). This dataset was accordingly written to fulfil the repository requirements (zenodo.org).

It is important to highlight three datasets that differ from previous ones and which were mainly used in chapter 5. Firstly, data from tidal gauges from Puertos del Estado (PdE) stations along the Spanish coast. These datasets are now included in CMEMS (The Copernicus Marine and Environment Monitoring Service). Port of Bonanza and Seville stations (figure 2.10) belong to this set. Secondly, it was also used datasets from IBI Ocean Reanalysis, which is based on NEMO v3.6 ocean general circulation model. Hourly timeseries of vertical profiles of salinity and temperature were obtained near the mouth. In some cases, it was required the water density at the shelf which was calculated with salinity and temperature records of a buoy placed at that location by PdE or with reanalysis datasets obtained from CMEMS.

2.3.1 Description of environmental quality data

The environmental quality stations recorded salinity (S), temperature (T), turbidity (C), conductivity, normalized turbidity, dissolved oxygen, oxygen, oxygen saturation, percentage of oxygen saturation, fluorescence, and normalized fluorescence every thirty minutes. In this thesis, only salinity, temperature and suspended particle matter (retrieved from turbidity) were analyzed.

Salinity

The total concentration of dissolved salts or salinity is an indicator of the degree of global alteration of the chemical composition of the water body, and a state variable which describes its quality. Usually, this variable is estimated from measurements of the electrical conductivity (EC), which is directly and linearly related with it, since the salts present a good behavior as conductive material. The salinity is measured in unit of PSU (Practical Salinity Unit), which is a unit based on the properties of sea water conductivity similar to to g/kg.

Temperature

The structure of the temperature field in the Guadalquivir estuary plays an important role in the along-channel energy transfer (Padilla et al., 2016). At the stations represented in figure 2.10, a record of 23 months was available from July 2008 to June 2010. During some periods, measurements at several depths were also recorded. The temperature range between 10 degrees in winter to nearly 29 degrees in summer.

Turbidity

Although, in comparison, episodes of high turbidity are scarce, they represent a huge problem because sometimes they remain for several months (Díez-Minguito et al., 2014). Most of the information available in river networks is referred to suspended particle matter (SPM). They constitute the majority of the contributions of sediments to the estuary from the watersheds. Thhe information about the SPM levels and its variability is obtained indirectly from measurements of the turbidity of the water body (in FNU). This state variable refers to the optical properties of the fluid to absorb, reflect and refract incident light, and for obvious reasons, it is related to the total content of solid material in the water mass. The turbidity also reduces the penetration degree

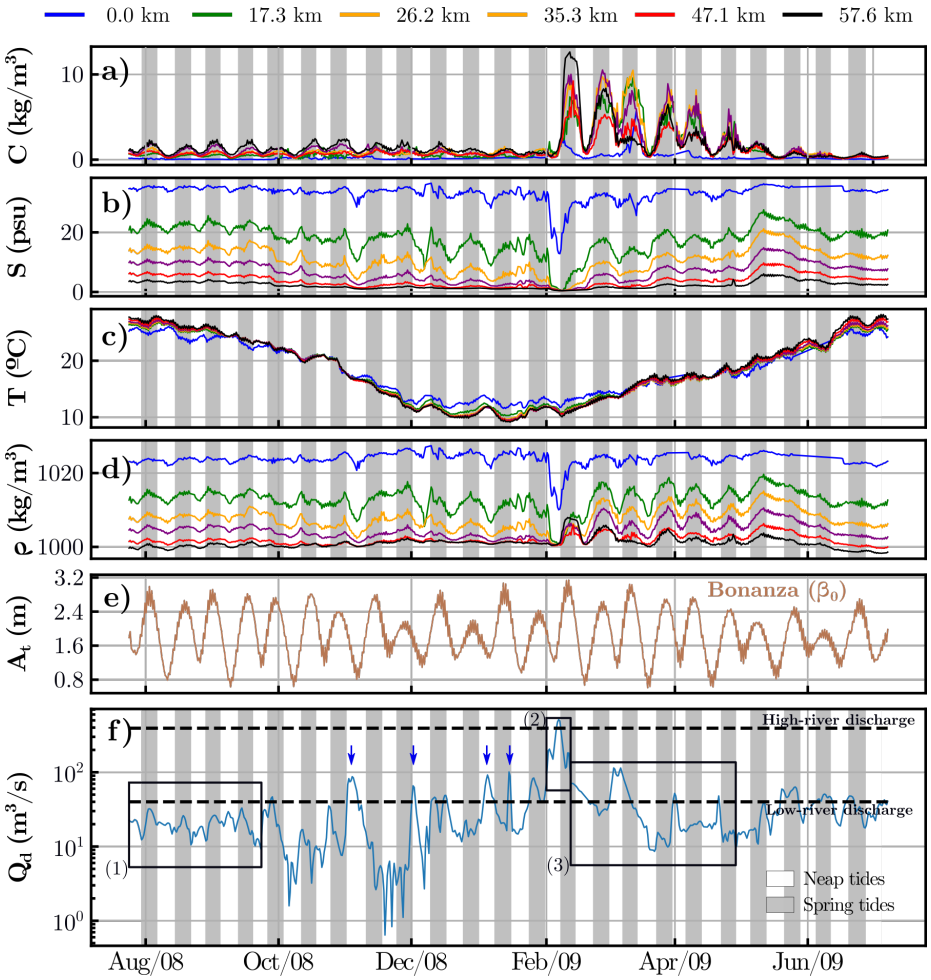

Figure 2.11: Time series of the tidal-averaged *a)* concentration of suspended particulate material; *b)* salinity; *c)* temperature; *d)* density; *e)* tidal range at Port of Bonanza; and, *f)* daily river discharges from the Alcalá del Río dam during the study period. Several boxes are displayed in panel *f*): (1) refers to the low-river flow regime; (2) refers to the high-river flow regime; and (3) stands for the recovery period. Spring and neap periods are also displayed. Blue arrows indicate pulsed discharges lasting various days, reaching 100 $m^3 s^{-1}$, which were not normal conditions for the estuary.

of solar radiation in the water column, alters the temperature of the water-sediment mixture and decreases the dissolved oxygen levels in the water.

The density field

From these data, the water density field $\rho(S,T,C)$ was calculated according to the Equation of State for seawater (UNESCO and SCOR, 1981), in which the sediment density was considered to be $\rho_s = 2650$ kg m^{-3}. The water density at any point is obtained as:

$$\rho(S,T,C) = \rho(S,T) + \left(1 - \frac{\rho}{\rho_s}\right) \cdot C \cdot c_f, \tag{2.17}$$

where $\rho(S,T)$ is the water density resulting from the sea water state equation and $c_f = 1.6015 \cdot 10^{-3}$ is a calibration factor.

Observational background

In figure 2.11, panels *(a)*, *(b)*, *(c)* and *(d)* show the tidal-averaged time series of the suspended solids concentration, salinity, water surface temperature, and density for different locations in the estuary (colored curves), respectively. Panel *(e)* shows the tidal range at the estuary mouth, and panel *(f)*, the fluvial discharge during the study period.

During the summer of 2008 (1), the estuary remained in a low-river flow regime with fluvial discharges of less than 40 m^3s^{-1}. In these conditions, tidal currents determine estuarine dynamics. The suspended particulate material throughout the estuary scarcely reached 2 $kg{\cdot}m^{-3}$ during the summer. In autumn and the beginning of the winter in that same year, pulsed discharges reached 100 m^3s^{-1} and lasted for various days (blue arrows in figure 2.11.f). This produced a marked decrease in salinity and density ($\Delta\rho \simeq 5$ kg/m^3).

In the middle of winter (2), intense rains made it necessary to open the floodgates of the dam upstream. The discharge reached the threshold of extreme fluvial conditions in the GRE ($Q > 400$ m^3s^{-1}). Density dropped sharply to freshwater levels in the entire estuary, except at the mouth, where the density reduction was 15 kg/m^3. The fluvial discharge caused the salt to be transported seaward from the estuary. It also increased the quantity of sediments suspended from the bed, which led to a turbidity peak approaching 10 $kg{\cdot}m^{-3}$ (fig. 2.11.a). During this period, the mouth showed the maximum horizontal density gradient of the estuary.

This episode was followed by a recovery period (3) in which the fluvial discharge of the dam again decreased with values below the threshold of 40 m^3s^{-1}. The salt that had been transported towards the mouth by the discharge began to move upstream again (figure 2.11.b). These conditions persisted until the beginning of the summer of 2009, when salinity levels and the sediment concentration were once more typical of low river flows. The summer was characterized by a slight linear reduction in density detected by all sensors. This was caused by the increase in water temperatures because of short-wave radiation (Padilla et al., 2016).

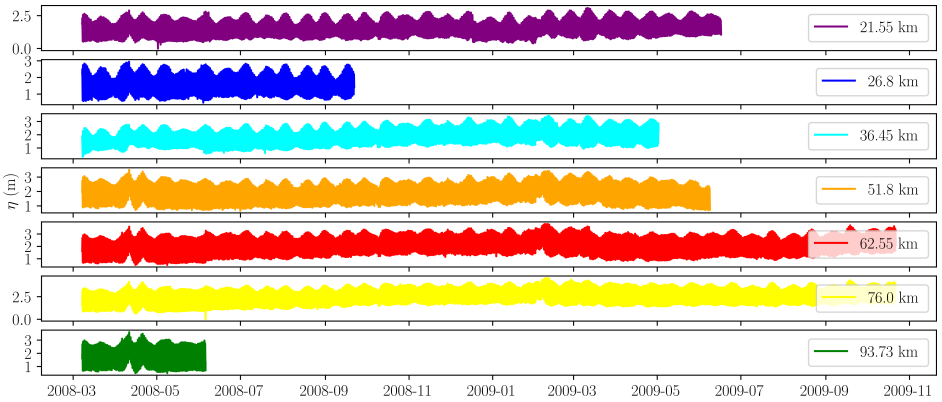

Figure 2.12: Corrected water levels along the GRE.

2.3.2 Description of water levels and currents

Water levels were provided every 10 min and current data were recorded every 15 min by Acoustic Doppler Current Profilers along the Guadalquivir estuary. The later datasets were obtained at several depths. In addition, it was also used water levels from gauges deployed by PdE located at the port of Bonanza (5 km upstream the mouth of the estuary) and Seville (85 km upstream).

Figure 2.12 shows the water levels from ADCPs. The water levels presented some jumps and gaps that were removed. As it is observed, the tidal range decrease to the middle part of the estuary,

then is maintained constant (convergence balance friction processes), and finally, increase upward due to reflection processes.

Figure 2.12 shows the corrected water levels which are finally used in this thesis.

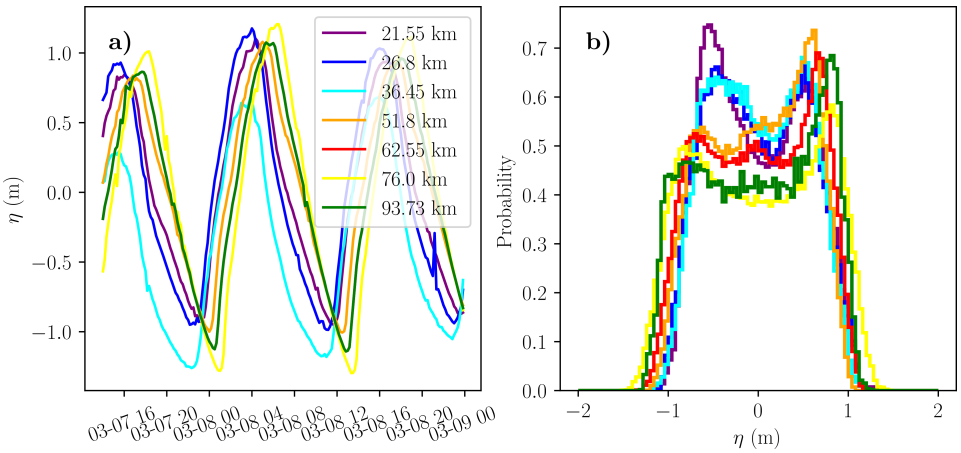

Figure 2.13: Water elevations during three tidal cycles measured at several locations along the GRE *a)* and probability of water levels at those locations *b)*.

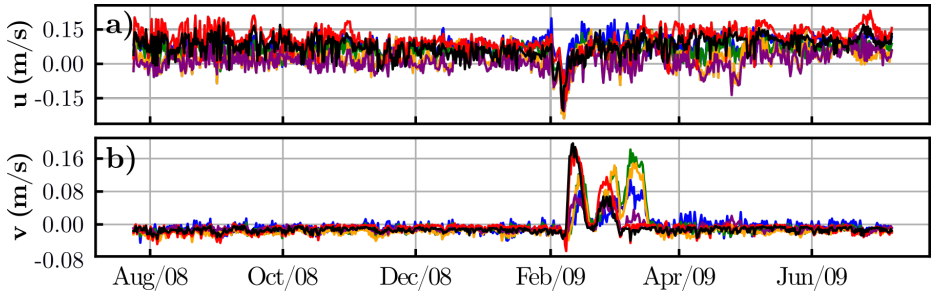

Figure 2.14: Time series of tidally- and vertically-averaged *a)* longitudinal velocity (positive points upstream); *b)* transversal velocity, along the GRE. The color rainbow is presented in Figure 2.11. Positive points normally to the thalweg 90 degrees clockwise.

In figure 2.13 is depicted the water elevations and probability plots. As it is observed, the tidal wave changes during the propagation along the GRE. The tidal wave presented a peaked ebb tide and a though flood at the mouth (purple line) and reverses landward (green line). Another importante difference is that the tidal amplitude also increases upward. In figure 2.14, residual longitudinal and transversal currents are generally upstream and confined between 0 and 0.15 m/s. Just during the high river discharge (at the beginning of February), longitudinal currents pointed downward and transversal currents points western ward.

2.3.3 Daily river discharges from Alcalá del río dam

Daily river discharges at Alcalá del Río dam have been measured from July 1, 1931 to the present by the Andalusian Water Agency (Junta de Andalucía) at the upper estuary boundary (figure 2.10.b). The median value is below 40 m^3/s, approximate, which delimits the tidal regime (Díez-Minguito et al., 2012). The limitant value is recorded more than 70 percent of the time. High river discharges larger than 2000 m^3/s were also recorded (figure 1.5).

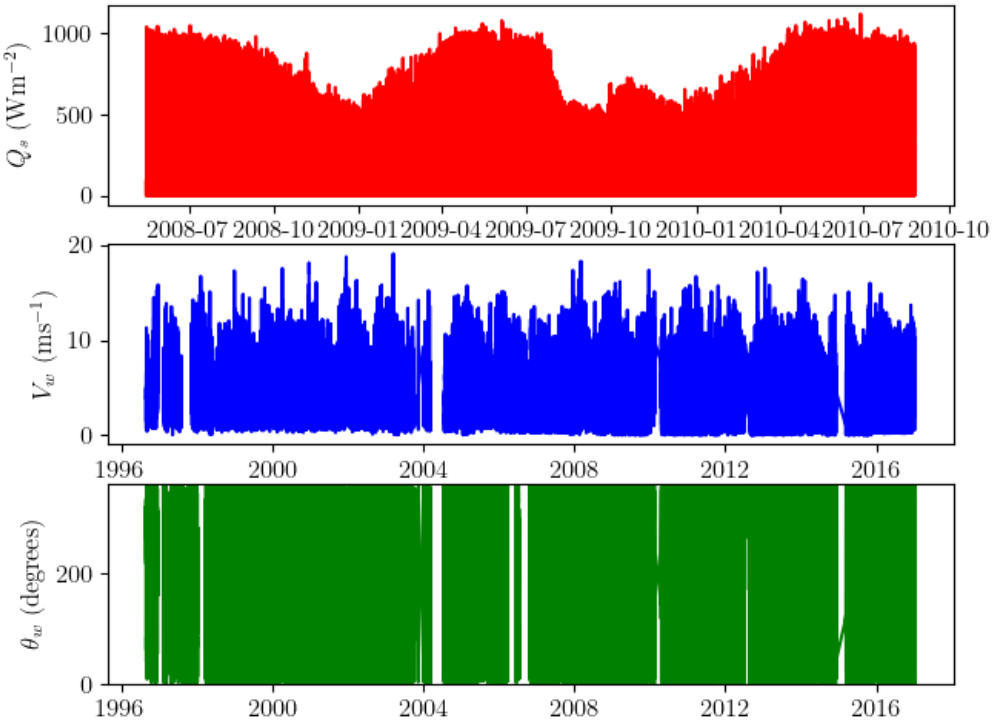

Figure 2.15: Time series of solar radiation (upper panel), wind velocity (mid panel) and wind direction (lower panel).

2.3.4 Meteorological dataset

Wind velocity and direction were measured every three hours for a REDEXT buoy of Puertos del Estado at the Guadalquivir continental shelf while solar radiation was measured every 10 minutes in a meteorological station at the mouth of the Guadalquivir estuary next to Chipiona (figure 2.10). Observations are depicted in figure 2.15.

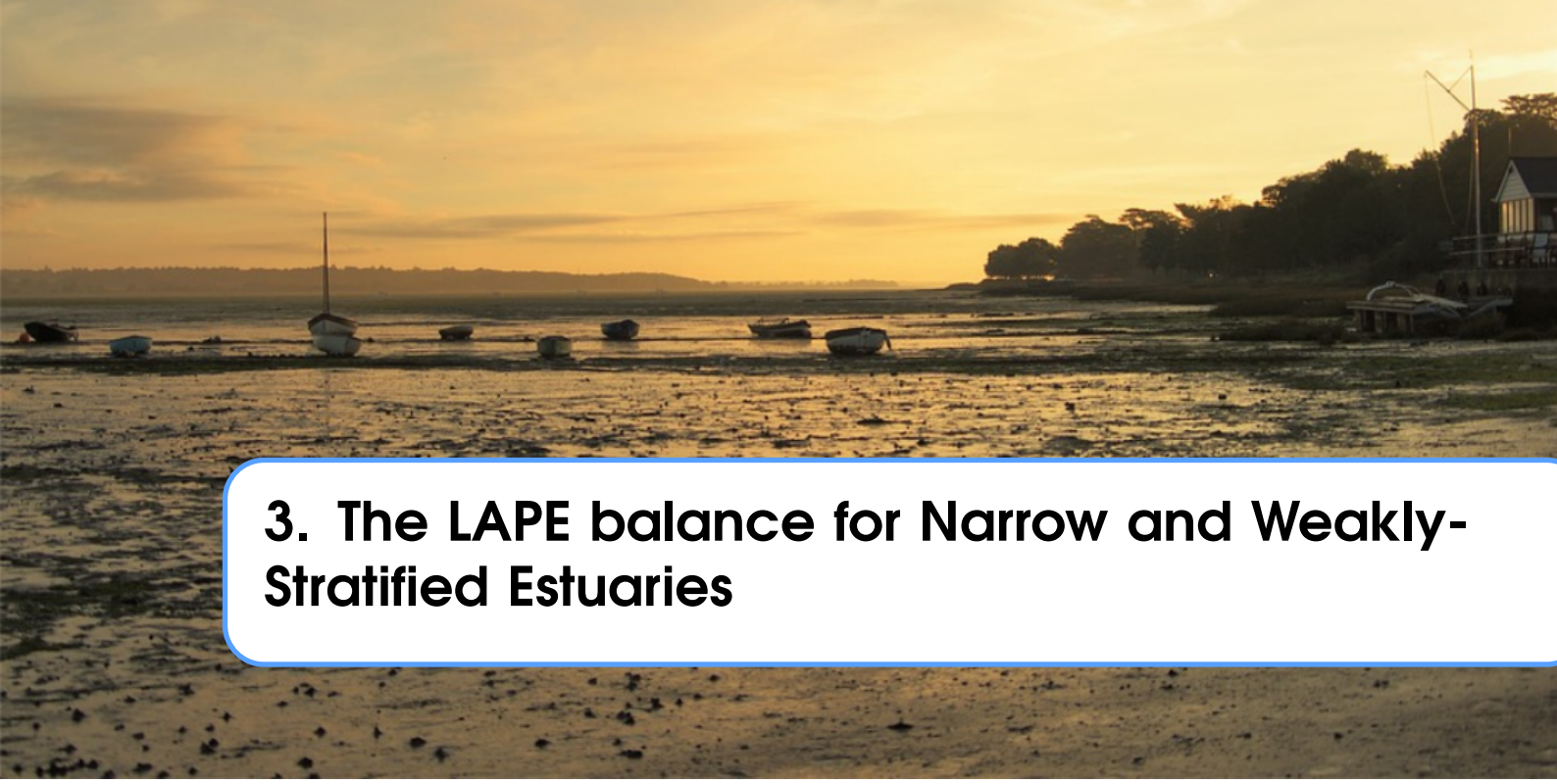

3. The LAPE balance for Narrow and Weakly-Stratified Estuaries

"Sometimes it is just needed to change the way it is interpreted what is written"

The usefulness of the balances in term of the potential energy were shown in chapter 2. The balances provide lot of information about how the estuary behaves and accounts and assesses the stratification-mixing competition (§ 3.1). However, in the case of the Guadalquivir River Estuary (GRE), a narrow, shallow and well-mixed estuary, the vertical density profiles are relatively vertical which means that the potential energy anomaly is generally null over the time.

This chapter led to the formulation of a subtidal-scale dynamic equation of energy that is able to evaluate the Longitudinal Anomaly of Potential Energy (LAPE), which integrates salinity, temperature, the suspended solids concentration and the flow velocity throughout the estuary and in different fluvial regimes (i.e. low-river flow, high-river flow, and post-riverflood recovery) and tidal regimes (neap and spring tides) and the transports that control them (§ 3.2). The objective of the present chapter is to demonstrate the informative capacity of the longitudinal anomaly of potential energy (LAPE) in the analysis of the magnitude and spatiotemporal variability of estuarine processes. For this purpose, a LAPE balance equation is formulated.

The LAPE general balance equation was applied to the dynamics of the GRE (§ 3.2.4). Since the GRE is a narrow, weakly stratified and highly anthropized estuary, these same characteristics made it possible to simplify the balance equation and segment the GRE in 5 boxes. This box model was applied to the GRE over a one-year period with all the previously mentioned hydraulic regimes. A high-resolution data set regarding salinity, suspended solids, tidal currents and elevations, and fluvial discharges, which had been recorded in 2008-2009 (§ 2.3) were used to quantify advective transports as well as the transports associated with longitudinal dispersion and vertical turbulent mixing in different hydraulic regimes (§ 3.3). After that, it is discussed the hypothesis taken and verified that the mechanisms explained by the LAPE are also observed in other variables (§ 3.4). The main conclusions are summarized at the end of this chapter.

3.1 Knowledge integration and simplification for estuary management

Human action is the main reason why many estuaries have experienced significant changes in recent decades. Such changes include: (i) modification of their hydrographic basins because of water diverted for irrigation, and the damming of the main water course and its tributaries; (ii) industrial and farming activities on their banks; and (iii) changes in estuary geometry because of depth and maintenance dredging (e.g.) (Hobbie, 2000; Reyes-Merlo et al., 2017; Ruiz et al., 2015). The anthropization of an estuary alters its biochemical and physical dynamics by modifying nutrient mixing as well as the sediment and oxygen transport in water bodies adjacent to rivers and seas (Officer, 2013; Simpson and Sharples, 2012).

In certain estuaries, such as the Guadalquivir River Estuary (SW Spain), these interventions are reflected in changes in hydro-morphodynamics all along the estuary as well as in different hydraulic regimes of the fluvial agents (low-river flow, high-river flow, and post-riverflood recovery) and marine agents (neap and spring tides) (Ruiz et al., 2015). From an estuary management perspective, it is a considerable challenge to integrate this scientific evidence in simple, manageable models such as box models that are capable of quantifying the effects of such changes on estuarine dynamics. Box models are generally used to describe processes and to establish balances based on volumetric averages of the main oceanographic and estuarine variables with a suitable spatiotemporal scale (Austin, 2002; Díez-Minguito et al., 2014; Hamilton et al., 1985; Officer, 1980; Rice et al., 2008; Sun et al., 2017). This type of model can facilitate decision-making based on knowledge of the sustainable use of the estuary (Leschine et al., 2003).

Such decisions should be regulated by a legal framework such as the Water Framework Directive 2000/60/EC (WFD), which establishes the need to adopt measures to protect and improve transitional water bodies, such as estuaries, whose quality depends on their ecological status (Ganju et al., 2016). The WFD describes the ecological status of an estuary in terms of the values of hydromorphological parameters, such as the current velocity, salinity, temperature, turbidity and mixing characteristics, among others.

3.2 Longitudinal Anomaly of Potential Energy (LAPE)

The potential energy anomaly is a magnitude that integrates those hydromorphological parameters (Simpson and Hunter, 1974; Simpson et al., 1990; Simpson, 1981) (chapter 2.2). Here, it is repeated for continuity. The potential energy anomaly, ϕ_S (Jm^{-3}), quantifies the water column stratification and is defined as the amount of mechanical energy per m^3 needed to instantaneously homogenize the water column (Simpson, 1981). This is mathematically expressed as follows:

$$\phi_S(\mathbf{x},t) = \frac{g}{d}\int_{-h}^{\eta}(\rho-\underline{\rho})z\,dz, \quad \text{where} \quad \underline{\rho}(\mathbf{x},t) = \frac{1}{d}\int_{-h}^{\eta}\rho\,dz, \tag{3.1}$$

where g is the gravity constant; t is the time; $\mathbf{x}$ defines the horizontal position; z, represents the vertical coordinate; $\rho(\mathbf{x},z,t)$ is the water density, and $\underline{\rho}(\mathbf{x},t)$ is the reference density in complete mixing conditions, both of which include the suspended sediment density; d is the total depth that is the sum of $\eta(\mathbf{x},t)$, the elevation over mean sea level and $h(\mathbf{x})$, the mean depth. From the time when it was first proposed in the mid-1970s (Simpson and Hunter, 1974), the potential energy anomaly has been widely used to identify physical processes that produce water exchanges in shelf seas (Hofmeister et al., 2009; Simpson et al., 1990; Yang et al., 2017), regions influenced by freshwater (De Boer et al., 2008; Simpson, 1997), estuaries (Garvine and Whitney, 2006; Rice et al., 2008; Sun et al., 2017), and lakes (Zhao et al., 2018).

Crucial to the present research study is the work of Garvine and Whitney (2006) (GW2006), who

used the potential energy anomaly to calculate the flow exchanges between the Delaware estuary and the adjacent continental shelf. The work of GW2006 establishes the potential energy anomaly budget in which the reference density is at a point, $\mathbf{x_0}$ located downstream on the continental shelf instead of the mean density in the water column (eq. 3.1). The definition of ϕ in GW2006 is henceforth referred to as the Longitudinal Anomaly of Potential Energy (LAPE) and is formulated as follows:

$$\phi(\mathbf{x},t) = \frac{g}{d}\int_{-h}^{\eta}(\rho - \underline{\rho_0})z\,dz, \quad \text{where} \quad \underline{\rho_0} = \frac{1}{d}\int_{-h}^{\eta}\rho(\mathbf{x_0},t)\,dz, \tag{3.2}$$

where ρ_0 is the mean density of slope water beyond the shelf at the location $\mathbf{x_0}$. This density is the reference density in complete mixing conditions, which are in this case, longitudinal. GW2006 represents the characteristics of the system with a single box to represent the estuary, which is directly connected to the continental platform at the subtidal scale.

The pionnering work of Pritchard (1960) and Stommel (1961) derived and applied a box model to explain the rate of salinity change from field observations and laboratory experiments. Following their methodology, many applications of box models to estuarine processes were subsequently developed (table 3.1). To examine the estuarine mixing processes for climate models, Garvine and Whitney (2006) (GW2006) defined the along-channel (longitudinal) potential energy anomaly (ϕ) by using a single box that represented the estuary.

Author and reference	Purpose	Location	No. boxes
Pritchard (1960)	salt balance	Chincoteague Bay	16
Stommel (1961)	ocean thermohaline circulation	Laboratory	2
Hamilton et al. (1985)	salt balance	Puget sound	13
Austin (2002)	ocean exchange salinity	Chesapeake bay	1
Garvine and Whitney (2006)	ocean-estuary water exchanges	Delaware estuary	2
Rice et al. (2008)	ocean-estuary water exchanges (two layer)	Delaware estuary	2
Díez-Minguito et al. (2014)	estuarine turbidity	Guadalquivir river estuary	5
Sun et al. (2017)	ocean exchange mixed-water volume	Columbia river	2

Table 3.1: Box models used in some ocean and estuarine applications.

They considered the change rate in the LAPE as induced by freshwater inflow, water outflow to the shelf, tidal and wind mixing, and surface heat flux. However, in relatively shallow estuaries that are weakly stratified or well-mixed, in addition to gravitational circulations, it is also necessary to consider other contributions to the LAPE, such as those associated with longitudinal dispersion, tidal pumping, and differential advection (Aken, 1986; Becherer et al., 2016; Burchard and Hetland, 2010). Differential advection includes two terms. The first term is associated with depth-mean straining due to the vertical mean horizontal density gradient strained by the deviation from the depth-mean velocity vector (depth-mean straining). The second term is associated with the deviations of the longitudinal velocities and the gradient of density deviations (non-depth-mean straining) (Burchard and Hofmeister, 2008).

This equation includes the impact of intratidal processes on the subtidal scale by means of the tidal decomposition method (Becherer et al., 2016; Burchard et al., 2018; Díez-Minguito et al., 2013; Scully and Friedrichs, 2007). It also extends the work of Garvine and Whitney (2006) by including the influence of the following: (i) longitudinal dispersion; (ii) tidal pumping associated with cross-correlations between density, elevations, and currents; and (iii) differential advection due to depth-mean straining, and non-depth-mean straining. These terms are particularly relevant to narrow estuaries (Burchard and Hetland, 2010; Jay and Musiak, 1994).

3.2.1 Interpretation of the LAPE

According to GW2006, the LAPE, ϕ, is the mechanical energy per m^3 needed to instantaneously homogenize the water mass between sections x_0 and x (eq. (3.2)). In weak stratification conditions, the LAPE can be simplified as follows:

$$\phi(x,t) \simeq \frac{[\underline{\rho_0} - \rho(x,t)]gd}{2}, \tag{3.3}$$

with $x_0 < x$, where x_0 is located beyond the shelfbreak (Garvine and Whitney, 2006). As can be observed in eq. (3.3), calculating $\phi(x,t)$ is the same as calculating the potential energy of the semi-difference of densities between x and x_0. For a single box, eq. (3.3) establishes that if the longitudinal density gradient is zero [$\underline{\rho_0} = \rho(x,t)$], then ϕ is zero. This is the same as finding conditions of complete longitudinal mixing, as can be observed, for example, in tidal river reaches. In normal conditions, density decreases upstream (Officer, 2013) and $\phi > 0$. However, in inverse estuaries or in regions where the profile of $\rho(x)$ is locally inverted, density increases upstream and $\phi < 0$.

This study focused on a relatively narrow estuary in which the Coriolis effect is negligible and the river flow is transversally uniform (Hansen and Rattray, 1966; Valle-Levinson, 2008; Valle-Levinson, 2010). The system of coordinates (x, z) has the origin at the estuary mouth, lying over the mean sea level. The positive x-axis follows the thalweg and the z-axis points upwards; $d = \eta + h$ is the total depth; $h(x)$, the mean depth of the bed; and $\eta(x,t)$ is the water surface that varies over time, t.

3.2.2 Development of the LAPE balance equation for weakly stratifies estuaries

The density, $\rho(x,z,t)$, is governed by the balance equation or the dynamic density equation (Aken, 1986; Burchard and Hofmeister, 2008) defined as:

$$\mathbf{D}(x,z,t) = 0, \tag{3.4}$$

where $\mathbf{D}$ is the density equation defined as:

$$\mathbf{D}(x,z,t) = \partial_t\rho + \partial_x(u\rho) + \partial_z(w\rho) - \partial_x(k_x\partial_x\rho) - \partial_z(k_z\partial_z\rho) - \mathbf{S}. \tag{3.5}$$

In eq. (3.5), $\partial_\chi\zeta$ denotes the derivative of the generic variable, ζ, in regard to the independent variable χ. The terms k_x and k_z denote the longitudinal and vertical eddy diffusivities that result from the parameterizations of turbulent fluxes (Burchard and Hofmeister, 2008). The term $\mathbf{S}(x,z,t)$, encompasses the local source and sink terms, which includes the non-linear effects that appear from the equation of state for sea water (Burchard and Hofmeister, 2008), the incident solar radiation, and the suspended sediment:

$$\begin{aligned}\mathbf{S}(x,z,t) = k_x\left[\partial^2_{T,x}\rho(\partial_x T)^2 + \partial^2_{S,x}\rho(\partial_x S)^2\right] + k_z\left[\partial^2_{T,z}\rho(\partial_z T)^2 + \partial^2_{S,z}\rho(\partial_z S)^2\right] \\ + \frac{g\rho\alpha}{\rho_0 c_p} I e^{-\varepsilon(\eta-z)} + \left(1 - \frac{\rho}{\rho_s}\right) C\partial_z(w_s C),\end{aligned} \tag{3.6}$$

where $\partial^2_{\chi,\varphi}\zeta = \frac{\partial^2\zeta}{\partial\chi\partial\varphi}$; the light penetration in the water column follows the Lambert-Beer Law, and where α_w, is the water expansion coefficient; c_p is the heat capacity of the water; ε is the light absorption coefficient; ρ_s is the sediment density; w_s is the settling velocity; and C is the suspended sediment concentration. Since the values for precipitation, evaporation, and water diverted for irrigation are relatively small compared to the fluvial discharges, they are not taken into

account. The first term of the RHS in eq. (6) can be usually neglected because it is several orders of magnitude smaller than its counterpart in eq. (5). Assuming weakly-stratified to well-mixed conditions, the second term of the RHS of eq. (6) can also be neglected. This simplification is similar to considering a linear equation of state for seawater.

The dynamic equation of ϕ is based on the expressions of $\mathbf{D}$ (eq. (3.5)), evaluated in x and x_0, and the equation of the longitudinal anomaly of the potential energy (eq. (3.2)). When $\mathbf{D}(x_0,z,t)$, is depth-averaged, taking into account the continuity equation, $\partial_x u + \partial_z w = 0$, and the dynamic and kinematic boundary conditions (see Appendix A), the result is the following:

$$\begin{aligned}\underline{\mathbf{D}(x_0,t)} = {} & \partial_t(\underline{\rho_0}) + \partial_x(\underline{u\rho_0}) - \partial_x(\underline{k_x\partial_x\rho_0}) - d^{-1}[k_x\partial_x\rho_0]_\eta\partial_x\eta - d^{-1}[k_z\partial_z\rho_0]_\eta \\ & - d^{-1}[k_x\partial_x\rho_0]_{-h}\partial_x h - d^{-1}[k_z\partial_z\rho_0]_{-h} \\ & - \frac{g\rho\alpha I}{\rho_0 c_p d}\left(1-e^{-\varepsilon(\eta-z)}\right) - \left(1-\frac{\rho}{\rho_s}\right)\frac{w_s}{2d}\left([C^2]_\eta - [C^2]_{-h}\right), \end{aligned} \tag{3.7}$$

where sub-indexes $_\eta$ and $_{-h}$ indicate the respective surfaces on which the terms ($z=\eta$ and $z=-h$) are evaluated. The chain rule is applied to the derivatives and Leibniz's rule to integrals with variable limits. To calculate the average of $\underline{\mathbf{D}(x_0,t)}$, each dependent variable ζ is decomposed in the superposition of the depth-averaged value $\underline{\zeta}$, and a deviation, ζ_v. The same operation is performed with the term $\underline{\mathbf{D}(x,t)z}$. By substituting the results obtained in eqs. (3.7) and (3.18), the following dynamic equation is obtained for the LAPE:

$$\begin{aligned} g(\underline{\mathbf{D}(x_0,t)}\,\underline{z} - \underline{\mathbf{D}(x,t)z}) \equiv {} & \underbrace{\partial_t\phi}_{t_0} + \underbrace{g\partial_x([\underline{\rho_0}-\underline{\rho}]\underline{u}\,\underline{z})}_{t_1} + \underbrace{\partial_x(\underline{u}\underline{\phi_S})}_{t_A} \\ & \underbrace{- g\partial_x(\underline{\rho}\,\underline{u_v z})}_{t_B} \underbrace{- g\partial_x(\underline{u_v}\,\underline{\rho_0}\,\underline{z} - \underline{u_v\rho_v z})}_{t_C} + \underbrace{g(\underline{w_v}\,\underline{\rho_v})}_{t_D} \\ & \underbrace{- g\underline{k_z\partial_z\rho}}_{t_E} + \underbrace{gd^{-1}k_z([\underline{z}\partial_z\rho_{0,v}]_\eta + [\underline{z}\partial_z\rho_{0,v}]_{-h})}_{t_F} \\ & \underbrace{- \frac{g\rho\alpha I}{\rho_0 c_p d}\left[\left(1-e^{-\varepsilon(\eta-z)}\right)\underline{z} + \left(\varepsilon^{-1} - e^{-\varepsilon(\eta-z)}\left(d+\varepsilon^{-1}\right)\right)\right]}_{t_{G,1}} \\ & \underbrace{+ \frac{w_s}{2d}\left([C^2]_\eta(1+\eta) - [C^2]_{-h}(1-h) - d\underline{C}\right)}_{t_{G,2}} \\ & \underbrace{+ \partial_x(g[\underline{k_x\partial_x(\underline{\rho}+\rho_v)(z-\underline{z})}])}_{t_H} \\ & \underbrace{+ gd^{-1}(\underline{z}-\eta)[k_x\partial_x(\underline{\rho}+\rho_v)]_\eta\partial_x\eta - gd^{-1}(\underline{z}-h)[k_x\partial_x(\underline{\rho}+\rho_v)]_h\partial_x h}_{t_I} = 0. \end{aligned} \tag{3.8}$$

The first term t_0 is the time variation of ϕ De Boer et al., 2008, eq. 6. The term t_1 represents the horizontal advection of the longitudinal density difference in relation to the average density. The term t_A is the longitudinal advection of the potential energy anomaly as defined by Simpson (1981), ϕ_S (eq. (3.1)), due to the vertical average of the longitudinal velocity; t_B is the depth-mean straining, based on the vertical mean horizontal density gradient strained by the deviation from the depth-mean velocity vector (Bowden, 1981), also called the differential advection term by Aken (1986) (see also Burchard and Hofmeister (2008)); t_C is the non-averaged differential advection based on the deviations of the longitudinal velocities and the gradient of the density deviations. Unlike for the

potential energy anomaly, t_B and t_C include velocity deviations u_v and their longitudinal gradients. The term t_D is the vertical advection due to the deviations in regard to the vertical average of the vertical velocity. The term t_E is an estimation of the turbulent flux of density that depends on the eddy diffusivity coefficient (Aken, 1986; Simpson and Sharples, 2012; Simpson and Bowers, 1981). The surface and bottom buoyancy transports are included in the term t_F. The source and sink terms related to heat transport on the free surface ($R = \left(1-e^{-kd}\right)\underline{z} + [\varepsilon^{-1} - e^{-kd}\left(d+\varepsilon^{-1}\right)]$, (first term) and the bed sediment resuspension (second term) are indicated in t_G. Finally, the mean turbulent transport divergence throughout the estuary is defined by t_H whereas t_I is the divergence of the mean turbulent transport through the boundaries $z=\eta$ and $z=-h$. To facilitate their tracking, these terms were renamed as follows: $\Psi_\zeta = gd^{-1}(\underline{z}-\zeta)[k_x\partial_x(\underline{\rho}+\rho_v)]_\zeta \partial_x\zeta$ for $\zeta = \eta, -h$.

In weakly stratified or well-mixed estuaries, the vertical density profile is practically constant, i.e. $\rho_v \simeq \rho_{0,v} \simeq 0$. The term t_E cannot be neglected since it is the mechanism that sustains mixing in the water column and determines the vertical mass exchange in weakly stratified estuaries (Jay and Smith, 1990). Assuming this hypothesis, eq. (3.8) is simplified as follows:

$$\begin{aligned} &\partial_t\phi + g\partial_x((\underline{\rho_0}-\underline{\rho})\underline{u}\,\underline{z}) \\ &-g\partial_x(\underline{\rho}\,\underline{u_v z}) - g\underline{k_z}\partial_z\underline{\rho} - \frac{g\rho\alpha}{\rho_0 c_p}R + \Psi_\eta - \Psi_{-h} = 0. \end{aligned} \tag{3.9}$$

In the case of other estuaries, different hypotheses can be adopted that simplify the general equation (eq. (3.8)).

3.2.3 Box model of the LAPE

The present section describes how the estuary was divided into a series of interconnected boxes that are representative of the subtidal-scale flow characteristics. For a box i (figure 3.1), eq. (3.9) is integrated with respect to a x between two sections, x_i and $x_i + L_i$. When the tidal decomposition of the resulting variables is substituted, this gives the LAPE equation for the box at the subtidal scale:

$$\begin{aligned} &\underbrace{\Delta_t\overline{\Phi}}_{\tau_0} + \\ &+\underbrace{\frac{gB}{2}\Delta_x F_2(d,\underline{\rho_0}-\underline{\rho},\underline{u})}_{\tau_1} - \underbrace{gB\Delta_x F_1(\underline{\rho},\underline{u_v z})}_{\tau_2} \\ &+\underbrace{\frac{4e_b}{3\pi}\frac{C_d\rho\overline{u}^3 A_s}{d} + \frac{e_w C_w \rho_a \overline{W}^3 A_s}{d}}_{\tau_3} - \underbrace{\frac{g\rho\alpha}{\rho_0 c_p}A_s\overline{R}}_{\tau_4} \\ &+\underbrace{\overline{\langle\Psi_\eta\rangle} - \overline{\langle\Psi_{-h}\rangle}}_{\tau_5} = 0, \end{aligned} \tag{3.10}$$

where for a generic variable ζ, $\langle\zeta\rangle = \int_{x_i}^{x_i+L_i}\zeta dx$ is the integral in the length of a box, L_i; and, $\overline{\zeta} = T_{M_2}^{-1}\int_t^{t+T_{M_2}}\zeta dt$ is the time average in a tidal cycle T_{M_2}, which permits the decomposition of $\zeta = \overline{\zeta} + \zeta'$, where ζ' is the deviation in regard to the average. At the same time, $\Delta_t\zeta$ represents the time difference of ζ evaluated in t and $t+T_{M_2}$; and $\Delta_x\zeta$ represents the spatial difference of ζ evaluated in x and $x+L$. The functions F_1 and F_2 are given by:

$$\begin{aligned} F_1(\zeta_1,\zeta_2) &= \overline{\zeta_1}\,\overline{\zeta_2} + \overline{\zeta_1'\zeta_2'} \\ F_2(\zeta_1,\zeta_2,\zeta_3) &= \overline{\zeta_1}\,\overline{\zeta_2}\,\overline{\zeta_3} + \overline{\zeta_1}\,\overline{\zeta_2'\zeta_3'} + \overline{\zeta_2}\,\overline{\zeta_1'\zeta_3'} + \overline{\zeta_3}\,\overline{\zeta_1'\zeta_2'} + \overline{\zeta_1'\zeta_2'\zeta_3'}. \end{aligned} \tag{3.11}$$

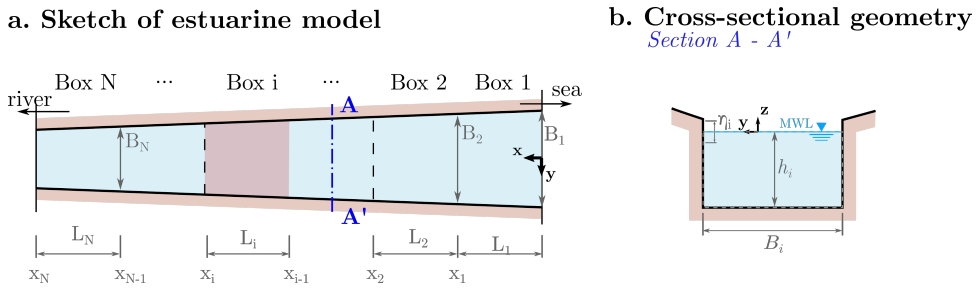

Figure 3.1: Diagram of the estuary box model and reference frame. *a)* Global diagram of the estuarine model. The red-shaded region stands for the surface area of box-i, $A_{s,i}$; *b)* geometry of the cross-section. The gray dashed rectangle is the geometry of the box cross-section, A_i.

In eq. (3.10), $\Phi = \int_{A_s} \phi \, dA$ (J·m^{-1}) represents the LAPE of the box. The term τ_0 is the variation experienced by Φ from the beginning to the end of the tidal cycle. The term τ_1 includes the superposition of the mean transport [$\tau_{1,1} = h\underline{\overline{u}}(\underline{\overline{\rho_0}} - \underline{\overline{\rho}})$], the Stokes transport [$\tau_{1,2} = (\underline{\overline{\rho_0}} - \underline{\overline{\rho}})\,\overline{\eta u'}$], and three tidal pumpings related to correlations between $\eta + h$, u' and $(\underline{\rho_0} - \underline{\rho})'$ [$\tau_{1,3} = \underline{\overline{u}}\,\overline{\eta(\underline{\rho_0} - \underline{\rho})'}$; $\tau_{1,4} = h\overline{\underline{u'}(\underline{\rho_0} - \underline{\rho})'}$; $\tau_{1,5} = \overline{\eta \underline{u'}(\underline{\rho_0} - \underline{\rho})'}$]. The term τ_2 considers the depth-averaged advection density, spatiotemporal depth changes, and mean vertical mass transports. The term τ_3, which is obtained from (t_E) in eq. (3.8), is empirically related to tidal and wind mixing (Aken, 1986; Simpson, 1981). According to Simpson and Bowers (1981), Simpson et al. (1991), and Simpson (1981), the mixing term is described by the cube of the tidal velocity $\overline{u}$ and the wind velocity $\overline{W}$. The constant parameters C_w, C_d, e_b and e_w represent the effective surface drag force, bottom drag force, tidal current mixing, and wind mixing, respectively. The term ρ_a denotes the air density at sea level. The surface solar radiation is τ_4. Finally, τ_5 describes the turbulent horizontal transport difference between $z = \eta$ and $z = -h$. The LAPE transports due to tidal pumping ($\tau_{1,4}$), differential advection (τ_2) and longitudinal dispersion (τ_5) were not contemplated by (Garvine and Whitney, 2006) in their box model.

In what follows, all variables are averaged in a tide cycle, although for the sake of simplicity, the lower bar in the equations indicating this has been eliminated.

3.2.4 Configuration of the model for the Guadalquivir River Estuary

The previously described LAPE formulation was applied to the GRE from 07/24/2008 to 07/24/2009. Figure 3.2 shows the following hydraulic regimes that were observed during this one-year period (Díez-Minguito et al., 2012): (1) low-river flow; (2) high-river flow; and (3) an intermediate riverflood recovery period. These regimes are discussed at length in the sections that follow.

The spatial domain extended from the mouth, $x = 0$ km, to $x = 57.6$ km upstream, the average position reached by the 2-psu isohaline (Monismith et al., 2002), which characterizes salt intrusion. The upper stretch of the estuary, which normally has the characteristics of a tidal river, was not considered. The GRE was divided into five boxes, whose length, width, and depth are defined in Table 3.2. These boxes are representative of estuarine dynamics regarding tidal wave propagation, salt transport, and suspended particulate material transport along the GRE.

Equation (3.3) was used to calculate ϕ in the five boxes, using the data observed (figure 2.11). In each box, the reference density, $\rho_{0,i}$, is the density at the point farthest downstream; ρ_i is the density at the point farthest upstream; and d_i is the average depth for i =1, 2, ..., 5. Typical average density values at these points are also shown in Table 3.2. The equation (3.10) evaluates the transports that control the LAPE also based on the data observed.

Box		Geometry					Density variability	
no.	Color	x_i (km)	L_i (km)	d_i (m)	A_i (10^2 m^2)	$A_{s,i}$ (10^6 m^2)	$\overline{\rho}$ (5%, 95%) kg · m^{-3}	ρ_v (5%, 95%) kg · m^{-3}
1	cyan	0	17.3	7.26	58.39	12.91	1023.75 (-4.30, 3.12)	0.41 (-0.31, 0.60)
2	green	17.3	8.9	7.13	43.82	5.22	1012.64 (-7.01, 6.82)	0.21 (-0.04, 0.24)
3	orange	26.2	9.1	7.05	37.80	4.54	1007.01 (-4.48, 4.70)	0.11 (-0.11, 0.44)
4	red	35.3	11.8	6.95	32.51	4.90	1004.22 (-3.12, 5.31)	1.42 (-1.20, 0.50)
5	purple	47.1	10.5	6.85	26.72	3.56	1001.67 (-1.99, 3.31)	0.07 (-0.05, 0.24)
-	-	57.6	-	6.80	22.45	-	1000.97 (-2.54, 3.37)	0.25 (-0.14, 0.20)
	TOTAL	-	57.6	-	-	31.13	-	-

Table 3.2: Morphological parameters of the boxes used in the subtidal box model. Each box is defined by its initial downstream position x_i; its final upstream position x_{i+1}, length L_i; and the limiting cross-sections of areas A_{i+1} and A_i (figure 3.1). The surface area of each box is defined by $A_{s,i}$. Also shown are typical vertical averaged density values and their deviations in regard to the vertical average value, ρ_v, in each box. Besides the density values, the percentiles 5 and 95 of the time-series of density deviations are shown in brackets.

In order to compare the results of our study with those of the seminal work of Garvine and Whitney (2006) in the Delaware estuary, the average LAPE was also calculated throughout the study zone, ϕ_e, as though it were a single box. This was obtained with the following expression:

$$\phi_e = A_{s,t}^{-1} \sum_{i=1}^{N} \phi_i A_{s,i} \qquad i = 1,2,...,5, \tag{3.12}$$

where $A_{s,t} = \sum_1^5 A_{s,i}$, the total surface area of the study zone. In the same way, the net LAPE transport of the estuary was calculated for a term j, as follows:

$$\tau_{e,j} = A_{s,t}^{-1} \sum_{i=1}^{N} \tau_{j,i} A_{s,i} \quad i = 1,2,...,5. \tag{3.13}$$

3.3 Results

3.3.1 Longitudinal variation of $\phi(x)$

Figure 3.2.a shows the results of eq. (3.3) at several sections representative of the conditions at the boxes defined in Table 1, where ϕ_i indicates the longitudinal anomaly of the potential energy (LAPE or ϕ) at x_i. The first third of the estuary (boxes 1 and 2) shows the highest values of ϕ, where the maximum average longitudinal density gradients occur as well as the greatest time variability. The LAPE for box 1 during the study period is $\phi_1 = 395.04 \pm 122.68$ Jm^{-3}, where the first term is the mean value and $\pm X$ is the standard deviation. The amplitude of the fortnightly modulation of ϕ_i and its mean value decrease upstream ($\phi_5 \simeq 90 \pm 45$ Jm^{-3}). In box 1, ϕ oscillates out of phase with the fortnightly constituent of the tidal range with minimums of ϕ during spring tides and maximums during neap tides. Upstream, just the opposite occurs. The dependence of ϕ on the neap-spring-tide cycles was no longer visible from October 2008 until February 2009 because the intermediate fluvial pulsed discharges became more numerous ($\simeq$100 m^3/s) (figure 3.2.d). The 2-psu isohaline (figure 3.2.c) reaches box 5, where ϕ_i remains almost constant during low river flow conditions. However, it retreats to $x = 40$ km with the pulsed discharges observed at the end of autumn which is manifested in a reduction of ϕ in boxes 4 and 5. Then, it moves to box 1 during the flood (2), causing a marked decrease in ϕ in all boxes. On a yearly scale, at the mouth, positive

temperature increases generated negative increases in ϕ. Upstream, the temperature oscillation is in phase with ϕ.

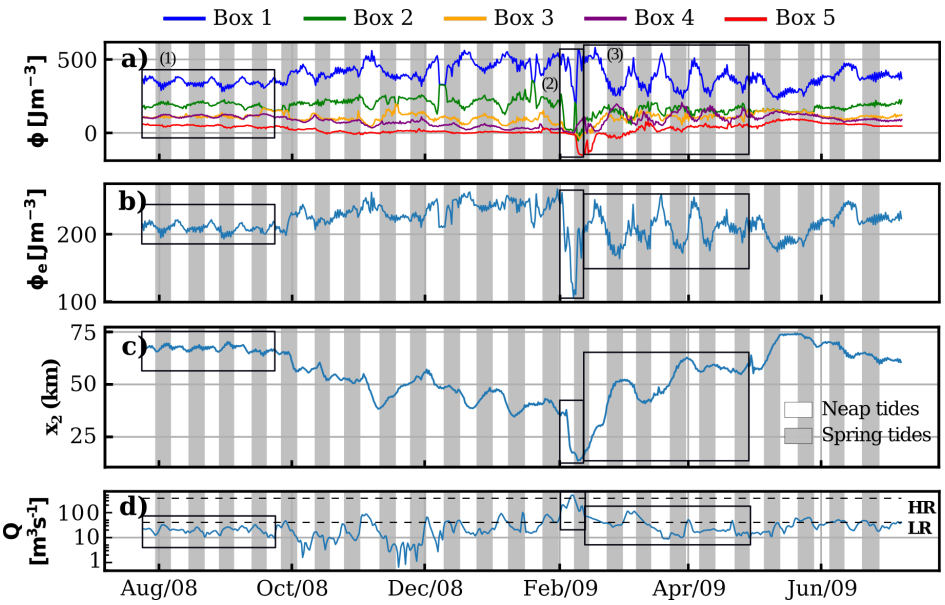

Figure 3.2: Time series of the longitudinal potential energy anomaly. *a)* ϕ_i at every box; *b)* ϕ_e of the estuary (eq. (3.12)); *c)* salt intrusion during the study period (2-psu isohaline from figure 8 of Díez-Minguito et al. (2013)); and, *d)* daily river discharges from the Alcalá del Río dam during the study period. HR and LR indicate high-river flow and low-river flow regime. Boxes represent the periods discussed in the main text.

Generally, the value of ϕ_e remains more or less constant in low-river flow conditions (1), which is to be expected because of the small-time variations in the density observed at the estuary mouth and head (figure 2.11.d). During the high-river flow regime (2), ϕ_e decreases by half because of the seaward movement of the salt intrusion. The dependence of the salt intrusion increases with the freshwater flow (Reyes-Merlo et al., 2013). The salt intrusion during (2) moves upstream to kilometer 15. During the subsequent recovery period (3), ϕ_e oscillates out of phase π with the tides. The mean value and variability of $\phi_e \simeq 218.82 \pm 36.89$ Jm^{-3} are in accordance with the values obtained by Garvine and Whitney (2006) in the Delaware estuary where the mean estuary depth is 8 m. The amplitude of the oscillation triples during the recovery period ranging from a little more than 15 Jm^{-3}, corresponding to what is observed in normal conditions, to almost 50 Jm^{-3}, mostly conditioned by the box of the estuary mouth.

3.3.2 Variation of $\phi(x)$ depending on fluvial regime

Figure 3.3 shows the profiles of $\rho(x)$ and $\phi(x)$ for the different regimes (low-river flow, high-river flow, and post-riverflood recovery). In all cases, it was observed that the variability in regard to that mean density profile (orange line, figure 3.3) decreases upstream.

In normal conditions (1) (fig. 3.3.a), the mean density in each box decreases from the mouth upstream. This decrease is linear to km 40. The LAPE decreases more gradually upstream. During the high-river flow regime (2) (figure 3.3.*b*), almost the entire estuary is composed of freshwater, which gives values of $\phi \simeq 0$ except for the mouth. In boxes 3 and 5, ϕ is negative, which means that the density is locally inverted ($\rho_3 > \rho_2$ and $\rho_5 > \rho_4$).

In the recovery period (3), the along-channel density (fig. 3.3.c, upper panel) shows a similar

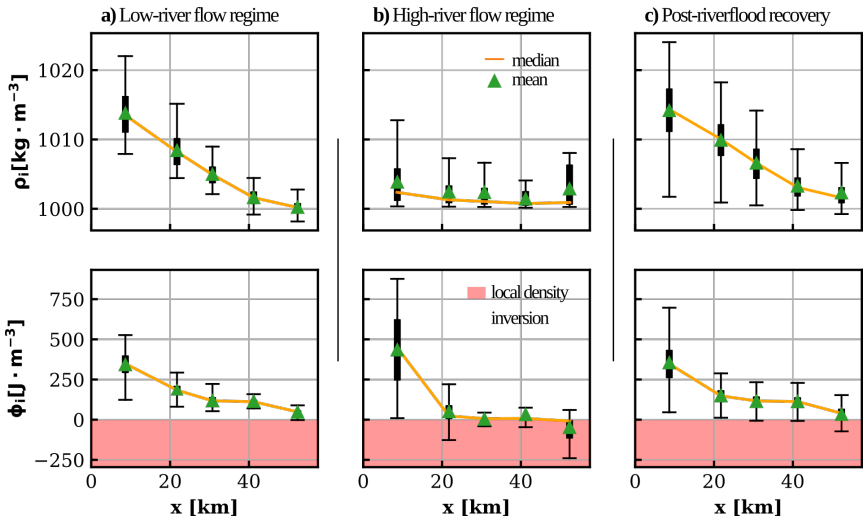

Figure 3.3: Along-channel density and longitudinal anomaly of potential energy for different regimes: *a)* low-river flow; *b)* high-river flow; and, *c)* post-riverflood recovery period. The rectangle in error bars indicate the corresponding $\pm$ 1 quartile from the median whereas line edges indicate 5 and 95 percentiles. Shaded areas indicate local density inversion $\rho_i > \rho_{i-1}$.

profile to that observed in normal conditions, where the variability in $\rho(x)$ as well as $\phi(x)$ is maximum during recovery. The negative values of ϕ persist until the density observed in normal conditions is recovered because the values approach the estuarine turbidity maximum (ETM) (Díez-Minguito et al., 2014).

3.3.3 Longitudinal variation of advective transports of ϕ

Figure 3.4 shows the main advective transport terms in each box, calculated in accordance with equation (3.10). Terms $\tau_{1,1}$, $\tau_{1,2}$ and $\tau_{1,4}$ represent the average non-tidal advective ϕ-transport, the LAPE transport due to Stokes and the tidal pumping ϕ-transport induced by the correlation between currents and densities. These terms represent more than 99% of the advective transport of ϕ. The terms $\tau_{1,3}$ and $\tau_{1,5}$ are not shown since they are various orders of magnitude lower than the latter ones ($\simeq 10^2$ Wm^{-1}). At the estuary mouth, the mean non-tidal advective LAPE transport, $\tau_{1,1}$, is negative $\simeq -1.5 \cdot 10^4$ Wm^{-1} (blue curve in fig. 3.4.a), which indicates that the non-tidal residual currents flow seaward. Upstream, this mean value becomes positive (green curve), then negative (purple curve), and then positive (red curve) again, which indicates the convergence and divergence zones of $\tau_{1,1}$ all along the estuary. This longitudinal ϕ-transport variation is also observed in Stokes-induced and tidal pumping transport processes.

During the low-river flow regime (1), ϕ-transports due to Stokes ($\tau_{1,2}$) and tidal pumping ($\tau_{1,4}$) are in phase with the tidal range. At the estuary mouth, the dependence of $\tau_{1,1}$ on the tidal range is not as clear. The term, $\tau_{1,1}$ has a greater magnitude than $\tau_{1,4}$ and $\tau_{1,2}$. More specifically, $\tau_{1,2}$ is approximately one-fourth of $\tau_{1,1}$.

The non-tidal mean advective ϕ-transport and tidal pumping are primarily responsible for the fortnightly change in density during the low-river flow ($\simeq 2 \cdot 10^4$ Wm^{-1}, in absolute value). Transport magnitude decreases upstream except in box 3 where it increases. Upstream transports (box 4 and 5) become negligible.

In the high-river flow regime (2), $\tau_{1,1}$ is inverted and the transport in boxes 2 and 3 drops to $\simeq -2.5 \cdot 10^4$ Wm^{-1}, whose absolute value exceeds that of the first box. Non-tidal mean advective

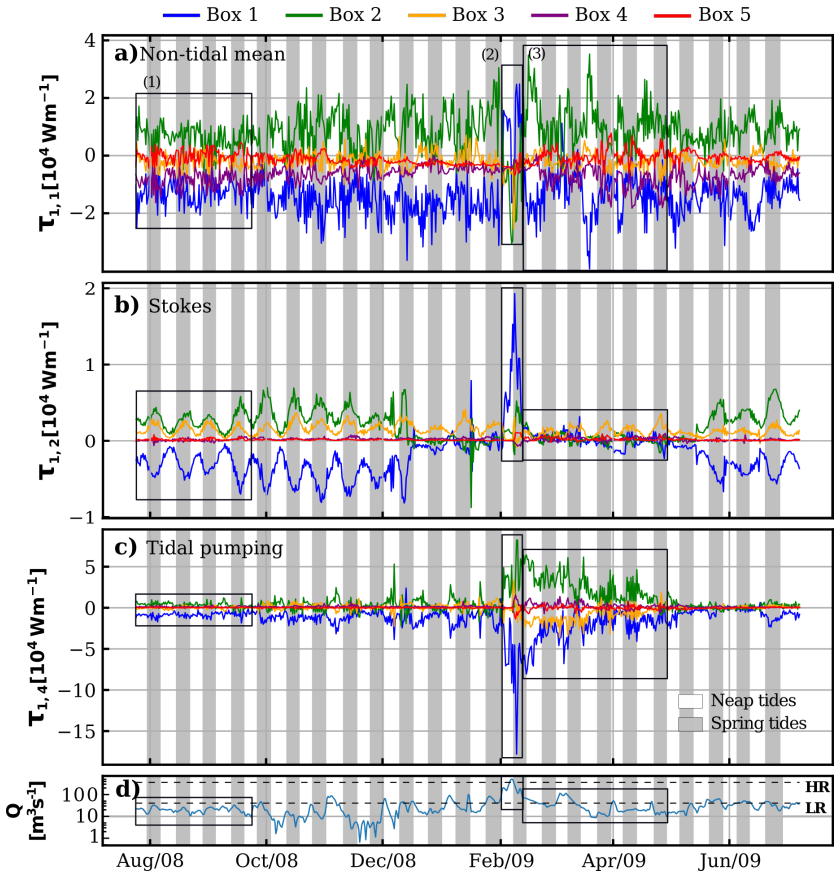

Figure 3.4: Time series of the most significant advective terms of the LAPE along the estuary. *a)* Non-tidal mean; *b)* Stokes; *c)* tidal pumping due to the correlation between currents, elevations and densities; and, *d)* daily river discharges from the Alcalá del Río dam over the study period. HR and LR indicate the high-river and low-river flow regime, respectively. Positive values are upstream. Boxes represent the periods discussed in the main text.

and Stokes ϕ-transports at the estuary mouth are in the upstream direction in contrast to what occurs in the following box. The $\tau_{1,2}$ and $\tau_{1,4}$ transports intensify with the discharge. This means that tidal pumping ($\tau_{1,4}$) is now the dominant process in the first third of the estuary, moving seaward at the mouth ($\simeq -15 \cdot 10^4$ Wm^{-1}) and upstream in the following box ($\simeq 5 \cdot 10^4$ Wm^{-1}).

During the recovery period (3), the mean transport regains its values in low-river flow conditions and when it is in phase with the tide. The Stokes-induced LAPE transport ($\tau_{1,2}$) recovers the values observed in (1). In the case of tidal pumping, maximums observed during the discharge progressively attenuated until the total recovery of the estuary in May 2009.

3.3.4 Longitudinal variability of ϕ-transports for different fluvial regimes

This section jointly analyzes, in terms of LAPE transport, the longitudinal variability of the dominant processes observed in the GRE during periods of neap and spring tides in normal conditions, recovery conditions, and during the high-river flow regime. Figure 3.5 shows the median values ($\hat{\tau}$) of the LAPE transport results.

During (1), non-tidal mean, Stokes-induced, and tidal pumping ϕ-transports at the mouth are seaward. This behavior is inverted upstream ($x = 26.2$ km), where the value is of the same order,

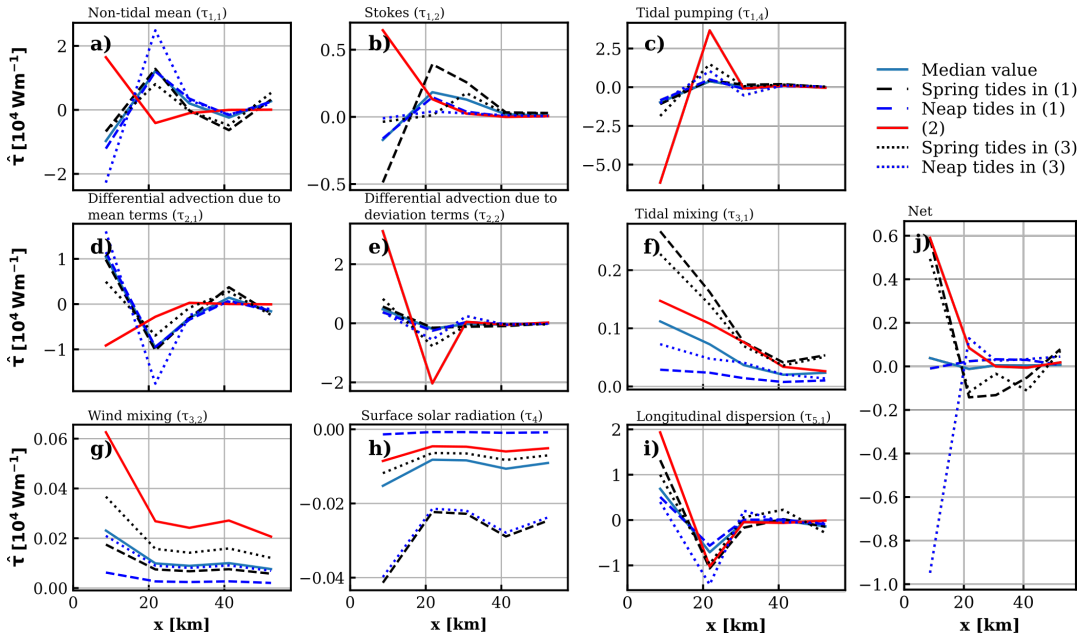

Figure 3.5: Median values of several LAPE transports along the estuary under different flow conditions. Low-river flow, high-river flow and recovery periods are indicated as (1), (2), and (3), respectively. Positive values are upstream.

but positive. From here upstream, these ϕ-transports decrease and show a negative value in $x = 47.5$ km. This variability causes various points of energy transport convergence and divergence to appear throughout the estuary. More specifically, near kilometer 15, there is a divergence point of $\tau_{1,1}$, $\tau_{1,2}$ and $\tau_{1,4}$. Near $x = 35$ km, another convergence point for the same transports is also identified. In spring tides, the mean LAPE transport value is greater near the mouth and decreases after the divergence point. The term $\tau_{1,1}$ varies considerably along the estuary, due to phase changes between the longitudinal velocity and density. Although the longitudinal transport profile intensifies during spring tides in the estuary recovery period, in neap tides, this same value visibly decreases in $x = 17.3$ km. It is important to highlight how the longitudinal profile of $\tau_{1,1}$ is inverted during the fluvial discharge (2). Moreover, as can be observed the net LAPE transport in spring tides (fig. 3.5.j) is positive at the mouth and negative, upstream, whereas in neap tides, it is practically zero in the entire estuary.

The Stokes-induced ϕ-transport (fig. 3.5.b) shows a similar pattern during flow conditions (1) and (2) except for the fact that it becomes practically negligible upstream from the divergence point and during the recovery phase. In any case, the Stokes-induced ϕ-transport has a magnitude that is slightly less than that obtained for the non-tidal mean advection. The upstream decrease in the Stokes-associated ϕ-transport is also controlled by the phase lag between elevations and tidal currents. This phase lag approached $\pi/2$ upstream because of the partial standing nature of tidal wave propagation due to the tide reflection in the dam at the head of the estuary (Díez-Minguito et al., 2012). Tidal pumping $\tau_{1,4}$ (figure 3.5.c) also has the same profile with the absolute maximum value of its magnitude at the estuary mouth. During the high-river flow regime (2), $\tau_{1,4}$ maintains the same longitudinal profile and significantly increases so as to become the dominant process in these conditions.

As can be observed in panels (d), (e), and (i) of figure 3.5, the LAPE transports due to differential advection and dispersion also have an important role in the balance. Transport values due to longitudinal dispersion are greater near the mouth and decrease upstream. In low-river

flow conditions, the transport median value approaches $1.3 \cdot 10^4\,\mathrm{Wm}^{-1}$ in spring tides and is about half that value in neap tides. This shows that dispersive transport is very important in the bottom third of the estuary with a contribution that in certain conditions reaches 30% of the total transport. Transport induced by differential advection of the average terms is the second dominant process in magnitude during (2), and is comparable to the dispersive transport, τ_5. After kilometer 35.3, transport induced by the differential advection of the mean terms and dispersion practically disappears.

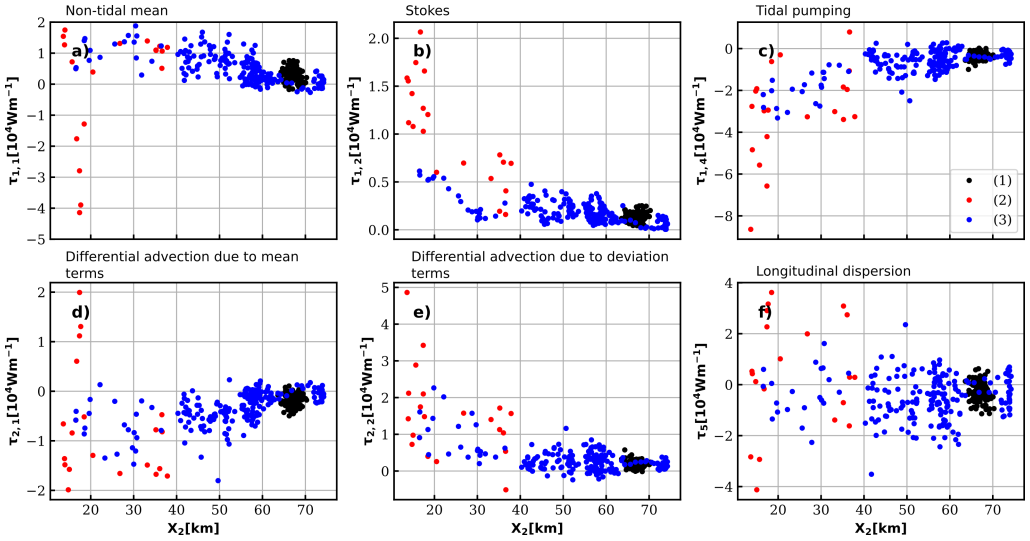

Figure 3.6: Net-estuarine transports of LAPE versus salt intrusion (2-psu isohaline). *a)* Non-tidal mean advection; *b)* Stokes advection; *c)* tidal pumping advection due to the correlation between currents, elevations and densities; *d)* differential advection due to mean terms; *e)* differential advection due to deviation terms; and, *f)* longitudinal dispersion. Colors refer to normal conditions (black), high-river flow (red), and post-riverflood (blue) conditions. Positive values are upstream.

The contribution of the surface solar radiation and mixing terms to ϕ-transport (panels (f), (g), and (h) of figure 3.5) is not significant. In the Delaware estuary studied in Garvine and Whitney (2006) and Rice et al. (2008), the solar radiation and tidal and wind mixing ϕ-transports are significant buoyancy terms. On the other hand, in the GRE case, the contribution of these terms are not significant because they depend on the surface area, and the boxes considered in the model (see Table 1) are two order of magnitude smaller than the surface area of the Delaware estuary ($2.1{\cdot}10^9\,\mathrm{m}^2$, Table 2 in GW2006).

Figure 3.6 shows the most significant net LAPE transports and their relation to the 2-psu isohaline in different hydraulic regimes. The magnitude of τ_i decreased upstream because the longitudinal density distribution depends to a great extent on the salinity of the estuary. This behavior is similar to that of the salt transport observed in Díez-Minguito et al. (2013). As can be observed, salt intrusion due to the river flow (Reyes-Merlo et al., 2013) is linked to LAPE transports. Although the relation between both variables is different for each transport, certain similarities can be observed. Firstly, in normal conditions (1), the absolute transport value does not reach $10^4\,\mathrm{Wm}^{-1}$ and the salt intrusion remains between kilometers 63 and 70. In high-river flow conditions (2), the salt intrusion travels approximately to kilometer 12. Insofar as their absolute value, transports are maximum although the non-tidal mean advective moves seaward the same as the tidal pumping, Stokes transport, and differential advection move upstream. LAPE transport due to longitudinal dispersion is a special case because during (2), its magnitude increases in absolute value. Nevertheless, its dependence on the spring and neap tide cycles is important and dispersion

increases its variability and maintains its mean value close to zero. During the recovery stage (3), the salt intrusion moves from the estuary mouth upstream and transports regain their values in (1).

Averaged ϕ-transports, τ_e in eq. (13) were compared with values obtained by GW2006 in the Delaware estuary. In normal conditions, the mean LAPE transport in the GRE, ranged from -1 to $1 \cdot 10^4\,\mathrm{Wm}^{-1}$. In fact, all individual transport modes were found to have similar magnitude $\sim 10^4\,\mathrm{Wm}^{-1}$. During the high-river flow regime, it is observed that the values of individual transports do depend significantly on the flow conditions even though the order of magnitude of τ_e hardly differs from its value in normal conditions. Furthermore, the order of magnitude of the mean transport coincides with the estimates made by Garvine and Whitney (2006) for high-river flows in the Delaware. This occurs because in our model the transport associated with tidal pumping compensates the transport associated with longitudinal dispersion and differential advection. This first term was not considered in Garvine and Whitney (2006).

3.4 Discussion

This study adopted the definition of the longitudinal anomaly of the potential energy in GW2006 and extended it to the zone of tidal river reaches by segmenting the estuary in stretches. The basic physics premises used led to the derivation of a general balance equation (eq. (3.8)). In realistic scenarios such as this one, balances are determined by only a few terms that can be different in time and space (Burchard and Hofmeister, 2008; Díez-Minguito et al., 2013). The initial hypotheses of a weakly stratified or well-mixed estuary of limited width allowed us to simplify the LAPE balance equation in the GRE for a box and average it in a tidal cycle (eq. (3.10)). The model includes the major intratidal processes in the GRE. The non-linear terms that appeared from the equation of state for sea water were neglected because their influence under weakly stratified to well-mixed conditions is limited. In addition, adiabatically corrected temperature and density (i.e., potential temperature and density, respectively), do not play a role in the GRE, where mean depths are about 7 m. However, these terms could be important in stratified estuaries. It is worth to note that the vertical mixing of density is expressed in terms of eddy diffusivity, and it is simplified with empirical mixing terms at a subtidal scale (Aken, 1986; Simpson and Bowers, 1981; Simpson et al., 1990; Simpson, 1981). A more rigorous definition of the mixing terms would require the analysis of high resolution spatial and temporal measurements that is out of the scope of this study.

The longitudinal variability of LAPE and of ϕ-transports in other fluvial regimes is evident as reflected in the previous analyses. In the low-river flow regime (1), the time variability of the density in neap and spring tides modulated the LAPE field and its transports all along the estuary. Although in our study, τ includes mass anomaly fluxes, the results show alterations similar to those observed in mass fluxes in other estuaries (Vaz et al., 1989), where the alterations were caused by the turbulence modulation induced by tidal currents, basically in fortnightly cycles. The longitudinal variability of τ produced convergence regions that corresponded to at least one of the ETMs, more specifically, to the one located near $\sim 17\,\mathrm{km}$ (Díez-Minguito et al., 2014). The net estuary transport was positive in box 1 and negative in 2, 3, and 4 during spring tides, whereas the opposite occurred during neap tides. Nevertheless, the magnitude of the net transport decreased considerably in neap tides in the box of the estuary mouth compared to its value in spring tides. This could suggest a lateral flow variability in that box, which has a larger transversal section than the rest. It is striking that the same did not occur in high river flows (2), where the net transport was directed upstream. Nor did it occur in the post-riverflood recovery (3), where the transport at the estuary mouth had the same magnitude in spring tides and neap tides, which mutually compensate each other.

After intermediate fluvial discharges (i.e. flows that are neither low nor high) of flow $Q \simeq$

$100\,m^3s^{-1}$, there was a slight increase in the contribution of the ϕ-transport associated with tidal pumping. If those pulsed discharges continued during the fortnightly semi-cycle, the magnitude of the Stokes-induced transport significantly decreased in the lower stretch of the estuary (boxes 1 to 3). This reduction in magnitude was apparently caused by the movement of the salt intrusion towards the estuary mouth (Reyes-Merlo et al., 2013). The phase lag between elevations and tidal currents, which to a great extent controls the Stokes transport, was not altered by these intermediate discharges.

During the high-river flow episodes (2), the longitudinal profile of ρ was constant inside the estuary and approximately equal to the freshwater density. As a result, the LAPE was minimum in these conditions except at the estuary mouth where it was at its maximum. This situation mainly intensified the magnitudes of the non-tidal mean advective transport and dispersive transport, which was expected. However, it also significantly increased the LAPE transports associated with tidal pumping and differential advection. For this reason, these contributions cannot be ignored in the GRE in high-river flow conditions. These results widen the vision of the GRE and extend it to other hydraulic regimes since in previous studies (Díez-Minguito et al., 2013; Díez-Minguito et al., 2014), only transports in low-river flow conditions were considered.

During the initial stages of the post-riverflood recovery phase (3), differential advection terms and longitudinal dispersion terms were positive (upstream) near the estuary mouth. This suggests that they are mechanisms that control the recovery of the LAPE in the estuary. The fact that the intrusion moved towards the mouth during high-river flows may be why there was an increase in the differential advection, which is generally related to the regime of strain-induced periodic stratification (Simpson et al., 1990). However, more research is needed to confirm this possibility.

The influence of sediment suspension was also relevant in the post-riverflood recovery phase. The sediment that was suspended with the discharge remained so because of the turbulence generated by the tidal currents (Losada et al., 2017). The high concentration of suspended solids during the recovery phase was reflected in greater time fluctuations of the LAPE and its transports. The larger difference between neap and spring tides also increased the landward transport of the tidal pumping (Scully and Friedrichs, 2007) in boxes 2 and 3.

In addition, the increase in the non-tidal mean ϕ-transport in the same boxes could be promoting salt transport towards the estuary. Erosion and suspension of the bed sediment favored tidal suspension (Van Leussen and Dronkers, 1988). Along with this, ϕ-transport due to longitudinal dispersion became significant during the recovery phase. At the intratidal scale, these conditions created periods during which stratification-induced turbulence decreased, which indicated an increase in the capacity to retain suspended sediment (Geyer, 1993; Jay and Musiak, 1996).

Finally, this chapter highlights the dependence of the LAPE on the following: (i) origin of the forcing agent; (ii) along-estuary position; (iii) neap and spring tide cycles; and (iv) hydraulic regime. A snapshot of the LAPE along the estuary provides information about the hydrodynamic and mixing conditions of the estuary and could be useful for the management and regulation of the freshwater flow in the head dam. Its use would allow estuary management at the subtidal and local scale (e.g. freshwater discharges in certain stretches of the estuary by taking advantage of the irrigation network).

3.5 Conclusions

With the objective of analyzing the spatiotemporal evolution of estuarine processes within the framework of a LAPE box-averaged approach, it is developed a dynamic equation of the longitudinal anomaly of the potential energy at the subtidal scale. This equation includes the non-tidal mean

advective and Stokes-induced LAPE transport, as well as empirical approximations of the tidal vertical turbulent mixing and the mixing due to wind and solar radiation. In addition, this research extends previous work by including the influence of (i) longitudinal dispersion; (ii) tidal pumping associated with cross-correlations between density, elevations, and currents; and (iii) differential advection due to depth-mean straining, and non depth-mean straining. The general balance equation was applied to the GRE, whose characteristics allowed for simplification and segmentation in five boxes. The analyzed data pertains to the salinity distribution, temperature, suspended solids, tidal elevation and currents, and fluvial discharges recorded along the estuary over a one-year period (2008-2009) in which low-river flow, high-river flow, and post-riverflood recovery conditions were found. These observations were used to evaluate the LAPE and transports throughout the GRE. The results can help to better understand the processes in a narrow and shallow water estuary under different hydraulic regimes.

The time variability of LAPE transport in low-river flows was modulated with neap and spring tides. At the estuary mouth, they were in phase with each other, and further upstream, they were out of phase. Time variability in regard to the mean value was similar in spring tides and neap tides ($\pm$10.65%). The only exception was the Stokes-induced LAPE transport, whose magnitude significantly increased in spring tides. The LAPE transports of all processes in the GRE changed sign on various occasions at approximately kilometers 17 and 35. This gave rise to transport convergence and divergence zones, respectively. The transport convergence region was consistent with the location of the ETM in previous studies. Transports due to dispersive and differential advection moved upstream from the estuary mouth, whereas the others went seaward.

In high-river flows, the longitudinal profiles of the LAPE transport were inverted. The opposite was true for tidal pumping, longitudinal dispersion and differential advection of the deviation in regard to the mean terms, which became considerably greater. The convergence and divergence zones of the non-tidal mean advective LAPE transport disappeared as well as those of the Stokes-induced, and differential advection transport because of the mean terms. Tidal pumping exported the LAPE through the estuary mouth, and was thus balanced with the transport associated with the longitudinal dispersion and differential advection because of the deviation terms that import it.

During the post-riverflood recovery, all transport processes intensified except for the Stokes-induced transport. In the vicinity of the tidal river reach, the magnitude of all LAPE transports was no longer significant. The differential advection and longitudinal dispersion terms moved upstream in the estuary mouth, which suggests that they are the terms that recover the LAPE of the estuary. The time variability in these conditions was considerable in the LAPE transport because of the longitudinal dispersion ($\pm$19.49% of the mean value). The greater difference between neap and spring tides increased the landward transport of tidal pumping in the middle stretch of the estuary. In addition to this, there was a significant increase in the non-tidal mean LAPE transport. In these conditions, the longitudinal gradient of LAPE transport was amplified, which caused the convergence and divergence zones to reappear.

Appendix A: Derivation of the LAPE Equation

The balance equation of the potential energy anomaly in a box (eq. (3.8)) is obtained by evaluating the dynamic density equation $\mathbf{D}(x,t)$ in one reference position x and another x_0 and substituting the values in the following expression:

$$g[\underline{\mathbf{D}(x_0,t)}\,\underline{z} - \underline{\mathbf{D}(x,t)z}] = 0, \tag{3.14}$$

where $\underline{\zeta}$ represents the depth average; the term, $\mathbf{D}(x,t)$, is defined by equation 3.5, (repeated below to clarify the derivation):

$$\mathbf{D}(x,z,t) = \partial_t \rho + \partial_x(u\rho) + \partial_z(w\rho) - \partial_x(k_x \partial_x \rho) - \partial_z(k_z \partial_z \rho) - \mathbf{S}, \tag{3.15}$$

where $\mathbf{S}$ includes the density variation due to heat transfer by the surface layer and the resuspension of sediment from the estuary bottom as:

$$\mathbf{S} = \frac{g\rho\alpha}{\rho_0 c_p} I e^{-\varepsilon(\eta - z)} + \left(1 - \frac{\rho}{\rho_s}\right) C \partial_z(w_s C), \tag{3.16}$$

where non-linear terms that appear from equation of state for sea water are neglected (see eq. (6)); α is the water expansion coefficient; c_p is the heat capacity of the water; ε is the light absorption along the vertical profile; w_s is the sedimentation velocity of the particulate material, assumed to be constant for a given grain size; and, C is the suspended solids concentration. The parameterization of heat transfer follows the Lambert-Beer Law where ε is the attenuation coefficient (Ruiz et al., 2013). In shallow basins, a significant portion of solar radiation can reach the bottom where it is transformed into heat (Wiles et al., 2006). By calculating

$$\begin{aligned} g(\underline{\mathbf{S}(x_0,t)}\,\underline{z} - \underline{\mathbf{S}(x,t)z}) = -\frac{\alpha_w \rho g I}{\rho_0 c_p}\left[\left(1 - e^{-\varepsilon(\eta - z)}\right)\underline{z} + \left(\varepsilon^{-1} - e^{-\varepsilon(\eta - z)}\left(d + \varepsilon^{-1}\right)\right)\right] \\ + \frac{w_s}{2d}\left([C^2]_\eta - [C^2]_{-h} + \eta[C^2]_\eta + h[C^2]_{-h} - d\underline{C}\right), \end{aligned} \tag{3.17}$$

term t_G of eq. (3.8) is obtained.

The processes related to transversal circulation are negligible in narrow low-friction channels (Valle-Levinson, 2008) and thus dependent on x, z, and time t.

For the sake of simplicity, the methodology is applied to the terms on the left of eq. (5.7), related to time variation, advection, dispersion, and density mixing. The term most to the left in eq. (3.8) is further developed in eq. (3.18) by applying the chain rule and Leibniz's rule to derivatives with variable limits and kinematic boundary conditions on the water surface $w_\eta = \partial_t \eta + u_\eta \cdot \partial_x \eta$, for a fixed bed, $w_{-h} = 0$:

$$\begin{aligned} \int_{-h}^{\eta} z\left[\partial_t \rho + \partial_x(u\rho) + \partial_z(w\rho) - \partial_x(k_x \partial_x \rho) - \partial_z(k_z \partial_z \rho)\right] dz = \\ \partial_t \int_{-h}^{\eta} z\rho\, dz + \partial_x \int_{-h}^{\eta} (zu\rho)\, dz - \int_{-h}^{\eta} w\rho\, dz - \partial_x \int_{-h}^{\eta} z k_x \partial_x \rho\, dz + \int_{-h}^{\eta} k_z \partial_z \rho\, dz \\ + \left[(z\rho)_\eta \partial_t \eta + (zu\rho)_\eta \partial_x \eta + (zw\rho)_\eta\right] + \left[(z\rho)_{-h} \partial_t h + (zu\rho)_{-h} \partial_x h + (zw\rho)_{-h}\right] - \\ (zk_x \partial_x \rho)_\eta \partial_x \eta - (zk_x \partial_x \rho)_{-h} \partial_x h + (zk_z \partial_z \rho)_\eta + (zk_z \partial_z \rho)_{-h} = \\ \partial_t(d\underline{z}\underline{\rho}) + \partial_x(d\underline{z}\underline{u}\underline{\rho}) - (d\underline{w}\underline{\rho}) + \partial_x(d\underline{z}\underline{k_x}\partial_x\underline{u}\underline{\rho}) + (d\underline{k_x}\partial_z\underline{\rho}) \\ (zk_x \partial_x \rho)_\eta \partial_x \eta + (zk_x \partial_x \rho)_{-h} \partial_x h - (zk_z \partial_z \rho)_\eta - (zk_z \partial_z \rho)_{-h}, \end{aligned} \tag{3.18}$$

where sub-indexes $_\eta$ and $_{-h}$ indicate that the terms are evaluated in $z = \eta$ and $z = -h$. Inserting eqs. (3.7) and (3.18) in the eq. (3.14),

$$\begin{aligned} \partial_t(g(\underline{\rho_0}\,\underline{z} - \underline{\rho z})) + \partial_x(g(\underline{u\rho_0}\,\underline{z} - \underline{u\rho z})) - g(\underline{w\rho}) \\ -g\underline{k_z}\partial_z\underline{\rho} + gd^{-1}(\underline{z}k_z\partial_z\rho)^\eta - gd^{-1}(\underline{z}k_z\partial_z\rho)^{-h} + \partial_x(g[k_x\partial_x\underline{\rho}](z - \underline{z})) \\ +gd^{-1}(\underline{z} - \eta)(k_x\partial_x\rho)^\eta\partial_x\eta - gd^{-1}(\underline{z} + h)(k_x\partial_x\rho)^{-h}\partial_x h. \end{aligned} \tag{3.19}$$

A general variable $\zeta = \underline{\zeta} + \zeta_v$ is composed of the sum of a depth-averaged value and its deviation. When this variable is applied in the equation, equation (3.8) is obtained. As in Burchard and Hofmeister (2008) and De Boer et al. (2008), no hypothesis has been formulated regarding the form of the longitudinal velocity profile.

4. A Management Model for Freshwater Outflow and Mixing Density

"I have not failed 999 times. I have simply found 999 ways how not to create a light bulb"

Thomas Alva Edison

The epigraph of this chapter refers to the fact that the creation of something new usually requires lots of attempts. In the present thesis, this chapter was the first work finished. However, the paper was rejected because, for the reviewers, the physical foundations of the model were not clearly explained. This situation forced to reformulate the box model in terms of a dynamic equation for LAPE, derived from the equations for salinity, temperature and turbidity presented in chapter 3. An updated version of the present chapter based on that work is under preparation and will be soon submitted to a journal.

This chapter presents an application of the longitudinal anomaly of potential energy (LAPE) in order to quantify the water-mass exchange fluxes and the density of mixed water during low river flows at a semidiurnal time scale in a well-mixed estuary.

The main geometrical and dynamic properties of GRE were applied to simplify the LAPE model as was presented in the previous chapter:The Guadalquivir River estuary was divided into five connected stretches where the model was applied over a period of six months, (July of 2008 to January of 2009), during which river inflow was $Q_d < 100$ m^3/s (§ 4.1). The model does not only include the effects of freshwater river flow, Stokes transport, solar radiation, and tidal and wind mixing, but also the tidal pumping term which was highlighted in § 3. It determines the water density and the water mass exchanges as the solution of a linear system of equations, which represents the LAPE conservation in the five-interconnected stretches of the estuary.

The results obtained are presented in § 4.2, and include (i) a comparison with the Garvine and Whitney (2006) model; (ii) the estimation of the volumes of the water mass exchanged and their densities; (iii) the time variation of the potential energy anomaly along the estuary; and (iv) the

analysis of the influence of the major contributors to estuarine dynamics. The results are discussed in § 4.4, where a specific mention is made to the blockage mechanism, the role of the variables in water mass exchanges and the relation between water mass exchange and flushing and residence time. Also, some management recommendations to unblock the estuary are given.

4.1 Formulation and resolution of the subtidal LAPE box model

4.1.1 Mass and LAPE balances

The estuary was divided into a series of N connected boxes, as shown in figure 4.1, numbered from the river mouth towards the head. Each box was defined by its alongshore starting position, x^i, length L^i and limiting cross-sections A^{i+1} and A^i, where the superscript i stands for the seaward edge of box-i. The boxes were selected so that each one aggregated the particularities of the longitudinal structure of tidal propagation, salt flux and transport of suspended particulate matter in terms of density variation.

The differential form of the Reynolds transport theorem for a given box volume, assuming incompressible fluid can be written in vectorial notation as:

$$\int\int\int_V \frac{\partial \rho}{\partial t}\, dV + \int\int_{S_V} \rho(\vec{u}\wedge\vec{n})\, dA = 0, \tag{4.1}$$

where S_v are the surfaces that define the contours of the box; $\vec{n}$ is the vector normal to the surface; and the $\wedge$ is the vectorial product. The first term of the LHS in eq. (4.1) represents the accumulation term of the density variation whereas the second term is the mass exchanges through the contours. The mass balance includes the contributions from the river discharge and Stokes transport as in GW2006. The tidal pumping term induced by the covariance between the current and salinity was also included since it represents a large contribution in some estuaries (Díez-Minguito et al., 2013). We assumed that freshwater fluxes from precipitation, evaporation and water outflow for irrigation were small in comparison to the river inputs, and thus were regarded as negligible. Hence, the mass balance of box i reads as:

$$\underbrace{V^i \frac{\partial \rho^i}{\partial t}}_{m_1} - \underbrace{Q^{i+1}\rho^{i+1}}_{m_2} + \underbrace{Q^i \rho^i}_{m_3} + \underbrace{(S^{i+1}+P^{i+1})\rho_e^i}_{m_4+m_5} - \underbrace{(S^i+P^i)\rho_e^{i-1}}_{m_6+m_7} = 0, \tag{4.2}$$

for $i = 1,...,N$, where ρ_e^i is the box-volume averaged density. Terms in eq. (4.2) are represented in figure 4.1.c. In this expression, m_1 is the accumulation term; and m_2 and m_3 are the incoming and outgoing water masses exchanged with box-i, in which Q^{i+1} and Q^i account for the Eulerian Stokes compensation, flow tidal pumping, and other circulation terms (Ianniello, 1979) that enter/leave the box with densities ρ^{i+1} and ρ^i respectively. The river density is represented by ρ^{N+1}.

The Stokes transport and tidal pumping were assumed to be negligible at the upstream edge of the landwardmost box. Q^{N+1} is the river discharge; S^i is the incoming Stokes drift (Longuet-Higgins, 1969); and P^i is the tidal pumping term.

As the depth along the estuary is almost constant, a simple relation was assumed between mixing densities at the box interfaces, ρ^i, and box-averaged densities, ρ_e^i, which take into account the cross-sectional areas: $\rho_e^i = \xi_i \rho^i + (1-\xi_i)\rho^{i+1}$ where $\xi_i = A_e^i/(A_e^i + A_e^{i+1})$. GW2006 also adopted linear dependence with $\xi = 0.69$ for the Delaware estuary.

The same argument was followed for the energy balance. The tidal propagation was assumed to be barotropic and the Earth's rotation, negligible. Therefore, the time variation of the potential

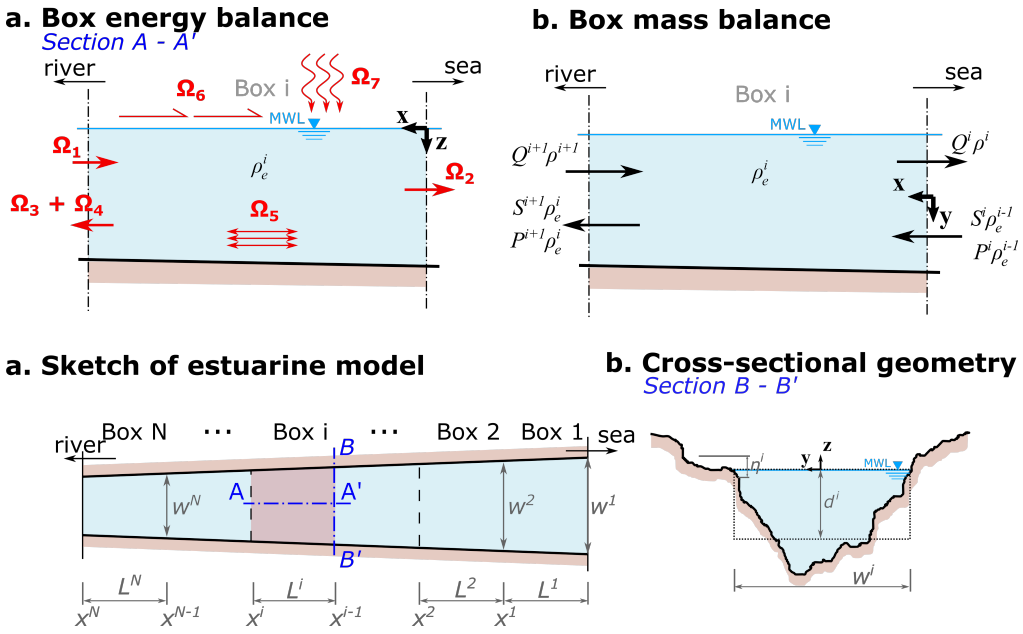

Figure 4.1: Diagram of the estuary box model and reference frame. *a)* Global diagram of the estuarine model. The red-shaded region stands for the surface area of box-i, A_e^i; *b)* geometry of the cross-section. The point-dashed rectangle is the mean geometry of the box cross-section, A^i; *c)* terms that establish the mass balance; *d)* contributions to the potential energy anomaly balance: IMW (incoming mixed water), OMW (outgoing mixed water), ST (Stokes transport), TP (tidal pumping), WM (wind mixing), SR (solar radiation), and TM (tidal mixing).

energy anomaly at box-i was estimated as:

$$\frac{\partial \Phi^i}{\partial t} - \underbrace{\alpha g(\rho_e^{i-1} - \rho^{i+1})Q^{i+1}}_{\Omega_1} + \underbrace{\alpha g(\rho_e^{i-1} - \rho^{i})Q^{i}}_{\Omega_2} + \underbrace{\beta g(\rho_e^{i-1} - \rho_e^{i})(S^i + P^i)}_{\Omega_3+\Omega_4} + \underbrace{\frac{4\varepsilon}{3\pi} C_d \rho_e^{i-1} u_T^3 A_e^i / d^i}_{\Omega_5} + \underbrace{\delta \kappa_s \rho_a W^3 A_e^i / d^i}_{\Omega_6} - \underbrace{\frac{\alpha_s g Q_s A_e}{2C_p}}_{\Omega_7} = 0. \tag{4.3}$$

The contributors to the energy balance are displayed in figure (4.1.d). In eq. (4.3), the parameterizations used in GW2006 and Rice et al. (2008) were adopted. The first term is the rate of change of the potential energy anomaly or accumulation term; Ω_1 is the incoming flux of mixed water. The counter-part is an outgoing flux of mixed water, Ω_2. Ω_3 stands for the Stokes transport; and Ω_4 is the tidal pumping, which leaves box i upwards. We assumed that the Stokes transport and tidal pumping move the water of box-i. The incoming Stokes transport and tidal pumping did not contribute to the energy balance because they had the reference density of box-i (ρ_e^{i-1}). α and β are empirical parameters used to compute the water flux of the potential energy by fresher water and the Stokes transport. As in GW2006, we assumed a parabolic expression for the incoming fresher water and a linear profile for the Stokes transport and tidal pumping. By considering these vertical profiles of water velocity, the coefficients for the vertically averaged rate of change of potential energy over the whole section yield $\alpha = 1/2$ and $\beta = 1/3$. The tidal and wind-mixing terms work to reduce stratification and read as Ω_5 and Ω_6. Tidal and wind mixing are represented by the cube of the tidal velocity and wind speed at box-i. ε, δ, C_d and κ_s are constants that represent the mixing efficiency by tides and wind, effective bottom and surface drag (Simpson et al., 1991). ρ_a is the air

density. Finally, the solar contribution at box-i acts to stratify the water column. This term reads as Ω_7 where α_s, Q_s, and C_p are the thermal coefficient of expansion, the net solar radiation, and the specific heat of sea-water, respectively. As in GW2006, the sensible heat and latent heat were ignored. Although the mixing terms defined in eq. 4.3 are widely applied in the literature, other formulas can be used instead.

4.1.2 Boundary and initial conditions

In eq. 4.3, the contributions due to the Stokes transport, tidal pumping, solar radiation, tidal mixing and wind drag are estimated from climate and tidal data. The boundary and initial conditions must then be set to solve the system of equations.

At the upstream boundary, river discharges measured at the Alcalá del Río dam were provided with a constant fresh water density set equal to $\rho^{N+1} = 1000\ kg \cdot m^{-3}$.

The reference density of the seawardmost box, ρ_e^0, was simply modeled as $\rho_e^0(t) = \overline{\rho_s} + \sum_{k=1}^{2} A_k \sin(2\pi t/T_k + \varphi_k)$, where $\overline{\rho_s}$ is the mean shelf density as in Garvine and Whitney (2006), and the harmonic part represents the effect of spring-neap tides on mixing (with T_1 = 14-day oscillation) and the influence of water temperature (with T_2 = 1-year oscillation). The fitting parameters of these modulations (amplitude, A_k and phase, φ_k) were derived from satellite imagery (Caballero et al., 2014).

Finally, the initial conditions of along-estuary densities and water mass exchanges should also be provided. The density at each section, ρ^i was modeled by assuming that the along-estuary density variation was a hyperbolic tangent function, similar to the formulation in Talke et al. (2009) to describe the salinity. In the discussion, a sensitivity analysis of the model to the value of the initial condition is presented. The initial values of the water mass exchanges were easily specified as the sum of the river discharge and the difference between upstream and downstream values of the Stokes transport and tidal pumping at the edges of each box.

4.1.3 Solution of the system

After specifying the values of the known variables and the initial and boundary conditions, eqs. 4.2 and 4.3 for $i = 1, \ldots, N$ constitutes, for each time step, a non-stationary linear system of 2N-equations. The unknowns are the water mass exchanges ($Q^i(t)$ and their mixing densities $\rho^i(t)$) at time t for $i = 1, ..., N$. The time period under study is discretized with a time step Δt equal to the semidiurnal period. The variables are depth-, box- and tidal-averaged. The solution is obtained through the iterative Newton method.

4.1.4 Implementation

The methodology proposed was applied at the GRE during a period of 6 months (from July 23, 2008 to January 23, 2009). We established the hydrodynamic balance of the downward part of the GRE ($x \leq 57.6$ km), according to the maximum upstream location of 2 psu isohaline (Díez-Minguito et al., 2013). The GRE was split into five boxes ($N = 5$) (Figure 2.10). These boxes are representative of the along-estuarine dynamics, based on uniform and stationary regimes under low river-flow conditions and at a subtidal scale (Díez-Minguito et al., 2012; Díez-Minguito et al., 2013; Díez-Minguito et al., 2014). The increase in water velocities due to river discharge was found to be negligible during low river flow (Losada et al., 2017), and the contribution of precipitation or evaporation to the box volume was also very small. Therefore, the box volume was asumed to be stationary, $\tilde{V} \simeq 0$ as shown in the model in section 2.2. We chose the main semidiurnal M2 period

as the reference time step since estuarine managers regulate the river discharge on a daily basis. The reference time periods used to compute the tidal mean values were the zero-upcross intervals of the mean water level at the Bonanza tidal gauge (β_0 in Figure 2.10).

The estimated mixing density at the shelf (ρ_e^0) was regarded as the reference density in the potential energy anomaly balance for box 1. This resulted in a simple model with a mean density of 1024 kg m^3 and two harmonics with amplitude and phases ($A_\varphi = 0.362_{3.77}$ and $0.9_{4.89}$) for periods of 14.77 and 365.25 days, respectively.

As in GW2006, the inflowing freshwater from the river and the outgoing exchange water mass were assumed to have uniform density profiles in depth (Díez-Minguito et al., 2014). The freshwater discharge from the Alcalá del río dam (Q^6) flows with the water density was computed from sensor γ_6.

The Stokes drift was calculated as $S^i = \overline{\eta^i u^i}$ (Longuet-Higgins, 1969; Miranda et al., 2017), where η^i and u^i are obtained from the harmonic constituents of tidal velocity and elevation (Díez-Minguito et al., 2012). Assuming that the vertical velocity profile of tidal pumping is similar to the Stokes transport under low river-flow conditions, tidal pumping can be modeled as a fraction of the Stokes transport $S_* = (1+\xi)S$ where ξ are coefficients obtained from Díez-Minguito et al. (2013). These coefficients express the rate of tidal pumping to Stokes transport with values ranging from -0.25 to 1.25 (Table 4.1). Wind and solar contributions were computed based on the observations at M.S. station. Tidal mixing was calculated by assuming a constant velocity at each box, given by the mean value of the harmonic analysis to tidal levels and current during the study period, according to Díez-Minguito et al. (2012). Table 4.1 summarizes the geometrical parameters of each box.

The model was analyzed during two time intervals. The first interval, period A, went from 23 July 2008 to 23 September 2008. It was characterized by almost permanent river flow conditions with a mean water discharge of 30 m^3/s, which is usual during the summer season. The physical requirements of the model were fulfilled during this period. In order to test the robustness of the model, its performance under deviations from low flow conditions was also analyzed. The second interval, period B, was from 23 September 2008 to 23 January 2009. During this time, intermittent conditions occurred, in which water pulses alternated with discharges reaching $\sim$ 100 m^3/s and persistent periods of water mass retention at the dam. These were typical of the winter season.

Table 4.1: Box parameters of the subtidal box model at the Guadalquivir river estuary. ξ^i, Ri_x^i and t_r^i refer to the coefficients used to estimate the reference density, horizontal Richardson number, and residence time (eq. 4.5). The total residence time is known as the flushing time. * stands for the SIPS regime.

Box		Geometry						Hydrodynamic		
no.	Color	x^i (km)	L^i (km)	d^i (m)	A^i (dam^2)	A_e^i (km^2)	V^i (hm^3)	ξ^i	Ri_x^i	t_r^i (days)
1	cyan	0	17.3	7.26	58.39	12.91	88.42	-0.23	0.11*	10.16
2	green	17.3	8.9	7.13	43.82	5.22	36.32	-0.13	0.28*	8.30
3	orange	26.2	9.1	7.05	37.80	4.54	31.91	0.55	0.23*	8.62
4	red	35.3	11.8	6.95	32.51	4.90	34.95	0.97	0.06	24.19
5	purple	47.1	10.5	6.85	26.72	3.56	25.81	1.26	0.06	26.76
6	-	57.6	-	6.80	22.45	-	-			
	TOTAL	-	57.6	-	-	31.13	217.41	-	-	84.67

4.2 Results

The consistency of the model was also tested by running it for a single box that comprised the whole estuary as in GW2006.

4.2.1 Comparison with the one box model of Garvine and Whitney (2006).

As previously mentioned, even though our goal was not to compute the ocean shelf-estuary exchange, this variable was the convergence point of the results of GW2006 and the N-box model presented in this work. The GW2006 model was modified with improvements in the mass and energy balances. Figure 4.2.b shows the water mass exchange between boxes. The blue dashed line stands for the results of the GW2006 one-box model whereas the light blue solid line is the water mass exchange of the seawardmost box with the shelf obtained for the five boxes. As can be observed, there are almost no differences between the water mass exchanges obtained in both cases. The maximum absolute difference and root mean square error were 0.7 and 0.02 m^3/s, respectively. Furthermore, the water mass exchange with the shelf is not sensitive to the number of boxes.

Figure 4.2.a depicts the box-estimated density of the model and observations. The model gives a good description of the box-estimated density observed during summer (period A). The maximum density of spring tides was overestimated while troughs in neap tides were reproduced fairly well. During period B, the model overestimated the values of the boxes. The simple formulation for the shelf density used to feed the model did not permit an accurate description of the density reduction due to water discharges over $40m^3/s$ (i.e. the density change at the beginning of November). However, after these discharge events, it returned to normal conditions in approximately 14 days (a spring-neap cycle) as observed by Díez-Minguito et al. (2013) in the salinity field. After this recovery period, the model provided a fairly good simulation of the density observed (see the third and fourth weeks of November).

4.2.2 Time-series of along-estuary estimated densities and water exchange fluxes.

Figure 4.2.a shows the comparison between the estimated densities obtained with the model and observations from the ADCP stations. Generally, the maximum density ocurred during spring tides as commonly observed in estuaries with a large convergence length (Savenije, 2005).

During period A, spring-neap variations were clearly identified. The Stokes transport was found to be maximum during spring tides, and hence, the inflow of a heavier water triggering the increase of the mixing density along the GRE was also maximum. Conversely, the mixing densities decreased during neap periods. Regarding water mass exchanges, the seaward box presents larger exchange fluxes where the density, Stokes transport (and the associated counter-current), and estuary width are maximum. The exchanged volumes decrease gradually landward (Officer, 2013). Once more, the water exchange reproduced not only the spring-neap cycle, but also the flood-ebb cycle. Optimum water exchanges were found to occur during spring tides. Tidal pumping gradually increased landward at a faster rate than the reduction of the Stokes transport (Díez-Minguito et al., 2013). This created a deficit of water mass that should be compensated with the incoming fresher water from the upstream adjacent box. Hence, the water flux out of boxes 4 and 5 (red and purple lines) are usually less than river discharge (black line). However, in some cases, this deficit was so large it triggered the compensation with the water mass from the adjacent seaward box. Then, a negative flux was obtained, meaning that the direction of the water mass reversed the usual seaside direction. Such periods usually occur during the neap-spring transitions.

The model was also validated for the study period B, during which intermediate river discharges

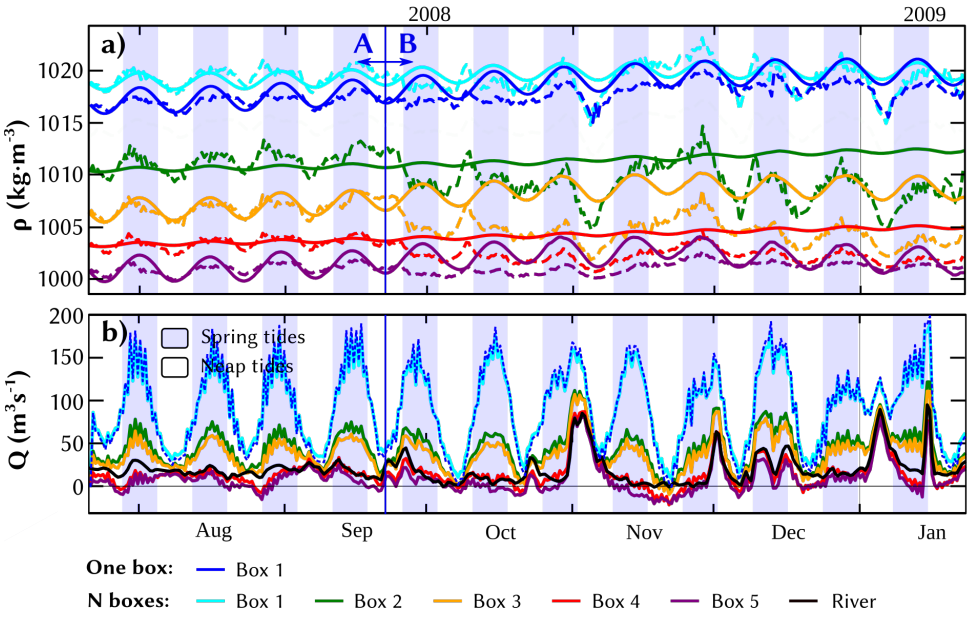

Figure 4.2: Estimated densities and water mass exchanges between boxes. *a)* Comparison between computed mixing densities (dashed lines) and observations (solid lines); *b)* water exchange fluxes of each box. The blue vertical line divides the regions of stationary and low river-flow conditions (A) and intermittent pulses with persistent period of water mass retention (B).

alternated with low flow conditions. At the end of September, the mean density of the estuary decreased, probably due to water discharges from adjacent rice crops previous to the collection campaign. However, this was something that the model was unable to capture. This influence was less sensitive at the estuary mouth where the corresponding box reproduces the observations fairly well. Furthermore, seasonal to annual variations in tidal transport (Stokes and tidal pumping) may be responsible for the differences found in the middle of the estuary (Gräwe et al., 2014). However, the density estimations reproduced the observed time variations even with the appearance of more frequent episodes of water discharges. The spring-neap cycles were still present in time-series but seemed to be less important in the intermediate estuary regime. The incidence of intermediate river discharges on water exchanges along the estuary was also found to be important (figure 4.2.b). During those episodes, Q^i gradually increased seawards to compensate the reduction of mixing density along the GRE. The water flux leaving the estuary was also reduced. As before, the along-estuary differences in the Stokes transport and tidal pumping gradient were not balanced during spring-neap transitions, thus triggering the reversal of the water mass exchanges. The longer the period of low river discharges, the greater the number of boxes that reverse the direction. The minimum exchange flow ocurred on November 22 when boxes 2 to 5 reversed the direction of the water mass exchanged, and a low flux of water left the estuary at a rate close to 10 m^3/s. This effect was intensified due to the low river conditions maintained under neap to spring tides (figure 2.11.e and .f).

4.2.3 Along-estuary time series of the potential energy anomaly

The averaged potential energy anomaly (PEA) establishes a reference value that is related to the mean spatial (along estuary) density gradient (figure 4.3.a). Both the modeled estimated potential energy anomaly and the observed estimated potential energy anomaly (Φ_e^i) were computed using eq. 3.12. The maximum along-estuary density gradient is shown at box 2 (green line), which

corresponds to the maximum PEA. The along-estuary density decreased further upstream after box 2. The PEA is defined by eq. 4.3 and represents an approximate overall energy of 875 Jm^{-3} at the GRE. Theoretically, tidal mixing reduces the stratification during spring tides, which avoids salt intrusion and reduces the PEA. The opposite occurs during neap tides. Periodic PEA patterns were found during period A. The mean values of the PEA and their variability were adequately reproduced with the model.

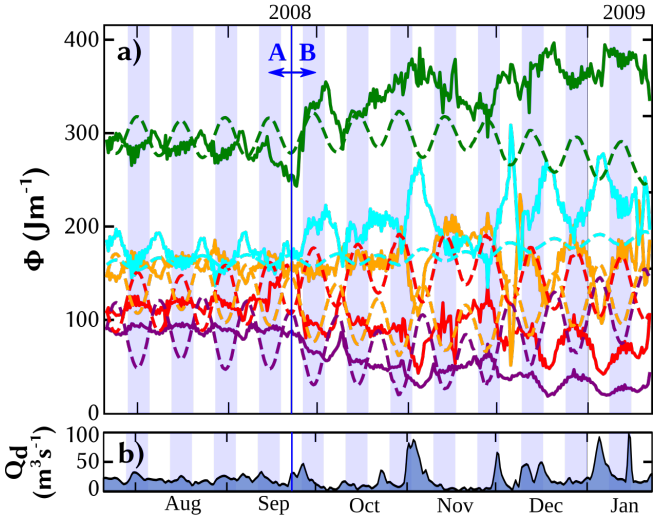

Figure 4.3: *a)* Computed (dashed line) and observed (solid line) estimated subtidal potential energy anomaly in each box; *b)* water discharge from the Alcalá del Río's dam. As in previous figures, blue shaded boxes represent spring tides whereas the white boxes stand for neap tides.

During period B, the seasonal variability of tidal elevations and currents and the water discharges from adjacent rice crops may explain the increase observed at box 2 and the subsequent decreases at boxes 4 and 5. As before, intermediate river discharges caused a steady decrease in the PEA from boxes 3 to 5. In contrast, there was an increase at seawardmost boxes. This difference in behavior was the responsible for the events occurring during low river discharges, when the landward boxes tended to retain water mass, which decreased the water exchange. For intermediate river flow conditions, the upward boxes also added water mass to the water exchange. The potential energy anomaly was found to oscillate out of phase with spring-neap cycles. In other words, maximum values of PEA during neap tides and minimum values during spring tides. The largest tidal velocities during spring tides mixed the water column, which increased the density, and reduced the PEA at the mouth. This pattern can also be observed at box 2. Conversely, boxes 3, 4, and 5 show the largest PEA during spring tides. With river discharges, $Q_d \sim 100\ m^3/s$, the PEA increased sharply at box 1 while it decreased at boxes 3, 4, and 5. As reflected, box 2 does not exhibit any change during these events that are probably associated with an effective across-channel flux (Basdurak et al., 2017).

4.2.4 Time series of along-estuary contributions to the potential energy anomaly

Figure 4.4 shows the variations and levels of the rates Ω^i computed from the box model. As an example, the potential energy anomaly contributors of box 1 are analyzed (eq. 4.3). The largest contributor was the incoming advection Ω_1, such as the river discharge in GW2006. It was followed closely in magnitude by the outgoing advective term, Ω_2, though with the opposite sign. The Stokes transport and tidal pumping terms, $\Omega_3 + \Omega_4$, were also important since they tended to reduce the energy gradient. In addition, solar heating made a somewhat more modest, though persistent,

contribution to the potential energy (Ω_6). Tidal mixing Ω_5 made a negative contribution. Finally, as observed by Rice et al. (2008), wind mixing made an important contribution since it strongly modified the potential energy gradient. When our values were compared to those obtained in the Delaware estuary, strikingly, ours were two orders of magnitude smaller, based on the ratio between the surface areas (A_e) of both estuaries.

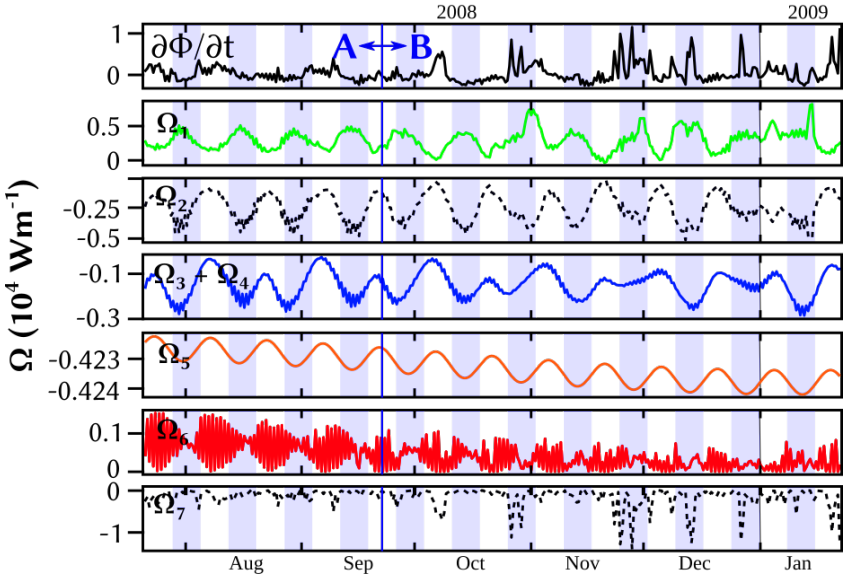

Figure 4.4: Time series of the rates of the potential energy anomaly change at box 1 for the various competing mechanisms.

The energy contributions showed a regular well-defined oscillating pattern during period A because of the absence of strong winds. On the contrary, the frequent river discharges and the presence of intense winds observed during period B, significantly modified the energy gradient at the mouth. This pattern was observed along the estuary and accentuated the irregular behavior of the density.

4.3 Supporting management strategies

4.3.1 The blockage mechanism

The along-estuary exchange flux between boxes i and $i+1$ are described by Q^i (eqs. 4.2 and 4.3). In terms of salt transport, the Stokes transport increased seaward at the GRE while tidal pumping increased landward (Díez-Minguito et al., 2013). These conditions favored a negative net water mass that entered and then flowed out due to Stokes transport and tidal pumping (m_4 to m_7 in eq. 4.2). During certain periods, this difference was larger than the incoming water mass from the upward box m_2. Then, a reversal of the water mass flux, a negative m_3-term, was needed to balance the density gradient

We refer to this situation as blockage conditions. During blockage, the water exchange does not gradually increase seaward, that is, $Q^i \not> Q^{i+1}$. Figure 4.5.a shows the periods in which a certain box of the estuary is blocked. As can be observed, these blockage events are related not only to low river-flow conditions (see figure 4.5.b) but also to tides. As previously mentioned, during normal conditions (period A), the worst conditions usually occur during the transition from neap to spring

tides. Boxes 4 and 5 show long periods of blockage that are intensified at two estuarine turbidity maxima (ETM) located at $x = 35$ km and $x = 58$ km (Díez-Minguito et al., 2014).

The effect of water discharges is also evident (period B). As can be seen, river discharges greater than $Q_d \sim 40\ m^3/s$ enhance the water outflux, and box blockage does not occur. However if low river conditions persist, the blockage starts at the upward box and propagates downstream, thus sequentially blocking the boxes towards the mouth. The worst conditions for the occurrence of this type of event were during November (see figure 4.5.a). The 20 days in which the dam retained the water discharge produced the successive blockage of boxes 5, 4, 3, and 2. The water exchange at box 1 was not canceled or reversed but rather decreased from a mean value of about 50 m^3/s at neap tides to approximately 10 m^3/s. Some of these conditions were also motivated by the wind (see figure 4.5.c). As shown in figure 4.5.c wind-induced upwelling/downwelling conditions favor (unblock) or harm (block) certain boxes. For instance, onshore winds ($W_{8d} \sim 5m/s$) in mid November favored the water exchange, which intermittently unblocked boxes 2, 3, and 4. Conversely, during the last neap tide in July and the first neap tide in December, the water outflow was about 40 and 20 m^3/s, respectively, which coincided with strong offshore winds that favored the reversal of the water outflux.

4.3.2 Contributors to the water mass exchanges

A simple decomposition of the components that describe Q^i includes the river discharge (Q^6), net tidal pumping (ΔP^i), and net Stokes transport counter-current (ΔS^i), but also the other estuarine flow circulations as residual circulation or SIPS (E^i). Hence, the circulation is computed as:

$$E^i = Q^i - \Delta(S^i_* - S^{i+1}_*) - Q^6 \tag{4.4}$$

where S_* is the sum of the Stokes transport and tidal pumping.

The circulation varied from -60 to 75 m^3/s at the GRE (figure 4.6.a). Positive (seaward) values were found during the entire study period only for box 1. However, intermediate and upstream boxes showed an asymmetrical pattern in which most of time E is negative (landward). The maximum residual circulation was found in mid-spring tides for the seawardmost boxes due to the immediate effect of tidal transport on the estuary mouth. However, moving upstream, the maximum showed a phase-lag of a mid-MSF tidal period (~ 7.4 days). The minimum values occurred between boxes 3 and 4 with an oscillating pattern following the monthly lunar cycle (MM).

4.3.3 Residence and flushing times

The intensity and time scale of water exchanges are characterized by the residence and flushing times since these areas are good indicators of the correct functioning of natural processes in an estuary for management purposes (Dyer, 1973; Monismith et al., 2002; Sheldon and Alber, 2002; Sheldon and Alber, 2006; Valle-Levinson, 2010). Accordingly, a simple residence time model was applied:

$$t^i_r = \frac{V^i}{Q^i} \tag{4.5}$$

where t^i_r is the residence time of box-i. The smaller the time scale, the faster the exchanges. The sum of the residence time of each box along the estuary is the flushing time (Sheldon and Alber, 2002). The flushing time is the time required to replace freshwater in an estuary at a rate equal

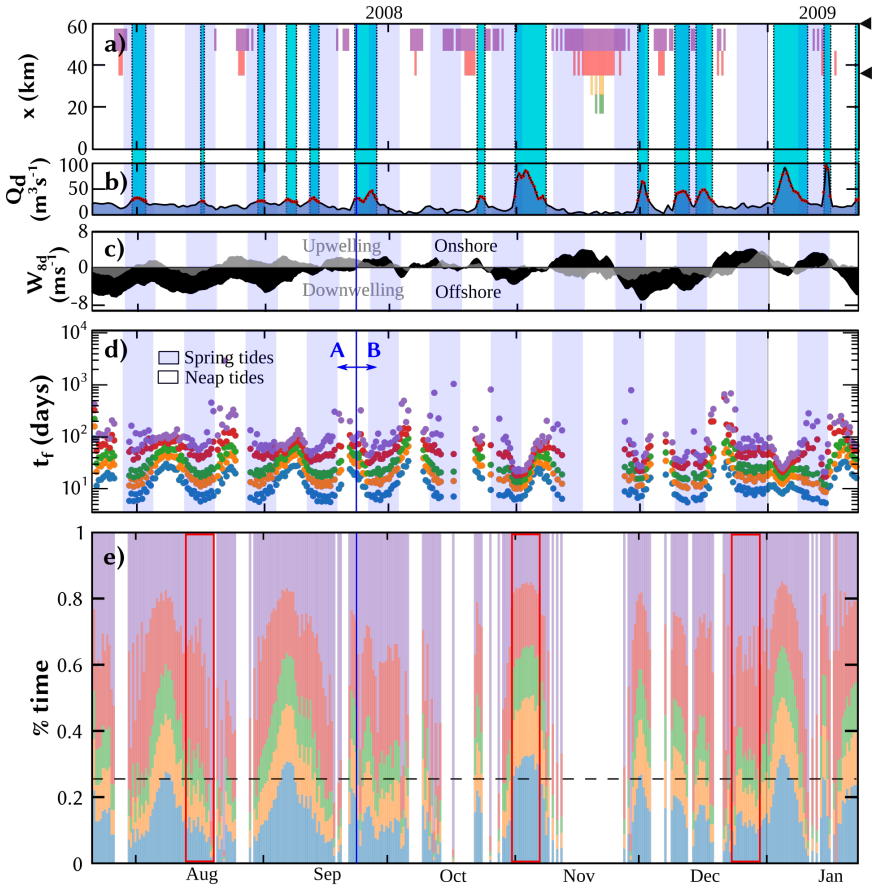

Figure 4.5: *a)* Blocking periods. Black triangles show the location of the estuarine turbidity maxima; *b)* river discharge. Red black-filled dots represent water discharges under the SIPS regime, according to estuarine parameter space Geyer and MacCready (2014); *c)* 8-day averaged wind speed. Upwelling/downwelling refers to wind-induced upwelling/downwelling conditions; *d)* cumulative residence time. The greenish-blue pointed line shows the partial residence time of box 1. Successive pointed lines represent the partial sum; *e)* residence time as a percentage of the total at each time step. The color scale for the boxes is the same as in previous figures. The horizontal dashed line shows the residence time of the two landwardmost boxes when blockage appears.

to that of river discharge. The residence time changes rapidly for variations in discharge under conditions of low river-flow, while it varies slowly for high water conditions.

Figure 4.5.c depicts the partial residence time of each box and the total flushing time of the GRE. It is important to consider the Stokes transport, tidal pumping, and estuarine circulation in eq. 4.5 because sometimes the water exchange may reverse the transport to compensate the density gradients. Those cases are not accurately reproduced if the residence time is only inversely proportional to the water mass exchanges. Unlike previous studies, we added some tidal contributors to the computation of the residence time, and this led to significant differences in the results.

For example, with a volume equal to $217.41 \cdot 10^6 m^3$ (Table 4.1), and values of Q_d, such as $Q_d = 40\ m^3/s$ and $Q_d = 100\ m^3/s$, the flushing times were about 63 and 26 days without considering the Stokes counter-current, tidal pumping, and other circulations. However, when these terms were included in the calculation, the flushing times were 80 and 18 days. The median and standard deviations of the GRE flushing time were 84.67 and 68.44 days, respectively. It should be highlighted that the residence time cannot be computed during blockage conditions because at least

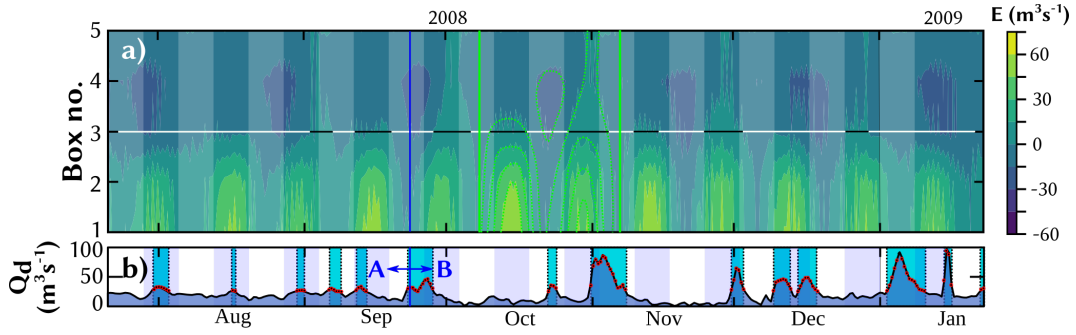

Figure 4.6: *a)* Estuarine circulation along the Guadalquivir River Estuary. Horizontal black lines show the periods when the estuarine circulation of box 3 is positive (seaward) whereas the white line shows periods of negative (landward) circulation. Green lines depict a standard pattern of along-estuarine circulation that is repeated in time; *b)* river discharge from the Alcalá del Río dam. Blue regions show the periods when strain-induced periodic stratification may be important.

one box does not contribute to the outflux water mass.

Figure 4.5.d shows the relation between the residence time of each box and the flushing time. The pattern of residence time is asymmetrical, as reflected in the short and pointed crests and shallower and deeper troughs. During spring tides, the residence time of box 1 decreased. This reduction is balanced with the increasing time of box 5. Conversely, during neap tides, the residence time of box 1 increased. As can be observed, on average, the water mass took 60% longer to travel through boxes 5 and 4 (22.3 km) and the remaining 40% to travel along the rest of the estuary (35.3 km). However, for intermediate river discharges, those times are balanced since they showed approximately the same percentage per box.

4.3.4 Management strategies to unblock the estuary

Evidently, water discharge plays a key role when it is necessary to unblock the estuary. It is thus necessary to identify the relationship between blocking periods, tides, river discharges and the competing estuarine processes in terms of the potential energy change. Tidal variation of stratification caused by advection may trigger SIPS conditions (Burchard and Schuttelaars, 2012; Simpson et al., 1990), which enhance the downward water mass exchange. Accordingly, the horizontal Richardson number (Ri_x) was used to describe the rate of turbulent kinetic energy due to straining (eq. 2.2):

$$Ri_{x,i} = \frac{(\partial b_i/\partial x)d_i^2}{C_d U_i^2} \tag{4.6}$$

where $b_i = -g(\rho_i - \rho_0)/\rho_0$ is the bouyancy force of each box; ρ_0 is the freshwater reference density; and, U is the depth-averaged tidal velocity amplitude from the harmonic analysis (M_2 is the most energetic constituent at the GRE). The seawardmost boxes show $Ri_x \sim 0.1 - 0.3$, which according to Stacey et al. (2001), induce the SIPS regime and enhance gravitational circulation (table 4.1).

Secondly, the results of our study provided valuable insights into the water discharge conditions that produce the SIPS and which unblock the GRE through the estuarine parameter space (Geyer and MacCready, 2014; Valle-Levinson, 2010). An estuary with weakly stratified to well-mixed conditions was placed at the lower-right quadrant (figure 2.3). This position was perturbed with a freshwater outflow that modified the Froude freshwater number and was conducive to the SIPS

regime. At the same time, the horizontal salinity gradient was found to drastically decrease along the GRE during high water discharges. This increased the estuarine parameter and produced well-mixed conditions. Therefore, there was a band of freshwater outflux during which the GRE was under the SIPS regime and where the gravitational circulation was maximum. This favored water mass exchanges. The minimum water discharge that promoted the SIPS regime at the GRE was $\sim 25 m^3/s$. The red dots in figure 4.5.b represent the water discharge reaching this threshold.

The strategies that managers have to improve the water quality, reducing the flushing time, or stabilizing the water density near a pipe of water supply for rice fields will be treated in depth in chapter 7.

4.4 Discussion

The previous results and analysis significantly clarify the relationship between the along-estuary exchange fluxes, river discharge, tidal transport, and estuary geometry. These relations allow managers to better understand estuary dynamics and to enable them propose and implement strategies aimed at the improvement of environmental conditions at sensitive natural resources.

The model was validated with the GW2006 one-box model at Delaware estuary. The N-box model results not only agree with the one-box model but also provide more information about the spatial fluxes within the estuary. The similarity in the processes studied, even with the difference in scales of the GRE and Delaware estuaries, shows that the model may be adapted to and used in other estuaries. Each estuary can be characterized by a different box number and geometry, depending on the processes that govern it. Furthermore, other processes, such as lateral circulation (Basdurak et al., 2017) or stratification (Rice et al., 2008) can be easily added to the model though their inclusion may blur the presentation. In addition, the selecction of the boxes size is not arbitrary, the along estuarine transport-processes should be adequately known. However, a wrong selection of the number or the size of the boxes, for example, due to homogeneity of the processes, will result in boxes with similar mixing density and water mass exchange.

The limitations of our model are the usual ones that emerge whenever a simplified box model is used to represent an idealized section of the estuary (Officer, 2013). We assumed a constant box volume that may vary with increased river discharges. However, a river discharge that is two orders of magnitude greater than our conditions (Q_d = 2000 m^3/s representing 99% of the Q_d time-series), would raise the mean water level in the Bonanza tidal gauge (β_0 in Figure 2.10) only 0.85 m (Losada et al., 2017), which suggests an error of less than 12%. This effect is negligible during low or mid river-flow conditions. Furthermore, the model determines shelf density with a simple sum of sinusoidal functions that account for tidal and temperature time variations. Upstream, a constant river density of 1000 kg/m^3 was assumed. Tidal transport was computed by the harmonic analysis of currents and sea levels. Even though this might be an important source of error since values should be section-averaged, it is also true that there is no accurate data regarding the vertical and across-channel variations of velocity. Moreover, as in previous PEA box models, no information is provided about the vertical and across-channel profiles of water velocities and densities, which are specified in (Garvine and Whitney, 2006). The influence of river discharges on tidal propagation may also be disregarded (Losada et al., 2017). The sensitivity of the model to initial conditions was tested with a simple linear density variation from the mouth to the head. The model reproduced the along-estuary water mass exchange and density after two semidiurnal tides.

Under low flow conditions, the GRE was found to be mainly governed by the influence of tides. Tidal transport plays an important role mainly due to the Stokes transport and tidal pumping induced by the covariance between the current and salinity (Díez-Minguito et al., 2014). Although

the role of tidal pumping was omitted in previous studies, it may very well represent up to 100% of the along-estuary tidal-transport variability at the GRE. Even though, the linear relationship between tidal pumping and Stokes transport worked fine under low river-flow conditions, further analyses are required to study the estuary under other conditions. The sign of the tidal pumping was found to change upstream from negative to positive at ($x \sim 30$ km) whereas Stokes transport decreased due to channel convergence (Parker, 1991).

The role of water discharge was important at mid estuary. Our results showed that water mass retention triggered a negative circulation that was very sensitive to water discharge, specifically, during neap-spring transitions. In some cases, negative water mass exchanges were found. The relationship between water fluxes and residence or flushing times suggests that water experiences a time and spatial variability as it travels along the estuary with similar box properties.

The methodology proposed was found to be robust under mid-river conditions. However, the error in box density estimation tended to increase. Tidal straining was found to be significant, and the GRE may thus periodically exhibit weakly stratified conditions. Theoretically, intermediate water discharges trigger the SIPS regime and promote water exchange fluxes that reduce flushing times. A comparison with Ri_x and the estuary space parameter showed that $Q_d \sim 25\ m^3/s$ enhanced the subtidal circulation at the estuary. Weak stratification greatly reduced the vertical mixing coefficient, mainly by limiting the vertical length scale of turbulent eddies (Geyer and MacCready, 2014), which drastically reduced the residence and flushing times.

Finally, the along-channel circulation at the GRE showed an asymmetrical and inflowing-estuary pattern at the estuary mouth with peaks at mid spring tides and troughs at neap tides. This pattern softened as it shifted upstream. At the same time, its mean value decreased upstream, and was negative in (seaward) box 4 during almost all of the study period. In all likelihood, this reduction was motivated by the presence of the estuarine turbidity maxima in the surrounding.

4.5 Conclusions

This research has presented an analysis of the potential energy anomaly (PEA) and the related water mass semidiurnal fluxes during low river flows in the well-mixed Guadalquivir river estuary (SW Spain). An N-box model of the PEA based on Garvine and Whitney (2006) was formulated and applied to five neighboring stretches for a period of six months, (July 2008 to January 2009) when river inflow, $Q_d < 100\ m^3/s$. The model includes not only the effects of freshwater river flux, Stokes transport, solar radiation, and tidal and wind mixing, but also the tidal pumping term which was not considered in previous studies. It can be used to determine the water density and water mass exchanges as the solution of a linear system of equations, which represents the PEA conservation in the N interconnected stretches of the estuary.

The joint analysis of the observations and results of the model permitted the evaluation of the water mass exchanges during two different conditions of the low river discharges: Study period A (July/October 2008) with quasi-stationary water-flow around 40 m^3/s Study period B, (October 2008/January 2009), characterized by water pulses with discharges of around $\sim 100\ m^3/s$ and persistent periods of near non-water flow associated with irrigation management strategies.

Under these conditions, a minimum water discharge of $Q_d = 40\ m^3/s$ provided positive (seaward) circulation along the estuary. Spring-neap tidal cycles with water exchange fluxes varying from 170 m^3/s to 30 m^3/s were found at the estuary mouth. The water exchange was reduced to 60 m^3/s and 20 m^3/s at the ~ 25 km because of the spatial distribution of the Stokes transport and tidal pumping. Tidal pumping was found to play a key role in the water mass exchange and thus should not be disregarded. The river discharge governed the water mass exchange along the convergence

balance friction region (25 - 60 km). The differences between incoming and outgoing water mass at the boxes induced by tidal transport revealed negative (landward) semidiurnal transport values mainly at the upper section of the estuary.

The water mass exchange flow is minimum at neap-spring transitions and at the mid-estuary (critical stretches), which lead to a negative water mass exchange. In our study, these conditions are referred to as blockage. The time period that comprised the neap-spring transition was particularly prone to blockage. The water mass exchange was directly related to the residence and flushing times. Spatial flushing times were found to be proportional during neap tides. Conversely, the water takes almost 80% of the time to travel along the landward boxes during spring tides. The model revealed that the GRE residence time in normal conditions ranged from 50 to 90 days, and increased during blockage conditions more than one month.

Under the conditions during period B, the circulation was intensified under the mid river-flow conditions associated with the strain-induced periodic stratification regime. River discharges greater than 40 m^3/s enhanced subtidal circulation and generally favored water exchange throughout the estuary. Accordingly, the residence time was drastically reduced from $\sim$ 120 to less than 30 days. Conversely, persistent low river flow significantly decreased the entire capacity of the estuary to exchange freshwater, which naturally increased the residence time as it will be shown in Chapter 7.

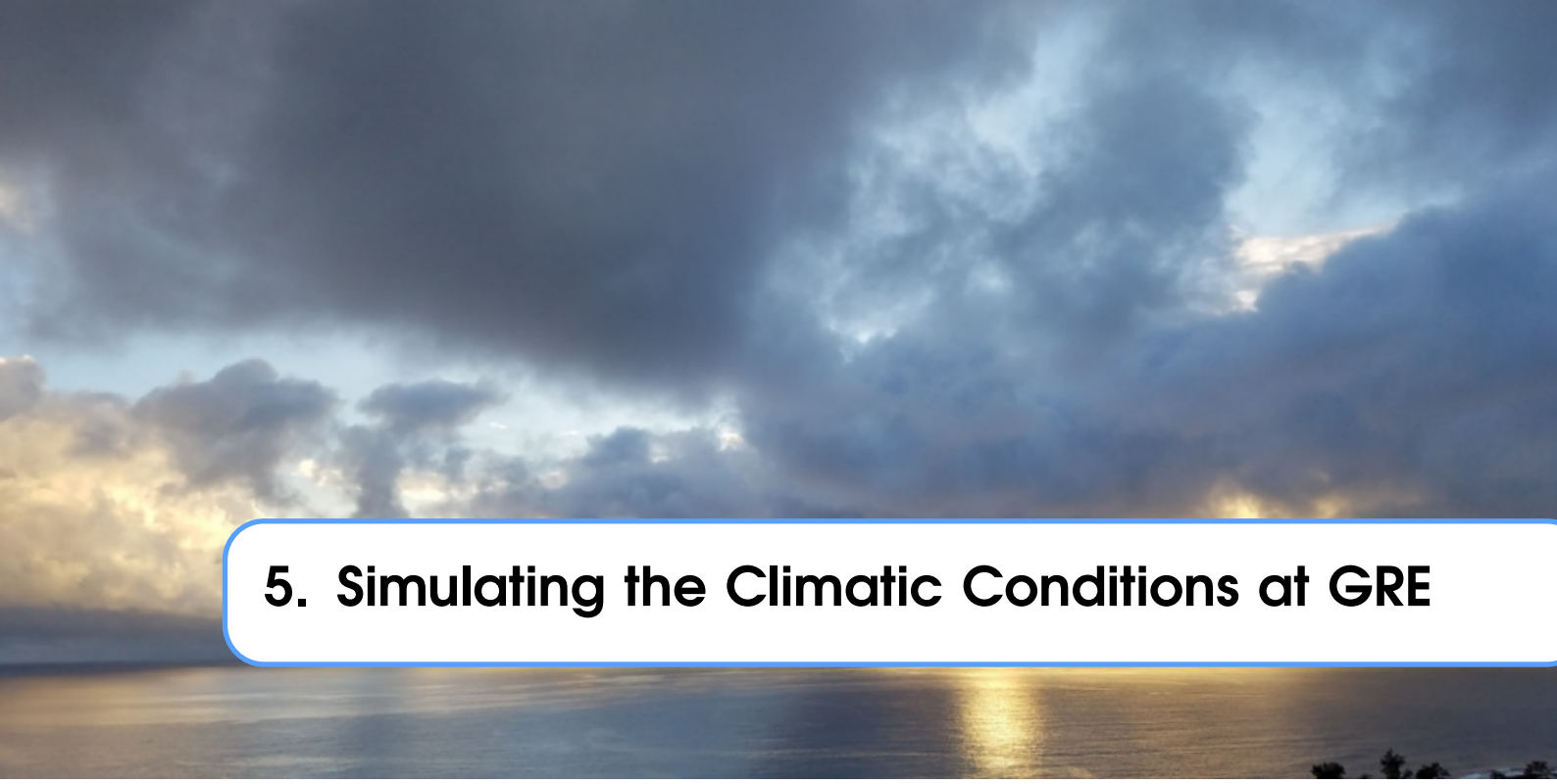

5. Simulating the Climatic Conditions at GRE

"The day before teaches the day that follows"

Píndaro, Greek Poet

For the assessment of the uncertainty related to the prediction of the effectiveness of management strategies (see chapter 7), it is necessary to simulate the variables that characterize the climatic conditions that will force the estuary. In the present chapter, several methodologies to simulate climatic conditions both, atmospheric and maritime that will affect the estuarine system are explored. Freshwater-river discharges and wind velocity are characterized by means of the joint or marginal distribution functions (§ 5.1). Tidal elevations and tidal currents, are really well reproduced through theoretical models with analytical solutions (§ 5.2). The solar radiation flux at the s and the shelf density were empirically reproduced (§ 5.3 and 5.4). The mean sea-level rise was also modeled using the GLSAR method described in § 5.5. The results are shown in § 5.6. Finally, in § 5.7 the uncertainty of the forecasted timeseries is assessed.

The methodology used to forecast time series of multivariate stochastic processes has been published in the journal Coastal Engineering (Lira-Loarca et al., 2020). An attempt to extend the model to a random field has been published in the book Contributions to Statistics (Cobos et al., 2018).

The methodology defined in this chapter was partially programmed by the author of this thesis in Python as part of the current Recommendations for Maritime Works ROM 1.1-18 (Example) (Losada, 2018).

5.1 Stochastic characterization of fresh-water discharges and wind velocity

The statistical characterization of one or several time series of random variables is a step prior to the simulation of time series that have the same statistical properties than the original ones. In

this section, the stochastic processes that are analyzed are: (i) the river discharge (Q_d), and (ii) the velocity (V_w) and direction (θ_w) of the wind. The stochastic characterization involves two steps:

1. The statistical analysis and adjustment of certain probability models for the random variables. Univariate non-stationary distributions F_{Q_d}, F_{V_w} and F_{θ_w} are fitted to the empirical distribution functions (see §5.1.1).
2. The analysis of the dependence of each variable on its values and the values of the other variables at previous times. A VAR(q) model, used to characterize the multivariate temporal dependence of $Q_d(t)$, $V_w(t)$ and $\theta_w(t)$, is presented in §5.1.2.

5.1.1 Univariate probability models

The univariate distributions of the involved random variables are estimated from the available time series. In the present thesis, it is followed the approach given by Lira-Loarca et al., 2020; Solari and Losada, 2011 where the probabilistic models are considered non-stationary by characterizing each parameter a ($a_i = \mu_i$, σ_i for $i = 1,...,n_v$) as a time-dependent function, where n_v is the number of variables, whose Fourier series expansion truncated to N_F oscillatory terms is:

$$a(t) = a_0 + \sum_{l=1}^{N_F} \left(a_l \cos(2\pi t) + b_l \sin(2\pi t)\right), \tag{5.1}$$

where a_0, a_l and b_l, $l = 1,...,N_F$ are the coefficients of the trigonometric (Fourier) expansion of parameter a. The time is, however, not explicitly included in the notation of the distributions hereinafter for the sake of simplicity.

Note that the random variables Q_d and V_w are non-negative, unbounded above, and have an asymptotic probability function showing heavy upper tails. The mean wind direction (θ_w) is bounded between 0 and 360. Unlike the previous studies, where non-stationary mixture probability density functions were used to characterize the stochastic processes, in this thesis the data was firstly transform into normal to facilitate the subsequent treatment (Jäger et al., 2019). A one-parameter (λ) Box-Cox transformation (Box and Cox, 1964) is used which reads as:

$$\zeta^* = \begin{cases} \frac{\zeta^\lambda - 1}{\lambda} & \lambda \neq 0 \\ \ln \zeta & \lambda = 0 \end{cases}, \tag{5.2}$$

where ζ is the studied variable. Other power transformations can also be applied (Yeo and Johnson, 2000). After ensuring normality, using Shapiro-Wilk, Kolmogorov-Smirnov or Lilliefors tests, a Gaussian probability model was used, which probability (f) and distribution (F) functions read as:

$$f(\zeta^*;\mu,\sigma) = \frac{1}{\sigma\sqrt{2\pi}} \int_{-\infty}^{\zeta^*} e^{-\frac{(\zeta^*-\mu)^2}{2\sigma^2}} dx, \quad \zeta^* \in \Re, \tag{5.3}$$

$$F(\zeta^*;\mu,\sigma) = \frac{1}{2}\left[1 + erf\left(\frac{\zeta^*-\mu}{\sigma\sqrt{2}}\right)\right], \quad \zeta^* \in \Re, \tag{5.4}$$

where μ and σ are the time dependent location and scale parameters. The best model performance is computed using the Bayesian Information Criterion (BIC) (Schwarz, 1978). The Bayesian Information Criterion (BIC) is used to select the order of the Fourier expansion for which the model gives the better performance. This criterion reads as:

$$BIC = \ln(n_t)k - 2\ln(\hat{L}), \tag{5.5}$$

where n_t is the length of the record; k is the number of parameters; and $\hat{L}$ is the maximum likelihood function.

5.1.2 Multivariate temporal dependence

The temporal dependence between variables is characterized by means of a stationary Vectorial AutoRegressive (VAR(q)) model which assumes a linear relationship between the variables and their past values (Lütkepohl, 2005). More than 20 models are available to characterize these relationships. Some of them are: ARMA, ARIMAX, DAR, EGARCH, GAS, Gaussian local level, among others (PyFlux for Python), however, the analysis of their applicability is out of the scope of this thesis. From the time series, $(Q_d(t),\ V_w(t),\ \theta_w(t))$, stationary normalized times series are obtained as:

$$\begin{aligned} Z_{Q_d}(t) &= N^{-1}(0,1;F_{Q_d}(Q_d(t))) \\ Z_{V_w}(t) &= N^{-1}(0,1;F_{V_w}(V_w(t))) \\ Z_{\theta_w}(t) &= N^{-1}(0,1;F_{\theta_w}(\theta_w(t))), \end{aligned} \tag{5.6}$$

where $N^{-1}(0,1;F_\zeta(\zeta(t)))$ is the inverse of the normal cumulative distribution function with null mean and standard deviation equal to 1 of the variable ζ. The VAR(q) model is applied to the stationary and normalized multivariate time series. For a detailed description of the VAR(q) model, the reader is referred to Lütkepohl, 2005.

The values of the variables at time t_i are denoted as $y_i^1 = Z_{Q_d}(t_i)$, $y_i^2 = Z_{V_w}(t_i)$, $y_i^3 = Z_{\theta_w}(t_i)$ and $Y_i = \left(y_i^1\ y_i^2\ y_i^3\right)^T$ where ^{T} stands for the vector transposition. The dependence in time and between variables in the VAR(q) model is given by:

$$Y_i = c + A^1 Y_{i-1} + A^2 Y_{i-2} + ... + A^q Y_{i-q} + e_i, \tag{5.7}$$

where $c = (c_1\, c_2\, c_3)^T$ contains the mean values of the variables, A^m, $m = 1,...,q$ are the 3×3 coefficients matrices and $e_i = \left(e_i^1\ e_i^2\ e_i^3\right)^T$ is the vector with the white noise error terms. Using equation 5.7 to relate data at an instant t_i to their previous q values, for $i = q+1,...,n_t$, it is obtained $Y = AX + E$, where $Y = (Y_{q+1}\, Y_{q+2} ... Y_{n_t})$, $X = (X_{q+1}\, X_{q+2} ... X_{n_t})$, with $X_i = (1\, Y_{i-1}^T ... Y_{i-q}^T)^T$, $A = (A^1\, A^2 ... A^q)$ and $E = (e_{q+1}\, e_{q+2} ... e_{n_t})$.

The solution is obtained by means of minimum least square error as: $\mathbf{A} = \mathbf{Y}\mathbf{X}^T(\mathbf{X}\mathbf{X}^T)^{-1}$, where; $\mathbf{E} = \mathbf{Y} - \mathbf{A}\mathbf{X}$.

5.2 Elevations and Currents along the GRE

The classical solutions for the linearized shallow-water equations are employed for tidal propagation along the GRE (Officer, 1976). This classical solution suggests the separation of elevations (η) and current (u) into two components: $\overline{\zeta}$, a tidal-averaged or subtidal-mean component, and $\tilde{\zeta}$, a tidal deviation component with respect to the mean component as follows:

$$\begin{aligned} \eta(x,t) &= \Re\{\overline{\eta} + \tilde{\eta}(x,t)\}, \\ u(x,t) &= \Re\{\overline{u} + \tilde{u}(x,t)\}. \end{aligned} \tag{5.8}$$

Following this process, exact analytical solutions for the amplitudes of tidal elevations and currents are obtained for convergent estuaries (Ippen and Harleman, 1961; Prandle and Rahman, 1980; Prandle, 1981; Savenije et al., 2008; Siles-Ajamil et al., 2019).

5.2.1 Tidal dynamics in convergent estuaries ($\tilde{\eta}$, $\tilde{u}$)

The Prandle and Rahman, 1980 analytical solution for the shallow-water wave equations in a one-dimensional convergent channel is applied. In that theory, the breadth ($b(x)$) and depth ($d(x)$) of the estuary are assumed to have the following expressions:

$$b(x) = b_L x^n, \qquad d(x) = d_L x^m, \tag{5.9}$$

where b_L and d_L are the breadth and depth at the channel mouth, x is the along channel distance from the head ($x = 0$), and m and n are the convergence parameters for breadth and depth, respectively. Prandle and Rahman (1980) rewrote the linearized equations of tidal propagation in dimensionless form assuming to rectangular and narrow channels. They used the vertical parameter d_L, the temporal parameter T to do the adimensionalization. These parameters coincided with tidal period of a given constituent, and a longitudinal parameter $\lambda_p = \sqrt{gd_L}T$, where g is the gravitational constant. The equations read:

$$\frac{\partial u}{\partial t} + \frac{\partial z}{\partial x} + su = 0, \tag{5.10}$$

$$\frac{\partial \eta}{\partial t} + \frac{1}{b}\frac{\partial}{\partial x}(bdu) = 0, \tag{5.11}$$

where $s = ST$ is the dimensional friction coefficient. (Hunt, 1964) approximated this coefficient as:

$$S = K\frac{8U}{3\pi d}, \tag{5.12}$$

where U is a representative value of current amplitude, i.e., the M_2 tidal amplitude.

They solved the eqs. 5.10 and 5.11 for two cases: (i) a free estuary, and (ii) an estuary with a wall located at $x = x_b$. Since the GRE has an upstream dam, it is used the solution with a cross-channel barrier. Assuming that the estuary is bounded upstream at $x = x_b$, $u(x_b) = 0$, and $\partial\eta/\partial x = 0$ at $y = y_b$, and inserting eq. 5.9 into eqs. 5.10 and 5.11, the solution for the water elevation ($\tilde{\eta}$) and velocity ($\tilde{u}$) reads:

$$\tilde{\eta} = A_0 \left(\frac{ky_x}{ky_0}\right)^{1-\nu} \frac{Y_{\nu-1}(ky_x)J_\nu(ky_b) - J_{\nu-1}(ky_x)Y_\nu(ky_b)}{Y_{\nu-1}(ky_0)J_\nu(ky_b) - J_{\nu-1}(ky_0)Y_\nu(ky_b)} e^{i(2\pi t+\vartheta_0)} \tag{5.13}$$

$$\tilde{u} = \frac{-iA_0 x^{-m/2}}{k} \left(\frac{ky_x}{ky_0}\right)^{1-\nu} \frac{J_\nu(ky_x)Y_\nu(ky_b) - J_\nu(ky_b)Y_\nu(ky_x)}{J_\nu(ky_b)Y_{\nu-1}(ky_0) - J_{\nu-1}(ky_0)Y_\nu(ky_b)} e^{i(2\pi t+\vartheta_0)} \tag{5.14}$$

where J_ν and Y_ν denote the Bessel function of the first and second kind and order ν, A_0 and ϑ_0 are, respectively, the amplitude and phase of the tidal constituent, and

$$\nu = \frac{n+1}{2-m}, \tag{5.15}$$

$$y_x = \frac{4\pi}{2-m} x^{(1-m/2)}, \tag{5.16}$$

$$k = \left(1 - \frac{is}{2\pi}\right)^{(1/2)}, \tag{5.17}$$

with i the imaginary unit.

5.2.2 Subtidal elevations and currents ($\overline{\eta}$, $\overline{u}$)

The subtidal-mean elevation and current greatly depend on tidal range and river discharges (Godin, 1983). Reyes Merlo (2016) broadly discuss about regression models in order to predict $\overline{\eta}$ and $\overline{u}$ at the GRE. For low river discharges, elevations and currents can be predicted as a linear superposition of the tidal and fluvial contributions. For high river discharges, tidal elevations and currents contains a substantial amount of variability associated with non-stationary processes which predictability is related. Following the suggestions made by Reyes Merlo (2016), (i) the locally tidal range will be taken into account in order to improve the goodness of fit of tidal elevations, (ii) it is preferably to use a simple model where isolated effects can be physically interpreted.

Therefore, it is assumed a constant box volume that may vary with increased river discharges. A river discharge that is two orders of magnitude greater than the low river-flow conditions (Q_d = 2000 m^3/s representing 99% of the Q_d time-series), would raise the mean water level in the Bonanza tidal gauge (β_0 in Figure 2.10) only 0.85 m (Losada et al., 2017), which suggests an error of less than 12%. This effect is negligible during low or mid river-flow conditions. Therefore, it is assumed $\overline{\eta} = 0$ and $\overline{u} = -Q_d/A_j$ where j are the location of the different sections along the GRE.

5.3 Solar radiation flux

The surface solar radiation flux, $Q_s(t)$, which controls the daily cycle of the main surface buoyancy source, is modeled as (Díez-Minguito and Swart, 2020):

$$Q_s(t) \begin{cases} (1-a_l)S\sin\Psi & \text{during daytime} \\ 0 & \text{during nighttime} \end{cases}, \tag{5.18}$$

where a_l is the albedo and S = 1368 Wm^2 is the solar constant. The local elevation angle of the Sun is Ψ, which is defined at a location with geographic coordinates (longitude(lon), latitude(lat)) as:

$$\sin(\Psi) = \sin(lat)\sin(\delta_s) - \cos(lat)\cos(\delta_s)\cos(2\pi t - lon), \tag{5.19}$$

with $\delta_s = \Phi_r \cos(2\pi(t-173)/365)$ given as t in days for a non-leap year and $\Phi_r = 23.45\ ^o$ is the axial tilt of the Earth's axis relative to the ecliptic. This formulation estimates seasonal and daily variations in net incoming radiation, including daytime seasonal variation.

5.4 Shelf density

The density at the shelf is an input of the box model. Several complex models have the challenge of reproduce the observations in oceanography. In this section is modeled using a harmonic analysis with the significant frequencies obtained from a power spectral density analysis.

The power spectral density $S(f)$ was compared to a pink signal of the same variability (dashed black line).

$$S > \frac{var(\rho)}{N}\frac{\chi(0.95, dof)/dof}{\Delta f \cdot f}, \tag{5.20}$$

where N is the number of data points, χ is the chi-square function; dof is the number of degrees of freedom; f is the frequency and Δf is the frequential resolution;. The points that overcame the pink signal correspond to significant frequencies

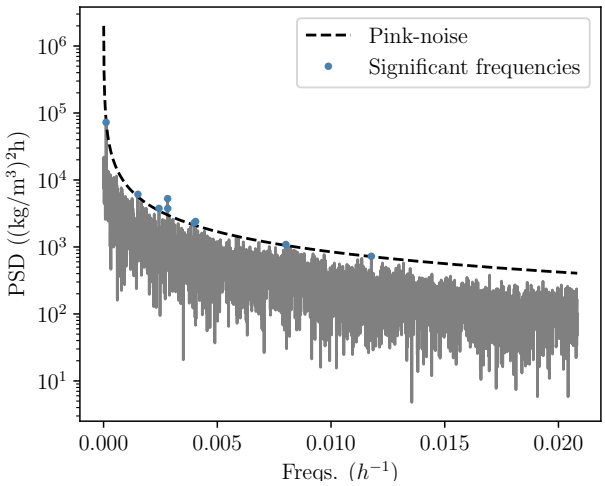

Figure 5.1: Power Spectral Density (PSD) of density timeseries at the Guadalquivir continental shelf. Dots stand for significant frequencies.

The shelf density is modeled as:

$$\rho(t) = \overline{\rho} + \left(\sum_{i=0}^{N_{sf}} a_i \sin(2\pi f_i t) + b_i \cos(2\pi f t) \right), \tag{5.21}$$

where a_0 and b_0 are fitting parameters; and f_i is the i significant frequency (table 5.1) and N_{sf} the number of significant frequencies.

Frequency	Period	a_0	b_0
0.00011407	Annual	2.408e-01	2.769e-01
0.00150954	Monthly	-2.042e-03	-1.635e-02
0.00243556	∼17d	2.917e-03	-5.410e-03
0.00281612	fornightly	1.010e-02	-1.240e-03
0.00282034	fornightly	2.482e-02	-3.377e-03
0.00397893	∼10d	4.130e-03	-3.996e-04
0.00404658	∼10d	-2.001e-03-	-3.253e-03
0.00801705	∼5d	-1.514e-04	-1.805e-03
0.01177187	∼3.5d	-4.465e-04	6.298e-05

Table 5.1: Fitting parameters for shelf density.

Table 5.1 shows the fitting parameters.

5.5 Mean Sea-level Rise due to Climate Change

In this thesis is used the Generalized Least Squares method with an Auto-Regressive (GLSAR) with a covariance structure approach (Barbosa et al., 2008; Becker et al., 2014; Marcos et al., 2016) to assess the linear trend of sea level rise from the monthly-averaged sea level time series. The GLSAR is described by $\mathbf{Y} = \mathbf{X}\beta + \varepsilon$, with $\varepsilon \sim N(0, \Sigma)$. Here $\mathbf{Y}$ is the elevation matrix; $\mathbf{X} = [1t]$; and β is the vector of parameters (slope and residual). A first order autoregressive process is employed in the specification of covariance matrix (Σ) and the maximization of log-likelihood, using the

Akaike information criterion, supports the estimation of the linear coefficients and error covariance (Sakamoto et al., 1986). Other configurations such as second or third order autoregressive process were tested and support the results obtained.

5.6 Results

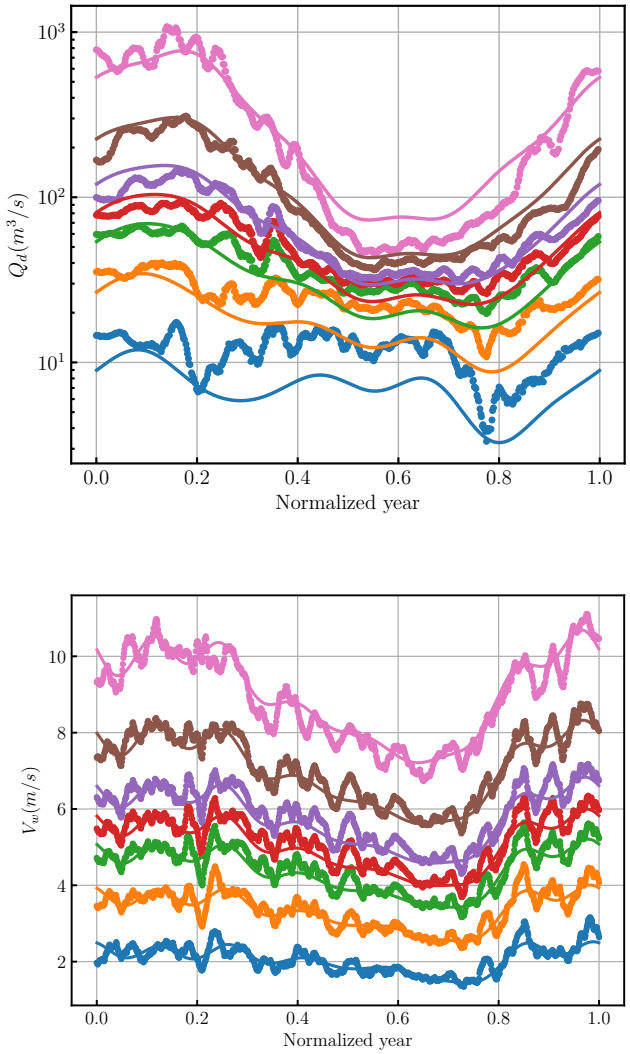

Figure 5.2: Iso-probability percentiles (10, 25, 40, 50, 60, 75, 90^{th}) of the empirical and fitted non-stationary distributions for Q_d and V_w.

5.6.1 Statistical Analysis of the Water Discharges and the Wind Field

First of all, eq. 5.2 is used to normalize river discharges, Q_w, and wind intensity, V_w. The corresponding parameters λ of the Box-Cox transformation are shown in table 5.2.

Variable	Q_d	V_w
λ	0.0760	0.5993

Table 5.2: Parameter of the Box-Cox transformations for the variables

The wind direction, θ_w was not normalized because it shows a bimodal distribution corresponding to the two mean directions and a simple normalization cannot be applied.

Once the water discharge and wind velocity data are normalized, a non-stationary Gaussian model is fitted to the data. Wind direction data is modeled with two non-stationary Gaussian probability models. The parameters of the models are computed up to the eighth Fourier order in the case of Q_d and V_w and to the fourth order for θ_w (see Table...). As example, figure 5.3 shows the BIC obtained for water discharge assessed with two to eight orders (the first mode is out below the window). As it can be observed in Figure 5.3, the fifth Fourier order presents the best fit. The number of parameters at this order and the BIC are equal to $4 * N_F + 2 = 22$ and -124236.7, respectively.

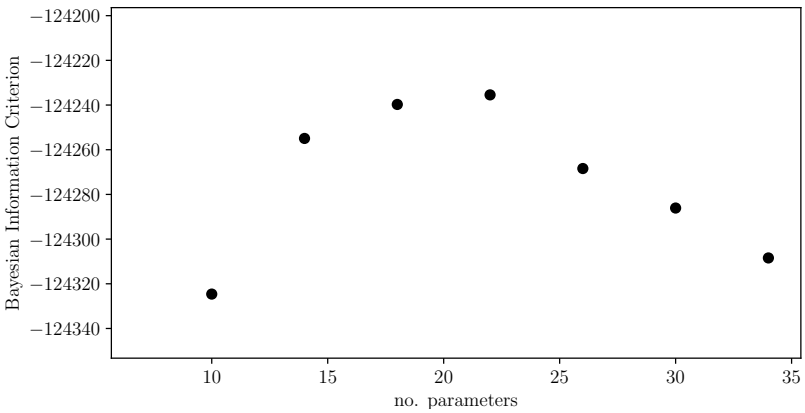

Figure 5.3: Bayesian Information Criterion for Q_d. From the left to the right are shown $N_F = 2$ (10 parameters) to $N_F = 8$ (34 parameters). The maximum BIC is found at $N_F = 5$ (22 parameters).

Figure 5.2 shows the iso-probability percentiles of the model and observed data. The y-axis is logarithmic for Q_d. In the case of the observed data, a moving window of 14 days length is used to compute the percentiles. The size of the window is large enough to create a sample of the computed percentiles. As it is observed in the upper panel, the non-stationary probability model adequately reproduces the non-stationary behavior during winter, spring and fall. However, it overestimates the maxima of water discharges that reach the 90-percentile and underestimated the minima. The mean water discharges are also well-reproduced. In the case of the wind velocity, the model reproduces fairly well the observations along the seasons.

In Table 5.3 are listed all the parameters of the best fit for Q_d and V_w.

Figure 5.4 shows the iso-probability percentiles of the model and observed data for wind direction. As it is observed, the non-stationary model of two Gaussian probability models reproduce surprisingly well the intra-annual variability of the observations. In table 5.4 are shown the fitting parameters.

To apply the VAR model, the period of time where the three variables are available was selected. Small gaps in time series were linearly interpolated and the sample frequency of the water discharge

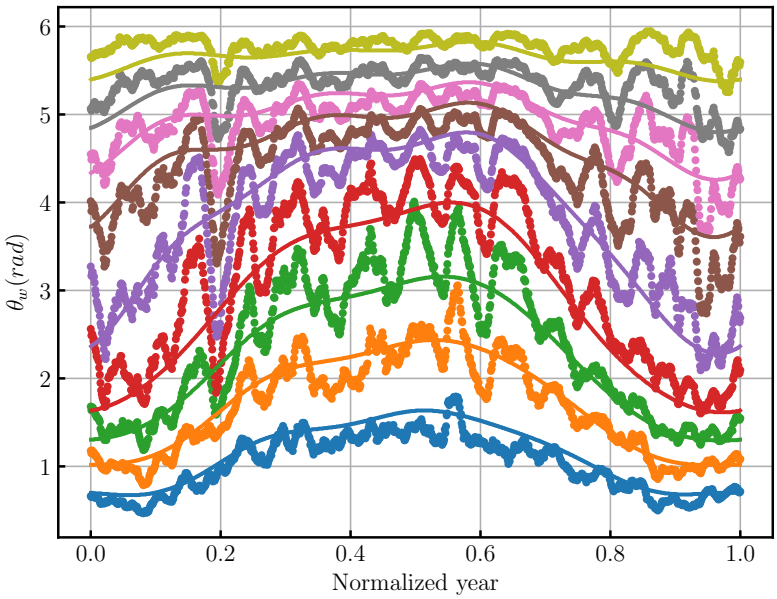

Figure 5.4: Iso-probability percentiles (10, 20, 30, 40, 50, 60, 70, 80, 90^{th}) of the empirical and fitted non-stationary distributions for θ_w.

was adapted to the sample frequency of the wind data also by interpolation. The time series used in the analysis begin in 1996-08-27 18:00:00 and end at 2016-04-27 00:00:00 with a three hours cadency. Finally, the time series of Q_d, V_w and θ_w were normalized using equation 5.6. The VAR model (eq. 5.7) was applied for several q until order 20, and the BIC is also applied to define the best model. The matrix parameters and covariance are obtained.

5.6.2 Simulation of Water Discharge and Wind Field

The simulation process begins with the multivariate simulation of q time steps of the variables Q_d, V_w and θ_w. The covariance matrix obtained from the VAR model is used in the Gaussian multivariate model with location parameter equal to zero. Later, the VAR(q) model with the previous time steps

	μ_{Q_d}		σ_{Q_d}		μ_{V_w}		σ_{V_w}	
N_F	a_l	b_l	a_l	b_l	a_l	b_l	a_l	b_l
0	4.3986		1.8165		2.7200		1.4321	
1	0.6713	0.7534	0.4983	0.3807	0.3512	0.2496	0.1256	0.0605
2	0.0951	0.1777	-0.1475	-0.0767	0.0530	-0.1188	-0.1825	-0.0211
3	0.0626	0.0287	-0.0429	-0.0489	-0.0688	-0.0906	-0.0212	0.00015
4	-0.0448	-0.0553	0.0233	0.0275	-0.01872	0.0096	0.01598	-0.01484
5	0.0310	0.02187	0.06005	-0.02157	0.0178	0.0306	-0.00276	-0.0201
6					-0.00507	-0.0369	-0.01199	-0.0075
7					0.0506	-0.08171	-0.02188	-0.0228
8					0.0273	-0.0201	-0.00643	-0.00642

Table 5.3: Parameters of non-stationary fit for Q_d and V_w. The models are Gaussian. a_l and b_l are the coefficients of the Fourier expansion as shown in §5.1.1.

	$\mu_{\theta_w,1}$		$\sigma_{\theta_w,1}$		$\mu_{\theta_w,2}$		$\sigma_{\theta_w,2}$	
N_F	a_l	b_l	a_l	b_l	a_l	b_l	a_l	b_l
0	1.9389		1.1020		5.15159		0.7045	
1	-0.8296	0.08617	-0.43717	0.0646	-0.2829	0.06061	0.2845	-0.0626
2	-0.0351	0.0475	-0.0609	0.0715	-0.0590	0.09127	0.06867	-0.07119
3	0.03649	-0.0590	0.0085	-0.0230	-0.050027	0.01868	0.00656	-0.04009
4	0.03406	0.0063	-0.0378	0.00916	-0.0700	0.0399	0.02139	-0.02761

Table 5.4: Parameters of non-stationary fit for θ_w. The models are Gaussian. a_l and b_l are the coefficients of the Fourier expansion as shown in §5.1.1. Sub-indexes refer to first and second Gaussian model. Values refer to radians.

is used to simulate the full normalized time series.

Figure 5.5 shows the time series of the variables involved. These time series describing Q_d, V_w, and θ_w are obtained after the application of the corresponding inverse cumulative distribution functions for each variable (§ 5.1.1) and the inverse of the Box-Cox model (table 5.2) to Q_d and V_w.

5.6.3 Tidal Water Levels and Currents

Knowing the characteristics of the channel width at the mouth ($B_0 = 795.15$ m) and at the barrier ($B_b = 180$ m), which are separated by a distance of $x_d = 110000/\lambda$, and using eq. 5.9, the parameter n is obtained as follow:

$$n = \frac{\ln(B_0) - \ln(B_b)}{\ln(x_d)} = 1.287. \tag{5.22}$$

This value is similar to other estuaries such as Potomac and St. Lawrence (Prandle and Rahman, 1980). Assuming that the depth is almost constant along the estuary (Díez-Minguito et al., 2012), an estuarine shape parameter equal to $\nu = 1.14$ is obtained. Finally, the friction coefficient, r, is obtained by minimizing the RMSE between the values of the theoretical model (eq. 5.13) and those obtained from the harmonic analysis (tables 1-7, Díez-Minguito et al. (2012)). The optimization is computed for one hundred-time intervals from $t = 0$ to $t = T_{M_2}$.

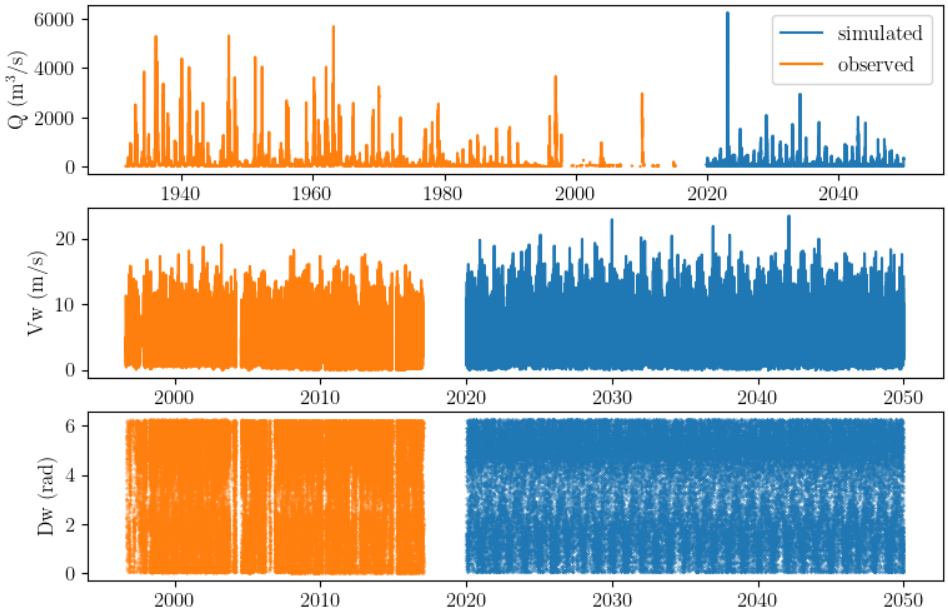

Figure 5.5: Data recorded (orange) and simulated (blue) of Q_d (upper panel), V_w (mid panel), and θ_w (lower panel). The simulations start at January 1st 2020 and cover a 30 years length period.

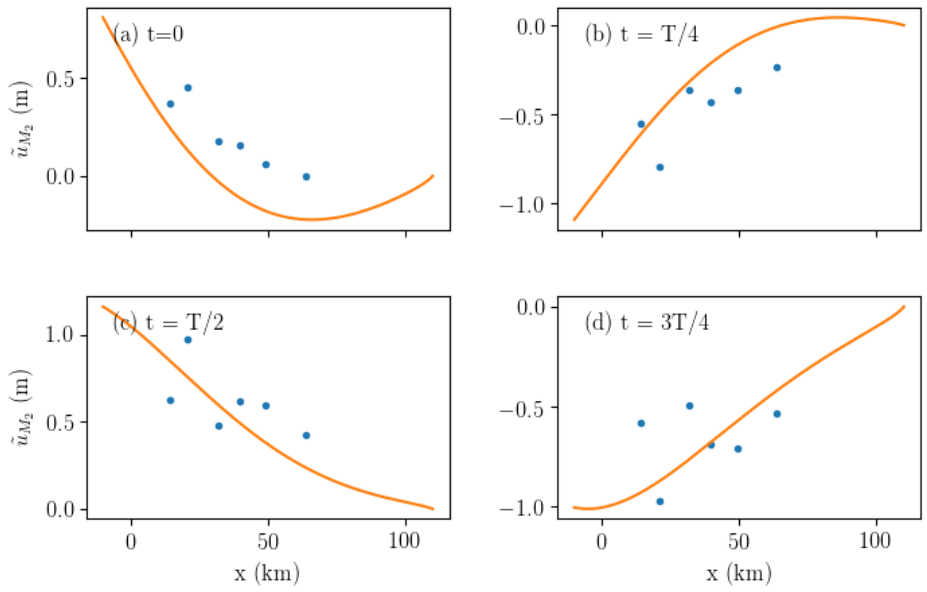

Figure 5.7: Along estuary tidal current due to M_2 at several time steps: *(a)* t = 0 s, *(b)* t = T/4 s, *(c)* t = T/2 s, and *(d)* t= 3T/4 s. Continuous orange line shows the theoretical tidal currents from eq. 5.14. Blue dots represent the observations.

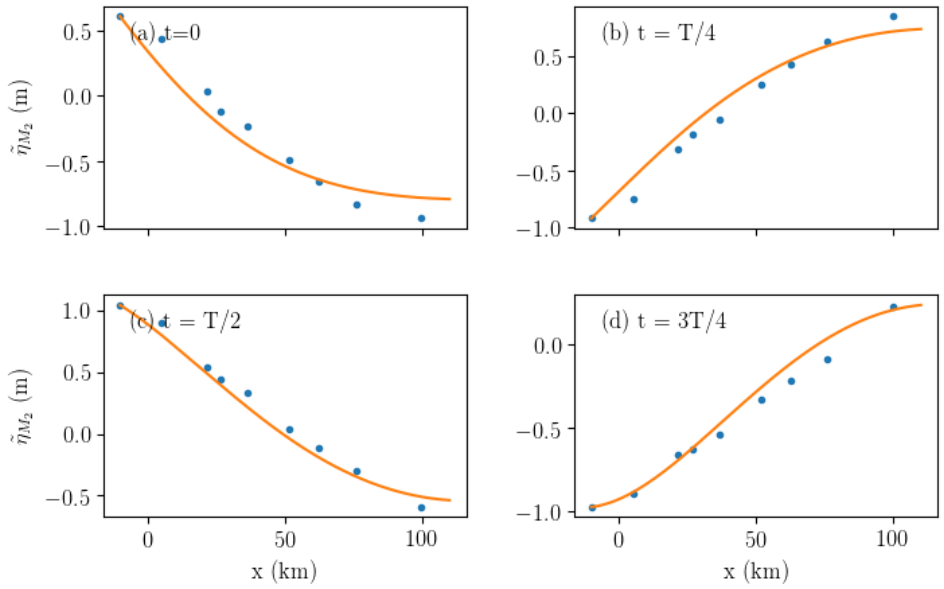

Figure 5.6: Along estuary tidal elevations due to M_2 at several time steps: *(a)* t = 0 s, *(b)* t = T/4 s, *(c)* t = T/2 s, and *(d)* t = 3T/4 s. Continuous orange line shows the theoretical tidal elevation from eq. 5.13. Blue dots represent the observations.

Figure 5.6 shows the results. Near the first third of the estuary, the largest differences are found at $t = 0$ while near the barrier ($x = 110$ km) the tidal elevation is underestimated at all times. However, in general, the tidal elevations are really well-reproduced with the errors smaller than 10 % (RMSE equals to 0.0783).

Using eq. 5.14, the along estuary tidal currents are obtained (figure 5.7). In this case, larger differences are found between observations and modeled. This is due to the use of a simplified channel that does not take into account the effects of the variability of the cross sections nor the presence of meanders. Nonetheless, their longitudinal behavior is adequately reproduced.

The friction parameter s is approximated with eq. 5.17 considering $K = 0.003$, a characteristic $U = 1.0$ m/s, and $d = 7.09$ m. The friction parameter $s = 16.35$ is appropriately chosen since the phases (φ) of previous figures are well-reproduced.

This methodology was applied to the major harmonics at the GRE, namely, M_2, S_2, N_2, O_1, K_1, M_4 and M_{SF}. The amplitude and phase of tidal harmonics is time-dependent as shown in chapter 5. The amplitude and phase at the mouth was computed following that methodology.

5.6.4 Surface Solar Radiation Flux

In Figure 5.8 the surface solar radiation flux at the estuary is presented. A simple sinusoidal with a lower bound at zero with increasing amplitude and duration in summer is observed. As it is noted, cloudiness is neglected.

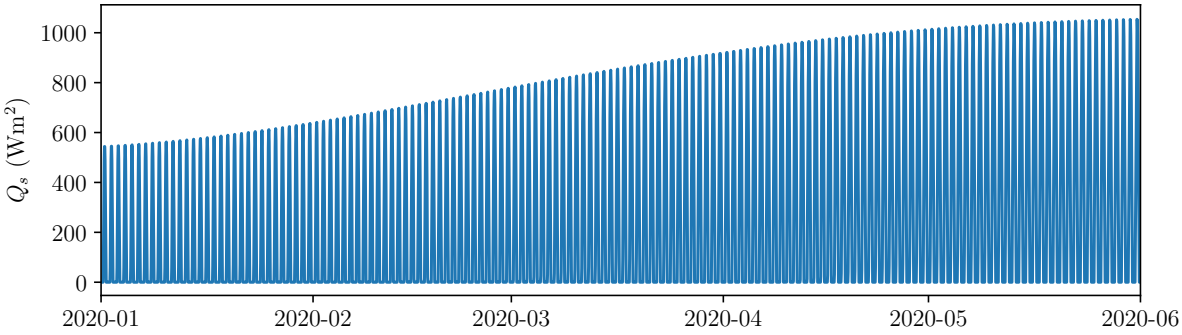

Figure 5.8: Time series of surface solar radiation flux

5.6.5 Shelf density

Using the amplitudes and frequencies of Table 5.1 and equation 5.21, the shelf density is modeled for low river-flow conditions. The root mean square error of the fit is 0.24036.

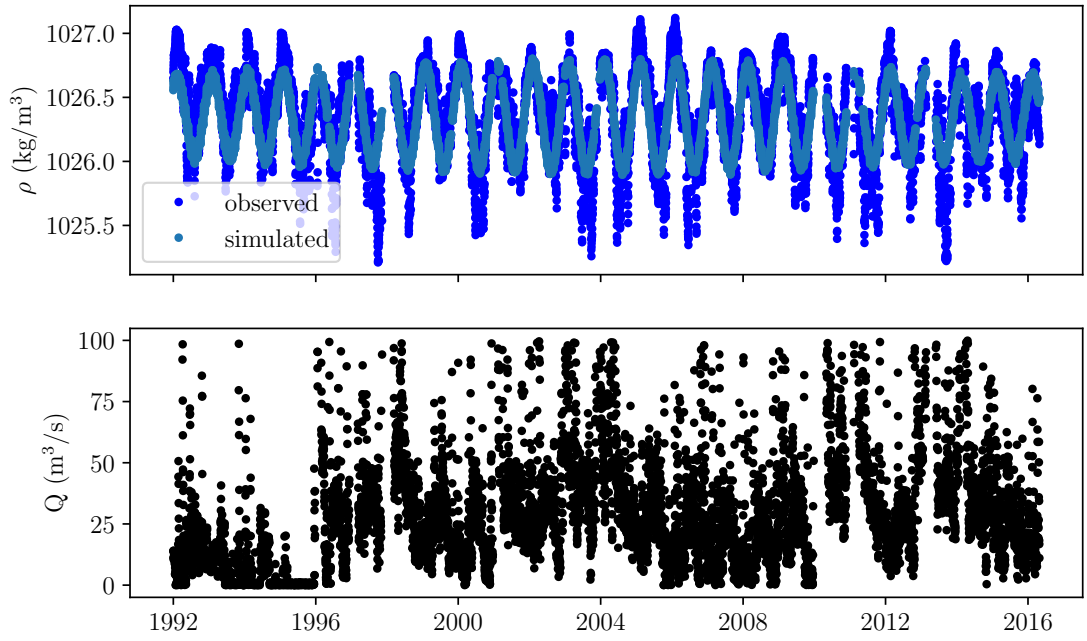

Figure 5.9: Shelf density measured near the mouth of the Guadalquivir River Estuary and modeled with eq. 5.21 under low river-flow conditions. Lower panel shows the water discharge at the Alcalá del Río dam during the same period for the low river-flow regimen.

As it is observed in Figure 5.9, the density variability is adequately reproduced.

5.6.6 Mean sea-level rise

Estimates of relative sea level trends are also obtained with the procedure above-described. The values obtained are compared with those from Marcos et al., 2005; Tsimplis et al., 2011. The procedure is validated by comparing estimated trends in mean sea level with trends found in the literature (e.g., Jevrejeva et al., 2012; Marcos et al., 2011; Meehl et al., 2007; Zhang et al., 2017). The results are object of the next chapter where the Spanish stations are treated and sea-level trends and harmonics will explain in-deep. Here, it is explained just for Bonanza station. Bonanza tidal gauge In the Gulf of Cádiz shows the highest increase for the Iberian Peninsula (10.529 mm/yr) (Marcos et al., 2005). Barbosa et al., 2008; Lennartz and Bunde, 2009 obtained an estimate of a minimum anthropogenic sea level trend of 1 mm/yr (Church et al., 2013; Becker et al., 2014; and, Marcos et al., 2016, among others).

Front	station	Marcos *et al.* (2005)	Tsimplis *et al.* (2011)	This study
Cantabric	Santander	2.12±0.09	1.91±0.27	1.98±0.06
Atlantic	Coruña	2.51±0.09	1.54±0.27	1.32±0.06
Atlantic	Vigo	2.91±0.09	2.04±0.31	2.67±0.06
Atlantic	Cádiz	-	4.05±0.30	3.39±0.06
S.of Gibraltar	Tarifa	-	-1.21±0.23	0.37±0.02
S.of Gibraltar	Algeciras	-	0.05±0.23	0.26±0.03
S.of Gibraltar	Ceuta	-	0.46±0.21	0.50±0.02

Table 5.5: Estimates of relative sea level trends by Marcos et al., 2005, Tsimplis et al., 2011, and those determined at the locations indicated.

5.7 Discussion

The discussion of this chapter is focused on the reliability of the simulations because they will be used to forecast and propose new management measures. This discussion will be done, therefore, in terms of the autocorrelation, as a measure of the temporal dependency, the seasonality or higher temporal variabilities of the forecasted data, on the cross-correlation between variables and the frequency of extreme events.

5.7.1 Seasonality of climatic descriptors

Figures 5.2 and 5.4 show how the statistical model reproduced the intra-annual variability of the observations. Only this modulation was considered because it is the most important in amplitude.

Figure 5.10 presents the Q-Q plots of the analyzed variables. As it is observed in panels, the time-dependent data is classified by months where the non-stationary probability models are assumed to be stationary. The time period of this classification depends on the Fourier order used in the analysis. In this case, the maximum order was eight which means that the probability model can capture from semiannual variabilities up until a few weeks. Nonetheless, it is enough to compute the Q-Q plot by monthly windows. As it is observed, good fits between the empirical distribution functions and the selected probability models are obtained. For Q_d a larger variability is observed in the tails than for V_w and θ_w.

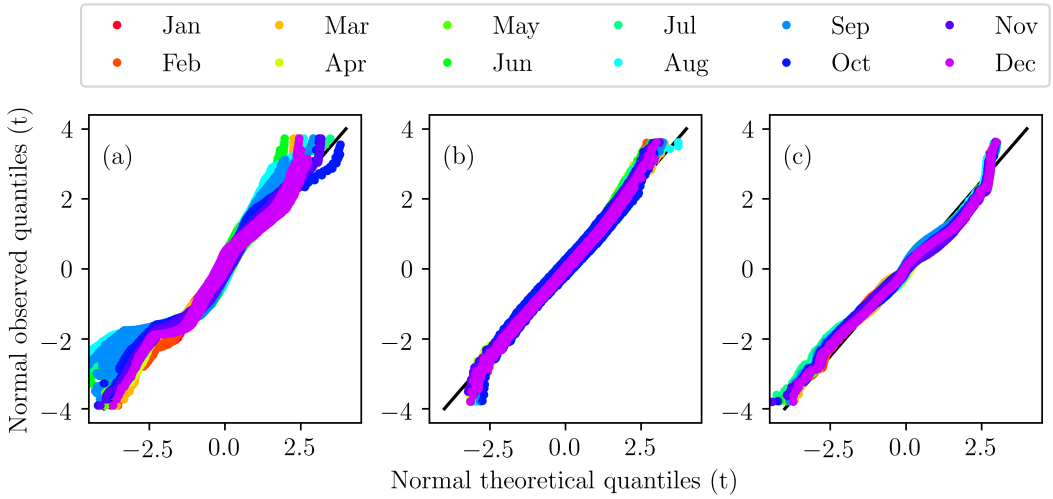

Figure 5.10: Q-Q plots of Q_d, V_w and θ_w. The Q-Q plots for the non-stationary distributions were computed monthly assuming stationarity. (a) Q_d; (b) V_w; and (c) θ_w.

5.7.2 Correlation and cross-correlation

A simple way to assess the temporal dependence of a time-series is computing their Auto-Correlation Function (ACF) defined as the correlation of a time-series with a delayed copy of itself as a function of the time-lag. If there is not dependency on time of the values of the series, such autocorrelations should be close to zero for all time-lag separations. Otherwise at some time lags the values of the ACF will be significantly non-zero (Natrella et al., 2003).

Figure 5.11 shows the autocorrelation plot of the observed and simulated time series involved. As it is noted, the data shows a positive strong autocorrelation. The autocorrelation is larger (slightly less than one) in both series at the first lag and the values are similar. Then, slowly decreases in time. It is observed that ACF of Q_d decreases linearly with time-lag while V_w and θ_w decreases exponentially until 0.8 where the ACF is horizontal. This effect is due to the interpolating re-sampling which increases the frequency from daily water discharge to 3 hours. Anyway, the results provided a high predictability. As it is observed, the simulation adequately reproduced the temporal dependence observed in all cases, better for Q_d and V_w.

Figure 5.12 shows the bivariate density functions of the pairs of observed and simulated data. As it was highlighted before, the ACF presented the same variability in observational and simulation timeseries, so, it was expected a good correspondence between the values of the variables of the joint distribution functions. As it is observed in that figure, the simulation maintains the bivariate relationship between variables. The bimodal behavior of the wind direction is surprisingly well reproduced, and the correspondence between Q_d and V_w is achieved as well. A small difference is just observed between wind velocity and direction (lower panel) next to first main direction (1.5 radians).

5.7.3 Frequency of extreme events

In order to assess that the statistics of the peaks or extreme values are well reproduced, an extreme characterization of the predominant variable (Q_d) is done. In this example, the study of annual

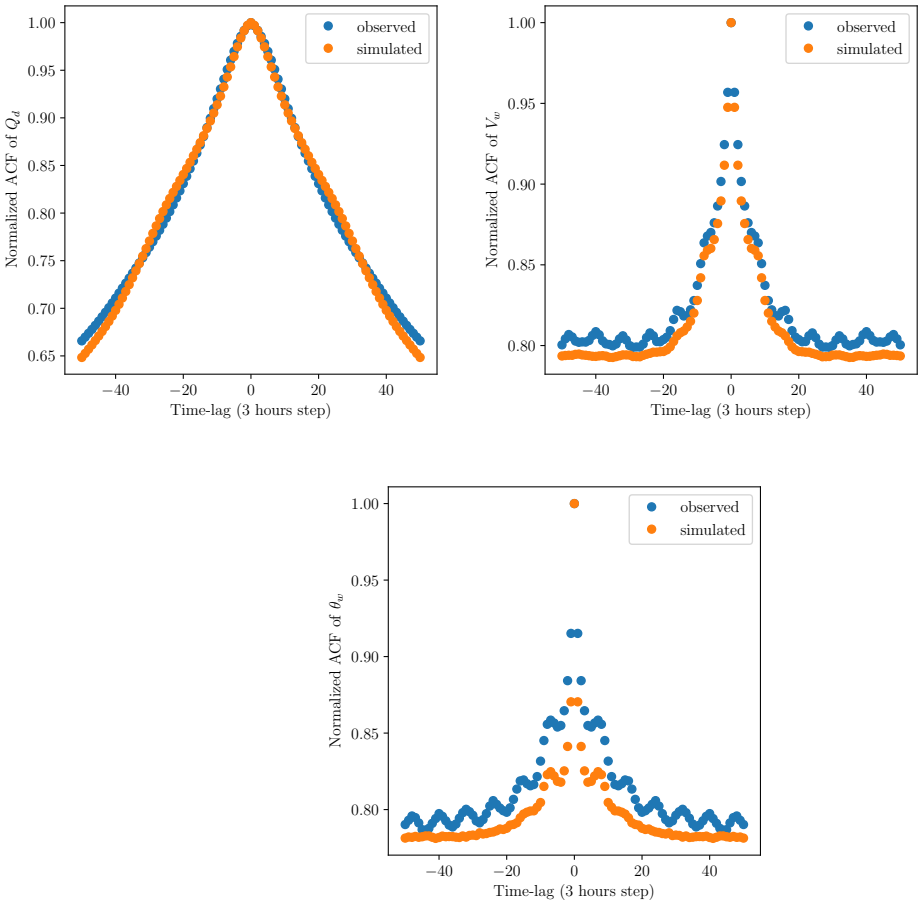

Figure 5.11: Normalized ACF of observed and simulated Q_d, V_w and θ_w. Every time step showed in the x-axis represents three hours.

maxima is developed between observed and simulated water discharges. A Generalized Extreme Value and Gumbel probability models are fitted to the peaks.

As it is observed in Figure 5.13, it is difficult to depict differences between the analysis of observed and simulated data. Scale, shape and location parameters of the Generalized Extreme Value function beside as the histogram of observations and forecasting data, are fairly well reproduced. Even the Gumbel distributions show larger scale and location parameters in both cases. The return period and maximum water discharge are kept in the simulation.

Nevertheless, when the focus is the characterization of the entire upper tail of any variable, a similar methodology to previous applied should be required (Lira-Loarca et al., 2020). In that case, the distribution should be split in several parts attending to the segmentation of data, in a similar way than in the description done for θ_w. That methodology defines theoretically a threshold for the main variable and computes the conditional and mixed probability functions. Since, in the present thesis is fundamentally required the observations (and simulations) during low river-flow conditions, the simple extreme analysis was used to validate the tail of the simulations.

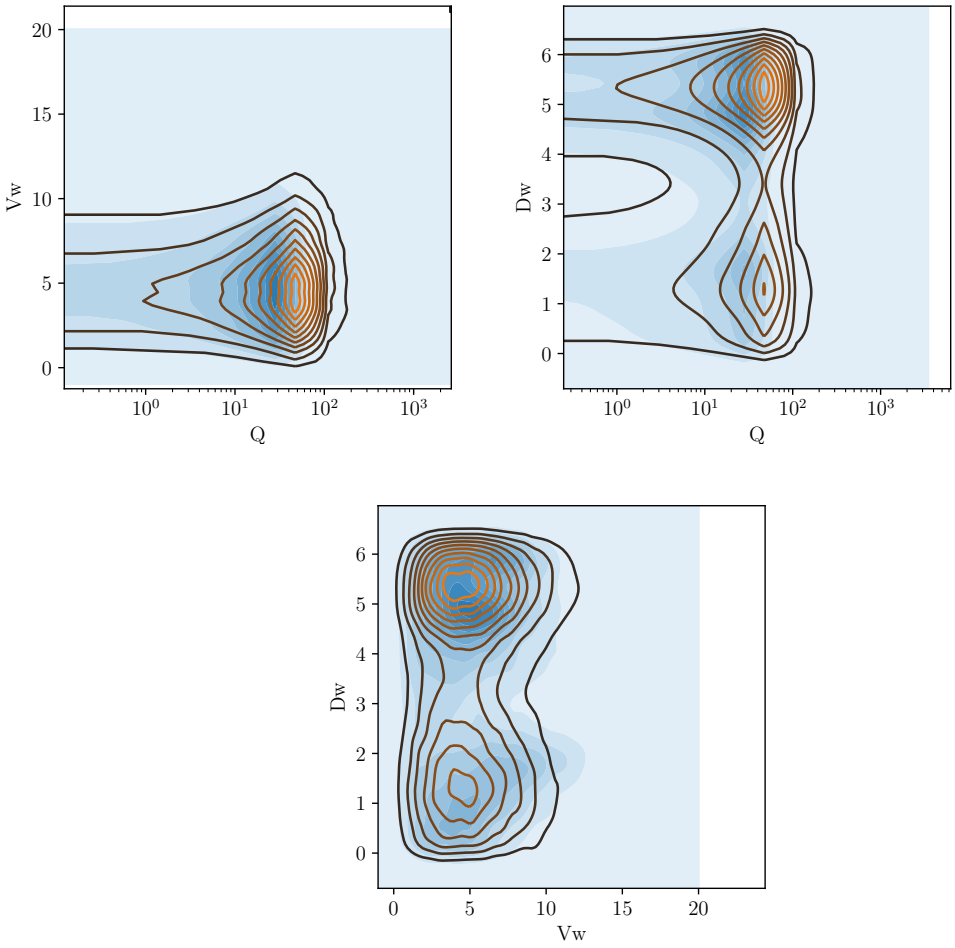

Figure 5.12: Bivariate empirical probability distributions for the pairs Q_d-V_w, Q_d-θ_w and V_w-θ_w. The blues stand for the mass probability of observations while black lines stand for the simulations. Note that the x-axis of upper panels is logarithmic.

5.8 Conclusions

The water river discharge and the wind field are stochastically characterized and their simulation adequately reproduces the intra-annual variability. The set of probability model adequately fit the non-stationarity of timeseries. The seasonality of water discharge and wind field retrieved the observations. Tails or extreme data is also well reproduced using just the a short-time scale temporal dependency. The high correspondence of correlations and cross-correlations between observed and simulated data points out that model adequately reproduced the time dependence of the data. Bivariate dependencies are also well reproduced using the VAR model.

Water currents and sea elevations are modeled theoretically by means of analytical formulas. Water elevations and currents were found to be consistent with observations. The Guadalquivir River Estuary shows a elevated friction as pointed out the calibrated frition factor. Those conditions were found in few estuaries along the World. The surface solar radiation is modeled with an empirical approach. The fit is agreement.

The present methodology provides a full characterization of the climatic records in the Guadalquivir River estuary. The forecasted datasets provide the boundary conditions required for

the definition of several management scenarios designed to improve the ecological state of the transitional water masses.

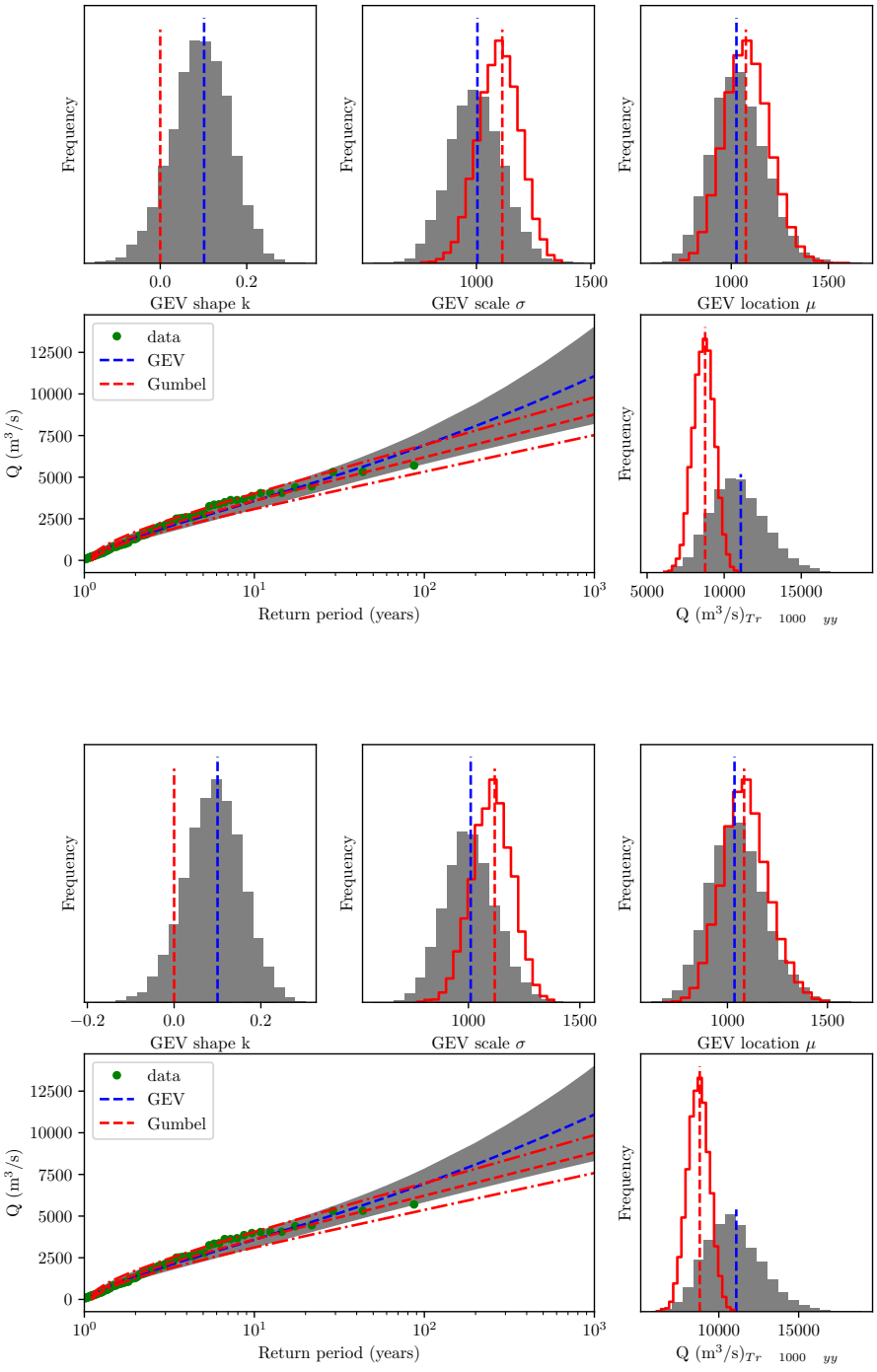

Figure 5.13: Annual maxima analysis of observed data (upper panels) and simulated data (lower panels). The histogram is computed using the fitting models and simulating new 10000 values. In every simulation, shape, scale and location parameters were computed.

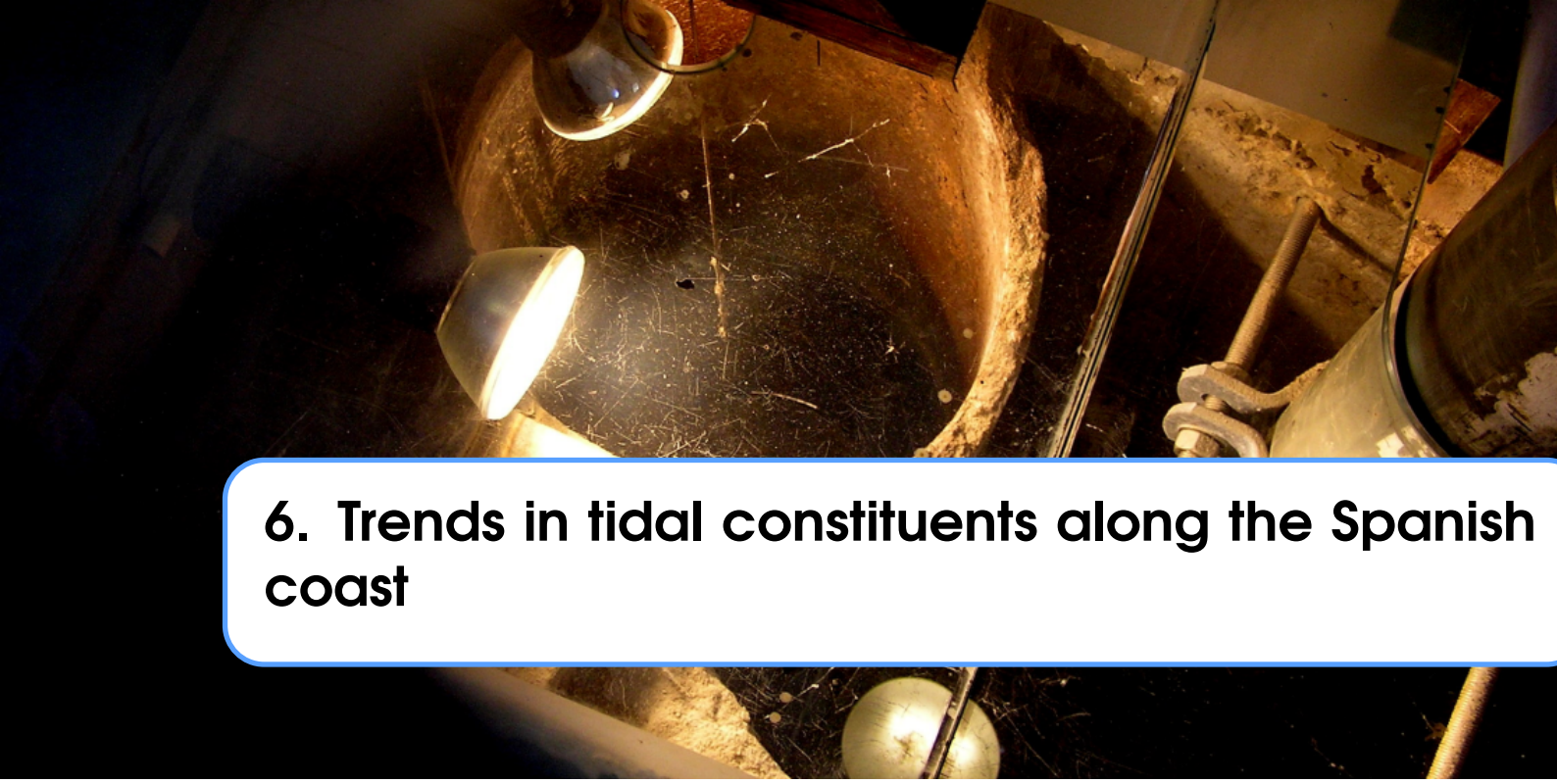

6. Trends in tidal constituents along the Spanish coast

"The sea is an ancient language that I can no longer decipher"

Jorge Luis Borges

In previous chapters was highlighted the important role that play the tides in the hydrodynamics of an estuary. This key role is greater during low river flow conditions, becoming to govern the estuarine dynamics.

The present chapter analyzes the changes of tidal constituents along the Spanish coasts, which exhibit prevailing tidal regimes that range from semidiurnal to mainly diurnal (§ 6.1). The purpose is not only the estimation of the trends of the major tidal constant but the seeking of physical interpretations to these observed changes. The analysis is based on the short-time harmonic analysis to extract M_2, S_2, N_2, K_1, O_1, and M_4 (§ 6.2). Hourly sea level records between 18 to 27 years long are analyzed at 15 stations (§ 2.3). The generalized linear squared fit method is applied to estimate the rates of change of the tidal amplitudes and phases. The values obtained are compared with those from the recent literature as a validation test for the procedure. Results of local trends in tidal amplitudes and phases are presented in section 6.3. Significance of trends in time-series of tidal amplitude and phase were detected using two complementary tests. Plausible processes responsible for the observed trends in tidal constants are discussed in Section 6.4, with a particular view on a region of freshwater influence, such as that of the Guadalquivir estuary, that mix its waters with those of the Atlantic Ocean. The Guadalquivir estuary is particularly convenient to analyze climatic trends in tidal constants since tidal gauges are maintained at the mouth and near the head, thereby allowing to discuss the influence of shallow water processes on tidal trends, and because it is experienced a notably freshwater reduction (60% in recent decades and near of 49% for the end of the century, § 1.3). In section 6.5, the results are discussed, and, finally, Section 6.6 concludes this chapter by summarizing the main findings.

6.1 Introduction

Tides are fluctuations of the sea level of precise astronomical frequencies or constituents associated with the gravitational pull of Sun and Moon. At any coastal location, each tidal constituent has a particular amplitude and phase (tidal constants) (Dronkers, 2005). In most world's oceans and seas semidiurnal periods predominate, being the most energetic constituents the M_2, S_2, and N_2. The superposition of M_2 (12.42 h) and S_2 (12.06 h) generates the fortnightly, spring-neap modulation of water level amplitudes ($\sim$14 days), whereas the effects of the ellipticity of the Earth-Moon system are dumped into the N_2 constituent (12.65 h). The diurnal periods K_1 and O_1 (23.93h and 25.81h, respectively), which account for the effect of the Moon's declination, produce a diurnal inequality in water level records. In regions with prevailing diurnal regimes, these constituents exhibit the largest amplitudes. Other short-period tidal constituents are not generated directly from the tidal generating potential. Shallow-water constituents (e.g., M_4, with period 6.21h) are subharmonics generated by non-linear interactions of primary constituents as they propagate (e.g., M_4 as the M_2 mutual interaction). These constituents are typically much smaller that the primary constituents, but they significantly contribute to the intra-tidal asymmetry and residual sediment transport (Parker, 1991). Long period astronomical motions of the Moon-Earth-Sun System also affect tidal records (Pugh, 1996). Nodal and apsidal lunar precession originate remarkable 18.6 yr and 8.85 yr cycles, but also declinational and perigean effects coming in and out of phase in cycles 4.4 yr (Ray and Merrifield, 2019). Annual 1 yr, SS, and semiannual 0.5 yr, SSA modulations of tidal amplitudes are caused by stratification and/or frictional effects and it may also be important regionally (e.g., Gräwe et al., 2014; Müller et al., 2014).

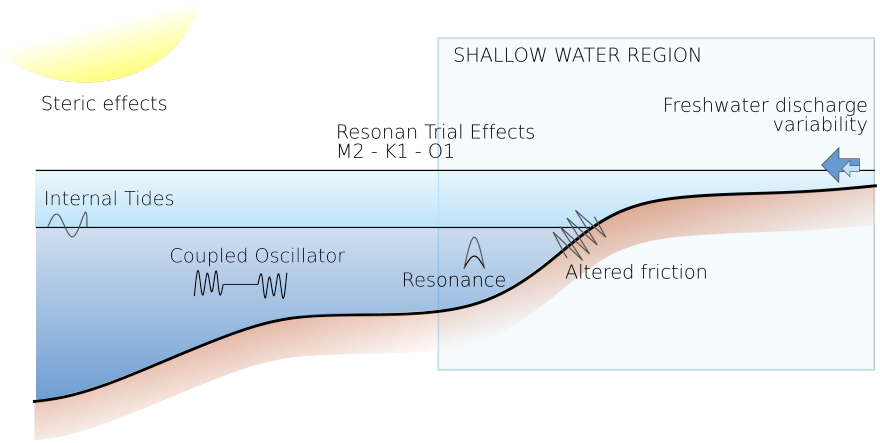

Figure 6.1: Some processes that induces local changes in tidal constants. Adapted from Devlin et al., 2017.

However, in figure 6.1 are depicted other non-astronomical processes that yield local and regional changes in tidal constants (Talke and Jay, 2019, for a wide review), from intratidal to secular scales (Devlin et al., 2017), mainly because of the local modification of the propagation and dissipation rates of the tidal wave (Osafune et al., 2014; Ray, 2009; Tsimplis and Josey, 2001). Changes in relative sea level rise influence long-term variability of ocean tides (Mawdsley et al., 2015; Schindelegger et al., 2018). Increasing water depth may also modify resonance conditions in marginal seas and estuaries (e.g., Church and White, 2011; Holleman and Stacey, 2014). Tidal amplitudes and phases depend on the water column structure that is controlled by the competition

between mixing and stratification (Munk et al., 2002; Munk and Bills, 2007). Solar radiation causes seasonal (Gräwe et al., 2014; Müller, 2012) and even daily stratification of the water column that modulate tidal constants (Godin, 1986). Variations in turbulent mixing from different sources, typically wind and tides themselves, also modulates the observed tidal constants (e.g., Antonov et al., 2002; Burchard et al., 2013; Church et al., 2010; Merrifield, 2011; Müller, 2012. River discharges, as a source of buoyancy, is another important contributor to the variability of both tides in regions of freshwater influence (Souza and Simpson, 1996). The straining of the salinity (density) field by tides, which typically occur in estuaries, also induces variations in the stratification and thus in the tide propagation (Burchard and Hetland, 2010; Simpson et al., 1990). Morphological changes (Araújo and Pugh, 2008) and non-linear interactions between the tide and non-tidal sea level variations (Cartwright and Edden, 1973) are other processes related with changing tides.

The relevance of studying the variability in tidal constants has been stressed by a number of authors regarding flood risk assessment in the current global change context (e.g., Barbosa et al., 2008; Hill, 2016). Nevertheless, despite notable exceptions, systematic analysis of trends in tides have received much less attention than the study of mean sea level trends. Positive time trends in semidiurnal amplitudes along the Pacific coast (Jay, 2009) and Atlantic coast of North America (Talke et al., 2018; Woodworth, 2010) were observed. In the eastern part of the North Sea, positive trends are observed, whereas locations at the western coasts of Europe shows a reduction of the M_2 amplitude in recent decades (Woodworth, 2010). Consistent negative trends of the M_2 phase are found at most locations along Europe (Shaw and Tsimplis, 2010). Most amplitudes of tidal trends are positive around Australia and negative at the north of Japan. Largely negative trends at phase lag are evidenced (Woodworth, 2010). In the Iberian Peninsula, small negative trends in semidiurnal tidal amplitudes are observed at Algeciras; an increase of the M_2 amplitude is estimated at Coruña (Woodworth, 2010).

This chapter represents a new effort to evaluate the spatial and temporal variability of tidal constituents along the Spanish coast. Interestingly, this region shows different prevailing tidal regimes, which vary from semidiurnal at the Atlantic coast to diurnal at some locations at the Mediterranean coast. Mixed tides are observed at the Alboran and Balearic seas. Trends (in mm/yr) of local amplitudes and phases of the main semidiurnal (M_2, S_2, N_2), diurnal (K_1, O_1), and quarti-diurnal (M_4) constituents are estimated from 15 statistically significant sea level records. In addition, first insights of reasons that motivate the changes on astronomical tides are given.

6.2 Data and Analysis Procedure

The procedure adopted here aims for estimating temporal variability and trends of tidal constants. Firstly, the selection of time-series from 15 available stations; after that, the determination of tidal amplitudes and phases by means of a short-time harmonic analysis (STHA); it is followed the estimation of trends in tidal constants by a generalized least square method; and, it is tested the statistical significance of trends by the ADF and KPSS tests. Details are given in the following subsections.

6.2.1 Data source

The sea level time-series are selected from CMEMS (The Copernicus Marine and Environment Monitoring Service) and Puertos del Estado (PdE) stations. The time-series were selected according to the following two criteria: time-series are longer of a nodal cycle (18.61 years). From the all available 40 stations located along Spain, only 15 the period length criteria. In order to extend the analysis at Balear coast, one exception was considered at Ibiza station. This station has 16

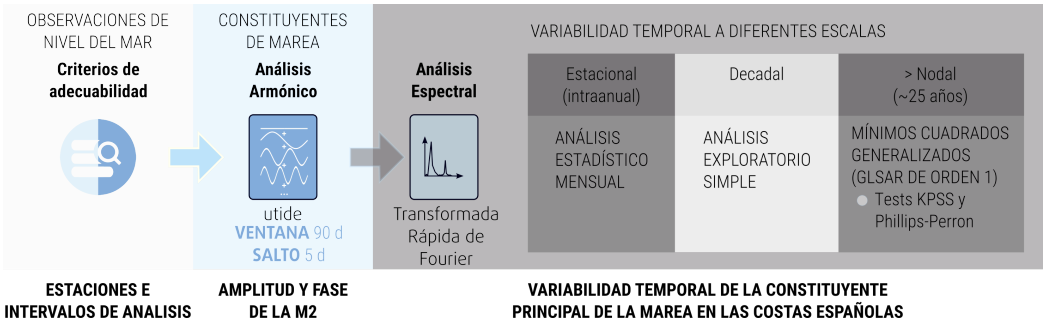

Figure 6.2: Sketch of the methodology.

year-long time-series because it began the measurements in 2003. Hourly raw data from 15 tidal gauges records operated by PdE are therefore considered in this study (figure 6.3). Time-series of PdE show averaged durations of ∼24.6 yr, 2.64% and 1.16 days of gaps. Table 6.1 shows overall information for every station.

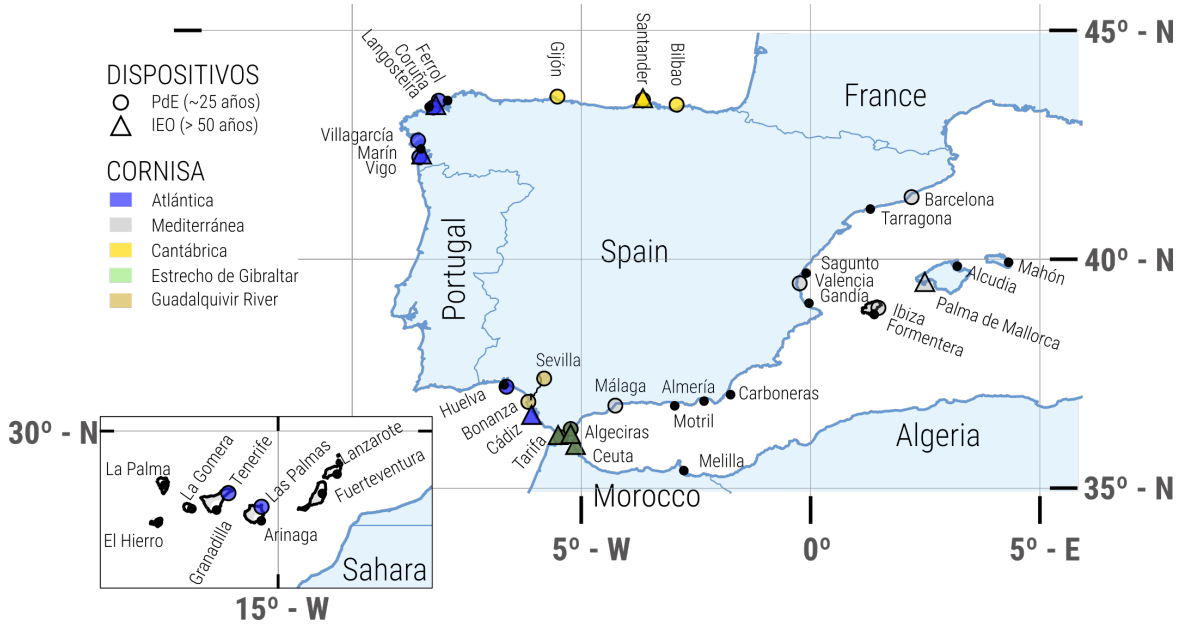

Figure 6.3: Study area and location of tide gauges. The circles indicate the positions of the tide gauges of Puertos del Estado. Locations mark with black points have a lower sample period than the nodal cycle.

Name	Front	Location			Sampling	Record length	Gaps			
		lon (º)	lat (º)	character	(min)	(years)	%	no.	Max. (days)	Med. (days)
Bilbao	Cantabric	-3.05	43.35	Ria	1	27	0.67	36	9.96	1.15
Santander	Cantabric	-3.79	43.46	Ria	1	27	0.49	23	12.92	1.33
Gijón	Cantabric	-5.7	43.56	Ria	1	24	5.28	53	256.4	1.54
Coruña	Atlantic	-8.39	43.36	Ria	1	27	3.15	42	192.92	1.52
Villagarcía	Atlantic	-8.77	42.6	Ria	1	22	1.92	41	23.96	1.25
Vigo	Atlantic	-8.73	42.24	Ria	1	27	1.91	41	56.08	1.29
Huelva	Atlantic	-6.83	37.13	Ria	1	23	0.92	32	23.88	1.15
Bonanza	Estuary mouth	-6.34	36.8	Coastal plain estuary	1	27	2.76	68	83.79	1.46
Seville	Estuary head (near)	-6	37.33	-	5	16	8.31	434	101.75	0.17
Málaga	Alboran	-4.42	36.71	Port	1	27	1.33	46	38.83	0.94
Valencia	Mediterranean	-0.31	39.44	Port	1	27	2.22	421	31.33	0.08
Barcelona	Mediterranean	2.17	41.34	Port	1	26	2.42	55	103.08	1.08
Ibiza	Balear	1.45	38.91	Port	1	16	1.50	36	25.2	0.875
Las Palmas	Atlantic	-15.41	28.14	Port	1	27	3.83	56	118.54	1.71
Tenerife	Atlantic	-16.24	28.48	Port	1	27	3.04	53	92.79	1.88

Table 6.1: Tide gauge information at each station. Information about where the station is located, sampling period, record length, and missing data or gaps is shown. The % of gaps, number of missing data, maximum and median gap length of the original time-series are indicated.

6.2.2 Extraction of Tidal Amplitudes and Phases

The short-time harmonic analysis (STHA) is applied to obtain amplitudes (A_i) and phases (φ_i) of the M_2, N_2, S_2, K_1, O_1 and M_4 constituents (Codiga, 2011). A moving window of 90 days length and 5 days shift is applied. The chosen window and shift optimize the STHA because of: (i) the window width is long enough to separate the tidal harmonics of interest; and, (ii) at the same time, provides larger number of samples than longer windows for the forthcoming statistical analysis and for analyzing seasonality. Several window widths up to one year and shifts up to one year were tested and no significant differences in trends were found.

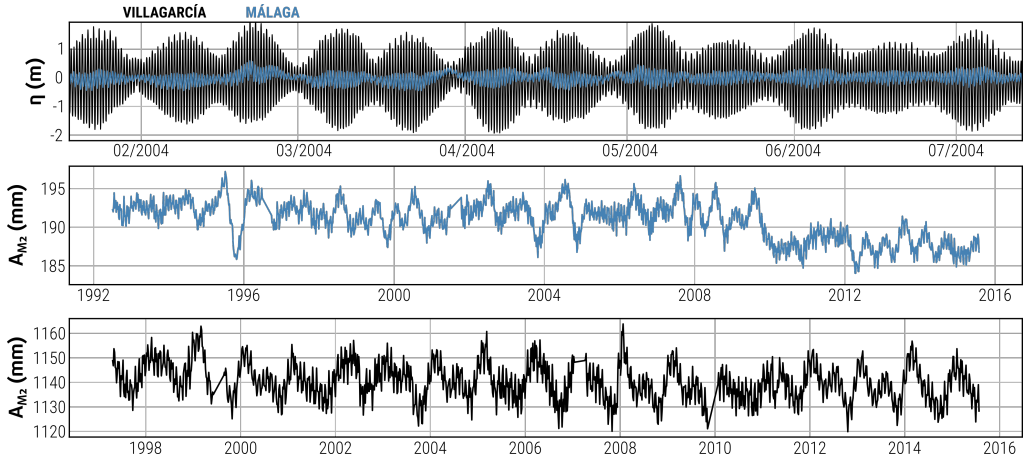

Figure 6.4: Sea-level and STHA results at some stations. *(a)* Sea-level at Málaga and Villagarcía; *(b)* M_2 tidal amplitude obtained from the STHA at Málaga; *(c)* M_2 tidal amplitude obtained from the STHA at Villagarcía.

Figure 6.4 shows, as example, the sea level at Málaga and Gijón stations and the M_2 amplitude obtained from STHA.

6.2.3 Temporal variability of Tidal Constants

The analysis of temporal variability consists of two parts: (i) the detection of patterns or cycles of main variability, and (ii) the analysis of the amplitude changes in those cycles.

For the first part, a spectral analysis of the amplitude series has been performed. From the spectral analysis it is determined the significant frequencies. These are identified because of they exceed the energy of a red noise signal in its same spectral band (the confidence interval selected is 95%) (Torrence and Compo, 1998). It was detected biweekly, monthly, semiannual and annual period oscillations.

In the second part, the intra-annual analysis must be separated from the long-term analysis. In the former case, it has been done a statistical analysis of the series of amplitudes per month, calculating the mean and standard deviation. In the latter case, a temporal linear regression of the variable of interest is performed. The long-term variability of sea-level records is done by using the Generalized Least Squares method with an Auto-Regressive (GLSAR) covariance structure approach (Barbosa et al., 2008; Becker et al., 2014; Marcos et al., 2016), which was described in chapter 5. Here $\mathbf{Y}$ is the amplitude or phase matrix of the harmonic component; $\mathbf{X} = [1t]$; and β is the vector of parameters (slope and residual).

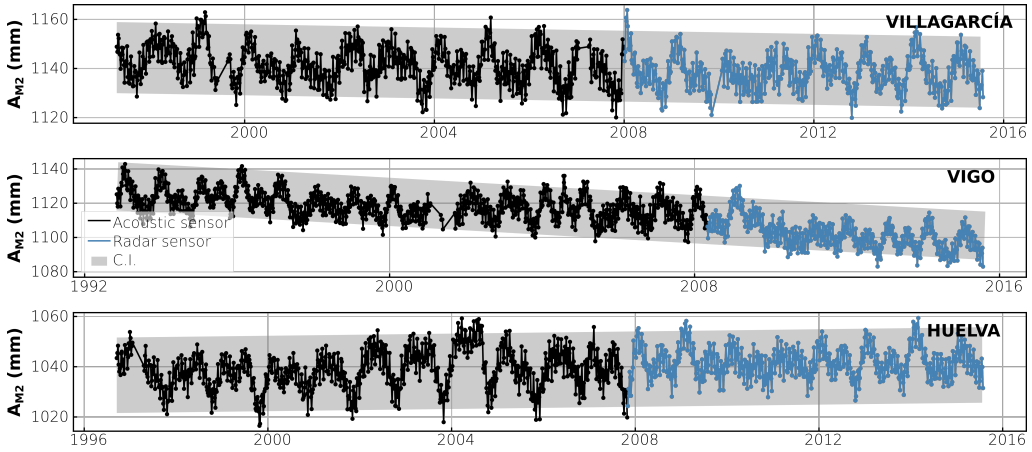

Figure 6.5: Trends and confidence intervals (filled regions) at *(a)* Villagarcía, *(b)* Vigo, and, *(c)* Huelva stations.

As a consequence of the change in tidal measurement technology all around the Spanish coast (from acoustic to radar technology), the trends were obtained for windows of several lengths. We computed the trend with a 10 yr window length, and repeated the process again increasing 1 yr the window length till the record length (table 6.1). The trends obtained with the record length for amplitude at Bonanza and Seville stations are -2.88 mm/yr [-3.00, -2.76] and 15.65 mm/yr [14.67, 16.64], respectively. In brackets are given the uncertainty intervals with 95% of confidence level.

6.2.4 Test of statistical significance of trends

Significance of trends in time-series of tidal amplitude and phase were assessed using two complementary tests: the Augmented Dickey-Fuller (ADF) and KPSS test (Dickey and Fuller, 1979; Kwiatkowski et al., 1992). These parametric statistical tests allow for discriminating between deterministic and non-stationary trends in time-series. Non-rejection of the unit root null hypothesis in the ADF test and rejection of the null hypothesis in the KPSS points to a unit root process. So, a deterministic trend is found when the ADF test rejects the unit root hypothesis and the KPSS test does not reject the null hypothesis. Every time the trend is computed, both tests were computed.

6.3 Results

First of all, the methodology presented was applied to the sea level rise. Tsimplis et al., 2011 estimates a rate of increase of 5 mm/yr at the Mediterranean coast of the Iberian Peninsula. The rates reported are approximate 2 mm/yr at the North Atlantic and Cantabric coast (Marcos et al., 2005) and negative (-4 mm/yr) at Huelva and (-1 mm/yr) at Tarifa. These values, however are rather uncertain (Tsimplis et al., 2011). Earlier analysis estimates a Spanish sea level rise 2.12 - 2.91 mm/y (Marcos et al., 2005). The Intergovernmental Panel on Climate Change's (IPCC) projected to horizon 2100 and increase of 0.28 - 0.98 m. For most of the stations, the confidence bands of the trends overlap indicating that the agreement is fair. Differences are still lower if atmospheric and steric components are included in previous authors results. Some PdE time-series did not fulfill the record length requirement of one nodal period ($<$ 18.69 yr) on that date. In all stations, fewer sloping trends were obtained (results not shown).

6.3.1 Variability of Local Tidal Amplitudes and Phases

Time-series of tidal amplitudes and tidal phases for the M_2, N_2, S_2, O_1, K_1 and M_4 constituents at all stations are plotted as a parametric dispersion diagram in figure 6.6. Variations along the Spanish coast are expected since amplitudes and phases are related to the relative position of the amphidromic point (Pugh, 1996), among others.

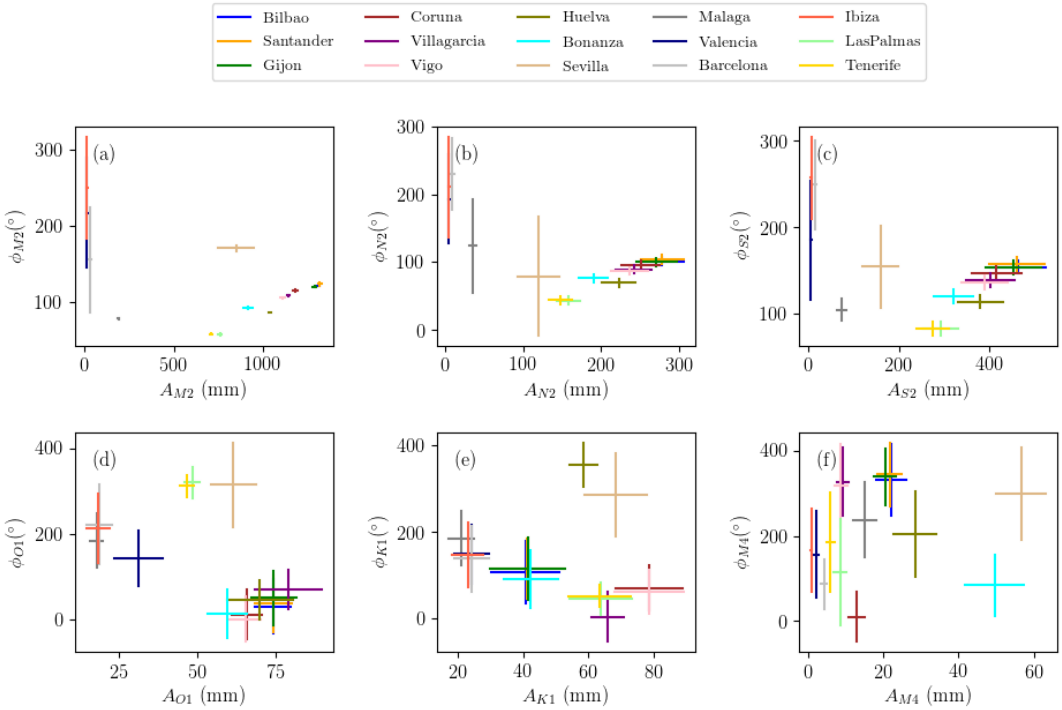

Figure 6.6: Phase-Amplitude dispersion diagram for the M_2, N_2, S_2, O_1, K_1 and M_4 harmonic constituents at all stations. Solid lines show the 95%-confidence intervals of amplitudes and phases.

Regarding the M_2 (figure 6.6.a), the lowest phase is found at Las Palmas and Tenerife stations, at the Canary Islands. A slight increase in phase and amplitude is observed at the coastal stations in the Gulf of Cadiz (Huelva, Bonanza). Phases are almost the same at those locations, which

means that the tidal wave presents an almost normal incidence at that shelf, i.e., no longitudinal propagation mode. Larger phase lags are observed at stations in estuaries, most notably Sevilla. This behavior is consistent with the propagation of a Kelvin tidal wave from South to North associated with the main amphidromic point of the central North Atlantic. The M_2 tide crosses the Strait of Gibraltar and propagates through the Alboran Sea, which partially co-oscillates with the Atlantic Ocean, increasing the phase lag and significantly reducing its amplitude (Malaga). The stations of the Eastern coast (Valencia, Barcelona) are in a prevailing diurnal region thereby showing very low semidiurnal amplitudes. This region does not co-oscillate with the Atlantic and tidal constants are the result of a movement generated directly by the tidal generating potential. The S_2 and N_2 constituents (figure 6.6.b and .c)show a similar behavior but with greater errors in amplitudes and phases (Fanjul et al., 1998).

Regarding the diurnal constituents O_1 and K_1 (figure 6.6.d and e), the phase differences between the Mediterranean sea and the Atlantic stations are again clearly observed. The smallest amplitudes, as expected, correspond with the stations located in the Mediterranean, although they are comparable or even greater than their corresponding semidiurnal constituents. This is coherent with a tidal prevailing regime that ranges from mixed (Barcelona) to mainly diurnal (Valencia) along the Balearic Sea. Regarding the over tide M_4 (figure 6.6.f), it is worthy to mention that Seville and Bonanza stations, near the head and the mouth of the Guadalquivir river estuary, shows higher M_4 amplitudes compared with other stations. Stations located in or in the vicinity of estuaries or estuaries show relatively large M_4 values, such as Huelva, Santander, Bilbao, Bonanza, and Sevilla. Although, the STHA does not explicitly distinguish locally generated M_4 amplitudes from those propagated into estuaries from the shelf, Díez-Minguito et al., 2012 suggests that the M_4 amplitudes in the Guadalquivir river estuary are mostly generated inside the estuary by the effects described by the non-linear terms in the governing equations (Devlin et al., 2017; Dronkers, 2005; Talke and Jay, 2019).

6.3.2 Seasonal variability of Tidal Amplitudes

Figure 6.7 shows the harmonic analysis of the M_2 amplitude at different representative locations of the Spanish coast. In all panels, vertical lines (or bands) stand for the frequencies of annual, semiannual, monthly and biweekly oscillations (from left to right in dark gray, light gray, blue and water marine, respectively). Points indicate significant frequencies.

As can be seen in Figure 6.7, the most irregular M_2 amplitude timeseries is presented by the stations of the Mediterranean (Barcelona). This fact was expected because of all tidal constituents are quite low and the sea level timeseries is similar to a noise signal (Figure 6.6). It resembles the red noise signal, so no frequency is expected to be significant. The rest of panels show a marked biweekly and monthly variability. Annual oscillations are observed in the Cantabrian regions and Atlantic, and not in the Strait and the Alboran Sea where the tidal regime is mixed (see how the stations of Tarifa and Bonanza do not show these significant frequencies). Only the Cantabrian cornice shows a component meaningful semiannual.

Since intra-annual oscillations are observed in some locations, a monthly analysis of the series of amplitudes is done. Figure 6.8 shows the average monthly value, the median, the quantiles 1 and 3 and the confidence band at 95% of the time series of amplitudes of the M_2 in stations of the five locations. The oscillations were observed detected in the spectral analysis. On the Atlantic side (e.g. the Tenerife station) the annual oscillation of the M_2 is clear, with the maximum in January and an approximate height of 16 mm. At Cantabrian side (Bilbao), the amplitude is approximately 15 mm, the maximum being in January and the minimum is observed in October. In the rest of the stations the oscillation is not so clear, however, the temporal variability is approximately equal to 10 mm.

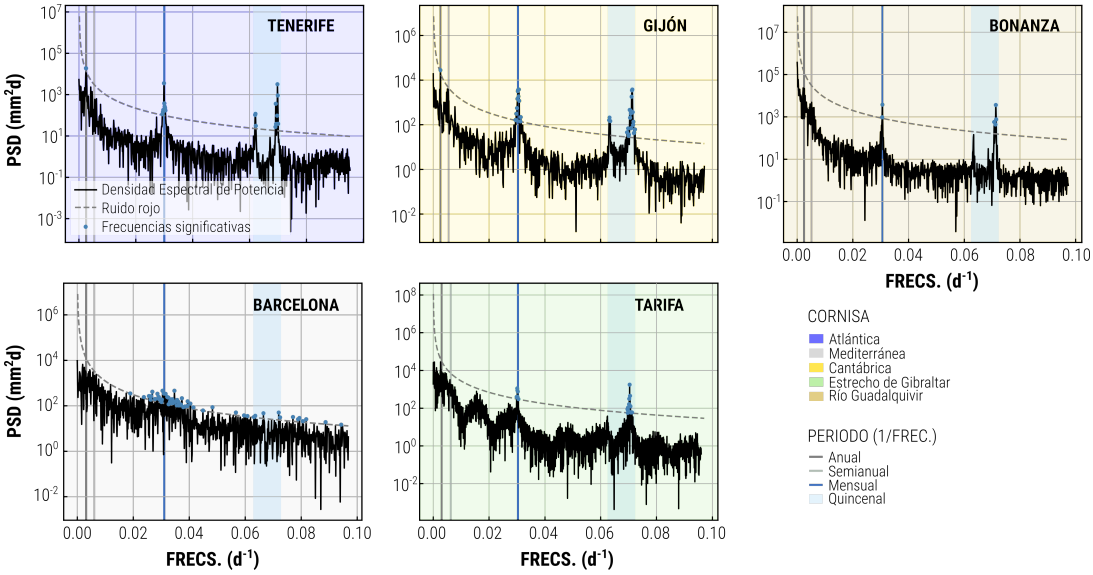

Figure 6.7: Power Spectral Density (PSD) in mm^{2}d of M_2 tidal amplitude at several representative stations of the Spanish coast.

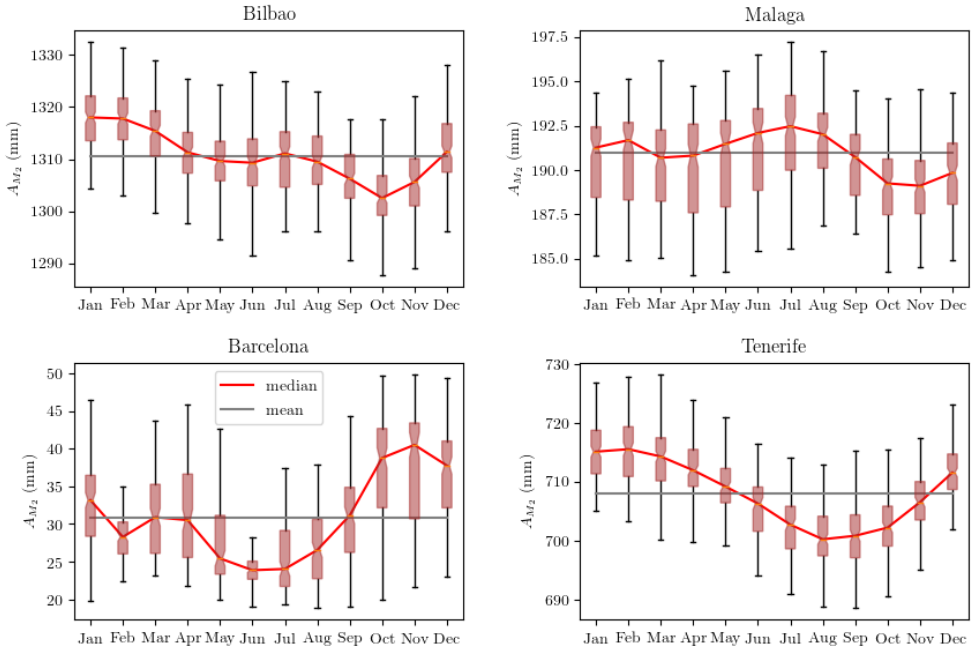

Figure 6.8: Intra-annual evolution of M_2 tidal constituent for some stations.

6.3.3 Trends in Local Tidal Amplitudes and Phases

Overall, negative trends are observed in semidiurnal amplitudes (figures 6.9), although there are notable exceptions most likely due to local features. Semidiurnal amplitudes decrease at the Gulf of Cádiz (except in the station of Huelva with 0.32 ± 0.09 and Sevilla with 15.65 ± 0.98, which are located inside their respective estuaries), and Mediterranean sea tidal gauges. The largest negative trend is found at the mouth of the Guadalquivir estuary (Bonanza tidal gauge) attaining a value of -2.88 ± 0.12. Decreasing trends are also observed in the stations of the Bay of Biscay (-0.15 ± 0.07).

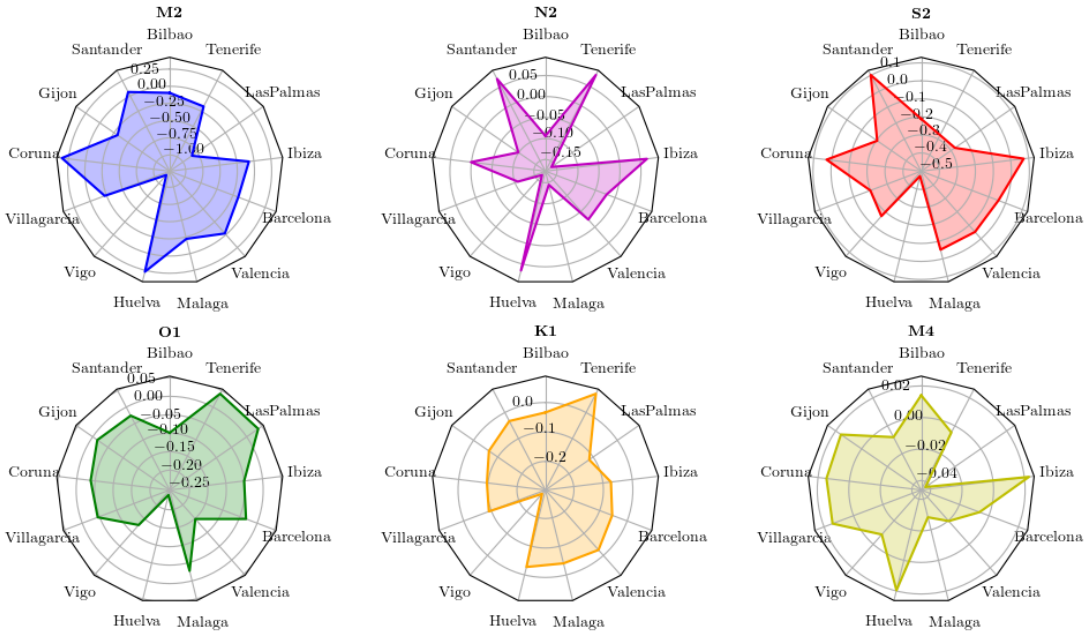

Figure 6.9: Trends in tidal amplitudes (mm/yr) of Spanish stations for several components. Trends at Bonanza and Seville stations are not showed for clarity.

Positive values are observed at Santander with 0.05 ± 0.09, although the error bar does not allow to rule out a negative trend (figure 6.9). The behavior in the Galician rias is more irregular thereby suggesting a strong dependence on local particularities. While Vigo station shows a negative trend of -1.28 mm/yr, in Coruña there is a consistent growth in 0.32 mm/yr. The latter results agree with previous estimates by (Tsimplis et al., 2011; Woodworth, 2010).

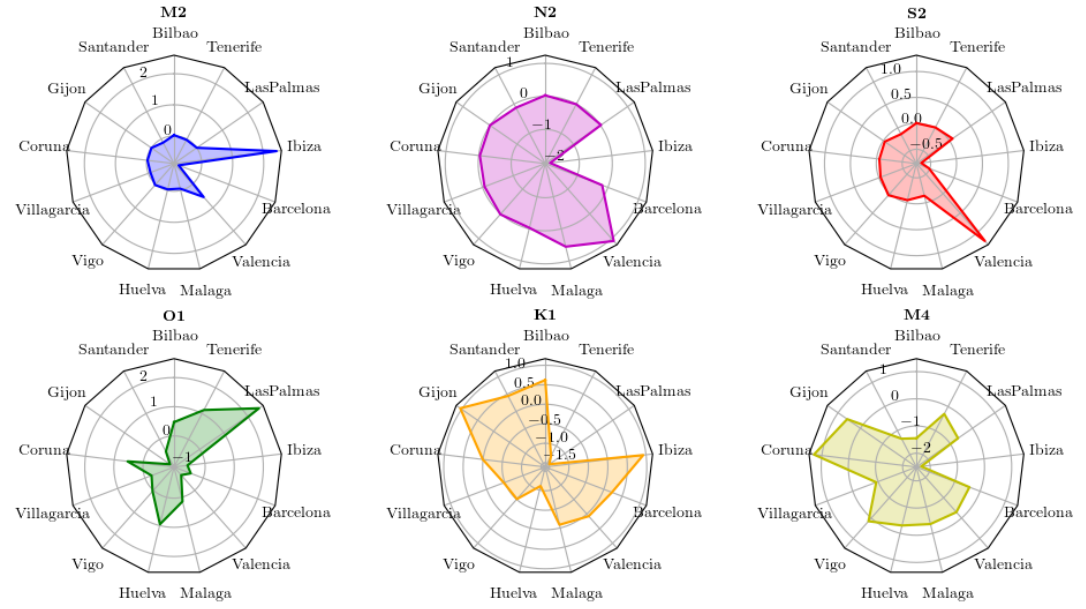

Figure 6.10: Trends in tidal phases (deg/yr) of Spanish stations for several components. Trends at Bonanza and Seville stations are not showed for clarity.

Similarly, to the semidiurnal amplitudes, most of the stations show decreasing rates in diurnal

amplitudes (figure 6.9), especially in the Gulf of Cádiz. Overall, the diurnal inequality in the tidal records is thus decreasing (with average rates of approx. -0.1 mm/yr). The lowest values for diurnal amplitudes are -0.15 mm/yr observed at Gijón and -0.3 mm/year at Huelva stations for the O_1 and K_1, respectively. In fact, negative trends are more acute in the southern, lower latitude locations (figure 6.9).

The M_2 phase at the estuary mouth tends to increase (0.064 ± 0.004). Trends in O_1 phases lay within the ± 0.2 deg/yr band. Low values of trends in phases are observed at the Cantabric region, whereas slightly positive trends are estimated (0.05 deg/yr) at Strait of Gibraltar. Regarding the quarti-diurnal M_4 amplitudes, stations near estuaries show relatively large values, such as Huelva. Santander and Bilbao show negative trends of the M_4.

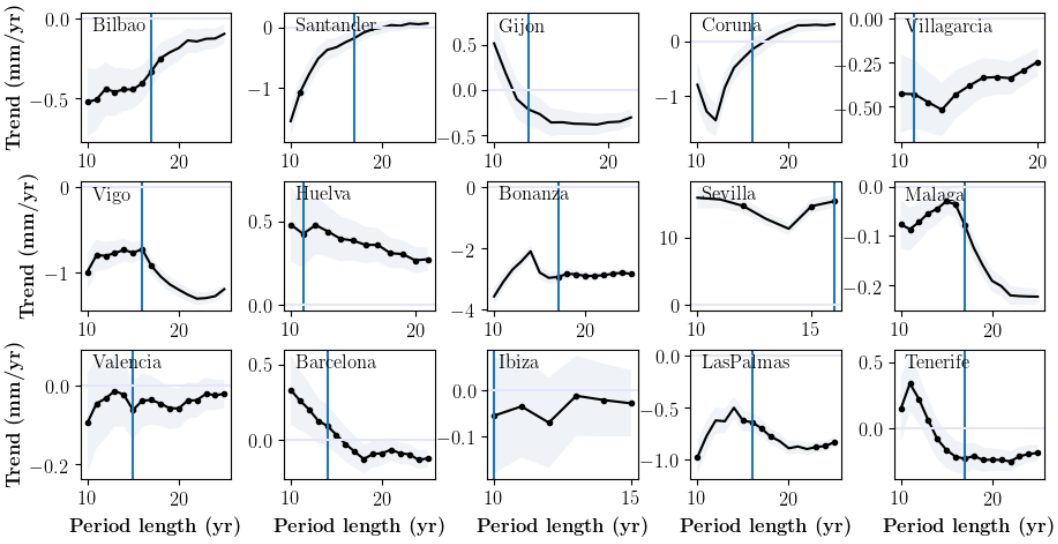

Figure 6.11: Trend of tidal amplitude M_2 for increasing window length at all stations. Vertical blue line shows the change from acoustic to radar sensor. Filled regions show the 95% confidence interval.

Trends in tidal amplitudes and phases are assessed for several windows' length in Spain (see figure 6.11 for M_2 constituent). The figure 6.11 highlighted two main results. The first one is that the change in the tidal measurement mechanisms do not infer in the magnitude of tidal constituents. The same amplitude trends are observed with acoustic and radar gauges. The second result is that it is again confirmed the need of a record period, at least, longer than a nodal cycle. As it can be noted at stations as Santander, Malaga, Barcelona, or Tenerife, among others, the record length period highly infers in the tidal trend computed. The trends converged with a window length longer than a nodal cycle. In some cases (see, i.e., Bilbao, Coruña, or Malaga stations on figure 6.11), the record period is not enough for confirming the existence of a stationary tendency (black dots).

In Appendix can be found the table 6.2 with the semidiurnal (M_2, S_2, N_2), diurnal (K_1, O_1), and quarti-diurnal (M_4) trends of amplitude and phases beside as the confidence level.

6.4 Trends in the Guadalquivir River Estuary

The M_2 phases in Seville tidal gauge are substantially greater than in Bonanza (table 6.2) due to the delay in the propagation of the tidal wave up-estuary. The phase lag doubles that from the

Gulf of Cádiz to the Bay of Biscay. This indicates that the effects of friction in the inner estuary are greater, compared to that of the tidal wave in the open sea. Despite the remarkable effect of friction, the amplitudes in Seville are slightly lower compared to Bonanza, due to the influence of the convergence of the channel and the partial reflection and in the Alcalá dam (Díez-Minguito et al., 2012). The M_4 amplitudes (table 6.2) are larger in Seville. Factors $A_{M_4}/A_{M_2} \sim 0$ are comparable to those in Huelva and other estuaries (Díez-Minguito et al., 2012). Lower values are observed in other stations analyzed.

Regarding the trends, the reduction of the M_2 amplitudes and the increase of the phases in the mouth of the Guadalquivir could indicate an increase of the effective friction on the tidal wave in this zone. This seems to be corroborated by the substantial increase observed in the M_4 amplitudes (table 6.2). Trends in amplitude and phases at the estuary mouth in Bonanza contrasts with what is observed upstream at the Seville station. The positive trend the M_2 amplitude exhibit in Sevilla is very significant (15.65 ± 0.98), thereby producing a subsequent increase in the M_4 constituent. The decrease in the M_2 phase is also remarkable (-0.40 ± 0.01). The phase difference between the upstream station (Sevilla) and the station at the mouth (Bonanza) suggests that the tidal wave would tend to propagate increasingly faster (0.073 hr/yr). This points to a reduction of the effects of friction inside the estuary. In addition, the amplification factor, defined as the ratio between A_{M_2} amplitudes at Sevilla and Bonanza (Cai et al., 2016; Wang et al., 2014), is increasing from current values lower than 1 to larger than 1 values, i.e., the trend is toward larger M_2 amplitudes in Seville than in Bonanza.

Figure 6.5 shows the sea level and some derivate tidal properties at the mouth (Bonanza) and 85 km upstream (Seville) of the Guadalquivir river estuary. The tidal range at the mouth is nearly 3 meters where at the head is . The mean M_2-tidal amplitudes and phases at the mouth and head (next to Seville) are 0.924 m (0.2 degrees) and 0.88 m (3.0 degrees), respectively. While M_2 amplitude is lower at the head, the M_4 amplitude is higher (3.81 and 5.0, respectively), showing a non-linearity during the wave propagation along the estuary. Difference in phases between the mouth and the head showed that the sea-level at Seville is observed with a lag of 4 hours regarding the mouth.

6.5 Discussion

As regional trends in total water levels are more relevant than global trends (Devlin et al., 2017), it is applied a methodology to identify regional/local changes in tidal constituents at Spanish coast. However, there are not available so many long records to study tidal processes locally. This is why it is currently observed a gradual decrease of the record length of studies from almost 50 years (Jay, 2009; Marcos et al., 2011; Ray, 2009; Woodworth, 2010) to time series slightly larger than a nodal cycle (Devlin et al., 2017; Gräwe et al., 2014; Ross et al., 2017). Sea-level timeseries slightly larger than a nodal cycle at 15 stations along the Spanish coast are used in this study.

Negative trends in tidal amplitudes are observed in most of stations. However, while it is hard to draw conclusive results at regional scale, some general patterns are inferred. Within the error bars, clear negative trends in the amplitudes of all analyzed tidal constituents are estimated in stations near the Strait of Gibraltar. Consistent negative values for tidal amplitudes are also found in the Atlantic coastal stations of the Gulf of Cádiz and Cantabric Sea, although Santander and Coruña stations exhibit a positive trend in semidiurnal amplitudes. Along the Mediterranean margin, negative values are observed for the semidiurnal amplitudes at all stations. Diurnal amplitudes also tend to increase at these stations, except in the Barcelona tidal gauge, which shows negative values for all constituents. The decreasing trends in their corresponding main tidal constituents at Vigo, Villagarcía, Barcelona, and Bonanza (-1.28, -0.35, -0.14, and -2.88 mm/yr) are particularly significant. Remarkably, although these coastal stations are in different regions of the Iberian

Peninsula, they are near the mouth of estuaries, thereby influenced by the freshwater to some extent.

The Guadalquivir estuary shows at its mouth at Bonanza tidal gauge the largest reduction in M_2 amplitudes. However, the opposite behavior is observed upstream in this estuary. The Sevilla stations, which is located 80 km upstream, shows the largest positive trend in M_2 amplitudes with 15.7 mm/yr. This result agrees with found by Pugh and Woodworth, 2014 in London, where more than 80 km up the River Thames from the North Sea, high water levels have increased by around 0.8 m per century whereas low water increases were only around 0.1 m per century. Only the value at Huelva station, which is also located inside an estuary (namely Tinto-Odiel estuary) or Coruña, are comparable to that with 0.32 mm/yr.

Exploring the mechanisms reducing tidal amplitudes at coastal areas, long-term increase in sea level emerges as one of the possible candidates. Sea level rise may favor flooding over shallow banks and marshes, thereby significantly enhancing the tidal energy dissipation (Du et al., 2018). Depth changes may shift resonance conditions on the continental shelves and semidiurnal and diurnal amphidromic points locations (Devlin et al., 2017). Estuaries that are near resonance are more likely to be sensitive to small changes (Cai et al., 2016; Talke and Jay, 2019). The results indicate that resonant characteristics of the estuary increase since the amplification of the M_2 amplitude in Sevilla even overcomes the reduction in the M_2 amplitude at the mouth. This phenomenon does not arise from natural way, but as a result of the human actions made in the channel. The presence of the tidal barrier in Sevilla and the dredged nearly constant depth, turn to the estuary into a semi enclosed body that generate resonance for the wave of period 12.42 hours (Álvarez et al., 2001).

The Guadalquivir inlet is progressively reduced their mouth width (López-Ruiz et al., 2012), which tendency is to limit the amount of water that flows into a bay, resulting in small tides. The computation of the choking parameter reveal that the Guadalquivir river estuary is experienced a tidal reduction in their mouth by choking effect. Similar to Venice, where a long-term trend of 0.22 mm/y in the M_2 constituent since 1940 is attributed found (Ferrarin et al., 2015). The results are corroborated with increase in stratification observed at the estuary mouth. The time series of potential energy anomaly showed a positive tendency, probably as results of the decrease in mixing energy by decreasing tides.

The trends of tidal amplitudes within the estuary suggest a significant reduction of the effects of friction, which is another plausible mechanism changing the stratification conditions Müller, 2012. Pérez-Gómez, 2014 already pointed to the possible effects of the deepening of the navigation channel that allows ships to reach the Port of Sevilla on the positive trends of the M_2 amplitude. Deepening of navigational channels and removal of intertidal areas are well-known human factors that increase tidal range estuaries (Jonge et al., 2014; Pethick, 2002; Stark et al., 2015). This increasement produces a reduction of friction due to the increase on stratification induced by an elevation of the suspended sediment concentration. Therefore, it is produced more tidal amplification (Winterwerp and Wang, 2013). This feedback process is identified by (Wang et al., 2014) and (Losada et al., 2017) as the cause of an hyperturbid state and tidal amplification in the Guadalquivir estuary. Regarding the intertidal flats, the Guadalquivir estuary lost about 85% of its intertidal areas during the twentieth century to answer agriculture and other land use demands (Ruiz et al., 2015). This transformed the estuary into a single, almost straight channel closed off from the surrounding natural areas. Song et al., 2013 found that removal of tidal flats resulted in a 0.11-m increase in regionally averaged M_2 amplitudes in the East China Sea.

From these results follow that human activities may have also an impact on long-term tidal constants variability, although more work is needed to substantiate the possible human influence, and could involve the approach of Lennartz and Bunde, 2009. This result can be extended of

peninsular estuaries which catchments are experiencing, from the second half of 20th century (e.g., Barranco et al., 2013), a significant reduction in the freshwater runoff.

In some stations, tidal trends are not significant, we cannot dismiss the possibility of a stationary trend. Conversely, trends at Guadalquivir river estuary are significant. The methodology proposed does not differ between natural or anthropogenic trends inasmuch as ADF and KPSS tests indicate the existence of a stationary trend but not the reason. The knowledge of processes in the Guadalquivir river estuary beside as the dredging actions, the reduction of freshwater discharges, tidal flat occupation, resonance and reflective conditions in the estuary, among others, supports our hypothesis that reduction of freshwater discharges-induced stratification modify the tidal amplitude.

6.6 Conclusions

The tidal constants trends indicate that, at most stations, both semidiurnal and diurnal tidal amplitudes decrease. Overall, their values are lower than relative sea level rates analyzed during the same time interval in one and two orders of magnitude, respectively. The largest negative trends are found at the mouth of some major estuaries, such as Ria de Vigo ($-1.28 \pm 0.07\,\mathrm{mm/yr}$) and the Guadalquivir River Estuary ($-2.88 \pm 0.12\,\mathrm{mm/yr}$). It is hypothesized that the overall decreasing trend in tidal amplitudes is induced by the choking effect experienced by human activities such as land reclamation near inlet. A notable exception to the overall trend is the Sevilla station, which is the land most station located 85 km upstream from the Guadalquivir estuary mouth. This station shows a significant positive trend for the M_2 amplitude of $15.7 \pm 1.0\,\mathrm{mm/yr}$ that points to the tidal amplification due to resonance conditions within the estuary and channel deepening.

Regarding the seasonal/annual variability of the M_2 amplitude: the Spanish coast can be divided into three sectors that correspond to the Atlantic/Cantabrian sides - Strait of Gibraltar - Mediterranean. On the ledge Atlantic/Cantabrian, an annual variability can be seen with a maximum in winter and an approximate amplitude of 10 mm/yr. In the Strait of Gibraltar there is a high monthly variability (80 mm) whose average oscillates in an annual cycle of 8 mm/yr amplitude and maximum in summer. In the Mediterranean side the amplitude of the M_2 is less than 100 mm and there is not a clear annual or semi-annual variability. In general terms, the amplitudes of M_2 show a negative trend. It is observed a local geographic dependence. The tidal gauges located at the mouth of estuaries showed a decline more pronounced than in general. Tidal gauges located within estuaries showed a rise. The seasonal variability of the M_2 is, in average terms, an order of magnitude greater than the level increase of the sea. Therefore, it is recommended that the temporal variability of the M_2 be included in the hydrodynamic and flood models, since its concomitance with storm events could lead to coastal flood extremes.

Appendix A. Trends of Tidal Constants at Bonanza.

Table 6.2 shows the trends of tidal amplitude and phases at Bonanza stations.

Tidal constituent	A (mm/yr)	ci (1%, 99%) (mm/yr)	φ (degrees/yr)	ci (1%, 99%) (degrees/yr)
M_2	-2.8417	(-2.9376, -2.7458)	0.0520	(0.0440, 0.0599)
N_2	-0.6182	(-0.7645, -0.4719)	0.0823	(0.0361, 0.1285)
S_2	-1.2282	(-1.5543, -0.9020)	0.0392	(-0.0217, 0.1001)
O_1	-0.0711	(-0.1208, -0.0214)	-1.0878	(-2.1147, -0.0609)
K_1	0.2961	(0.2335, 0.3588)	-0.6719	(-1.3509, 0.0071)
M_4	0.25174	(0.1920, 0.3115)	1.19847	(0.4060, 1.9909)
M_{sf}	-0.2404	(-0.32278, -0.1580)	0.45218	(-0.5652, 1.4696)

Table 6.2: Trends of tidal amplitude and phases at Bonanza for the major tidal constituents.

7. Strategies for Enhancing the Water Quality

"If you want different results, do not do the same things"

Albert Einstein

Full datasets and/or simulations of climatic conditions (chapter 6) provide the required inputs to the LAPE model described in chapter 4. Therefore, energy and mass balances can be established and water quality parameters such as water mass exchanges, mixing densities and flushing can be assessed.

In this chapter the evolution of such water properties in the GRE under the expected climatic conditions up to the mid-century ($\sim$ 30 years) is analyzed. In section 7.1, it is presented the analysis of quality parameters in the current situation (the so-called business as usual) and also considering the effects of climate change on tidal components (scenarios A and B, respectively). It is found that climate change modifies slightly the quality parameters, increasing the blockage periods. Its effect, however is not significant for the study period. For both scenarios, A and B, the GRE showed a low capacity to renew its water masses.

In section 7.2, the model is also used to investigate the effects of different management strategies for scenario B under realistic situations (table 7.1). First, a reduction of the water discharge from the Alcalá del río dam due to an increase of freshwater demand according to the trend of the last decades (Case B1). Second, an increase in water depth, similar to the one claimed by the Seville harbor authority was proposed (Case B2). Case B3 and B4 correspond to a strong regulation of the water discharge aimed at minimizing the blockage periods (Case B3) and water density at given location (case B4), respectively. The results of the simulation of cases B1 and B2 showed that the fragile situation of the GRE will be worsen in the future. Cases B3 and B4 reduce both the blockage periods and the flushing times in different ways.

Finally, the ecological flow required to maintain the environmental richness is discussed beside as the hypothesis provided (§ 7.3). Some conclusions and recommendations are finally reported

(§ 7.4). The figures of the results obtained for different cases are provided in the Appendix (§ 7.4).

Scenarios	Cases	Tidal constituents	River discharge	Water depth
A		Non affected by CC	SHD	Current maintenance of 7 m depth
B		Affected by CC	SHD	Current maintenance of 7 m depth
B	1	Affected by CC	SHD with 1% per year decrease	Current maintenance of 7 m depth
B	2	Affected by CC	SHD	Dredging and maintenance to 8.5 m depth
B	3	Affected by CC	Strong regulation (minimize the blockage occurrence)	Current maintenance of 7 m depth
B	4	Affected by CC	Regulation strategy (minimize the salinization of section 4)	Current maintenance of 7 m depth

Table 7.1: Characteristics of scenarios and cases. CC stands for 'climate change conditions' while SHD defines 'simulated from historic data'.

7.1 Climatic Scenarios at Horizon 2050

7.1.1 Setting up the model

The atmospheric, hydrodynamic and morphological conditions were simulated at a mid-temporal scale, the scale that decision makers usually need to implement management strategies. Therefore, the simulations comprise 30 years, from January 1st, 2020 to the January 1st, 2050. The changes in the blockage conditions, flushing times, mixing density and water mass exchanges are assessed for the current situation (scenario A) and using as inputs the simulations under a climate change scenario where the sea level rise (chapter 5) and the changes in the tidal constituents are effected (chapter6) (scenario B).

For scenario B, the sea-level rise was considered by assuming a progressive increase of water depth in all boxes of 1.02 mm/yr (Marcos et al., 2011). This increase is reflected not only on the water depth but also on the cross-sectional area and volume of every box. Due to the configuration of the model, the width increase is not accounted for although, in some cases, can be important. The changes in tidal amplitude and phase were included by annually updating the constituents with the values given in table 6.2, and reconstructing tidal elevation and current as in § 6. This procedure produces a small jump in the graphs at the beginning of every year that is not significant. The water discharge reduction of Case B1 is applied linearly to the simulated time series. For the configuration B2, the amplitudes and currents are obtained from the model by Prandle and Rahman, 1980. In all the cases, the Stokes-tidal pumping rates ζ were obtained fitting the data obtained from Díez-Minguito et al., 2013 to a hyperbolic tangent function (eq. 7.1) similar to Talke et al., 2008 did for describing the longitudinal profile of salt. The parameters a, b and c are fitting coefficients (see figure 7.1).

$$\tau_4 = \tanh\left(\frac{\tau_2 - a}{b}\right) + c, \tag{7.1}$$

the minimization algorithm provides $a = 34.461$, $b = 17.932$, and $c = 0.408$, with a rmse equals to 0.070.

Following the methodology provided in chapter 4, the estuary is divided into 5 boxes of equal length 12 km. The upstream boundary of the model is located at 60 km, where it is assumed that the density is equal to the river freshwater density. Eqs. 4.2 and 4.3 are applied for the scenarios and cases described in the previous section. As it was seen in chapter 4, the selection of the boxes depends on the heterogeneity of the transport processes along the estuary.

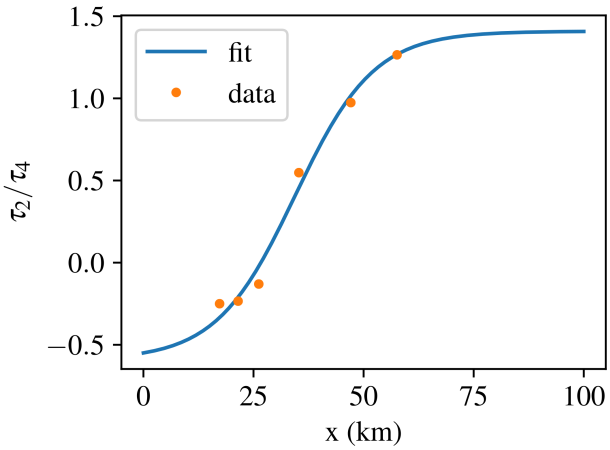

Figure 7.1: Relationship of mean Stokes transport and tidal pumping along the GRE. Data refers to Stokes transport - tidal pumping rates given in Díez-Minguito et al., 2013.

A large number of simulations (a hundred) were done to statistically analyze the response of the estuary. In the following, to facilitate the comparison between the scenarios/cases, the focus is on the realizations obtained with the same seed to initialize the simulation model, which means that the same time series of Q_d (water discharge), W (wind velocity) and D (wind direction) are used.

7.1.2 Comparison between scenarios

With the model presented in chapter 4, the water mass exchanges and mixing densities, the blockage periods and the conditions that promote them, as well as the residence and flushing times were obtained to assess in both scenarios until 2050.

Figure 7.2 shows the density time series, blockage conditions and water mass exchange for scenario A during the whole period. Water density varies along the year showing a significant decrease during winter and spring. This variability is lower near the mouth because the water density at section 0 is quite stable, and only high river discharges reduce the water density there. It is also observed that the mixing density of two adjacent boxes becomes closer right before the blockage conditions and, accordingly, the water exchange gradually decreases seaward. The blockage events are related not only to low river-flow conditions but also to tides. As previously mentioned, during low flow, the worst conditions usually occur during the transition from neap to spring tides. It is observed that the landward most box (box 5), located between the sections 4 and 5, is frequently blocked (purpled boxes in the mid panel). During low-river flow conditions, it is promoted that the tide pumps salt upstream, which contributes to the promotion of the saline intrusion in the estuary and limits the washing of the suspended sediment at the upper part ot the study area, at the same time, increases the water density there, and, gives the characteristic brown color to the water. On average, blockage affects the last box about 42% of the year, while the landward boxes blockage events are less habitual. This blockage period is so high, the current scenario of the Guadalquivir River Estuary represents a highly anthropized estuary where natural dynamic is poor and infrequent.

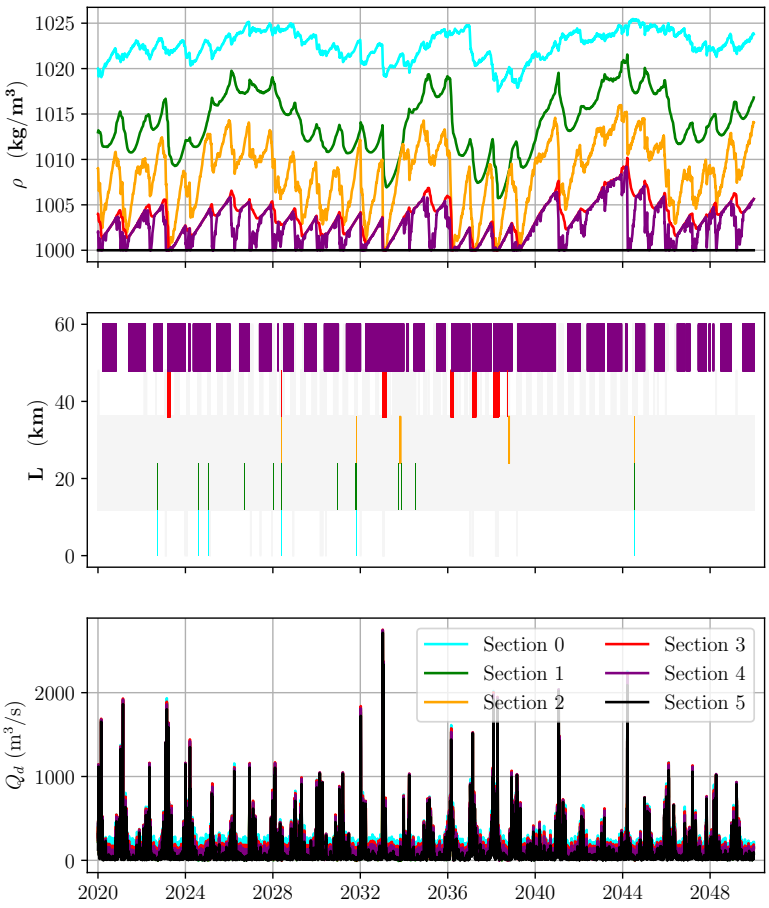

Figure 7.2: Results of the model in the current scenario (A). Mixing density (upper panel), box blockage (mid panel), and water mass exchange (lower panel). In mid panel is represented with colored boxes the time periods when a given box is blocked. Gray boxes indicated a downstream reduction of the water mass exchange which remains positive (outflow).

Box 5 is blocked almost all the time and only recovers during neap tidal conditions. At the same time, the densities at sections 4 and 5 coincide and increase linearly at a rate of 0.31 kg/m^3 per month. Seaward, at section 2, the density increase rate exceeds $\sim$1 kg/m^3 per month. The temporal gradient of density at section 1 is 0.24 kg/m^3 per month, a value lower than at section 2 when the estuary is blocked at the landward region.

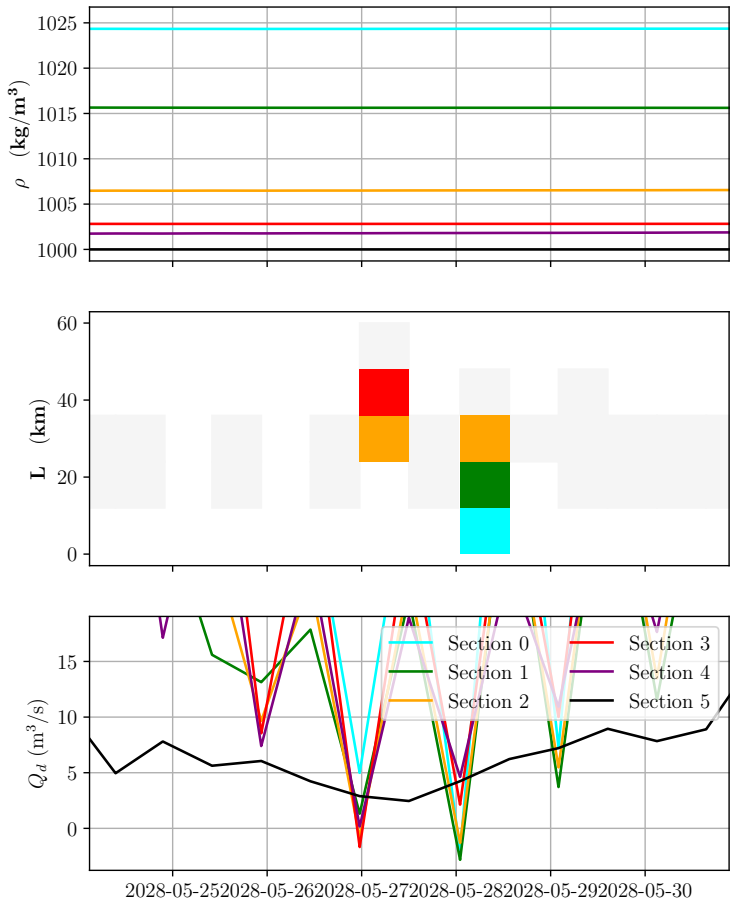

Figure 7.3: Results of the model in scenario A. Mixing density (upper panel), box blockage (mid panel), and water mass exchange (lower panel).

During high river-flow conditions, when a significant reduction of estuarine density can be observed, the differences found in the density rates could promote long periods of blockage conditions. However, as it will be seen, the recovery rates of density are significantly greater than the rates observed under partial blockage conditions.

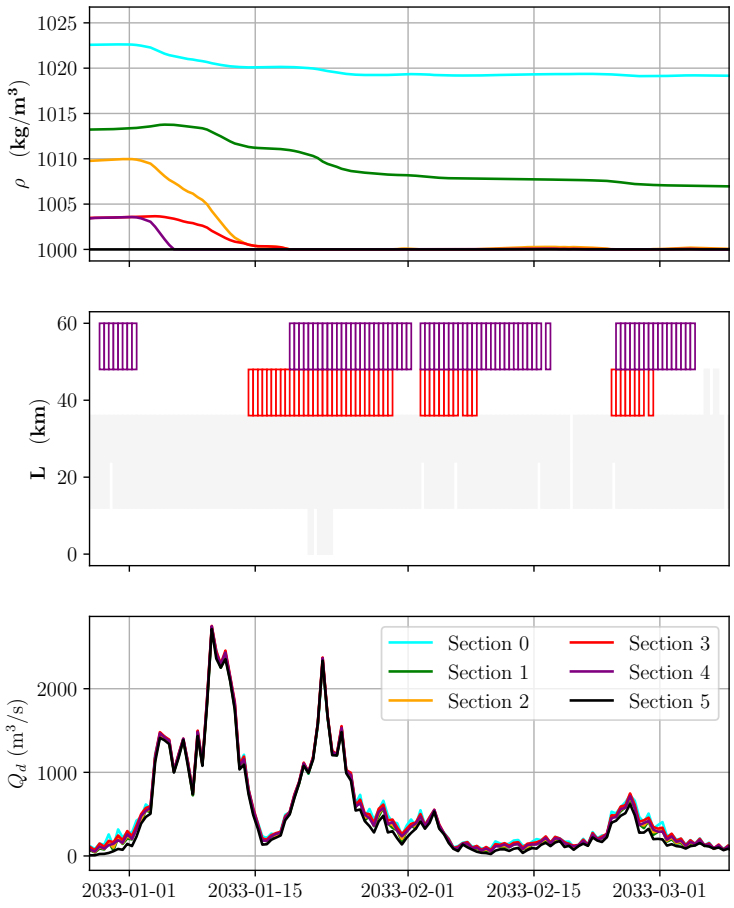

Figure 7.4: Results of the model in scenario A. Mixing density (upper panel), box blockage (mid panel), and water mass exchange (lower panel).

As it was highlighted in chapter 4, the Stokes transport increased seaward at the GRE while tidal pumping increased landward (Díez-Minguito et al., 2013). These conditions favored a negative net water mass that entered and then flowed out due to Stokes transport and tidal pumping (m_4 to m_7 in eq. 4.2). During certain periods, this difference was larger than the incoming water mass from the upward box m_2. Then, a reversal of the water mass flux, a negative m_3-term, was needed to balance the density gradient. River discharges lower than 5 m^3/s promote the blockage of the whole estuary as it is observed in figure 7.3. In this case, the blockage occurred motivated by the reversal of the exchange flow. The differences between Stokes transport and tidal pumping terms create an imbalance that the low river discharge cannot compensate.

As can be seen in figure 7.4, river discharges greater than $Q_d \sim 1000$ m^3/s enhance the water outflux, and refresh the estuary water mass. The intensity and duration of the water pulses highly modify the density profile along the GRE, preventing the salinization of the estuary. It is important to note that the water density drops down significantly in sections 5 and 3 with similar density rates ($\sim$ -1 kg/m^3 per day). This density rate is two orders of magnitude greater than the increasing rates

during blockage conditions ($\sim$ 0.5 kg/m^3 per month) which indicates the possibility of regulation and control of the water density with small 'pulses'. The aforementioned pulses appear every year mainly associated to winter storms and if their durations are long enough, they may blockage the estuary in boxes 4 and 5 may last after the river discharge, which indicates that the estuary is recovering its natural density with salt from the sea. As it is observed, the along-channel 'hyperbolic tangent' density profile moves its inflection point seawards. This behavior suggests to regulate in such a way that water density is controlled and tried to be maintained below the maximum salinity that allow farmers to grow rice fields.

The results of water exchange and mixed density in scenario B are in the appendix (figure 7.9). As it is observed, changes are in general small and a slightly increase in the blockage periods is observed.

7.2 Some management strategies

Some of the more usual management strategies under realistic scenarios are discussed in this section. In case B1, it is assumed that freshwater discharge Q_d follows the trend observed during the last fifteen years (CEDEX, 2010; Reyes-Merlo et al., 2013) and decreases at a rate of 1% per year. The corresponding time series is obtained by modifying the simulation with the linear trend. Case B2 reproduces a management strategy that consists in an increase of water depth to 8.5 m (a 23% of its actual depth) as proposed by the Port Authority of Seville. Two management strategies for river discharge are considered in cases B3 and B4, aimed at (i) avoiding the occurrence of blockage (case B3) or (ii) maintaining water density at a given location where a pipe intakes water to supply rice fields below a certain threshold (case B4).

The figures with the results of situations B1 and B2 are in the Appendix. The decrease in the freshwater discharge by a 1% per year (case B1) allow to control the density of sections 4 and 5 with the freshwater pulses and significant fluctuations of water density are only observed at sections 2 and 3. The largest differences between scenario A and case B1 are found during the last five years of the study period. The water discharges observed in 2045 - 2050 ($\sim$1000 m^3/s) are reduced more than 25%, reducing the intensity of the water pulses in the scenario B1 and increasing the water density significantly in the whole estuary.

For case B2 the area of influence of tides extend due to the deepening of the bed. Accordingly, the mean densities of the boxes increase, moving landward the inflection point of the longitudinal density profile and, therefore, increasing the saline intrusion. In this case, it would be necessary to extend the study area landward until Seville ($\sim$ 85 km) or the Alcalá del río dam (110 km). The potential damage of the estuarine salinization for fauna, flora, and agriculture crops that require freshwater might not be tolerable.

The longitudinal profile of salinity can also be obtained from the results during low-river flow conditions, high-river flow conditions or under recovery periods. Some helpful empirical relationships between Q_d and X_2 (or X_1, X_5 and X_{10}, for instance) can also be obtained as Díez-Minguito et al., 2013 proposed.

7.2.1 Controlling the blockage periods with a strong water regulation (case B3)

The figure 7.5 shows the results with a strong regulation of the water aimed at minimizing the blockage time (case B3). The gray line in the lower panel depicts the difference between the regulated water discharge and the available from the simulation. It is observed that in order to reduce the blockage time, it is necessary to increase the discharge during the low-river flow

conditions, on average, to 100 m^3/s. Furthermore, the water pulses that promote the reduction of water density are significantly reduced its volume. Only in some periods when persistent water pulses are released, such as in the winters of 2031-2032 and 2038-2039, a strong density reduction is observed.

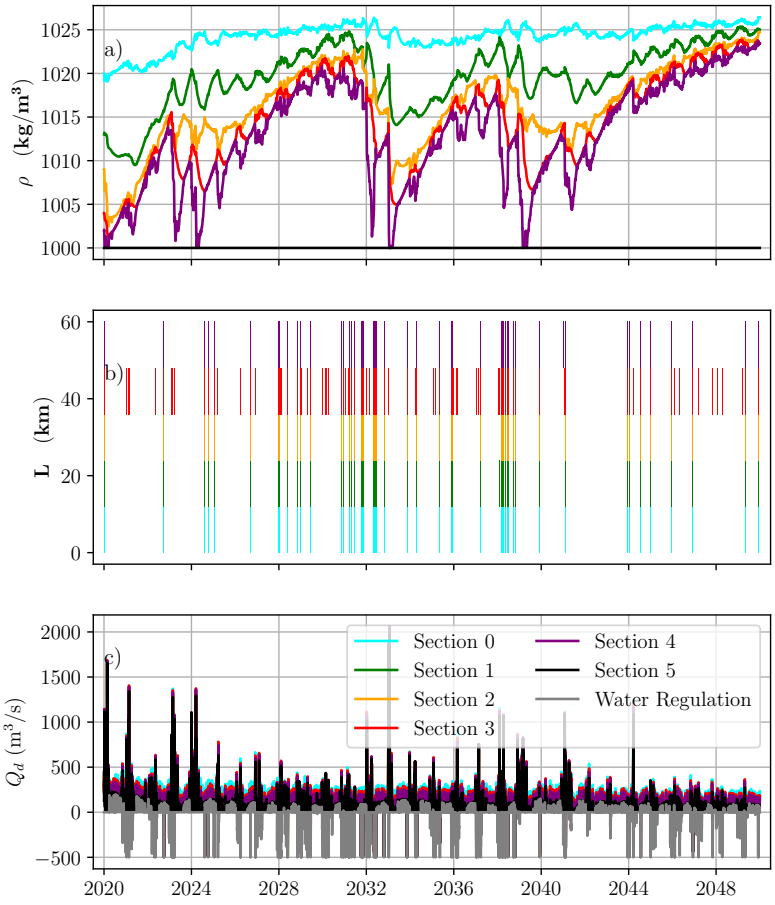

Figure 7.5: Results of the model by considering the sea-level rise and the change of tidal constant by imposing a high-water discharge regulation and minimum blockage time (case B3). Mixing density (upper panel), box blockage (mid panel), and water mass exchange (lower panel).

In general, the estuary does not block as much as without regulation, however, when it occurs, it affects the whole estuary. An important consequence of the strong regulation is the generalized increase of water density along the GRE, even reaching the upward limit of the domain. The salinization of the estuary is ensured due to flood dominance.

7.2.2 Controlling the water density (case B4)

The figure 7.6 shows the results with a density restriction at section 4 where river discharge is aimed at avoiding water density to be above 1005 kg/m^3. In this case the density requirements are fulfilled. It can be appreciated a significant reduction of the blockage periods that. Do not start at the landward box but at box 4. This strategy requires a larger amount of water than the one in case B3 with smaller water pulses volumes that enable density at section 4 falls during high-water discharges.

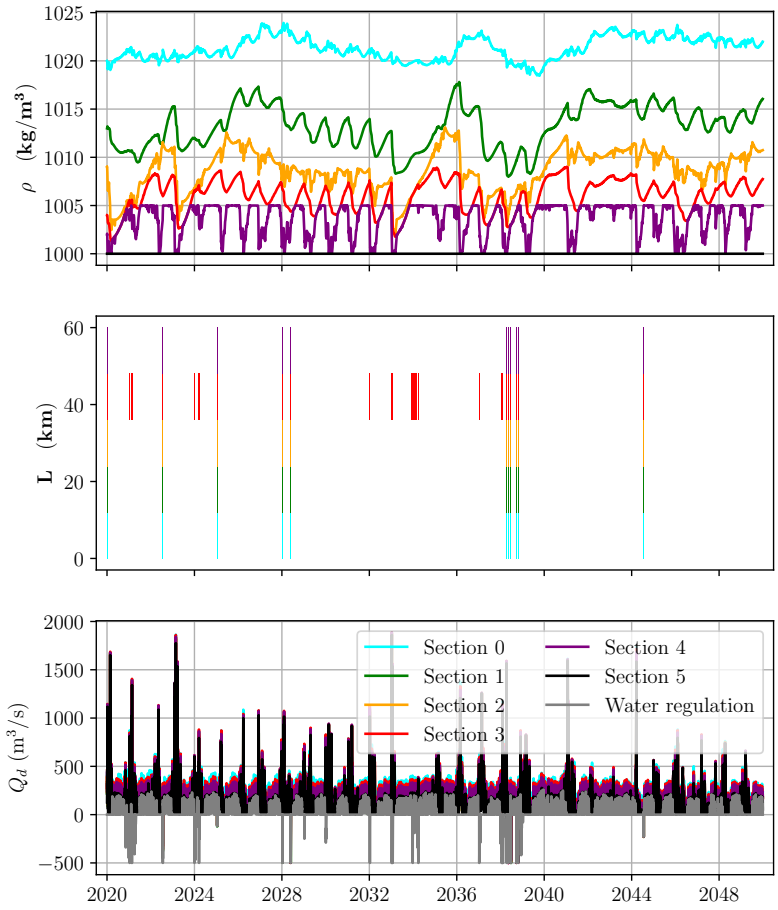

Figure 7.6: Results of the model by considering the sea-level rise and change of tidal constants and by imposing a controlled water density at section 4 (case B4). Mixing density (upper panel), box blockage (mid panel), and water mass exchange (lower panel).

During the periods of low water discharges, the density of section 4 reaches the limiting density of 1005 kg/m^3. Figure 7.7 shows a zoom on the water regulation of figure 7.6 during the period given. As it is observed, during this period, ρ_4 is constantly equal to 1005 kg/m^3. During low river-flow conditions, tides dominate the estuarine dynamics, therefore, tidal range can be related to freshwater discharge required to keep the given density. An oscillating behavior is observed with

peaks found in the middle of spring and neap tides and throughs at the transitions. The green line in figure 7.7 is the tidal range that was multiplied by 50 in order to ease the comparison.

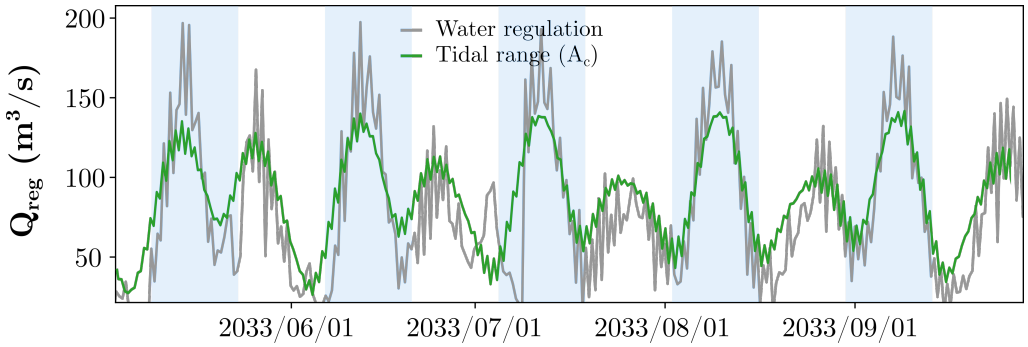

Figure 7.7: Water regulation under low-river flow aimed at keeping the water density ρ_4 below or equal to 1005 kg/m^3. Blue regions represent spring tides while white regions indicate neap tides. Tidal range was multiplied by 50 to compare the results.

7.2.3 Comparison of flushing times between scenarios

The comparison of the different scenarios/cases is also done through the flushing times, that measure the time required for the water mass to cross the estuary. They were computed as the sum of the residence times of each box (box volume divided by the water mass exchange). Figure 7.8 depicts the probability density function of the flushing time for the scenarios. As it can be clearly observed, the climatic conditions imposed for the scenarios B, and cases B1 and B2 produce an increase of the flushing time from the current conditions. The mean flushing times increase from 33 m^3/s to 47 m^3/s for B2. The deviation and upper tail of the flushing time series also increase. The future climatic conditions would affect the estuary capacity of water renovation. Conversely, the water regulation promotes the water mass renovation as it is observed in cases B3 and B4.

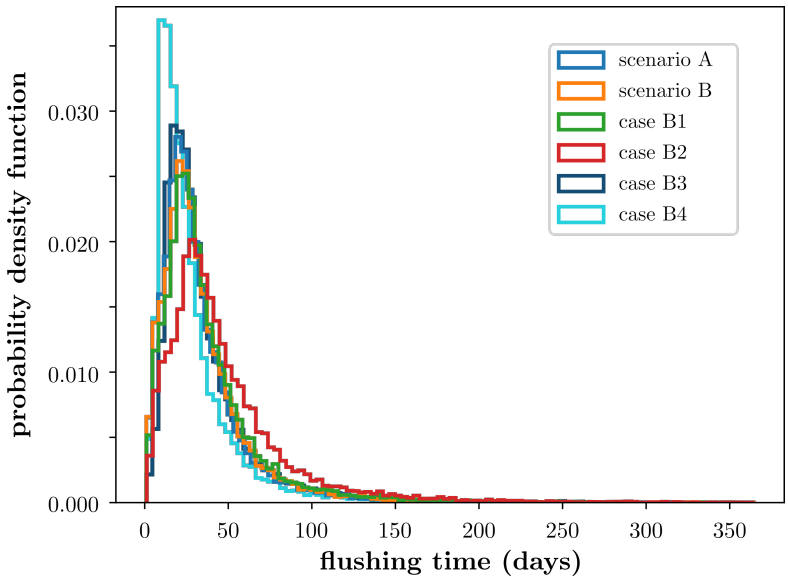

Figure 7.8: Probability density function of the flushing time for several scenarios and cases.

Imposing the density restrictions (case B4), the 75% of time the flushing time was below one

month, the total water outflow is 120440.11 Hm^3 ($\overline{Q_d} = 127.23$ m^3/s) and the blocking periods fall from 45% in the current situation to 1.1%.

7.3 Discussion

The alternatives presented in this chapter facilitate the understanding of the impact of their implementation on water mass exchanges, density mixing and evolution of residence times under the most likely scenarios. However, it is worth noting that the requirements of managers would possibly include a combination of strategies. The model adequately reproduces the processes that are observed in the estuary; hence, many other cases could be analyzed.

Another important aspect is that the water pulses higher than ~ 1000 m^3/s pick up the bed sediment and put it into suspension. The fine part of the suspended particle matter may last in suspension even two months (Díez-Minguito et al., 2014). This is an important source of turbidity which consequences are significant as they not only increase the water density but also limit the penetration of light into the water column. Furthermore, the dredging works might induce not only resuspension, that is not accounted for in the system of equations, but also shifts in the tidal current amplitude along-channel distribution. Under such circumstances, the use of a constant friction value in the one-dimensional tidal model might not be adequate to reproduce elevations and currents.

Other studies that analyze other estuaries under similar situations, have focused on the definition of a system of discharges that ensure saline conditions close to the reference 'natural' conditions for the different estuarine areas, comparing the obtained regime with the proposed one for the mass upstream of it. A minimum flow regime of 50 Hm^3/yr (1,584 m^3/s) was established in 1995 by the hydrological planning of the GRE. This value is two orders of magnitude lower than the water discharge recommended by WWF (150 - 300 m^3/s) or the discharges estimated for case B4 ($\overline{Q_d} = 127.23$ m^3/s). As seen in cases A and B3 during the persistent low-river flow regimes (figures 7.2 and 7.5), the consequences of a high-water regulation are a continuous blockage at the most landward box that result in an increase of the residence times and the salinization of the estuary. As it was seen in chapter 4, the wrong selection of the number or the size of the boxes, for example, due to homogeneity of the processes, will result in boxes with similar mixing density and water mass exchange, or, as it can be observed in 7.5, the unkown regions of the density field of the estuary.

In the report of the Guadalquivir Hydrological Plan (2015-2021), it is said that the ecological flows that were not defined in the first cycle Planning 2009-2015, would be updated by the Guadalquivir Hydrographic Confederation when there be enough studies to justify them. This model provides information to assess (i) the exchange rate, (ii) the regime of maximum flows, (iii) the regime of ecological flows in transitional waters and (iv) the environmental water requirements for transitional waters and wetlands.

7.4 Conclusions

An efficient model (with runtimes of a few hours for 30 years simulation) with a relatively simple design is proposed for its use by estuary managers. It can be applied to the GRE in order to estimate, under different scenarios and management strategies, the exchange flows, mixing densities and flushing times that are related to water quality. It might, therefore, help managers to make knowledge-based decisions.

The model was tested under several scenarios that represent realistic conditions, and showed

that an effective control of residence and flushing times can increase the water quality. A more detailed strategy can be run to found the 'optimal' natural dynamics of the estuary.

As it is observed from the model, a minimum water discharge ranging from 80 to 120 m^3/s is required to improve the water quality along the estuary, reducing the blocking periods and, at the same time, returning the estuary to its known natural dynamics.

Appendix: Results of scenarios B, B1 and B2

This appendix shows the figures of the scenarios and cases proposed.

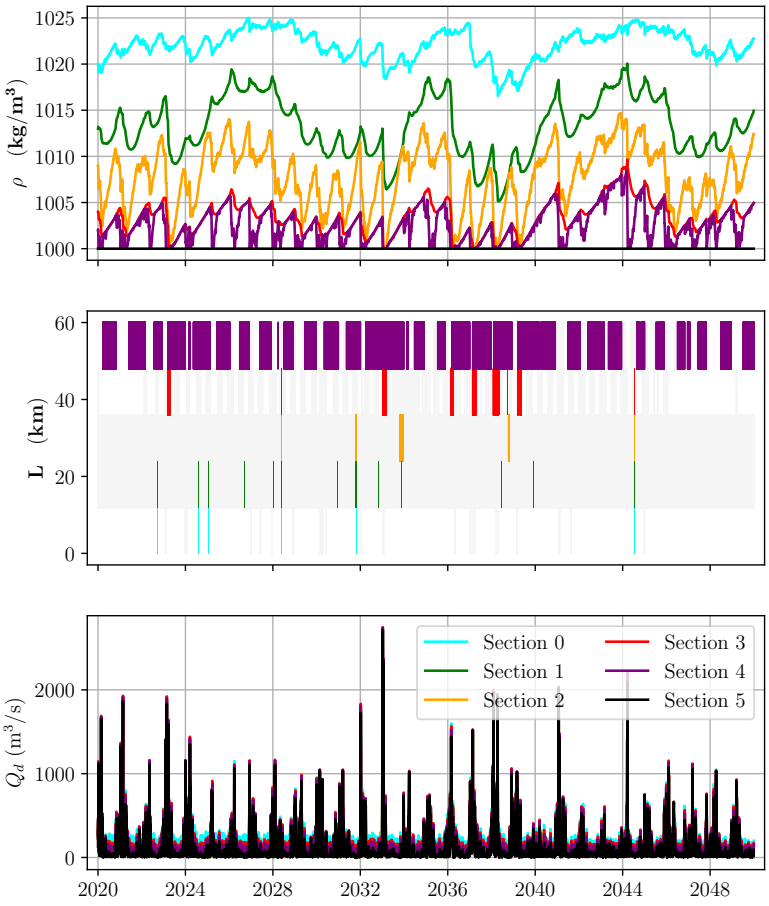

Figure 7.9: Results of the model in the scenario B. Mixing density (upper panel), box blockage (mid panel), and water mass exchange (lower panel).

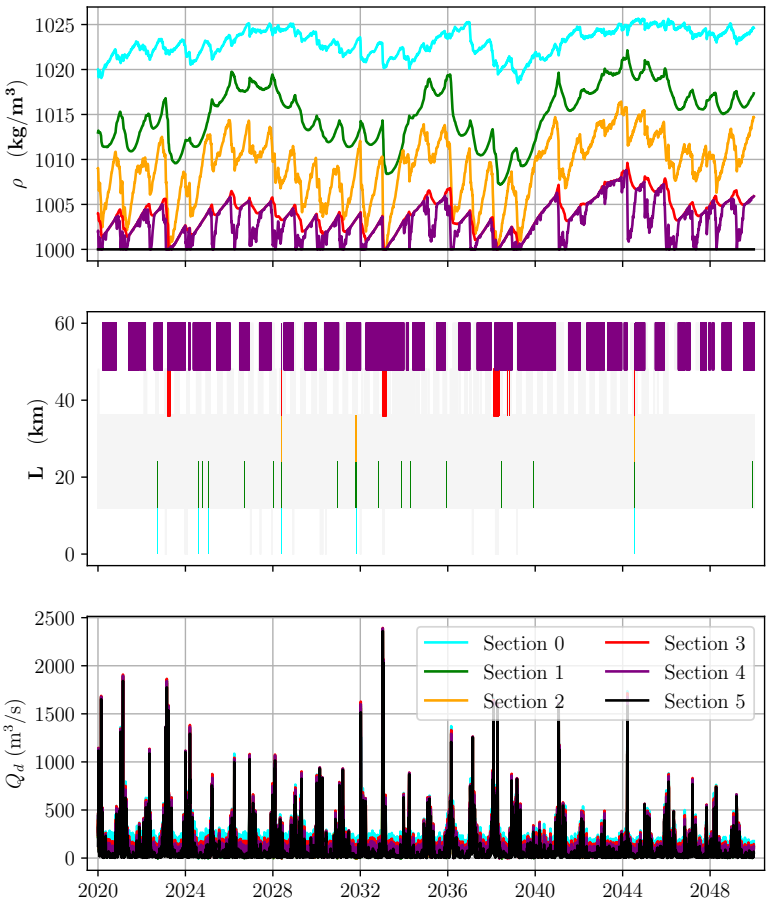

Figure 7.10: Results of the model in the case B1. Mixing density (upper panel), box blockage (mid panel), and water mass exchange (lower panel).

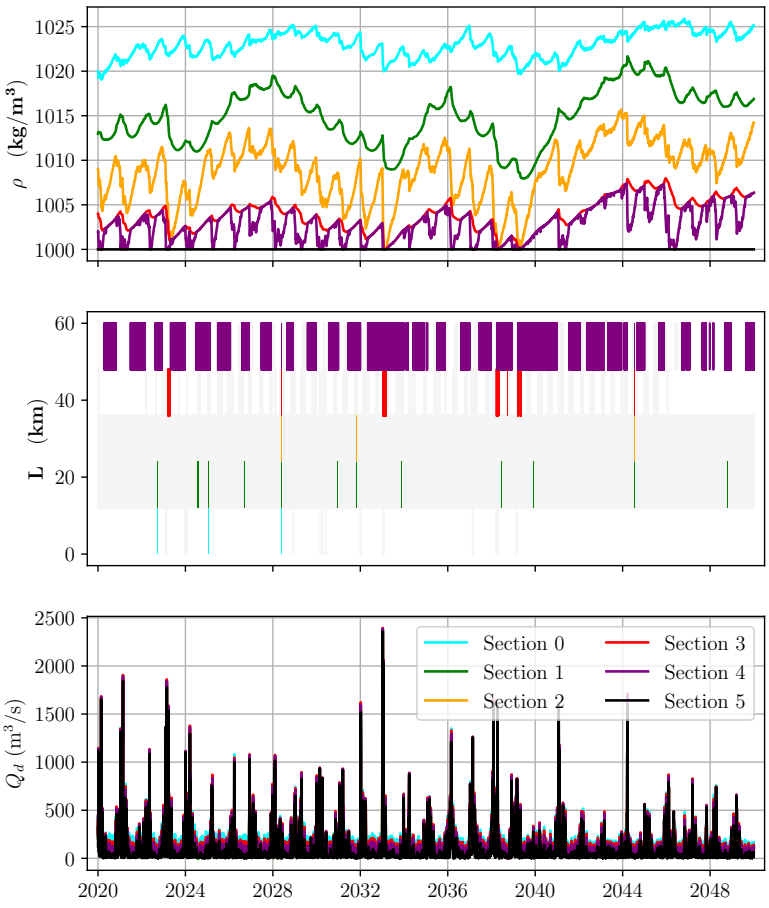

Figure 7.11: Results of the model in the case B2. Mixing density (upper panel), box blockage (mid panel), and water mass exchange (lower panel).

8. Conclusions and Future Research

"Each solution still gives rise to a new question as difficult as the foregoing, ..."

David Hume

During the last decade much knowledge was gained about estuarine dynamics. Previous work about the GRE has provided measurements, plausible hypotheses and arguments that allowed me to play with the information and give shape to it in an abstraction process with the aim of obtaining a simple and useful tool to help estuarine managers. It is time to give a step back and to examine some of the well-known local requirements or conditions imposed on the model that works at the temporal and spatial scale that managers require for decision making (chapter 7).

Along this thesis, findings of different branches of knowledge were used to pose and solve a problem and apply it to the particular situation of the Guadalquivir River Estuary. The present chapter gives a general overview of the main and subsidiary conclusions that respond to the objectives proposed in chapter 1 and focuses on the new challenges that appeared or were not treated in the thesis.

8.1 General and Specific Conclusions

The gap between the number of theoretical studies and the lack of practical applications of these evaluations are due to the fact that: a) a natural time lag may be necessary for decision-makers to identify, understand and actually use those studies, so, it may be too early to assess their usefulness; b) the skepticism about the reliability of the methodologies (Turner et al., 2003) combined with the high cost of carrying out those studies; c) the lack of economic expertise among decision-makers; and, d) the weak support of the regulatory system.

In this research thesis, a knowledge-based physical model capable to assess the consequences of human-induced actions in the Guadalquivir river estuary in regard to water quality has been

developed. The model accounts for the main estuarine hydrodynamic processes through mass and energy balances. More precisely, the model assesses the capacity of the estuary to exchange water mass with the adjacent sea and the flushing time. A semi-empirical methodology combined with statistics tools is used to simulate the future conditions to feed the several management scenarios and strategies proposed.

The specific objectives were defined to accomplish the main objective and are discussed in the following subsections.

8.1.1 The analysis and review of the estuarine processes that govern the dynamics of the Guadalquivir river estuary

The review and identification and characterization of the local estuarine processes in the GRE enable the proposal and assessment of some simplifying hypothesis such as the assumptions of a narrow, well-mixed to weakly-stratified estuary in which the Coriolis effect is negligible and where river flow is transversally uniform.

8.1.2 The development of a box model to represent the spatial-temporal energy balances within the estuary

A dynamic equation of the Longitudinal Anomaly of Potential Energy is developed to assess the longitudinal water mass exchange in a similar fashion to in Burchard and Hofmeister, 2008. After the simplifications due to the knowledge of local characteristics in regard to estuary shape and estuarine processes, a simple, useful and computationally efficient approach is proposed. These assumptions highlighted that five boxes are required to characterizated the estuarine processes; Stokes transport, tidal pumping, longitudinal advection and dispersion are important processes that have to be considered at GRE; the convergence of LAPE transport locate the estuarine turbidity maxima; and, finally, the differential advection and longitudinal dispersion are processes that recover the normal conditions of the estuary after high river discharges.

8.1.3 Model validation with episodes of low water quality during the past

The estuary is modeled by stretches or boxes where energy and mass balances are applied. It includes not only the effects of freshwater river flux, Stokes transport, solar radiation, and tidal and wind mixing, but also the tidal pumping term which was not considered in previous studies. It provides the water mixing density and water mass exchanges as the solution of a linear system of equations, which represents the LAPE conservation in the five interconnected stretches of the estuary. At the stretch where convergence equals friction is found a kind of sink of water mass due to the differences between Stokes transport and tidal pumping. Tidal transport under low river-flow regime showed landward semidiurnal transport at the upper section of the estuary.

8.1.4 Simulation of the agents that force the estuary with statistical, empirical and theoretical models

Some theoretical, empirical and hybrid formulations were proposed to provide a full characterization of the climatic conditions in the Guadalquivir River Estuary. They were verified with data from tidal gauges, quality stations, meteorological stations and hindcasted data. The water river discharge and the wind field were stochastically characterized and simulated using non-stationary probability models beside a vectorial autoregressive model. Water currents and sea surface elevations were adequately modeled using the model by Prandle and Rahman, 1980. Finally, surface solar radiation

was obtained with an empirical approach. As result, non-stationary climatic conditions, even of water discharge, is obtained. The water regulation showed a seasonal regulation which obey to weather seasons. Bi-modal wind direction and extreme conditions of water discharge and wind field are adequately reproduced.

8.1.5 Analysis of the trend of tidal constituents during low river-flow regime

Data from tidal gauges deployed by Puertos del Estado is analyzed, focusing not only on the estimation of the trends of the major tidal constituents (amplitudes and phases) but also on the physical interpretation of the observed changes. A characterization of tides along the Spanish coast based on semiannual and annual variability, tidal amplitude and phase and trends of tidal constituents is presented. The temporal variability of the M_2 should be included in the hydrodynamic and flood models, since its concomitance with storm events could lead to coastal flood extremes. At the GRE, the choking effect experienced by human activities such as land reclamation near inlet should be one factor that produce the observed negative trends of M_2 tidal amplitude at the mouth. At the head, the high positive rate (15.7 ± 1.0 mm/yr) should be due to an amplification due to resonance conditions within the estuary and channel deepening.

8.1.6 Proposal and analysis of management strategies aimed at increasing the ecological status of estuarine waters

The full model was applied to several management alternatives in order to evaluate the state of the water mass in terms of the flushing time and estuarine dynamics through the occurrence of blockage. The analysis illustrates the potential of the model to test the performance of different strategies. In particular, it is shown its capability to predict the estuary response to controlled river discharges. The model shows the location of water mass retention, the location with more blockage periods, and where the maximum flushing times are observed. The strategies used indicates that the ecological flow (minimum water discharge) should be in the range 80 - 120 m^3/s.

8.2 Analysis of strategies: future research lines

The results obtained in this thesis and the conclusions derived from them open several research lines related to the proposed hydrodynamic model and also to its ability to help managers in decision making about the multiple stressors that threaten the sustainability of estuarine systems and in particular the GRE; more precisely, questions about the regulation of water discharges, the effect of morphological changes and the legislative framework.

Water discharge regulation

It is a challenging task to perform a hydrological study taking into account the water demand upward of the dam to analyze the water regulation because of:

- The characterization and model of the water that is collected in the upstream dam will allow the effective control of the water discharge for instance to laminate the water discharges or reducing the high peaks that strongly altered the natural dynamic.
- The development of a warning system of rainfall to efficiently regulate the water reservoir capacity. As before, the extreme peaks of water discharges when the estuary does not need them should be controlled.
- The use of port branch or the construction of a storm water overflow tank may also improve the regulation of the impact of high-river discharges.

The later research lines highlighted that the strong impact of high-river discharge in the estuary is due to the human-induced modifications on tidal flat occupation, river shortening or the removal of the branches.

The proposed hydrodynamic model

The hydrodynamic model was set-up on different situations. Some of new research lines might:

- Improve the model by including longitudinal and lateral processes that might be important at the seaward part of the estuary (Losada et al., 2017).
- Improve the model by including the sediment resuspension that is critic during high-river conditions and the post-recovery regime.
- Explore the blockage conditions for other management strategies and search for optimum alternatives to improve the water conditions.
- Implement and verify some new strategies proposed in real conditions.

Some Morphological Changes

As previous environmental research show, some morphological modifications of the estuary might modify the estuarine hydrodynamic, which, as it was seen in this thesis, may improve the water quality. Therefore, it should be necessary:

- To study the possibility of recovering the tidal marshes that reduce the impact of high river discharges (the flow in the main channel will decrease).
- To study the possibility of recovering old river arms whose action allows a similar reduction of the peaks of the high-river discharges.

Legislative Framework

Some legislative efforts are also necessary to update and enhance the current planning. Specifically, it should be addressed:

- the creation of new indicators to evaluate the hydromorphological quality of estuaries, such as hydrologic alteration, fluvial habitat and riverbank vegetation,
- the update of the Hydrological Planning accounting for the new model that leads to excellent opportunities to manage the estuary based on knowledge.

Furthermore, some of the proposed strategies as the density regulation may impact on the fish community. A constant water density (which will exhibit nearly constant water salinity) may alter the fish habitats. Some studies about this issue should be also addressed.

At the light of the present thesis, it exists enough information about the exchange water masses, maximum and minimum flow in accordance to the natural behavior of the estuary or ecological flows for the transitional waters to update the management strategies regarding the ecological flow at Guadalquivir River Estuary.

Bibliography

Books

Codiga, D. L. (2011). *Unified tidal analysis and prediction using the UTide Matlab functions*. Graduate School of Oceanography, University of Rhode Island Narragansett, RI.

Dean, R. G. and Dalrymple, R. A. (1991). *Water wave mechanics for engineers and scientists*. Volume 2. World Scientific Publishing Company.

Dronkers, J. (2005). *Dynamics of coastal systems*.

Dyer, K. R. (1973). *Estuaries: a physical introduction*. John Wiley and Sons: Londen. ISBN: 0471-22905-9.

Girard, A. (2006). *La rivalidad comercial y marítima entre Sevilla y Cádiz: hasta finales del siglo XVIII*. Volume 4. Editorial Renacimiento.

Lütkepohl, H. (2005). *New introduction to multiple time series analysis*. Springer Science & Business Media.

Miranda, L. B. de, Andutta, F. P., Kjerfve, B., and Castro Filho, B. M. de (2017). *Fundamentals of Estuarine Physical Oceanography*. Volume 8. Springer.

Natrella, M., Croarkin, C., and Guthrie, W. (2003). *Engineering Statistics Handbook*. Statistical Engineering Division, NIST2003.

Officer, C. B. (2013). *Physical Oceanography Of Estuarines*. john wiley.

Pritchard, D. W. (1960). *The movement and mixing of contaminants in tidal estuaries*. publisher not identified.

Pugh, D. and Woodworth, P. (2014). *Sea-level science: understanding tides, surges, tsunamis and mean sea-level changes*. Cambridge University Press.

Pugh, D. T. (1996). *Tides, surges and mean sea-level (reprinted with corrections)*. John Wiley & Sons Ltd.

Savenije, H. H. (2005). *Salinity and tides in alluvial estuaries*. Elsevier.

Simpson, J. H. and Sharples, J. (2012). *Introduction to the physical and biological oceanography of shelf seas*. Cambridge University Press.

Valle-Levinson, A. (2010). *Contemporary issues in estuarine physics*. Cambridge University Press.

Articles

Agua, O. d. l. P. del (2014). "Evaluación del primer ciclo de planificación". In: *Urbana* 5347.13.

Aken, H. M. van (1986). "The onset of seasonal stratification in shelf seas due to differential advection in the presence of a salinity gradient". In: *Continental Shelf Research* 5.4, pages 475–485.

Alebregtse, N. and Swart, H. de (2016). "Effect of river discharge and geometry on tides and net water transport in an estuarine network, an idealized model applied to the Yangtze Estuary". In: *Continental Shelf Research* 123, pages 29–49.

Álvarez, O., Tejedor, B., and Vidal, J. (2001). "La dinámica de marea en el estuario del Guadalquivir: un caso peculiar de resonancia antrópica". In: *Física de la Tierra* 13, pages 11–24.

Antonov, J. I., Levitus, S., and Boyer, T. P. (2002). "Steric sea level variations during 1957–1994: Importance of salinity". In: *Journal of Geophysical Research: Oceans* 107.C12.

Araújo, I. B. and Pugh, D. T. (2008). "Sea levels at Newlyn 1915–2005: analysis of trends for future flooding risks". In: *Journal of Coastal Research* 24.sp3, pages 203–212.

Austin, J. A. (2002). "Estimating the mean ocean-bay exchange rate of the Chesapeake Bay". In: *Journal of Geophysical Research: Oceans* 107.C11.

Barranco, L. M., álvarez-Rodríguez, J., Olivera, F., Potenciano, á., Quintas, L., and Estrada, F. (2013). "Assessment of the expected runoff change in Spain using climate simulations". In: *Journal of Hydrologic Engineering* 19.7, pages 1481–1490.

Basdurak, N., Huguenard, K., Valle-Levinson, A., Li, M., and Chant, R. (2017). "Parameterization of mixing by secondary circulation in estuaries". In: *Journal of Geophysical Research: Oceans*.

Becker, M., Karpytchev, M., and Lennartz-Sassinek, S. (2014). "Long-term sea level trends: Natural or anthropogenic?" In: *Geophysical Research Letters* 41.15, pages 5571–5580.

Becherer, J., Flöser, G., Umlauf, L., and Burchard, H. (2016). "Estuarine circulation versus tidal pumping: Sediment transport in a well-mixed tidal inlet". In: *Journal of Geophysical Research: Oceans* 121.8, pages 6251–6270.

Bowden, K., Fairbairn, L., and Hughes, P. (1959). "The distribution of shearing stresses in a tidal current". In: *Geophysical Journal International* 2.4, pages 288–305.

Bowden, K. (1981). "Turbulent mixing in estuaries". In: *Ocean Management* 6.2-3, pages 117–135.

Box, G. E. and Cox, D. R. (1964). "An analysis of transformations". In: *Journal of the Royal Statistical Society: Series B (Methodological)* 26.2, pages 211–243.

Burchard, H. and Hofmeister, R. (2008). "A dynamic equation for the potential energy anomaly for analysing mixing and stratification in estuaries and coastal seas". In: *Estuarine, Coastal and Shelf Science* 77.4, pages 679–687.

Burchard, H. and Hetland, R. D. (2010). "Quantifying the contributions of tidal straining and gravitational circulation to residual circulation in periodically stratified tidal estuaries". In: *Journal of Physical Oceanography* 40.6, pages 1243–1262.

Burchard, H. and Schuttelaars, H. M. (2012). "Analysis of tidal straining as driver for estuarine circulation in well-mixed estuaries". In: *Journal of Physical Oceanography* 42.2, pages 261–271.

Burchard, H., Schuttelaars, H. M., and Geyer, W. R. (2013). "Residual sediment fluxes in weakly-to-periodically stratified estuaries and tidal inlets". In: *Journal of Physical Oceanography* 43.9, pages 1841–1861.

Burchard, H., Schuttelaars, H. M., and Ralston, D. K. (2018). "Sediment trapping in estuaries". In: *Annual review of marine science* 10, pages 371–395.

Caballero, I., Morris, E., Prieto, L., and Navarro, G. (2014). "The influence of the Guadalquivir River on spatio-temporal variability of suspended solids and chlorophyll in the Eastern Gulf of Cádiz". In: *Mediterranean Marine Science* 15.4, pages 721–738.

Cai, H., Toffolon, M., and Savenije, H. H. (2016). "An analytical approach to determining resonance in semi-closed convergent tidal channels". In: *Coastal Engineering Journal* 58.03, page 1650009.

Cartwright, D. and Edden, A. C. (1973). "Corrected tables of tidal harmonics". In: *Geophysical journal international* 33.3, pages 253–264.

CEDEX (2010). "Evaluación del impacto del cambio climático en los recursos hıdricos en régimen natural". In:

Church, J. A., Aarup, T., Woodworth, P. L., Wilson, W. S., Nicholls, R. J., Rayner, R., Lambeck, K., Mitchum, G. T., Steffen, K., Cazenave, A., et al. (2010). "Sea-level rise and variability: synthesis and outlook for the future". In: *Understanding sea-level rise and variability*, pages 402–419.

Church, J. A. and White, N. J. (2011). "Sea-level rise from the late 19th to the early 21st century". In: *Surveys in geophysics* 32.4-5, pages 585–602.

Cobos, M., Baquerizo, A., Díez-Minguito, M., and Losada, M. (2020). "A Subtidal Box Model based on the Longitudinal Anomaly of Potential Energy for Narrow Estuaries. An Application to the Guadalquivir River Estuary (SW Spain)". In: *Journal of Geophysical Research: Oceans*. DOI: 10.1029/2019JC015242.

Contreras, E. and Polo, M. (2012). "Measurement frequency and sampling spatial domains required to characterize turbidity and salinity events in the Guadalquivir estuary (Spain)". In: *Natural Hazards and Earth System Sciences* 12.8, pages 2581–2589.

Cronin, E. (1967). "The role of man in estuarine processes". In:

Cushman-Roisin, B. (1994). "Introduction to geophysical fluid dynamics Prentice-Hall". In: *Englewood Cliffs, NJ* 7632.

Dalrymple, R. (1992). "A conceptual model of estuarine sedimentation". In: *Journal of Sedimentary Petrology* 62, pages 1130–1146.

De Boer, G. J., Pietrzak, J. D., and Winterwerp, J. C. (2008). "Using the potential energy anomaly equation to investigate tidal straining and advection of stratification in a region of freshwater influence". In: *Ocean Modelling* 22.1-2, pages 1–11.

Devlin, A. T., Jay, D. A., Zaron, E. D., Talke, S. A., Pan, J., and Lin, H. (2017). "Tidal variability related to sea level variability in the Pacific Ocean". In: *Journal of Geophysical Research: Oceans* 122.11, pages 8445–8463.

Dickey, D. A. and Fuller, W. A. (1979). "Distribution of the estimators for autoregressive time series with a unit root". In: *Journal of the American statistical association* 74.366a, pages 427–431.

Díez-Minguito, M., Baquerizo, A., Ortega-Sánchez, M., Navarro, G., and Losada, M. (2012). "Tide transformation in the Guadalquivir estuary (SW Spain) and process-based zonation". In: *Journal of Geophysical Research: Oceans* 117.C3.

Díez-Minguito, M., Contreras, E., Polo, M., and Losada, M. (2013). "Spatio-temporal distribution, along-channel transport, and post-riverflood recovery of salinity in the Guadalquivir estuary (SW Spain)". In: *Journal of Geophysical Research: Oceans* 118.5, pages 2267–2278.

Díez-Minguito, M., Baquerizo, A., Swart, H. de, and Losada, M. (2014). "Structure of the turbidity field in the Guadalquivir estuary: Analysis of observations and a box model approach". In: *Journal of Geophysical Research: Oceans* 119.10, pages 7190–7204.

Díez-Minguito and Swart, H. de (2018). "Obervational evidences of strain-induced periodics stratification (SIPS) in the Guadalquivir Estuary". In:

— (2020). "Relationships between Chlorophyll-a and Suspended Sediment Concentration in a High-nutrient Load Estuary: An Observational and Idealized Modeling Approach". In: *Journal of Geophysical Research: Oceans*. DOI: 10.1029/2019JC015188.

Dionne, J. (1963). "Towards a more adequate definition of the St. Lawrence estuary". In: *Zeitschrift fur Geomorphologie* 7, pages 36–44.

Dronkers, J. J. (1964). "Tidal computations in rivers and coastal waters". In:

Du, J., Shen, J., Zhang, Y. J., Ye, F., Liu, Z., Wang, Z., Wang, Y. P., Yu, X., Sisson, M., and Wang, H. V. (2018). "Tidal response to sea-level rise in different types of estuaries: the importance of length, bathymetry, and geometry". In: *Geophysical Research Letters*.

Fairbridge, R. (1980). "The estuary: its definition and geodynamic cycle". In: *Chemistry and biochemistry of estuaries*.

Fanjul, E. A., Gomez, B. P., Carretero, J. C., and Arevalo, I. R. S. (1998). "Tide and surge dynamics along the Iberian Atlantic coast". In: *Oceanologica Acta* 21.2. International Conference on Oceanography of the Bay of Biscay, pages 131–143. ISSN: 0399-1784.

Feely, R. A., Alin, S. R., Newton, J., Sabine, C. L., Warner, M., Devol, A., Krembs, C., and Maloy, C. (2010). "The combined effects of ocean acidification, mixing, and respiration on pH and carbonate saturation in an urbanized estuary". In: *Estuarine, Coastal and Shelf Science* 88.4, pages 442–449.

Ferrarin, C., Tomasin, A., Bajo, M., Petrizzo, A., and Umgiesser, G. (2015). "Tidal changes in a heavily modified coastal wetland". In: *Continental Shelf Research* 101, pages 22–33.

Ganju, N. K., Brush, M. J., Rashleigh, B., Aretxabaleta, A. L., Del Barrio, P., Grear, J. S., Harris, L. A., Lake, S. J., McCardell, G., O'Donnell, J., et al. (2016). "Progress and challenges in coupled hydrodynamic-ecological estuarine modeling". In: *Estuaries and coasts* 39.2, pages 311–332.

Garvine, R. W. and Whitney, M. M. (2006). "An estuarine box model of freshwater delivery to the coastal ocean for use in climate models". In: *Journal of Marine Research* 64.2, pages 173–194.

Geyer, W. R., Chant, R., and Houghton, R. (2008). "Tidal and spring-neap variations in horizontal dispersion in a partially mixed estuary". In: *Journal of Geophysical Research: Oceans* 113.C7.

Geyer, W. R. and MacCready, P. (2014). "The estuarine circulation". In: *Annual Review of Fluid Mechanics* 46.

Geyer, W. R. (1993). "The importance of suppression of turbulence by stratification on the estuarine turbidity maximum". In: *Estuaries* 16.1, pages 113–125.

Giddings, S. and MacCready, P. (2017). "Reverse Estuarine Circulation Due to Local and Remote Wind Forcing, Enhanced by the Presence of Along-Coast Estuaries". In: *Journal of Geophysical Research: Oceans* 122.12, pages 10184–10205.

Godin, G. (1983). "On the predictability of currents". In: *The International Hydrographic Review* 60.1.

— (1986). "Is the abnormal response of the tide at the frequency of S2 really due to radiational effects?" In: *Continental Shelf Research* 6.5, pages 615–625.

Gräwe, U., Burchard, H., Müller, M., and Schuttelaars, H. M. (2014). "Seasonal variability in M2 and M4 tidal constituents and its implications for the coastal residual sediment transport". In: *Geophysical Research Letters* 41.15, pages 5563–5570.

Hamilton, P., Gunn, J. T., and Cannon, G. A. (1985). "A box model of Puget Sound". In: *Estuarine, Coastal and Shelf Science* 20.6, pages 673–692.

Hansen, D. V. and Rattray, M. (1966). "New dimensions in estuary classification". In: *Limnology and Oceanography* 11.3, pages 319–326.

Hill, D. F. (2016). "Spatial and temporal variability in tidal range: evidence, causes, and effects". In: *Current Climate Change Reports* 2.4, pages 232–241.

Hobbie, J. E. (2000). "Estuarine science: the key to progress in coastal ecological research". In: *Estuarine science: A synthetic approach to research and practice*, pages 1–11.

Hofmeister, R., Burchard, H., and Bolding, K. (2009). "A three-dimensional model study on processes of stratification and de-stratification in the Limfjord". In: *Continental Shelf Research* 29.11-12, pages 1515–1524.

Holleman, R. C. and Stacey, M. T. (2014). "Coupling of sea level rise, tidal amplification, and inundation". In: *Journal of Physical Oceanography* 44.5, pages 1439–1455.

Hunt, J. (1964). "Tidal oscillations in estuaries". In: *Geophysical Journal International* 8.4, pages 440–455.

Ianniello, J. P. (1979). "Tidally induced residual currents in estuaries of variable breadth and depth". In: *Journal of Physical Oceanography* 9.5, pages 962–974.

Ippen, A. T. (1966). "Estuary and coastline hydrodynamics". In:

Jäger, W. S., Nagler, T., Czado, C., and McCall, R. T. (2019). "A statistical simulation method for joint time series of non-stationary hourly wave parameters". In: *Coastal Engineering* 146, pages 14–31.

Jay, D. A. and Smith, J. D. (1990). "Residual circulation in shallow estuaries: 2. Weakly stratified and partially mixed, narrow estuaries". In: *Journal of Geophysical Research: Oceans* 95.C1, pages 733–748.

Jay, D. A. and Musiak, J. D. (1994). "Particle trapping in estuarine tidal flows". In: *Journal of Geophysical Research: Oceans* 99.C10, pages 20445–20461.

— (1996). "Internal tidal asymmetry in channel flows: Origins and consequences". In: *Coastal and Estuarine Studies*, pages 211–249.

Jay, D. A. (2009). "Evolution of tidal amplitudes in the eastern Pacific Ocean". In: *Geophysical Research Letters* 36.4.

Jevrejeva, S., Moore, J. C., and Grinsted, A. (2012). "Sea level projections to AD2500 with a new generation of climate change scenarios". In: *Global and Planetary Change* 80, pages 14–20.

Jonge, V. N. de, Schuttelaars, H. M., Beusekom, J. E. van, Talke, S. A., and Swart, H. E. de (2014). "The influence of channel deepening on estuarine turbidity levels and dynamics, as exemplified by the Ems estuary". In: *Estuarine, Coastal and Shelf Science* 139, pages 46–59.

Kallis, G. and Butler, D. (2001). "The EU water framework directive: measures and implications". In: *Water policy* 3.2, pages 125–142.

Kwiatkowski, D., Phillips, P. C., Schmidt, P., and Shin, Y. (1992). "Testing the null hypothesis of stationarity against the alternative of a unit root: How sure are we that economic time series have a unit root?" In: *Journal of econometrics* 54.1-3, pages 159–178.

Lennartz, S. and Bunde, A. (2009). "Trend evaluation in records with long-term memory: Application to global warming". In: *Geophysical Research Letters* 36.16.

Leschine, T. M., Ferriss, B. E., Bell, K. P., Bartz, K. K., MacWilliams, S., Pico, M., and Bennett, A. K. (2003). "Challenges and strategies for better use of scientific information in the management of coastal estuaries". In: *Estuaries* 26.4, pages 1189–1204.

Lira-Loarca, A., Cobos, M., Losada, M. A., and Baquerizo, A. (2020). "Storm characterization and simulation for damage evolution models of maritime structures". In: *Coastal Engineering* 92, pages 15–34.

López-Ruiz, A., Ortega-Sánchez, M., Baquerizo, A., Navidad, D., and Losada, M. Á. (2012). "Nonuniform alongshore sediment transport induced by coastline curvature". In: *Coastal engineering proceedings* 1.33, page 29.

Losada, M., Díez-Minguito, M., and Reyes-Merlo, M. (2017). "Tidal-fluvial interaction in the Guadalquivir River Estuary: Spatial and frequency-dependent response of currents and water levels". In: *Journal of Geophysical Research: Oceans* 122.2, pages 847–865.

Luketina, D. (1998). "Simple tidal prism models revisited". In: *Estuarine, Coastal and Shelf Science* 46.1, pages 77–84.

Malone, T., Crocker, L., Pike, S., and Wendler, B. (1988). "Influences of river flow on the dynamics of phytoplankton production in a partially stratified estuary." In: *Marine ecology progress series. Oldendorf* 48.3, pages 235–249.

Marcos, M., Gomis, D., Monserrat, S., Álvarez-Fanjul, E., Pérez, B., and García-Lafuente, J. (2005). "Consistency of long sea-level time series in the northern coast of Spain". In: *Journal of Geophysical Research: Oceans* 110.C3.

Marcos, M., Puyol, B., Wöppelmann, G., Herrero, C., and García-Fernández, M. J. (2011). "The long sea level record at Cadiz (southern Spain) from 1880 to 2009". In: *Journal of Geophysical Research: Oceans* 116.C12.

Marcos, M., Marzeion, B., Dangendorf, S., Slangen, A. B., Palanisamy, H., and Fenoglio-Marc, L. (2016). "Internal variability versus anthropogenic forcing on sea level and its components". In: *Surveys in Geophysics* 38.1, pages 329–348.

Mawdsley, R. J., Haigh, I. D., and Wells, N. C. (2015). "Global secular changes in different tidal high water, low water and range levels". In: *Earthś Future* 3.2, pages 66–81.

Meehl, G. A., Stocker, T. F., Collins, W. D., Friedlingstein, P., Gaye, T., Gregory, J. M., Kitoh, A., Knutti, R., Murphy, J. M., Noda, A., et al. (2007). "Global climate projections". In:

Merrifield, M. A. (2011). "A shift in western tropical Pacific sea level trends during the 1990s". In: *Journal of Climate* 24.15, pages 4126–4138.

Miles, J. W. (1961). "On the stability of heterogeneous shear flows". In: *Journal of Fluid Mechanics* 10.4, pages 496–508.

Monismith, S. G., Kimmerer, W., Burau, J. R., and Stacey, M. T. (2002). "Structure and flow-induced variability of the subtidal salinity field in northern San Francisco Bay". In: *Journal of Physical Oceanography* 32.11, pages 3003–3019.

Monismith, S. G., Burau, J. R., and Stacey, M. (1996). "Stratification dynamics and gravitational circulation in northern San Francisco Bay". In: *San Francisco Bay: The Ecosystem*, pages 123–153.

Morales, J. A. and Borrego, J. (2008). "El litoral de Huelva: fisiografía y dinámica". In:

Moral, L. del (2018). "La navegación en el estuario del Guadalquivir. Dimensiones ecológicas, económicas, sociales, jurídicas y políticas". In:

Müller, M., Cherniawsky, J. Y., Foreman, M. G., and Storch, J.-S. von (2014). "Seasonal variation of the M 2 tide". In: *Ocean Dynamics* 64.2, pages 159–177.

Müller, M. (2012). "The influence of changing stratification conditions on barotropic tidal transport and its implications for seasonal and secular changes of tides". In: *Continental Shelf Research* 47, pages 107–118.

Munk, W., Dzieciuch, M., and Jayne, S. (2002). "Millennial climate variability: Is there a tidal connection?" In: *Journal of climate* 15.4, pages 370–385.

Munk, W. and Bills, B. (2007). "Tides and the climate: some speculations". In: *Journal of Physical Oceanography* 37.2, pages 135–147.

Navarro, G., Gutiérrez, F. J., Díez-Minguito, M., Losada, M. A., and Ruiz, J. (2011). "Temporal and spatial variability in the Guadalquivir estuary: a challenge for real-time telemetry". In: *Ocean Dynamics* 61.6, pages 753–765.

Navarro, G., Huertas, I. E., Costas, E., Flecha, S., Dıez-Minguito, M., Caballero, I., López-Rodas, V., Prieto, L., and Ruiz, J. (2012). "Use of a real-time remote monitoring network (RTRM) to characterize the Guadalquivir estuary (Spain)". In: *Sensors* 12.2, pages 1398–1421.

Officer, C. B. (1976). "Physical oceanography of estuaries (and associated coastal waters)". In:

Officer, C. (1980). "Box models revisited". In: *Estuarine and wetland processes with emphasis on modeling*, pages 65–114.

Osafune, S., Masuda, S., and Sugiura, N. (2014). "Role of the oceanic bridge in linking the 18.6 year modulation of tidal mixing and long-term SST change in the North Pacific". In: *Geophysical Research Letters* 41.20, pages 7284–7290.

Pachauri, R. K., Allen, M. R., Barros, V. R., Broome, J., Cramer, W., Christ, R., Church, J. A., Clarke, L., Dahe, Q., Dasgupta, P., et al. (2014). "Climate change 2014: synthesis report. Contribution of Working Groups I". In: *II and III to the fifth assessment report of the Intergovernmental Panel on Climate Change* 151.

Padilla, E. M., Díez-Minguito, M., Ortega-Sánchez, M., and Losada, M. A. (2016). "A Subtidal Model of Temperature for a Well-Mixed Narrow Estuary: the Guadalquivir River Estuary (SW Spain)". In: *Estuaries and coasts* 39.3, pages 605–620.

Parker, B. B. (1991). "Tidal interactions". In: *Tidal hydrodynamics* 237.

Pethick, J. (2002). "Estuarine and tidal wetland restoration in the United Kingdom: policy versus practice". In: *Restoration Ecology* 10.3, pages 431–437.

Prandle, D. and Rahman, M. (1980). "Tidal response in estuaries". In: *Journal of Physical Oceanography* 10.10, pages 1552–1573.

Prandle, D. (1981). "Salinity intrusion in estuaries". In: *Journal of Physical Oceanography* 11.10, pages 1311–1324.

Pritchard, D. (1955). "Estuarine circulation patterns". In: *Proc. Amer. Sco. Civil Eng.* 81, pages 1–11.

Ray, R. and Merrifield, M. (2019). "The Semiannual and 4.4-year Modulations of Extreme High Tides". In: *Journal of Geophysical Research: Oceans*.

Ray, R. D. (2009). "Secular changes in the solar semidiurnal tide of the western North Atlantic Ocean". In: *Geophysical Research Letters* 36.19.

Reyes-Merlo, M. á., Díez-Minguito, M., Ortega-Sánchez, M., Baquerizo, A., and Losada, M. A. (2013). "On the relative influence of climate forcing agents on the saline intrusion in a well-mixed estuary: Medium-term Monte Carlo predictions". In: *Journal of Coastal Research* 65.sp2, pages 1200–1205.

Reyes-Merlo, M. á., Ortega-Sánchez, M., Díez-Minguito, M., and Losada, M. A. (2017). "Efficient dredging strategy in a tidal inlet based on an energetic approach". In: *Ocean & Coastal Management* 146, pages 157–169.

Rice, A. E., Whitney, M. M., Garvine, R. W., and Huq, P. (2008). "Energetics in Delaware Bay: Comparison of two box models with observations". In: *Journal of Marine Research* 66.6, pages 873–898.

Ross, A. C., Najjar, R. G., Li, M., Lee, S. B., Zhang, F., and Liu, W. (2017). "Fingerprints of Sea Level Rise on Changing Tides in the Chesapeake and Delaware Bays". In: *Journal of Geophysical Research: Oceans* 122.10, pages 8102–8125.

Ruiz, J., Macías, D., Losada, M., Díez-Minguito, M., and Prieto, L. (2013). "A simple biogeochemical model for estuaries with high sediment loads: Application to the Guadalquivir River (SW Iberia)". In: *Ecological modelling* 265, pages 194–206.

Sakamoto, Y., Ishiguro, M., and Kitagawa, G. (1986). "Akaike information criterion statistics". In: *Dordrecht, The Netherlands: D. Reidel*, page 81.

Savenije, H. H., Toffolon, M., Haas, J., and Veling, E. J. (2008). "Analytical description of tidal dynamics in convergent estuaries". In: *Journal of Geophysical Research: Oceans* 113.C10.

Schindelegger, M., Green, J., Wilmes, S.-B., and Haigh, I. (2018). "Can we model the effect of observed sea level rise on tides?" In: *Journal of Geophysical Research: Oceans*.

Schwarz, G. (1978). "Estimating the dimension of a model". In: *The annals of statistics* 6.2, pages 461–464.

Scully, M. E., Friedrichs, C., and Brubaker, J. (2005). "Control of estuarine stratification and mixing by wind-induced straining of the estuarine density field". In: *Estuaries* 28.3, pages 321–326.

Scully, M. E. and Friedrichs, C. T. (2007). "Sediment pumping by tidal asymmetry in a partially mixed estuary". In: *Journal of Geophysical Research: Oceans* 112.C7.

Shaw, A. and Tsimplis, M. (2010). "The 18.6 yr nodal modulation in the tides of Southern European coasts". In: *Continental Shelf Research* 30.2, pages 138–151.

Sheldon, J. E. and Alber, M. (2002). "A comparison of residence time calculations using simple compartment models of the Altamaha River Estuary, Georgia". In: *Estuaries* 25.6, pages 1304–1317.

— (2006). “The calculation of estuarine turnover times using freshwater fraction and tidal prism models: a critical evaluation”. In: *Estuaries and Coasts* 29.1, pages 133–146.

Siles-Ajamil, R., Díez-Minguito, M., and Losada, M. (2019). “Tide propagation and salinity distribution response to changes in water depth and channel network in the Guadalquivir River Estuary: An exploratory model approach”. In: *Ocean & Coastal Management* 174, pages 92–107.

Simpson, J. and Hunter, J. (1974). “Fronts in the Irish sea”. In: *Nature* 250.5465, page 404.

Simpson, J. and Bowers, D. (1981). “Models of stratification and frontal movement in shelf seas”. In: *Deep Sea Research Part A. Oceanographic Research Papers* 28.7, pages 727–738.

Simpson, J. H., Brown, J., Matthews, J., and Allen, G. (1990). “Tidal straining, density currents, and stirring in the control of estuarine stratification”. In: *Estuaries and Coasts* 13.2, pages 125–132.

Simpson, J., Sharples, J., and Rippeth, T. (1991). “A prescriptive model of stratification induced by freshwater runoff”. In: *Estuarine, Coastal and Shelf Science* 33.1, pages 23–35.

Simpson, J. (1981). “The shelf-sea fronts: implications of their existence and behaviour”. In: *Phil. Trans. R. Soc. Lond. A* 302.1472, pages 531–546.

— (1997). “Physical processes in the ROFI regime”. In: *Journal of marine systems* 12.1-4, pages 3–15.

Smith, R. (1976). “Longitudinal dispersion of a buoyant contaminant in a shallow channel”. In: *Journal of Fluid Mechanics* 78.4, pages 677–688.

Solari, S. and Losada, M. a. (Sept. 2011). “Non-stationary wave height climate modeling and simulation”. In: *Journal of Geophysical Research: Oceans* 116.C9, page C09032.

Song, D., Wang, X. H., Zhu, X., and Bao, X. (2013). “Modeling studies of the far-field effects of tidal flat reclamation on tidal dynamics in the East China Seas”. In: *Estuarine, Coastal and Shelf Science* 133, pages 147–160.

Souza, A. and Simpson, J. (1996). “The modification of tidal ellipses by stratification in the Rhine ROFI”. In: *Continental Shelf Research* 16.8, pages 997–1007.

Stacey, M. T., Burau, J. R., and Monismith, S. G. (2001). “Creation of residual flows in a partially stratified estuary”. In: *Journal of Geophysical Research: Oceans* 106.C8, pages 17013–17037.

Stacey, M. T. and Ralston, D. K. (2005). “The scaling and structure of the estuarine bottom boundary layer”. In: *Journal of Physical Oceanography* 35.1, pages 55–71.

Stark, J., Oyen, T., Meire, P., and Temmerman, S. (2015). “Observations of tidal and storm surge attenuation in a large tidal marsh”. In: *Limnology and Oceanography* 60.4, pages 1371–1381.

Stommel, H. (1961). “Thermohaline convection with two stable regimes of flow”. In: *Tellus* 13.2, pages 224–230.

Sun, Q., Whitney, M. M., Bryan, F. O., and Tseng, Y.-h. (2017). “A box model for representing estuarine physical processes in Earth system models”. In: *Ocean Modelling* 112, pages 139–153.

Talke, S., Swart, H. de, and Schuttelaars, H. (2008). “An analytical model of the equilibrium distribution of suspended sediment in an estuary”. In: *Dohmen-Janssen and Hulscher, eds: River, coastal and estuarine morphodynamics 2008*, pages 403–411.

Talke, S. A., Swart, H. E. de, and De Jonge, V. (2009). “An idealized model and systematic process study of oxygen depletion in highly turbid estuaries”. In: *Estuaries and coasts* 32.4, pages 602–620.

Talke, S., Kemp, A., and Woodruff, J. (2018). “Relative Sea Level, Tides, and Extreme Water Levels in Boston Harbor From 1825 to 2018”. In: *Journal of Geophysical Research: Oceans* 123.

Talke, S. A. and Jay, D. A. (2019). “Changing Tides: The Role of Natural and Anthropogenic Factors”. In: *Annual review of marine science* 12.

Thompson, S. and Turner, J. (1975). “Mixing across an interface due to turbulence generated by an oscillating grid”. In: *Journal of Fluid Mechanics* 67.2, pages 349–368.

Torrence, C. and Compo, G. P. (1998). "A practical guide to wavelet analysis". In: *Bulletin of the American Meteorological society* 79.1, pages 61–78.

Tsimplis, M. N. and Josey, S. A. (2001). "Forcing of the Mediterranean Sea by atmospheric oscillations over the North Atlantic". In: *Geophysical Research Letters* 28.5, pages 803–806.

Tsimplis, M., Spada, G., Marcos, M., and Flemming, N. (2011). "Multi-decadal sea level trends and land movements in the Mediterranean Sea with estimates of factors perturbing tide gauge data and cumulative uncertainties". In: *Global and Planetary Change* 76.1-2, pages 63–76.

Turner, R. K., Paavola, J., Cooper, P., Farber, S., Jessamy, V., and Georgiou, S. (2003). "Valuing nature: lessons learned and future research directions". In: *Ecological economics* 46.3, pages 493–510.

Turner, J. and Kraus, E. (1967). "A one-dimensional model of the seasonal thermocline I. A laboratory experiment and its interpretation". In: *Tellus* 19.1, pages 88–97.

Valle-Levinson, A. (2008). "Density-driven exchange flow in terms of the Kelvin and Ekman numbers". In: *Journal of Geophysical Research: Oceans* 113.C4.

Vaz, R. A. N., Lennon, G. W., and Silva Samarasinghe, J. R. de (1989). "The negative role of turbulence in estuarine mass transport". In: *Estuarine, Coastal and Shelf Science* 28.4, pages 361–377.

Wang, Z. B., Winterwerp, J. C., and He, Q. (2014). "Interaction between suspended sediment and tidal amplification in the Guadalquivir Estuary". In: *Ocean Dynamics* 64.10, pages 1487–1498.

Wiles, P. J., Duren, L. A. van, Häse, C., Larsen, J., and Simpson, J. H. (2006). "Stratification and mixing in the Limfjorden in relation to mussel culture". In: *Journal of marine systems* 60.1-2, pages 129–143.

Winterwerp, J. C. and Wang, Z. B. (2013). "Man-induced regime shifts in small estuaries—I: theory". In: *Ocean Dynamics* 63.11-12, pages 1279–1292.

Wong, K.-C. (1994). "On the nature of transverse variability in a coastal plain estuary". In: *Journal of Geophysical Research: Oceans* 99.C7, pages 14209–14222.

Woodworth, P. (2010). "A survey of recent changes in the main components of the ocean tide". In: *Continental Shelf Research* 30.15, pages 1680–1691.

Yang, W., Wei, H., and Zhao, L. (2017). "Observations of Tidal Straining Within Two Different Ocean Environments in the East China Sea: Stratification and Near-Bottom Turbulence". In: *Journal of Geophysical Research: Oceans* 122.11, pages 8876–8893.

Yeo, I.-K. and Johnson, R. A. (2000). "A new family of power transformations to improve normality or symmetry". In: *Biometrika* 87.4, pages 954–959.

Zazo, C., Goy, J.-L., Somoza, L., Dabrio, C.-J., Belluomini, G., Improta, S., Lario, J., Bardaji, T., and Silva, P.-G. (1994). "Holocene sequence of sea-level fluctuations in relation to climatic trends in the Atlantic-Mediterranean linkage coast". In: *Journal of Coastal Research*, pages 933–945.

Zhang, X., Church, J. A., Monselesan, D., and McInnes, K. L. (2017). "Sea-Level Projections for the Australian region in the 21st Century". In: *Geophysical Research Letters*.

Zhao, Q., Ren, Y., and Wang, J. X. (2018). "Temporal and spatial characteristics of potential energy anomaly in Lake Taihu". In: *Environmental Science and Pollution Research*, pages 1–10.

Becoming natural

Manuel Cobos Budia

Estuaries are places located in the transition region between rivers and seas. Their waters may be used for navigation and fishing and their lands for farming activities. They are among the most productive, complex and vulnerable ecosystems on Earth. Despite their fragility, they have been suffering the effects of many human interventions, such as the occupation of plains, modification of channels, meander cuts and deepening works and control of the flowing water. This situation has been a constant source of conflict of interests and competencies between users and the administration due to the adoption of uncoordinated and inefficient management decisions. The Guadalquivir River Estuary, located in the southwest of Spain, is a hot spot that is not alien to this situation. The future of the GRE in the shadow of climate change adds more uncertainty to the current critical situation. In this context, the main objective of this thesis is to analyze and characterize the dynamics of the GRE by developing a model for the analysis of the temporal and spatial variation of the longitudinal anomaly of the potential energy. The model can be used with management purposed to improve the water quality of the estuary.

2020